

UNIVERSITY OF BIRMINGHAM

DEVELOPMENT OF GELATIN-SILICA HYBRID HYDROGELS FOR BONE TISSUE ENGINEERING AND *IN VITRO* MODELLING

by

FRANCESCA K LEWNS

A thesis submitted to the University of Birmingham for the degree of DOCTOR OF PHILOSOPHY

School of Dentistry
College of Medical and Dental Sciences
University of Birmingham

March 2024

UNIVERSITY OF
BIRMINGHAM

University of Birmingham Research Archive

e-theses repository

This unpublished thesis/dissertation is copyright of the author and/or third parties. The intellectual property rights of the author or third parties in respect of this work are as defined by The Copyright Designs and Patents Act 1988 or as modified by any successor legislation.

Any use made of information contained in this thesis/dissertation must be in accordance with that legislation and must be properly acknowledged. Further distribution or reproduction in any format is prohibited without the permission of the copyright holder.

This thesis is dedicated to my Grandad who sadly passed away during the final year of my PhD, in loving memory.

ABSTRACT

Naturally derived biopolymers have received considerable attention for use as hydrogel materials for tissue engineering due to their innate ability to mimic the natural extracellular matrix. However, low mechanical strength and uncontrolled degradation limit their use within bone tissue engineering applications. Hybrid hydrogels are interpenetrating networks of organic and inorganic moieties and, when made via sol-gel processing, present an attractive route to address the drawbacks of biopolymers. Hybrid hydrogels can be classified as Class I (weak non-covalent interactions) and Class II (covalent bonds) depending on the interactions between the organic and inorganic component. This thesis presents the development of gelatin-silica organic-inorganic hybrid hydrogels using various organosilane crosslinkers, including 3-glycidyloxypropyl trimethoxysilane (GPTMS) and 3-mercaptopropyl trimethoxysilane (MPTMS), to functionalise gelatin to provide covalent coupling of the organic and inorganic moieties. The efficiency and degree of functionalisation of gelatin with GPTMS, an epoxide-containing organosilane crosslinker, were studied with various techniques (^{1}H NMR spectroscopy, ninhydrin assay and titration). Significant challenges with the functionalisation reaction, including hydrolysis and condensation of trimethoxysilyl groups, led to a lack of efficiency and low degree of functionalisation. Thiol-ene click chemistry was therefore used to develop a novel alternative method to synthesise organosilane-functionalised gelatin. The reaction of norbornene-functionalised gelatin (GelNB) and MPTMS was rapid, reaching completion in less than 30 seconds using a 2:1 thiol- : -ene ratio and 0.03 wt% of photoinitiator, LAP. Mechanical tests revealed the yield stress and toughness significantly increased in Class II hydrogels during ageing, suggested to be due to the continuous formation of a covalent network. However, the compressive mechanical properties of the hybrid systems (<10 kPa) were still far from those of bone (15 to

20 MPa). CryoSEM imaging revealed subtle differences in the microarchitectures of the different hydrogel formulations. When seeded on the Class II hydrogels, Saos-2 cells demonstrated improved cell spreading over a seven-day culture when imaged using actin/DAPI staining and cell penetration to depths of up to ~2300 μm as observed by light sheet fluorescence microscopy, compared to the Class I hydrogel. It is hypothesised that the dynamic mechanical properties and differences in microarchitecture of the Class II hydrogels, compared to Class I, were able to influence cell behaviour. Thus, the hybrid materials developed in this thesis could be utilised in soft tissue applications, as well as minimally invasive injectable hydrogels in spinal fusion and fracture repair.

ACKNOWLEDGEMENTS

I would like to thank my supervisors, Dr Gowsihan Poologasundarampillai, Dr Liam Cox, Professor Liam Grover and Professor Ricky Wildman for their time, support, and guidance throughout my PhD. I am particularly grateful for Dr Liam Cox who was not originally part of my supervisory team but joined when I needed extra support within his area of expertise. A further thanks to the MRC for the financial support provided as part of the Integrated Midlands Partnership for Biomedical Training Doctoral Training Programme.

A huge thanks to the technicians at the School of Dentistry – particularly Helen Wright, Lisa Shriane and Jianguo Liu – for being there to teach, help and support me with all my lab work and answer the many questions I had. My time in the labs was difficult but it was made easier by all of you. I was incredibly fortunate to share an office and lab with a group of amazingly talented, bright and friendly researchers at the School of Dentistry. Thank you for being such kind colleagues and friends – and listening to me stress and rant over many a lunchtime! It was a pleasure to share my journey with you, but also to share all your journeys too.

Thank you, Paris – my business partner but also a great friend. Bloomwise was a huge, but wonderful, surprise whilst doing this PhD and I'll always be grateful for the exciting experiences we have shared. To my three best friends, Amy, Evie and Emily, that moved to Birmingham to live with me when I started my PhD and were there from day one. From the Colin the Caterpillar you got me when I passed my first annual progress review, to sending me voice notes to check in with me during write up, your support has never gone unnoticed.

I want to thank my mum, dad, sisters, and grandparents, for providing moral support and being a sounding board when required. I feel lucky to know that I always had that support system in the background. I think you will probably all be glad that this is over, and you don't have to try and explain to people what I actually do anymore.

Finally, I cannot express how grateful I am to Matt, my partner, for his unwavering emotional and practical support throughout this experience. There's been lots of highs and lows, but you've been there every step of the way championing me and I genuinely could not have got through this without you.

TABLE OF CONTENTS

CHAPTER 1. INTRODUCTION 1

1.1. The Barriers to Bone Tissue Engineering 3
1.2. Biomaterial challenges: material properties 6
1.2.1. Cell attachment and organisation 8
1.2.2. Cell growth: migration, proliferation and differentiation 9
1.2.3. Bone tissue deposition and remodelling 16
1.2.4. Concluding remarks 21
1.2.5. Thesis aims 21

CHAPTER 2. INTERACTION OF GLYCOL-MODIFIED SILANES WITH GELATIN IN GELATIN-SILICA HYBRID HYDROGELS 23

2.1. Introduction 24
2.1.1. Hybrid hydrogels 24
2.1.2. Sol-gel 25
2.1.3. Issues with sol-gel for encapsulation of a protein/biomolecule 30
2.1.4. Aims and objectives 33
2.2. Methods 35
2.2.1. Transesterification of polyol-modified silane precursors 35
2.2.2. Interactions of gelatin- and silica-based components 38
2.2.3. Synthesis of gelatin-silica hybrid hydrogels 42
2.2.4. Chemical characterisation 43
2.2.5. Hydrogel degradation properties 44
2.3. Results and discussion 46
2.3.1. Chemical characterisation of polyol-modified silane structure and reaction kinetics 46
2.3.2. Chemical characterisation of GelMA 54
2.3.3. Characteristics of hydrogels with varying compositions 55
2.3.4. Chemical characterisation of hybrid hydrogels 67

2.3.5. Degradation behaviour of gelatin-based-silica hybrid hydrogels *69*
2.4. Summary 75

CHAPTER 3. INVESTIGATING AND OPTIMISING GELATIN FUNCTIONALISATION WITH EPOXIDE ELECTROPHILES 76

3.1. Introduction 77
3.1.1. GPTMS as a coupling agent *77*
..... *80*
3.1.2. Formation of GPTMS-functionalised gelatin *80*
3.1.3. Issues with GPTMS functionalisation reactions *85*
3.1.4. Aims and objectives *88*
3.2. Methods 90
3.2.1. Materials *90*
3.2.2. Attempted preparation of GPTMS functionalised gelatin (Gel-GP) *91*
3.2.3. Attempted preparation of AGE functionalised gelatin (Gel-AGE) *92*
3.2.4. Post-reaction processing – removal of unwanted small molecules *93*
3.2.5. Hydrogel formulation: formation of Class I and Class II hybrids *94*
3.2.6. Hydrogel degradation properties *95*
3.2.7. Alternative functionalisation reaction conditions *95*
3.2.8. Characterisation of Gel-GP *96*
3.2.9. Statistical analysis *97*
3.3. Results and Discussion 98
3.3.1. GPTMS-gelatin functionalisation study *98*
3.3.2. Gelatin and GPTMS ^{1}H NMR spectra *104*
3.3.3. AGE-gelatin functionalisation study *113*
3.3.4. Dialysis: a post reaction processing method *118*
3.3.5. Dialysis of AGE-based functionalisation products *125*
3.3.6. Degradation behaviour of gelatin-silica hybrid hydrogels *131*
3.3.7. Extending reaction time in an attempt to increase extent of gelatin functionalisation *135*
3.4. Summary 143

CHAPTER 4. NOVEL SYNTHESIS OF GELATIN-BASED HYBRID HYDROGELS FORMED VIA THIOL-NORBORNENE CLICK CHEMISTRY 146

4.1. Introduction 147
4.1.1. Thiol-ene click chemistry 147
4.1.2. GelNB hydrogels formed via thiol-ene reaction for sol-gel processing 157
4.1.3. Aims and objectives 158
4.2. Methods 160
4.2.1. Materials used for functionalisation and hydrogel preparation 160
4.2.2. GelNB functionalisation preliminary study 160
4.2.3. GelNB functionalisation optimisation study 163
4.2.4. Fabrication of GelNB-Silica hydrogels 164
4.2.5. Hydrogel degradation properties 166
4.2.6. Mechanical characterisation – compressive properties of hybrid hydrogels 168
4.2.7. Rheological properties of hybrid hydrogels 172
4.2.8. Structural characterisation 174
4.2.9. Biological characterisation 175
4.2.10. Cell location 179
4.2.11. Statistical analysis 182
4.3. Results and discussion 183
4.3.1. GelNB functionalisation preliminary study 183
4.3.2. GelNB functionalisation optimisation study 188
4.3.3. GelNB-silica hydrogels 193
4.3.4. Degradation behaviour of GelNB-silica-based hydrogels 196
4.3.5. Mechanical characterisation – compressive properties of hybrid hydrogels 202
4.3.6. Rheological properties of hybrid hydrogels 216
4.3.7. Architectural characterisation 225
4.3.8. Biological characterisation 229
4.4. Summary 242

CHAPTER 5. SUMMARY OF RESULTS AND CONCLUDING REMARKS 243

5.1. Summary of results 243

5.2. Limitations 246
5.2.1. Materials used and their limitations 246
5.2.2. Potential adverse cell-material interactions 247
5.3. Concluding remarks 247

CHAPTER 6. FUTURE WORK 249

C.4.2.2. GelNB-MPTMS functionalisation reaction controls 296
C.4.3.1.4. GelNB-MPTMS functionalisation reaction controls 296

LIST OF FIGURES

Figure 1. a) Bone structure, from whole bone to cortical and trabecular bone with vascularisation which cannot be recapitulated by current models. Current in vitro models of highly organised bone-like structures – b) brightfield image and enlarged inset showing a bone-like structure with c) confocal image of mineralised bone structure at day 28, d) highly dendritic osteocyte-like networks with osteocytes embedded within mineralised lacunae, e) confocal microscopy shows the 3D bone-like structures and layers of interconnected osteocytes. Reproduced (Adapted) under the terms of the CC-BY license. 2020 (19). f) Long-term in vitro model of osteocyte with images demonstrating the development of bone matrix and mineralisation over time (12 days to 1 year). Reproduced (Adapted) under the terms of the CC-BY license. 2018 (20). g) Schematic illustration of approaches employing hydrogels in BTE, combining hydrogels e.g. natural or synthetic, cells e.g. MSCs, and growth factors e.g., bone morphogenetic protein 2, with 3D bioprinting to lead to tissue maturation. Created on the BioRender website (https://biorender.com) by the authors. 4

Figure 2. a) Illustration of the biophysical cues of a microenvironment that impact cell behaviour, including stiffness and viscoelasticity, which are involved in mechanotransduction, degradation, and 3D architecture, including nanotopography. b) Cellular processes of mechanosensing and response with several biological components, not mutually exclusive, depicted in a bone cell such as an osteocyte. Created on the BioRender website (https://biorender.com) by the author. 7

Figure 3. a,b) Effect of hydrogel stiffness and c–f) viscoelasticity on cellular response. a) A biomimetic gradient for osteochondral tissue regeneration. Created on the

BioRender website (https://biorender.com) by the author. b) MSCs stained for actin cytoskeleton on three different gels: LMWGs, LMWG-poly(ethylene glycol) diacrylate (PEGDA), and PEGDA gels for 14 days. Reproduced (adapted) with permission (57). Copyright 2021, Elsevier. c) Schematic showing molecular weight (MW) of alginate crosslinked by calcium with entanglement and connectivity of the network, with both molecular weight and PEG spacers increasing the rate of stress relaxation (68). Created on the BioRender website (https://biorender.com) by the author. d) The effect of a 3D matrix on a cell – resulting in forces and stresses acting on the cell. When forces are maintained, there is no remodeling, whereas, if there are cycles of stress and strain relaxation it results in cell spreading (68). Created on the BioRender website (https://biorender.com) by the author. e) Chemical structure of an aliphatic hydrazone-linked hydrogel, showing reversible gelation (76). f) Dynamic nature of the aliphatic hydrazone-linked hydrogel results in filopodia and lamellipodia extension, facilitating cytoskeletal outgrowth. Reproduced with permission (76). Copyright 2014, Wiley-VCH GmbH. 11

Figure 4. Role of a, b) hydrogel viscoelasticity and c) degradation on remodelling, a) Day 3 LIVE/DEAD showing increased spreading in thiol-containing hydrogels, and b) cell shape on day 3, remaining rounded in the control and spread in excess thiol hydrogels. Reproduced (adapted) with permission (77). Copyright 2023, Elsevier. c) Degradation, with focus on degradation fraction and cleavage rate on endothelial network formation. Reproduced (adapted) with permission (98). Copyright 2023, American Chemical Society. 14

Figure 5. Classes of organic-inorganic hybrid hydrogels. Class I hydrogels have organic and inorganic components embedded within one another, with weak non-covalent

interactions. Class II hydrogels have organic and inorganic networks linked by covalent bonds. Created on the BioRender website (https://biorender.com) by the author. 25

Figure 6. Representation of the sol-gel process. A solution of precursors containing a metal alkoxide and H_2O undergoes hydrolysis and condensation to result in chain growth, leading to gelation and a self-supporting gel through an increase in viscosity. Created on the BioRender website (https://biorender.com) by the author. 26

Figure 7. Transesterification apparatus set-up. Created on the BioRender website (https://biorender.com) by the author. 36

Figure 8. ^1H NMR spectra of starting reagents TEOS and GL (D_2O solvent), as well as GLMS after 20 minutes, 1, 2, and 6 hours, followed by the final sample at 8 hours ($CDCl_3$, 400 MHz). Both signals from TEOS at δ_H = 3.75 ppm (a_1) and δ_H = 1.15–1.20 ppm (a_2) for the protons on CH_2 and CH_3, respectively, are not present by the final sample. The GL resonances between δ_H = 3.20–3.45 ppm (b_1 and b_2) correspond to the protons in CH and CH_2 groups, respectively, which are present in the final sample. These changes in the resonances suggests that alcohol exchange of the ethoxy groups of TEOS with GL had occurred. The reaction scheme and a suggested chemical structure of GLMS is shown. 47

Figure 9. Resonance intensity (a.u.) of CH_2 (a_1, 3.75 ppm) and CH_3 (a_2, 1.15–1.20 ppm) in TEOS over time, using δ_H = 3.20–3.45 ppm GL resonance as 1.00 standard. 49

Figure 10. ^1H NMR spectra of starting reagents TEOS and PG (D_2O solvent), as well as PGMS after 20 minutes, 1, 2, and 6 hours, followed by the final sample at 8 hours ($CDCl_3$, 400 MHz). Both signals from TEOS at δ_H = 3.85 ppm (a_1) and δ_H = 1.20 ppm (a_2) for the protons on CH_2 and CH_3, respectively, reduced in relative area

during the reaction. The signals at δ_H = 3.55 ppm (b_1), 3.35 ppm (b_2), and 1.10 ppm (b_3) correspond to the CH_3, CH_2 and CH groups in PG, respectively. which are present in the final sample. These changes in the resonances suggests that alcohol exchange of the ethoxy groups of TEOS with propylene glycol occurred. The reaction scheme and a suggested chemical structure of PGMS is shown. 50

Figure 11. Resonance intensity (a.u.) of CH_2 (a_1) and CH_3 (a_2) in TEOS over time, using δ_H = 3.55 ppm PG resonance as 1.00 standard. 52

Figure 12. ^{1}H NMR spectra of starting reagents GPTMS and PG (D_2O solvent), as well as GPTPGS after 20 minutes, 1, 2, 4, and 6 hours, followed by the final sample at 8 hours ($CDCl_3$, 400 MHz). The reduction in δ_H = 3.55 ppm (a_1) for the protons on the CH_3 methoxy group of GPTMS suggests exchange of methoxy groups occurred. All other resonances from GPTMS and PG remained throughout the reaction. The reaction scheme and a suggested chemical structural of GPTPGS is shown. 53

Figure 13. Resonance intensity (a.u.) of a_1, $_2$, $_3$, and $_4$ in GPTMS and c_1 from the production of MeOH, using δ_H = 3.55 ppm PG resonance as 1.00 standard. 54

Figure 14. ^{1}H NMR spectra of unmodified gelatin (Gelatin) and methacryloyl functionalised gelatin (GelMA) (D_2O, 400 MHz). 55

Figure 15. Visualisation of hybrid hydrogels. The following variables were altered to result in different compositions; gelatin type (gelatin, GelMA, Gel-GPTPGS or GelMA-GPTPGS), O:I ratio, media/water, and silica source with varying components, with numbers (#) corresponding to Table 2 . The variable colour is a result of different components used in the hydrogel formulation. Generally, hydrogels where the wt% of organic and inorganic a similar e.g. 40:60 and 60:40, precipitated, phase

separated and were opaque, whereas all transparent hydrogels that gelled did not phase separate. For scale, diameter of the universal tube = 25 mm. 61
Figure 16. Gelation time of Gel-Silica hydrogels with varying O:I. The points plot on each bar represent a repeat measure and errors bars represent the SD (n=3). Ns is shown for clarity, all other comparisons were statistically significant (****; p≤0.0001) [ns = non-significant].....65
Figure 17. FTIR spectra of a GelMA-Silica hydrogel (Class I), Gel-GPTPGS-Silica (Class II) and GelMA-GPTPGS-Silica (Class II) hydrogels and their starting components GelMA, gelatin, GPTPGS, and PGMS (n=3).....68
Figure 18. Mass remaining (%) of GelMA-Silica, Gel-GPTPGS-Silica, and GelMA-GPTPGS-Silica hybrid hydrogel formulations immersed in PBS at 37 ºC over a 28 day time period (n=3). Degradation trend has been split into three distinctive regions; initial, intermediate and plateaued degradation. There was no significant difference in the mass of hydrogel remaining (%) for each formulation at any time point throughout the assay. Inset shows the first 24 hours. Error bars represent the SD (n=3). 71
Figure 19. pH of PBS, with GelMA-Silica, Gel-GPTPGS-Silica, and GelMA-GPTPGS-Silica hybrid hydrogel formulations immersed at 37 ºC over a 28 day time period. pH change has been split into three distinctive regions; initial, intermediate and plateaued degradation. Inset shows the first 24 hours. Error bars represent SD (n=3). 73
Figure 20. Structure of GPTMS. 78
Figure 21. Hydrolysis of the trimethoxysilyl functional group in GPTMS to form Si–OH and subsequent condensation to form Si–O–Si and ultimately a silica network.....79

Figure 22. Epoxide ring opening of GPTMS allows functionalisation of amine-containing and carboxylic acid-containing biopolymers. 80

Figure 23. Gel-GPTMS functionalisation reaction, showing the sources of variation and uncertainties within the reaction reagents, conditions, and characterisation pipeline. Created on the BioRender website (https://biorender.com) by the author. 82

Figure 24. Two mechanisms by which the epoxide of GPTMS can react with gelatin; via hydrogen bonding of a protonated carboxylic acid which activates the epoxide (left) or via a carboxylate to form an ester (right). 83

Figure 25. Competing reactions occurring during reaction of gelatin and GPTMS in aqueous solution; a) hydrolytic ring opening of the epoxide in GPTMS to form a 1,2-diol and b) hydrolysis of the methoxy groups to form MeOH, and condensation of Si–OH to form a silica network. 86

Figure 26. Structure of GPTMS and AGE. 90

Figure 27. Reaction of GPTMS with both amine and carboxylic acid groups on gelatin backbone. 91

Figure 28. Reaction of AGE with both amine and carboxylic acid groups on gelatin backbone. 93

Figure 29. pH as a function of time for reaction of GPTMS and gelatin in, experiment 1: 10 mM $HCl_{(aq)}$ reaction solvent with no intervention measures taken to control the reaction pH; experiment 2: 10 mM $HCl_{(aq)}$ reaction solvent with intervention measures made to manually change the pH to pH 4.9 every 1 hour; and experiment 3: PB reaction solvent. Starting pH of all reactions was 4.9 ± 0.02 (n=3). 101

Figure 30. ^{1}H NMR spectrum of gelatin, with amino acid residues labelled. The resonances correspond to the follow amino acid (type of protons): 1: glycine (α-CH_2),

hydroxyproline (γ-CH); 2: proline (δ-CH_2); 3: arginine (δ-CH_2), histidine (β-CH_2); 4: lysine (ε-CH_2); 5: aspartic acid (β-CH_2); 6: glutamic acid (β- and γ-CH_2), hydroxyproline (β-CH_2); 7: proline (β-, γ- and δ-CH_2), methionine (β-CH_2 and CH_3); 8: alanine (CH_3); 9: valine (γ- and δ-CH_2), leucine (γ- and δ-CH_2), isoleucine (γ- and δ-CH_2) [D_2O, 400 MHz]. The structure of lysine (left) and glutamic acid (right) is shown with corresponding protons labelled (216).....106

Figure 31. ^1H NMR spectrum of GPTMS, with key resonances labelled on the chemical structure ($CHCl_3$, 400 MHz).....107

Figure 32. Schematic showing possible sites of functionalisation – amine (-NH_2) and carboxylic acid (-COOH), with salient groups with for analysis by ^1H-NMR spectroscopy highlighted in green with corresponding resonances labelled from Figure 31.....108

Figure 33. ^1H NMR spectra of starting reagents gelatin (D_2O, 400 MHz) and GPTMS ($CDCl_3$, 400 MHz), and the progressing reaction at 1, 2, and 3 hours in $HCl_{(aq)}$ (D_2O, 400 MHz). Note, the reaction had gelled at 4 and 8 hours and so it was not possible to take a sample. Chemical structures are shown. See Table 3.1 to assign gelatin amino acid structure.....109

Figure 34. Epoxide remaining (%) calculated from relative area of resonances a_3 and a_3* at δ_H = 2.50 and 2.35 ppm (shifting to δ_H = 2.95 and 2.80 ppm) in Gel-GP, reacted in experiment 1, 2 and 3. 111

Figure 35. pH as a function of time for reaction of AGE and gelatin in, experiment 1: 10 mM $HCl_{(aq)}$ reaction solvent with no intervention measures taken to control the reaction pH; experiment 2: 10 mM $HCl_{(aq)}$ reaction solvent with intervention measures made to manually change the pH to pH 4.9 every 1 hour for 8 hours, and then at 24 hour

intervals until 72 hours; and experiment 3: PB reaction solvent. Starting pH of all reactions was 4.9 ± 0.02 (n=3). 114

Figure 36. ^{1}H NMR spectra of starting reagents gelatin (D_2O, 400 MHz) and AGE ($CHCl_3$, 400 MHz), and the progressing reaction at 1, 2, 3, 4, 8, 24, 48 and 72 hours in $HCl_{(aq)}$ (D_2O, 400 MHz). Chemical structures are shown. See table 3.1 to assign gelatin amino acid structure..... 116

Figure 37. Epoxide remaining (%) calculated from relative area of resonances a_3 and a_3* at δ_H = 2.50 and 2.35 ppm (shifting to δ_H = 2.95 and 2.80 ppm) in Gel-AGE, reacted in experiment 1, 2 and 3. 117

Figure 38. ^{1}H NMR spectra of (a) the Gel-GP product from $HCl_{(aq)}$ pH reaction conditions and further dialysis for 96 hours, with key resonances for GPTMS noted (D_2O, 400 MHz). The spectra show the removal of resonances a_3 and a_3*, as well as the MeOH resonance. Other resonances present from GPTMS are difficult to examine due to the complexity of the spectra and resonance overlap. 119

Figure 39. ^{1}H NMR spectra of (a) the Gel-GP product from $HCl_{(aq)}$ reaction conditions and further dialysis reaction for 72 hours, with residual GPTMS and MeOH labelled (arrow) (D_2O, 400 MHz). 120

Figure 40. Schematic illustration of preparation of Gel-GP. GPTMS undergoes ring opening of the epoxide to form an ester (RCOOR'). * represents the protons on the carbon attached to the alkoxide that would have a characteristic downfield chemical shift in the ^{1}H NMR spectrum (h = hours). Part of this figure was created on the BioRender website (https://biorender.com) by the author. 122

Figure 41. ^{1}H NMR spectrum of native gelatin compared with the dialysed Gel-GP products from experiment 1, 2 and 3 (D_2O, 400 MHz). Differences in spectra are indicated with *. Arrows identify resonances for unreacted GPTMS and by-products. 123

Figure 42. ^{1}H NMR spectrum of gelatin and Gel-GP after reaction with GPTMS for 8 hours in $HCl_{(aq)}$ (experiment 1) to form Gel-GP and dialysed for 120 hours. Differences in the spectra are indicated with arrows at 1) δ_H = 0.65 ppm and 2) δ_H = 2.35 ppm corresponding to -CH_2 next to the Si on GPTMS and glutamic acid group on gelatin, respectively (D_2O, 400 MHz). 124

Figure 43. ^{1}H NMR spectra of (a) the Gel-AGE final product from experiment 1 and dialysis reaction for 96 hours, with key resonances for AGE noted (D_2O, 400 MHz). The spectra shows the retention of resonances at a_1, a_2, and a_3, but removal of resonances a_4 and a_4*, corresponding to the epoxide protons in AGE. 126

Figure 44. Schematic illustration of preparation of Gel-AGE. AGE undergoes ring opening of the epoxide to bond with gelatin backbone, forming an ester (RCOOR'). * represents the protons on the carbon of the ester alkoxy group (h = hours). Part of this figure was created on the BioRender website (https://biorender.com) by the author. 127

Figure 45. ^{1}H NMR spectrum of native gelatin compared with the dialysed Gel-AGE products from experiments 1, 2 and 3 (D_2O, 400 MHz). Differences in the spectra are indicated with *. Arrows show unremoved, unreacted AGE and by-products. 128

Figure 46. a) Change in mass of Gel-Silica, Gel-GP-Silica undialysed, and Gel-GP-Silica dialysed hydrogels over a 7-day period in PBS. b) Si species release in PBS, giving Si concentration (μg/ml) in PBS over a 7-day period. Insets of both show the 0–4 hours (n=3). 132

Figure 47. Available primary/secondary amines for Gel-GP after four different functionalisation reactions with varied conditions; pH 5, pH 3, DMSO, and 0.5 wt%. The results were normalised against the control, with the control representing native gelatin within the same solvent, without GPTMS (n=3; * p≤0.05; ** p<0.01).....138

Figure 48. Graphical representation of a titration curve of three solutions: A, B and C. The grey arrows represent where the carboxyl region ends at pH 6.5 on the different solutions. Solution A would have the least free carboxylic acid groups as a shorter portion of the curve is within the carboxyl region, followed by B and then C. The left shift of the curve occurs because the solution requires a lower volume of titrant to be added to cause the carboxyl groups to deprotonate, demonstrating there are less free carboxyl groups in solution (251). 140

Figure 49. Titration curves of a gelatin control compared to different HCl-based functionalisation reactions; a) gelatin control (5 wt%), Gel-GP (pH 5) and Gel-GP (pH 3), and b) gelatin control (0.5 wt%) and Gel-GP (0.5 wt%). Focussing between pH 1.5 and 6.5 (the carboxylic acid region), both titration curves demonstrate a left shift and so decrease in available carboxylic acid groups. 142

Figure 50. Scheme of a photoaddition thiol-ene reaction with an LAP photoinitiator, to form a thioether. 147

Figure 51. Thiol-ene reaction of norbornene functionalised 8arm-PEG with a diothiol functionalised linker to form a synthetic thioether crosslinked hydrogel. The black square represents the chemical structure shown and the bridged cyclic hydrocarbon is the norbornene group. Adapted from Wiley et al. (267). Part of this figure was created on the BioRender website (https://biorender.com) by the author.....149

Figure 52. Scheme of thiol-ene hydrogels with variable degradability, created from controlling the proportions of a MMP cleavable peptide crosslinker and a non-degradable dithiol crosslinker in a norbornene functionalised 4arm-PEG polymer network with CGRGDS (a pendant fibronectin-binding sequence for cell adhesivity). Adapted from Anderson et al. (277). Created on the BioRender website (https://biorender.com) by the author. 151

Figure 53. Light-mediated polymerisation, demonstrating random chain-growth based on methacrylate prepolymers, such as GelMA, and structurally uniform step-growth based on click reactions such as thiol-ene (PI = photoinitiator; UV = ultraviolet; Vis = visible light) (256). Created on the BioRender website (https://biorender.com) by the author. 155

Figure 54. Scheme representation of the proposed thiol-ene reaction of GelNB and MPTMS. 157

Figure 55. Schematic of a) GelNB synthesis, conducted by Claro™, b) thiol-ene reaction of GelNB with MPTMS to form GelNB-MP, c) GelNB-MP-Silica hybrid hydrogel synthesis through the condensation of Si–OH groups on the MPTMS of GelNB-MP with Si–OH groups on PGMS. 161

Figure 56. Form Cure set-up a) closed and b) open for 405 nm light irradiation of the GelNB-MPTMS solution. 162

Figure 57. Chemical structure of 5-Norb. 162

Figure 58. Chemical structure of DTT and (3-mercaptopropyl)trimethoxysilane (MPTMS). 163

Figure 59. Schematic diagram of the hydrogel preparation and manufacturing methods, involving the mixture of DMEM-dH_2O solution (1:1 or 1:2) with PGMS and

vortexing for 15 seconds. GelNB-based solution was then added to the PGMS solution and left to gel and form a self-supporting hydrogel (s= seconds). Created on the BioRender website (https://biorender.com) by the author. 166

Figure 60. Schematic diagram of hydrogel preparation for degradation assay and compression tests. Created on the BioRender website (https://biorender.com) by the author.... 167

Figure 61. Example stress strain curve with the following shown: yield stress; the point at which elastic deformation of a material ends and plastic deformation begins, Young's modulus; stiffness calculated from two points in the linear region at zero tangent, and toughness; the area under the stress strain curve. 170

Figure 62. a) hydrogel sample preparation in acrylic moulds and b) extracted onto a rheometer plate for rheological testing. 173

Figure 63. 96 well plate layout for cell culture experiments; 3CDEF – control (represented as grey), 5CDEF – GelNB-Silica, 7CDEF – GelNB-MP-Silica (1:1), and 9CDEF – GelNB-MP-Silica (1:2). All other wells were filled with PBS to help with evaporation. Created on the BioRender website (https://biorender.com) by the author. 176

Figure 64. Culture dish filled with agar, with a cuboid hydrogel sample in a middle well. Created on the BioRender website (https://biorender.com) by the author..... 180

Figure 65. ^{1}H NMR spectra of GelNB-MPTMS (1:4) reacted with LAP (0.3 wt%) for 30 minutes, 405 nm light. Spectra shown for starting reagents, samples taken pre-irradiation, and 5, 15 and 30 minutes of irradiation (D_2O, 400 MHz). Reaction chemistry is shown with notable resonances δ_H = 2.70 ppm (b) and δ_H = 6.15 ppm (a) labelled. 185

Figure 66. ^{1}H NMR spectra of GelNB-MPTMS (1:4) reacted with LAP (0.3 wt%) for 4 minutes, 405 nm light. Spectra shown for starting reagents, samples taken pre-irradiation, and 10 and 30 seconds, and 1, 2 and 4 minutes of irradiation (D_2O, 400 MHz).....186

Figure 67. ^{1}H NMR spectra of 5-Norb-MPTMS (1:4) reacted with LAP (0.3 wt%) for 4 minutes, 405 nm light. Spectra shown for starting reagents 5-Norb, MPTMS, and LAP, as well as samples taken pre-irradiation, and 10 and 30 seconds, and 1, 2 and 4 minutes of irradiation (D_2O, 400 MHz). Reaction chemistry is shown with notable resonances δ_H = 2.70 ppm (b) and δ_H = 6.15 ppm (a) labelled.....187

Figure 68. ^{1}H NMR spectra of GelNB-MPTMS (1:2) reacted with LAP (0.3 wt%) for 4 minutes, 405 nm irradiation. Spectra shown for starting reagents GelNB, MPTMS and LAP, as well as samples taken pre-irradiation, and 10 and 30 seconds, and 1, 2 and 4 minutes of irradiation (D_2O, 400 MHz).....189

Figure 69. ^{1}H NMR spectra of GelNB-MPTMS (1:2) reacted with LAP a) 0.15 wt% and b) 0.03 wt% for 4 minutes, 405 nm light. Spectra shown for starting reagents GelNB, MPTMS and LAP, as well as samples taken pre-irradiation, and 10 and 30 seconds, and 1, 2 and 4 minutes of irradiation (D_2O, 400 MHz).....190

Figure 70. C=C remaining over time with varying LAP wt% in a GelNB-MPTMS (1:2) thiol-ene reaction irradiated for 4 minutes with 405 nm light. Measured as relative intensity of δ_H = 6.15 ppm corresponding to the two vinyl protons of norbornene. 191

Figure 71. ^{1}H NMR spectra of GelNB, MPTMS, LAP and GelNB-MP product, as well as GelNB-MP dialysed for 24 and 48 hours (D_2O, 400 MHz). Differences in GelNB-MP spectra compared to native GelNB are labelled with *. Signals, corresponding

to excess starting reagents and reaction by-products removed with dialysis are labelled with an arrow. Inset shows the disappearance of the resonances at δ_H = 3.45 ppm and 3.30 ppm from GelNB to GelNB-MP dialysed (d = dialysis; h = hours). 192

Figure 72. Images of the three hydrogel formulations investigated: a) GelNB-Silica (Class I), b) GelNB-MP-Silica (1:1) [Class II] and c) GelNB-MP-Silica (1:2) [Class II], where the ratio represents DMEM:dH_2O. 194

Figure 73. Gelation time of three hydrogel formulations; GelNB-Silica (Class I), GelNB-MP-Silica (1:1) [Class II], and GelNB-MP-Silica (1:2) [Class II], demonstrating a higher ratio of media results in a shorter gelation time. Individual plots are repeat measures and error bars represent SD (n=3; **** $p \leq 0.0001$). 195

Figure 74. Mass remaining after a degradation assay of three hydrogel formulations aged for 1 day and incubated in a) PBS and b) PBS with collagenase, and 7 day aged hydrogels incubated in c) PBS and d) PBS with collagenase at 37 ºC over a 28 day time period. Insets show the first 24 hours of the degradation assay. Error bars represent the SD (n=3). 197

Figure 75. Release profile of silicon from a degradation assay of three hydrogel formulations aged for 1 day and incubated in a) PBS and b) PBS with collagenase, and 7-day aged hydrogels incubated in c) PBS and d) PBS with collagenase at 37 ºC over a 28-day time period. Insets show the first 24 hours of the degradation assay. Error bars represent the SD (n=3). 200

Figure 76. Release profile of gelatin from a degradation assay of three hydrogel formulations aged for 1 day and incubated in a) PBS and b) PBS with collagenase, and 7 day aged hydrogels incubated in c) PBS and d) PBS with collagenase at 37 ºC over a 28

day time period. Insets show the first 24 hours of the degradation assay. Error bars represent the SD (n=3), where * is used n=2.....202
Figure 77. Uniaxial compressive test of hydrogel samples using Bose ElectroForce 5500 Test Instrument equipped with a 200 N load cell.....203
Figure 78. Uniaxial compressive data for three hydrogel formulations a) GelNB-Silica, b) GelNB-MP-Silica (1:1), and c) GelNB-MP-Silica (1:2) aged for 1, 3, 7 and 14 days (d: day). Results presented include i) Stress-strain curve, ii) Yield stress, iii) Young's Modulus, iv) Toughness (AUC), and v) Height of gel (d = day). Note, toughness values are not shown for 7 days because of issues with the quality of data. Error bars represent the SD and non-significance is not shown, p≤0.05 (*), p≤0.01 (**), p≤0.001 (***), and p≤0.0001 (****).....204
Figure 79. Hysteresis loss from three hydrogel formulations aged for 1 day and 7 days, at constant cyclic compression, 20% strain for 20 cycles, a) GelNB-Silica, b) GelNB-MP-Silica (1:1), c) GelNB-MP-Silica (1:2). Note, the different scale for y axis for a). Error bars represent the SD (n=3). 209
Figure 80. Hysteresis loss from the first cycle of constant cyclic compressive loading for three hydrogel formulations aged for a) 1 day and b) 7 days. The points plot on each bar represent a repeat measure and SD is shown (n=3). Non-significance is not shown, p≤0.01 (**), p≤0.001 (***), and p≤0.0001 (****).....210
Figure 81. Hypothesised organic-inorganic structure in the GelNB-Silica-based hydrogels, depicting only weak non-covalent interactions in the Class I GelNB-Silica, but both weak non-covalent and MPTMS-facilitated covalent bonding in the Class II hydrogels, with a higher degree of MPTMS-facilitated covalent bonding in the 1:2

formulation. Created on the BioRender website (https://biorender.com) by the author. 212
Figure 82. Stress-strain curves for incremental cyclic loading of a) GelNB-Silica, b) GelNB-MP-Silica (1:1), and c) GelNB-MP-Silica (1:2), aged for i) 1 day and ii) 7 days. The cyclic envelopes are shown, with the elastic region and strain softening highlighted. The dotted vertical line represents yield stress (n=3). 214
Figure 83. Frequency sweep shear strain controlled curves of a) GelNB-Silica, b) GelNB-MP-Silica (1:1), and c) GelNB-MP-Silica (1:2), aged for i) 1 day and ii) 7 days. G' and G" are shown as a function of frequency. Mean values are shown (n=3 [c-i; n=2]). 218
Figure 84. Amplitude sweep strain controlled curves of a) GelNB-Silica, b) GelNB-MP-Silica (1:1), and c) GelNB-MP-Silica (1:2), aged for i) 1 day and ii) 7 days. G' and G" are shown as a function of strain. Mean values are shown (n=3). 221
Figure 85. Single frequency time sweep showing gelatin kinetics of a) GelNB-Silica, b) GelNB-MP-Silica (1:1), and c) GelNB-MP-Silica (1:2). The arrows represent the crossover point in each hydrogel formulation (n=3). 223
Figure 86. Representative cryo-SEM images of the GelNB-MP-Silica (1:1) hydrogel aged for 7 days, with sublimation time during sample preparation varied; a) 30 seconds, b) 1 minute, c) 2 minutes, and d) 6 minutes. Images were taken at variable magnification (a) 20,000x; b) 25,000x; c) 35,000x; and d) 25,000x. All are shown with a 5 μm scale bar. 226
Figure 87. Representative cryo-SEM images of the inorganic and organic component of the GelNB-silica-based hydrogels; a) hydrolysed and condensed silica network from PGMS, and b) irradiated GelNB with DTT as the crosslinker (to ensure gelation for

experimental set-up). Images were taken at 10,000x magnification. Both are shown with a 10 μm scale bar. 227

Figure 88. Representative cryo-SEM images of GelNB-Silica, GelNB-MP-Silica (1:1), and GelNB-MP-Silica (1:2), aged for 1 day and 7 days. Images were taken at 50,000x magnification. All images are shown with a 3 μm scale bar. Insets demonstrate a magnified sample of the image. 228

Figure 89. Representative confocal fluorescence microscopy images of 2D-cultured Saos-2 cells for LIVE/DEAD staining on a tissue plastic culture control and three hydrogel formulations; GelNB-Silica, GelNB-MP-Silica (1:1), and GelNB-MP-Silica (1:2) at 1, 3, 5 and 7 days of culture. Images were taken using 494/517 nm (excitation/emission [calcein; live]) and 528/617 nm excitation/emission [ethidium homodimer-1; dead]). An illustration of the live cells at day 7 is presented. Scale bar = 100 μm (biological repeats n=2, technical repeats n=3 due to time constraints). Part of this figure was created on the BioRender website (https://biorender.com) by the author. 230

Figure 90. Saos-2 cell viability (%) from LIVE/DEAD at day 1 and day 3 of culture, the control was carried out on tissue culture plastic. Images were taken using confocal fluorescence microscopy and counted with Image J. The points plot on each bar represent the repeat measures and the error bars represent the SD (biological repeats n=2, technical repeats n=3 due to time constraints). 232

Figure 91. Mean metabolic activity of Saos-2 cells cultured for 14 days on a control (tissue culture plastic), and three hydrogel formulations; GelNB-Silica, GelNB-MP-Silica (1:1) and GelNB-MP-Silica (1:2). The points plot on each bar represent a repeat

measure and the error bars represent the SD (biological and technical repeats n=3). 233

Figure 92. Actin/DAPI images of Saos-2 cells cultured for 1, 4, 7 and 14 days on three hydrogel formulations; GelNB-Silica, GelNB-MP-Silica (1:1) and GelNB-MP-Silica (1:2) and a control (tissue culture plastic). Phalloidin was used to stain the actin cytoskeleton and DAPI to stain the cell nuclei. Fluorescence images taken with confocal fluorescence microscopy of actin and nuclei at 495/518 nm (actin) and 358/461 (DAPI). The images were collected with a magnification of 20x and the scale bar = 50 μm (biological and technical repeats n=3). 235

Figure 93. Representative images taken from Alizarin Red S staining of Saos-2 cells cultured for 14 days on a) control (tissue control plastic, b) GelNB-Silica, c) GelNB-MP-Silica (1:1) and d) GelNB-MP-Silica (1:2). Insets represent the blank images taken for each condition, where no cells were cultured. Images were taken at 10x magnification, and the scale bar represents 500 μm (biological and technical repeats n=3). 238

Figure 94. Representative light sheet fluorescence microscopy data for Saos-2 cells cultured on a) GelNB-Silica, b) GelNB-MP-Silica (1:1) and c) GelNB-MP-Silica (1:2) for 7 days, showing i) a 3D scatterplot of cell location within hydrogel samples and ii) the frequency of cells at a specific cell penetration. Note the different axis scale for different samples (biological and technical repeats n=3).. 240

LIST OF TABLES

Table 1. Hydrogel formulations, varying gelatin type (gelatin, GelMA, Gel-GPTPGS or GelMA-GPTPGS), O:I, solvent (media or dH_2O), and silica source (GLMS or PGMS). Note, the contribution of organic and inorganic from GPTPGS was included in the O:I ratio. 41

Table 2. Gelation characteristics of 17 different compositions of gelatin-based-silica hybrid hydrogels. The following variables were altered to result in numerous different compositions; gelatin type (gelatin, GelMA, Gel-GPTPGS, or GelMA-GPTPGS), O:I ratio, solvent (DMEM or dH_2O), and silica source. When dH_2O was used, the same protocol as Section 2.3 was used to synthesise the hydrogels. Gelation time, phase separation, appearance, and pH change were investigated. Results were highlighted grey if the hydrogel gelled, did not phase separate, and was transparent in appearance as these properties were key for further use of the hydrogels. Gelation time and pH transition were performed in triplicate and the average is shown. 58

Table 3. Identification of the amino acids in gelatin and their respective chemical shift in ^1H NMR spectrum in D_2O. Modified from (217). 105

Table 4. Different hydrogel formulations developed, with varying GelNB source (GelNB or GelNB-MP) and DMEM:dH_2O content. 165

Table 5. G' and G" at 0.1 and 1 Hz, derived from a frequency sweep of three hydrogel formulations; GelNB-Silica (Class I), GelNB-MP-Silica (1:1) [Class II], and GelNB-MP-Silica (1:2) [Class II]. *Corresponds to the non-linear G" as observed in Figure 83b-i). Mean values are shown, along with SD (n=3 [c-i; n=2]). 219

ABBREVIATIONS AND ACRONYMS

^{13}C NMR	carbon-13 nuclear magnetic resonance
^{1}H NMR	proton nuclear magnetic resonance
^{29}Si MAS NMR	^{29}Si magic angle spinning nuclear magnetic resonance
2D	two-dimensional
3D	three-dimensional
5-Norb	5-Norbornene-2-carboxylic acid
a.u.	arbituary unit
ADA	alginate dialdehyde
AGE	allyl glycidyl ether
ALP	alkaline phosphatase
APTES	(3-aminopropyl) triethoxysilane
ASC	adipose-tissue stem cell
AUC	area under curve
BCA	bicinchoninic acid
BMP-2	bone morphogenetic protein-2
BSA	bovine serum albumin
BTE	bone tissue engineering
$CaCl_2$	calcium chloride
$CDCl_3$	deuterated chloroform
CF	coupling factor
CryoSEM	cryogenic scanning electron microscopy
CTLS	Cleared Tissue Light Sheet
D_2O	deuterium oxide
DAPI	4′,6-diamidino-2-phenylindole

DGS	diglycerylsilane
dH_2O	deionised water
DLS	dynamic light scattering
DMEM	Dulbecco's modified eagle medium
DMSO	dimethyl sulfoxide
DoF	degree of functionalisation
DoS	degree of substitution
dPBS	Dulbecco's phosphate-buffered saline
DSC	differential scanning calorimetry
DTT	dithiothreitol
ECM	extracellular matrix
EGMS	ethylene glycol modified silane
FA	focal adhesion
FBS	fetal bovine serum
FTIR	Fourier-transform infrared
G'	storage modulus
G"	loss modulus
GelMA	gelatin methacryloyl
GelNB	gelatin norbornene
GelSH	thiolated gelatin
GF	growth factor
GL	glycerol
GLMS	glycerol-modified silane
GPTMS	3-glycidyloxypropyl trimethoxysilane
GPTPGS	propylene glycol-modified GPTMS

HA	hyaluronic acid
hASC	human adipose-derived stem cell
hBMSC	human bone marrow mesenchymal stem cells
HBSS	Hanks Balanced Salt Solution
HCl	hydrochloric acid
$HCl_{(aq)}$	aqueous hydrochloric acid
HDMEC	human dermal microvascular endothelial cell
HEK	human embryonic kidney
HMBC	Heteronuclear Multiple Bond Correlation
hMSC	human mesenchymal stem cell
I2959	Irgacure 2959
ICP-OES	Inductively Coupled Plasma Optical Emission spectroscopy
iPSC	induced pluripotent stem cell
IR	infrared
ISO	International Organisation for Standardisation
LAP	lithium phenyl-2,4,6-trimethylbenzoylphosphinate
LVE	linear viscoelastic
MA	methacrylic anhydride
MeOH	methanol
MMP	matrix metalloproteinase
MPTMS	3-mercaptopropyl trimethoxysilane
MSC	mesenchymal stem cell
NA	numerical aperture
Na_2CO_3	sodium carbonate
$NaHCO_3$	sodium bicarbonate

NaOH	sodium hydroxide
ns	non-significance
O:I	organic:inorganic ratio
OCN	osteocalcin
OPN	osteopontin
PAH	polyallylamine hydrochloride
PB	phosphate buffer
PBS	phosphate-buffered saline
PEG	poly(ethylene glycol)
PEGDA	poly(ethylene) glycol diacrylate
PFA	paraformaldehyde
PG	propylene glycol
PGMS	propylene glycol-modified silane
PGS	polyglycerol silicate
pI	isoelectric point
PLL	poly-L-lysine
PMS	polymethyl silicate
PTH	parathyroid hormone
RGD	arginine-glycine-aspartic acid
ROS	reactive oxygen species
Saos-2	sarcoma osteogenic
SAXS	small-angle X-ray scattering
SD	standard deviation
SEM	scanning electron microscopy
SF	silk fibroin

Si–O–Si	siloxane
Si–OH	silanol
SWA	single-wavelength array
TEOS	tetraethyl orthosilicate
TGA	thermogravimetric analysis
TMOS	tetramethyl orthosilicate
TRIS	trisaminomethane
UV	ultraviolet
VEGF	vascular endothelial growth factor
WR	working reagent
XRD	X-ray diffraction

Commonly used functionalisation and hydrogel abbreviations

Gel-AGE	AGE functionalised gelatin
Gel-GP	GPTMS functionalised gelatin
Gel-GP-Silica	GPTMS functionalised gelatin-silica hybrid
Gel-GPTPGS	GPTPGS-functionalised gelatin
Gel-GPTPGS-Silica	GPTPGS functionalised gelatin-silica hybrid
Gel-Silica	gelatin-silica hybrid
GelMA-GPTPGS	GPTPGS-functionalised GelMA
GelMA-GPTPGS-Silica	GPTPGS-functionalised GelMA-silica hybrid
GelMA-Silica	GelMA-silica hybrid
GelNB-MP	MPTMS functionalised GelNB
GelNB-MP-Silica	MPTMS functionalised GelNB-silica hybrid
GelNB-Silica	GelNB-silica hybird

CHAPTER 1. INTRODUCTION

This section is adapted from the review paper 'Hydrogels and Bioprinting in Bone Tissue Engineering: Creating Artificial Stem Cell Niches for In Vitro Modelling' by Lewns et al. (1) *published in Advanced Materials (2022).*

Bone is a highly complex, active, and hierarchically structured tissue formed of different types of bone cells and calcified collagen matrix, structured from the nano- to the macroscale (2,3). Its dynamic and vascularised nature means it undergoes constant remodelling (4). Bone can be categorised into two different types of tissue: cortical and trabecular bone, both of which have a rich abundance of vascular supply (5,6). Vascularisation plays a key role in bone formation and remodelling processes, contributing to the immigration of mesenchymal stem cells (MSCs), the supply of oxygen and nutrients to metabolically active tissues, and the removal of waste by-products (7,8). Specific vascular microenvironmental niches also support tissue-resident unique adult stem cells, key to bone formation and remodelling (9). Without vascularisation and specific vasculature, the formation of new functional bone tissue is not possible. Historically, bone tissue engineering (BTE) has concentrated on regeneration, focusing on creating implants using scaffolds, cells, mechanical stimuli, and soluble factors for patients with significant bone defects. Due to bone's natural ability to regenerate and remodel, tissue-engineered bone-like structures can stimulate regeneration even if they do not mimic the intricate extracellular matrix (ECM) structure of real human bone. There is currently a growing interest in the application of BTE for *in vitro* three-dimensional (3D) human models of healthy and pathological bone for drug development and systemic interactions. However, current models are unable to accurately model bone hierarchy and perfusable vasculature. Therefore, the development of more sophisticated models needs to be explored.

Creating an *in vitro* mimic in which hierarchical structures and properties are replicated wherein the various cell cohorts are assembled and orchestrated to form functional bone remains a major challenge for BTE. The *in vitro* fabrication of bone tissue requires the use of a material that can support sufficient diffusion of oxygen, nutrients, and cell metabolites to

maintain cell viability throughout. Hydrogels are hydrophilic 3D polymeric networks that have the ability to mimic the natural ECM, support cell attachment, proliferation, and differentiation, and enable oxygen and nutrient exchange, and because of this, they have received considerable attention for use as a suitable material for BTE (10,11). Hydrogels can be made from natural or synthetic polymeric substances, with their structure controlled by two types of crosslinking chemistry existing in the macromolecular chain: chemical or physical. Moreover, it is possible to finely tune hydrogel properties, such as viscoelasticity, to tightly regulate stem cell behaviour (12–15). When hydrogels and their stem cell directive cues are implemented together with an appropriate method to produce constructs, such as 3D bioprinting (the precise positioning of biological molecules, biomaterials, and cells in a complex 3D architecture with spatial control of the constituents), there is the potential to take both biological and structural complexity to another level of hierarchy to create a complex architecture that is analogous to that found in bone (16–18). The following sections provide an overview of the important roles that both hydrogels play in achieving biological and structural complexity in bone tissue mimics and their responsibilities in directing stem cells to recapitulate the stem cell niche.

1.1. The Barriers to Bone Tissue Engineering

BTE requires several components, including stem cells, appropriate stimuli, and scaffolding, along with a manufacturing process to assemble these components, and a tissue-maturation process that allows self-organisation into a complex architecture, from whole bone to cortical and trabecular bone whilst enabling vascularisation (Figure 1a). Thus, dynamic presentation of biophysical and biochemical cues to direct bone formation and remodelling via scaffolds and signals must be homogenised with both the manufacturing process and the maturation

phase. At present, it is possible to engineer *in vitro* several structures of bone hierarchy individually (2).

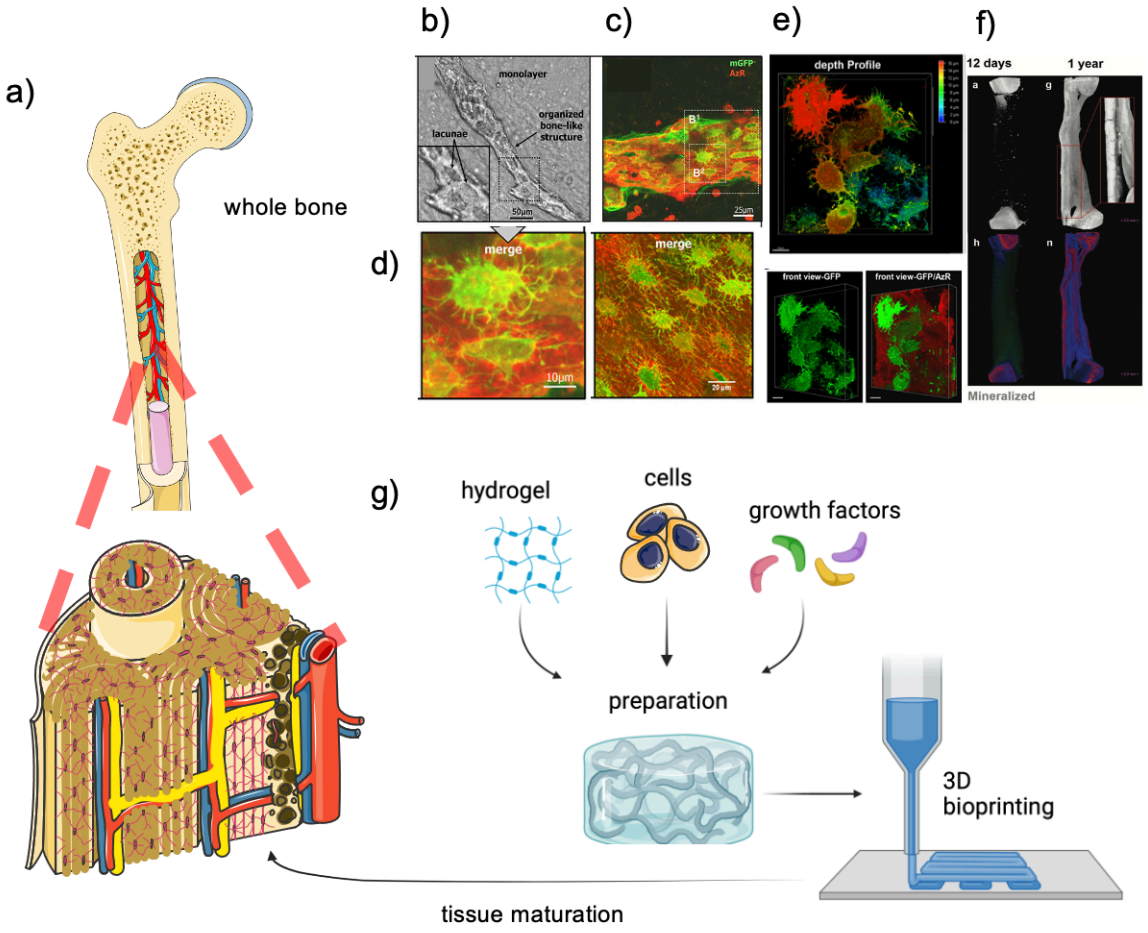


Figure 1. a) Bone structure, from whole bone to cortical and trabecular bone with vascularisation which cannot be recapitulated by current models. Current in vitro models of highly organised bone-like structures – b) brightfield image and enlarged inset showing a bone-like structure with c) confocal image of mineralised bone structure at day 28, d) highly dendritic osteocyte-like networks with osteocytes embedded within mineralised lacunae, e) confocal microscopy shows the 3D bone-like structures and layers of interconnected osteocytes. Reproduced (Adapted) under the terms of the CC-BY license. 2020 (19). *f) Long-term in vitro model of osteocyte with images demonstrating the development of bone matrix and mineralisation over time (12 days to 1 year). Reproduced (Adapted) under the terms of the CC-BY license. 2018* (20). *g) Schematic illustration of approaches employing hydrogels in BTE, combining hydrogels e.g. natural or synthetic, cells e.g. MSCs, and growth factors e.g., bone morphogenetic protein 2, with 3D bioprinting to lead to tissue maturation. Created on the BioRender website (https://biorender.com) by the authors.*

Wang et al. (19) highlighted the need for new tools and cell models to understand the biology of osteocytes. An osteogenic and osteocyte cell model was created, capable of differentiating from osteoblast to early osteocyte to mature osteocyte, and also forming 3D mineralised bone-like structures similar to those seen *in vivo*. Using confocal and electron microscopy, lacunocanalicular ultrastructure and 3D spacing of *in vivo* osteocytes was observed (Figure 1b–e). The cell model expressed early, differentiation and late osteocyte markers, as well as producing a mineralised type I collagen matrix (19).

Iordachescu and colleagues created a micro-organ model that functions as a complete unit that can detect and recapitulate in fine detail the early stages of cellular processes, including bone resorption and the subsequent osteo-proliferation and mineral deposition (Figure 1f) (20). Also, it has also been possible to create an organoid *in vitro* model that mimics osteogenesis both in physiological and pathological situations, as demonstrated by the Iordachescu and Hofmann groups (21,22). Reader is directed to reviews involving co-culture of osteoblasts and osteoclasts to generate bone (23,24).

Despite recent advances, there remain obstacles for functional BTE (19,20,25–28). BTE has not delivered tissue mimics containing mature lamella bone together with the appropriate vascular tree structure and bone marrow. This is primarily due to three principal barriers:

1) Difficulty in recapitulating bone architecture and organisation, and its dynamic remodelling processes,
2) Difficulty incorporating functional and mature vascularisation,
3) Difficulty in delivering appropriate organ-level stimulation (mechanical loading and fluid flow).

To bridge the gap between engineered and native tissues it is important to overcome the limited spatial resolution barrier associated with 3D printing strategies, and to innovate to produce complex hierarchical architectures with hosts of cells and material formulations (Figure 1g) (29). The processes (signals – chemical, physical, and mechanical) involved in constructing specialised microenvironments through to cellular phenotypic effects using material formulations and biophysical cues should also be considered synchronously when investigating biological and structural functionality.

1.2. Biomaterial challenges: material properties

The ECM supports and influences important cellular processes including morphology, migration, and fate. Cells sense and modify their matrix in response to biochemical and biophysical stimuli (Figure 2a), as well as oxygen levels and nutrient concentration, all factors that contribute to the microenvironmental niche (30–32). Mechanosensitive feedback is important in bone tissue, as osteoprogenitors, but also bone cells, such as osteocytes, osteoblasts, and osteoclasts, alter their phenotype and function as a result of external physical and fluid forces from the surrounding environment to regulate tissue formation (Figure 2b).

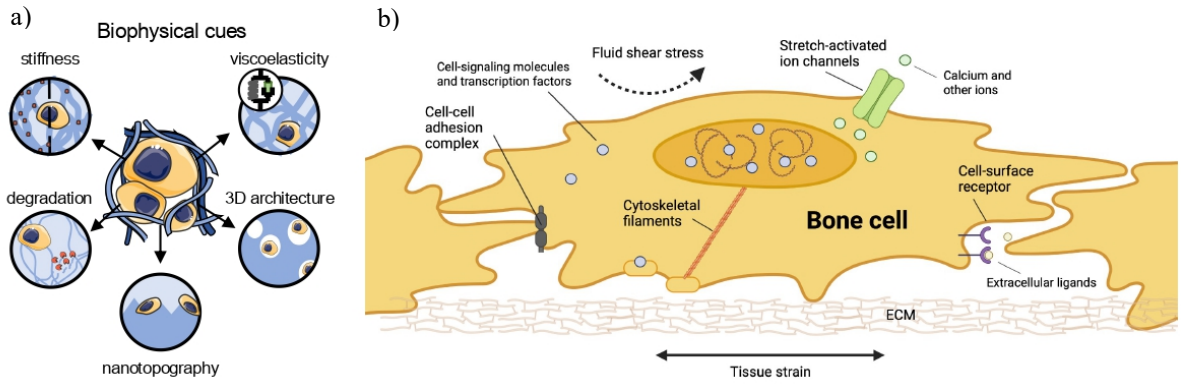


Figure 2. a) Illustration of the biophysical cues of a microenvironment that impact cell behaviour, including stiffness and viscoelasticity, which are involved in mechanotransduction, degradation, and 3D architecture, including nanotopography. b) Cellular processes of mechanosensing and response with several biological components, not mutually exclusive, depicted in a bone cell such as an osteocyte. Created on the BioRender website (https://biorender.com) by the author.

Hydrogels show great promise for BTE from both a biological and an engineering standpoint (33,34). Their ability to mimic the fibrous structure of natural ECM, their pliability, high processability and porous structure, enabling oxygen and nutrient exchange whilst supporting cell attachment, proliferation, and differentiation, make them a 'go to' class of material for BTE (34).

The body of literature reviewing hydrogels is extensive and the reader is directed to excellent reviews on compositions (35–37) and properties (38–40) for BTE. Therefore, the following section explores hydrogel biophysical cues such as mechanics, architecture, and degradation in regulating *in vitro* cell behaviour, namely: 1) cell attachment and organisation; 2) cell proliferation and differentiation; and 3) tissue formation and remodelling. It is important to note that the hydrogel biophysical properties are highly interdependent and thus varying one will influence the other; thus, it is challenging to isolate the effect of one variable over the other on cell behaviour. In this section we attempt to identify those biophysical properties that have the greatest effect in each of the key cell processes in bone formation and remodelling.

1.2.1. Cell attachment and organisation

Bone formation *in vitro* involves the delivery of stem and/or specialised cells, with or without appropriate signalling cues, often employing a supporting scaffold (41). Delivery does not necessitate cell attachment; however, bone cells, and specifically osteoblasts, are adherence-dependent cells, rendering regulation of cell attachment an exigency for subsequent cellular function. Thus, promotion of cell attachment to a hydrogel matrix via biochemical and biophysical cues is a key aspect to optimise. The biochemical composition of a hydrogel is an important factor that controls cell attachment, and in some cases, biochemical cues can dominate over biophysical cues at this stage of BTE (42,43). Biochemical cues, including ligand chemistry, cryptic peptides, and bound growth factors (GFs) and extracellular vesicles are mostly used to enhance cell attachment. The literature on biochemical cues is extensive and the reader is directed to other reviews for more information (44–46). Whilst hydrogels can present cell-attachment motifs, such as the arginine-glycine-aspartic acid (RGD) peptide, and deliver GFs, 3D bioprinting has the potential to facilitate the production of BTE constructs with spatiotemporally defined patterns of GFs to promote the organisation and self-assembly of specific cells to stimulate bone tissue formation, vascularisation, and remodelling (47).

1.2.1.1. Role of hydrogel architecture in cell attachment and organisation

Nanostructures, such as nanoparticles, have been used to control cell attachment and organisation through manipulation of cell exposure to motifs (48,49). RGD-functionalised silica nanoparticles were conjugated onto a thiolated methacrylated hyaluronic hydrogel. The 1.3-fold increase in the percentage of initial cell attachment when silica nanoparticles were used on a methacrylated hyaluronic hydrogel, when compared to no nanoparticles, highlights how unique surface topographic inputs can be used as directive cues for cells (48).

Bioorthogonal strategies have been employed to crosslink and encapsulate cells within controlled nanostructured hydrogel networks (50). Nanostructures have also been used within DNA hydrogels. A rapidly formed supramolecular polypeptide–DNA hydrogel was prepared and used for *in situ* multilayer 3D bioprinting (51). Designed structures were printed using two complementary bio-inks that were alternately deposited. This bioprinter-based method created various 3D tissue-like patterns and structures with the necessary scales and dimensions, through varying droplet size and the number of layers printed (51). Additionally, DNA hydrogels have been used to create large, centimetre-scale constructs with excellent haemo- and cytocompatibility (52). For further information regarding structural DNA nanotechnology, the reader is directed to a comprehensive review (53).

As described before, cell attachment and organisation are a fundamental requirement for further key cellular processes involved in bone formation *in vitro*. The architecture of hydrogels, including nanostructures and molecular assembly, is a biophysical cue that dominates at the early stages of the bone formation process and can be exploited to promote and optimise cell attachment and organisation for the next stage, namely, cell growth.

1.2.2. Cell growth: migration, proliferation and differentiation

Variations in hydrogel mechanics, such as stiffness and viscoelasticity, and altering the 3D architecture, such as pore size and nanotopographical features, affect and instigate changes in cell behaviour, activity, and phenotype. Stiffness and viscoelasticity are key mechanical properties that are converted into biochemical signals in a process called mechanotransduction. Mechanosensitive feedback is particularly important in bone tissue, as bone cells, such as osteocytes, osteoblasts, and osteoprogenitors, alter their phenotype and function in response to external physical forces from the surrounding environment, to

regulate tissue formation and remodelling (54). Several approaches have been explored to control cell migration, proliferation, and differentiation in hydrogels. Work has been focused on mechanotransduction; thus, stiffness and viscoelasticity will be discussed first. An overall summary of biophysical cues covered in the following sections is presented in Figure 2a.

1.2.2.1. Role of hydrogel stiffness on cell growth: migration, proliferation and differentiation

In vivo cell migration is attributed to chemotaxis; however, *in vitro*, cells can also follow a gradient in mechanics, also known as durotaxis (55). Tugging traction dynamics within cell-ECM focal adhesions (FAs) are key to durotaxis. This sensing mechanism is capable of operating over a broad range of matrix stiffness and tension, such that directional migration of cells can be tightly controlled along highly localised or dynamically changing ECM-rigidity gradients (56).

There is a close relationship between hydrogel stiffness and cell migration and differentiation (57). He et al. (57) created a gel to engineer osteochondral tissue with an increasing stiffness gradient from the cartilage (20 kPa) to the bone layer (300 kPa) (Figure 3a). The different domains had the capacity to induce differentiation of MSCs towards the chondrocytic and osteoblastic lineages (Figure 3b). Although stiffness-dependent mechanoregulation impacts many cellular processes, its impact on stem cell spreading, differentiation, and migration has been clearly demonstrated (58–61). Additionally, cell proliferation has been shown to have a biphasic dependence on matrix elasticity, peaking in intermediate stiffness gels (60 kPa), which also supported osteogenic lineage commitment (62). Matrix stiffness plays a key role in regulating MSC differentiation into specific mature cell types. Dynamic modulation of stiffness can result in the activation of different transcription factors that upregulate genetic

pathways (YAP/TAZ). These pathways are responsible for the initiation and progression of particular cell-lineage differentiation (63). The genes responsible and pathways involved are beyond the scope of this review, so the reader is directed to another comprehensive review for details (63).

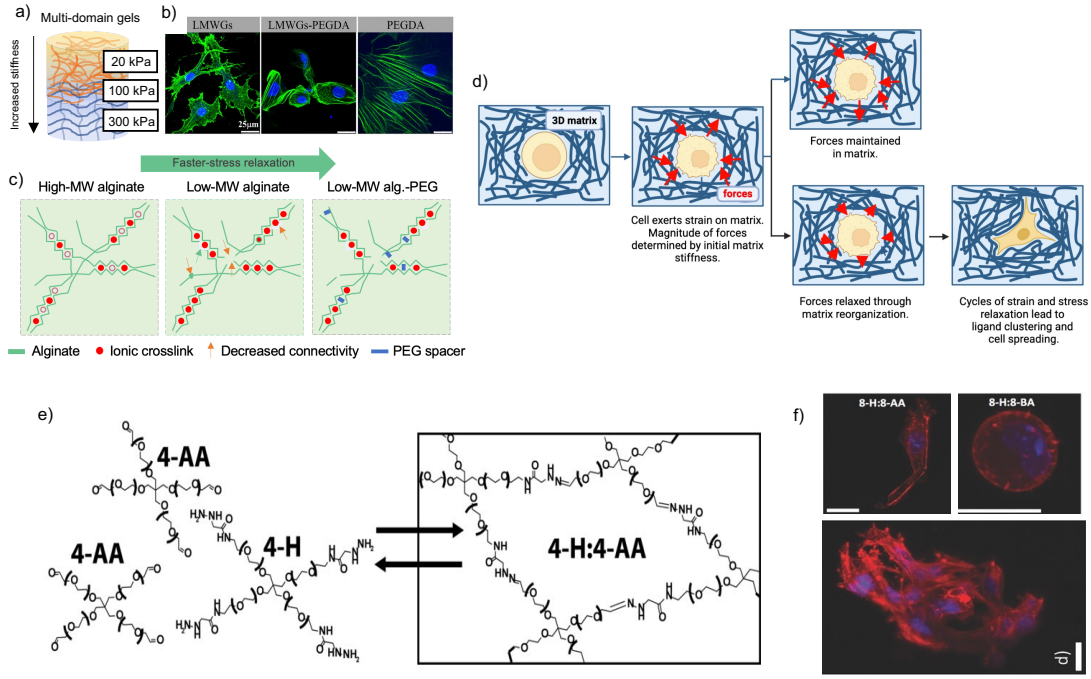


Figure 3. a,b) Effect of hydrogel stiffness and c–f) viscoelasticity on cellular response. a) A biomimetic gradient for osteochondral tissue regeneration. Created on the BioRender website (https://biorender.com) by the author. b) MSCs stained for actin cytoskeleton on three different gels: LMWGs, LMWG-poly(ethylene glycol) diacrylate (PEGDA), and PEGDA gels for 14 days. Reproduced (adapted) with permission (57)*. Copyright 2021, Elsevier. c) Schematic showing molecular weight (MW) of alginate crosslinked by calcium with entanglement and connectivity of the network, with both molecular weight and PEG spacers increasing the rate of stress relaxation* (68)*. Created on the BioRender website (https://biorender.com) by the author. d) The effect of a 3D matrix on a cell – resulting in forces and stresses acting on the cell. When forces are maintained, there is no remodeling, whereas, if there are cycles of stress and strain relaxation it results in cell spreading* (68)*. Created on the BioRender website (https://biorender.com) by the author. e) Chemical structure of an aliphatic hydrazone-linked hydrogel, showing reversible gelation* (76)*. f) Dynamic nature of the aliphatic hydrazone-linked hydrogel results in filopodia and lamellipodia extension, facilitating cytoskeletal outgrowth. Reproduced with permission* (76)*. Copyright 2014, Wiley-VCH GmbH.*

1.2.2.2. Effect of hydrogel viscoelasticity on cell growth: migration, proliferation and differentiation

Natural tissues and cells themselves are viscoelastic (64,65). Cells probe their environments at several frequencies (66). Influence of hydrogel viscoelasticity in directing cell phenotype and migration has been covered by Chaudhuri, Mooney, and co-workers (65,67–70). Within viscoelasticity and cell migration, literature often contradicts. Early studies suggested that decreased viscosity and increased stiffness promoted cell spreading through cell traction forces (71,72). However, cell spreading has also been reported to be upregulated in 3D viscoelastic matrices. Similarly, viscoelasticity was found to promote and regulate the proliferation of multiple cell types in hydrogels (68,73). Disagreement may arise from difficulty in varying and controlling hydrogel mechanics accurately and independently over other biophysical and chemical cues.

Fast stress relaxation has been shown to allow for better cell spreading in calcium-crosslinked alginate hydrogels when compared to alginate gels with slow stress relaxation times with similar elasticity (Figure 3c). Mooney and co-workers showed that fast stress-relaxing matrices undergo mechanical remodelling to result in adhesion-ligand clustering, cell spreading, proliferation, and matrix formation (Figure 3d) (68,69). Initial moduli of ~9 kPa or 17 kPa induced MSCs to differentiate into fat and bone, respectively (68). However, the stiffer matrices with faster relaxation kinetics, which are usually characteristic of moving toward a progressively softer modulus, showed an increase in osteogenic differentiation as a function of matrix viscoelasticity. It was hypothesised that the cells sense matrix relaxation in real-time, rather than integrating the mechanical signal over time.

Bioorthogonal covalent crosslinking has been explored together with ionic crosslinking to produce alginate networks, providing a way to control viscoelasticity and stress relaxation times (74,75). Further to this, fibrillar collagen matrix was integrated into the system. The various levels of crosslinking resulted in a range of storage moduli and elastic moduli (1.5–7.5 kPa). Increased elasticity of the matrix, as a result of covalent crosslinks, altered the cells' response to mechanical cues with respect to regulation of gene expression of immunomodulatory markers by human mesenchymal stem cells (hMSCs) (74).

Anseth and co-workers have employed hydrazone crosslinks to produce hydrogels that remain dynamic under physiological conditions (76). The dynamic stress-relaxing crosslinks allow for rearrangement of the gel over a timescale that is suitable for filopodia and lamellipodia extension (Figure 3e and f) (76). Furthermore, Anseth and co-workers developed a covalent adaptable thioester-crosslinked hydrogel with viscoelastic properties ranging over several orders of magnitude, by modifying pH, gel stoichiometry, and crosslinker structure. In these adaptable thioester hydrogels, hMSCs were able to spread within 1 day of culture and developed stellate morphologies in contrast to the rounded shape of cells observed in the static, control hydrogels lacking the thioester functionality. This study highlights the potential of adaptable crosslinking strategies to mimic ECM viscosity, and the use of these crosslinking strategies within hydrogels to remodel their surroundings (Figure 4a and b) (77).

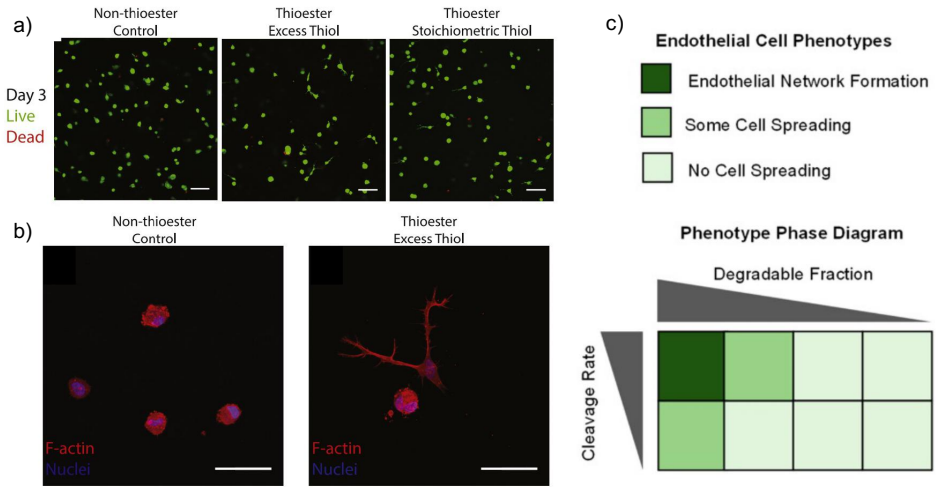


Figure 4. Role of a, b) hydrogel viscoelasticity and c) degradation on remodelling, a) Day 3 LIVE/DEAD showing increased spreading in thiol-containing hydrogels, and b) cell shape on day 3, remaining rounded in the control and spread in excess thiol hydrogels. Reproduced (adapted) with permission (77)*. Copyright 2023, Elsevier. c) Degradation, with focus on degradation fraction and cleavage rate on endothelial network formation. Reproduced (adapted) with permission* (98)*. Copyright 2023, American Chemical Society.*

Knowledge of how cells sense, interpret, and react to changes in mechanical signals on timescales ranging from seconds to hours is key in improving the design of dynamic hydrogels for cell growth (78). Additionally, mechanical signals will vary significantly due to the formation of precellular matrix and hydrogel degradation over a timescale of hours to weeks, respectively. It is therefore important to design hydrogels and implement strategies that exploit the cell-mediated dynamical changes across a large time scale.

1.2.2.3. Role of hydrogel degradation on cell growth: migration, proliferation and differentiation

Matrix degradation is a key factor that influences cell motility and migration (79). It was found that in poly(ethylene glycol)- (PEG) based hydrogels, cell migration was independent of proteolytic degradation within a low-stiffness matrix, whereas, at higher levels of matrix

stiffness, proteolytic migration dominated (80). Further, hMSC migration decreased with increasing stiffness in a matrix metalloproteinase- (MMP) degradable, peptide-functionalised PEG hydrogel (81). The cell-mediated degradation of the pericellular matrix increased with increasing post-encapsulation time. This observation suggests that over time, hMSCs secrete MMPs to degrade and remodel the matrix to enable migration, with relatively higher rates in softer matrices than stiffer ones. In addition to higher stiffness, a high density of matrix (i.e. polymer concentration) is also known to reduce the speed of cell migration (80,82). Both higher stiffness and density of matrix had the effect of limiting the space available or the geometry of pores for cell migration. Cell migration is therefore facilitated by proteolytic degradation; however, degradation should be tuned with remodelling (83). Thus, hydrogel network geometry and architecture are other factors that influence cell movement in 3D hydrogels and must therefore be optimised together with mechanics and degradation to facilitate cell growth, organisation, and assembly (84).

1.2.2.4. Role of hydrogel 3D architecture on cell growth: migration, proliferation and differentiation

3D Hydrogel mesh size or confinement heavily influences cell motility and migration. Literature reporting hydrogel mesh size on cell growth is sparse due to the difficulty in measuring and controlling hydrogel mesh size in 3D. The main take-home message from the literature is that the nucleus acts as the main steric hindrance when cells migrate in confined 3D spaces (85). In addition, cell-migration speeds are highest in intermediate channel widths (12 μm). Multiple cell types were confined in spaces smaller than the individual cells, but bigger than the nucleus; cells displayed the fastest migration speeds through either porous scaffolds or 3D channels (85,86). Additionally, 3D cell migration in the absence of proteolytic degradation is significantly limited when pore diameter reaches below 4 μm,

which is comparable to the size of most cell nuclei (85,87). At these levels of confinements, pore size dominates over substrate matrix stiffness in controlling migration.

Nanofibrillar structures, formed from gellan gum hydrogels and arranged by thermally driven self-assembly, facilitated both cell adherence and proliferation (88). Increased adherence and proliferation were hypothesised to originate from the change in density and pore size decrease from thermal annealing, which resulted in microstructural rearrangements (88). Hydrogels held at 65 °C for 16 hours exhibited the best results for cell adhesion and proliferation. The nanotopography further influenced hydrogel stiffness, with an increase in local stiffness observed in fibrillar structures with a number of nodes, which in turn represented a more attractive architecture for FA (88).

Here, it is demonstrated that by applying the numerous concepts within 3D architecture, such as patterning, fibrillar structures, and mesh size, directive cues for specific cellular growth can be created.

Cell spreading, migration, proliferation, and differentiation are essential processes in ECM synthesis and tissue regeneration. Hydrogel biophysical properties can be used to influence cell behaviour and must be finely tuned to achieve the desired cell proliferation, migration, and differentiation. Once the necessary cells are organised in place, the key stage of mineralised matrix deposition and remodelling can occur.

1.2.3. Bone tissue deposition and remodelling

In normal physiology, bone resorption and formation are in a homeostatic equilibrium, meaning that the rate of bone resorption is matched with the replacement of neotissue in

response to mechanical load and strain (89). *In vitro*, before the point of remodelling, osteoprogenitors are required to be delivered within a hydrogel and allowed to reorganise, resulting in a sequential cascade of biological processes including spreading, migration, proliferation, and differentiation.

All of these processes are highly influenced by a plethora of chemical and mechanical properties, along with degradation and 3D architecture as discussed before in Sections 1.2.1 and 1.2.2. Eventually, bone formation occurs through collagen secretion and ECM mineralisation, followed by remodelling by osteoclasts (90).

Upon tissue maturation, cells begin to interact with the hydrogel and native environment, leading to dynamic reorganisation of both hydrogels and cells, which enables both cell proliferation and differentiation, as well as cytoskeletal tension. On top of this, construct morphogenesis begins as cells synthesise and deposit nascent ECM proteins and proteoglycans within the hydrogel (91). Within the first 24 hours, these nascent proteins can mask hydrogel properties and influence cell–hydrogel interactions within the extracellular space. The newly secreted proteins within the ECM can cause much of the initial, and proceeding, cell–hydrogel interactions to be lost, highlighted by studies that show MSCs' ability to escape and override matrix stiffness cues to remain quiescent (91,92). Newly secreted proteins and proteoglycans can influence cell-hydrogel interactions in two ways, first, by acting as a physical barrier by separating the cell from the hydrogel, and second, by permeating within the engineered hydrogel (93). Understanding and being able to control the latter will influence the outlook of hydrogel design.

The role of the deposited nascent protein is commonly overlooked when studying cell–hydrogel interactions, despite their newly acquired biochemical and biophysical influences which can be quite dissimilar to those originally engineered (91). Little work has been carried out to study how the newly secreted matrix affects the cell–hydrogel interface on local, intermediate, and long-term interactions. It is suggested that the lack of research in this area can be attributed to limitations in visualising and measuring secreted matrix dynamics (93,94). The spatiotemporal aspects of ECM assembly and remodelling remain unanswered, and better comprehension is necessary to contribute to our understanding of how cell–hydrogel interactions regulate matrix synthesis and tissue morphogenesis (95). Hydrogel design in the future should pay increased attention to the timing (non-linear elastic nature of tissue) and accessibility of engineered hydrogel biochemical and biophysical signals on cells (93).

At the point of collagen secretion and ECM mineralisation, the hydrogel must degrade at an appropriate rate to facilitate neotissue formation, thus hydrogel degradation properties dominate in this point of BTE and will be discussed first.

1.2.3.1. Role of hydrogel degradation and 3D architecture on bone tissue deposition and remodelling

Hydrolysis and enzymatic proteolysis are two of the main mechanisms by which hydrogels undergo degradation. Both natural and synthetic hydrogels require incorporation of MMP substrate crosslinkers to allow and aid cell-triggered proteolysis. During remodelling, MMPs digest the hydrogel to make way for cells to form a new matrix (96). A PEG-based hydrogel has been used to exploit this property, which, in the presence of cell-secreted MMPs, was able to deliver bone morphogenetic protein (BMP)-2 (97). The process resulted in the

formation of bony tissue and mimicked the matrix remodelling observed in natural ECM. Additionally, proteolysis has been used to control the degradation kinetics of a PEG-based hydrogel from <12 hours to over 9 days (98). This was achieved by using the proteolytic enzyme urokinase plasminogen activator to control the rate of peptide bond hydrolysis. In turn, the degradation was responsible for a loss in hydrogel architecture. Degradation in combination with architecture plays a key role in endothelial network formation (Figure 4c) (98). Endothelial network formation was only observed in the PEG-based hydrogels with rapid proteolytic cleavage kinetics that could fully disrupt the infiltrated hydrogel architecture.

Hydrogel network structure and mesh size are key architectural components that influence neotissue formation. Architectural cues in scaffolds play a particular role in regulating vascularisation and hence are important within bone remodelling. A hydrogel with open pores and a fully interconnected microchannel network, as small as 40 μm, was created by removing uncrosslinked gel within the structure by soaking the scaffolds in water (H_2O) (99). To achieve a controlled architecture, piezo inkjet 3D printing was used to create an architecture that facilitated vessel formation in vivo following implantation of endothelial cell-seeded scaffolds (99). Although this study demonstrated vascularisation in wound models, the technique and process can also be applied to bone tissue and demonstrates the importance of 3D architecture on vascularisation.

Nanoscale symmetry and disorder patterns, in the form of nanocues, have been shown to act as biologically active designs (100). When highly ordered, disordered, and totally random topographies were compared, a disordered square array resulted in significantly higher expression of osteopontin (OPN) and osteocalcin (OCN), along with dense aggregates,

reminiscent of bone nodule structures (100). This study outlines the important role of different nanotopographies, as well as how developing various orders of design can elucidate specific cell functions.

It is clear from these studies that when designing a hydrogel, degradation and 3D architecture are key considerations to be taken together, not only because of their impact on cell behaviour but also because of their close interplay, which in turn can affect cell function for tissue maturation (101).

1.2.3.2. Role of hydrogel mechanics on bone tissue deposition and remodelling

Bulk matrix stiffness has been shown to exhibit a marked dependence on new bone formation *in vivo*, with intermediate stiffness gels (60 kPa) demonstrating optimal regeneration (62). Two gelatin methacryloyl (GelMA)-based hydrogels with differing stiffnesses, both co-cultured with primary human adipose-derived stem cells (hASCs) (osteogenic) and primary human dermal microvascular endothelial cells (HDMECs) (angiogenic), demonstrated the interplay between HDMECs and hASCs in co-culture. This study showed successful direction of cell fate when exposed to hydrogels of differing stiffness (102). After 14 days of culture, the stiffer hydrogels induced the hASCs to express collagen I and fibronectin, as well as OPN and alkaline phosphatase (ALP) – key matrix proteins and bone-specific proteins. Additionally, co-culture resulted in higher viscoelastic properties of the bone gels than monoculture (102). Conversely, the softer gels induced vascularisation while co-culture promoted a significant increase in stability and complexity of vascular networks. As stated in Section 1.1, successful vasculature within these hydrogel constructs remains a hurdle in achieving tissue mimics for BTE. However, this work demonstrates that stiffness and co-

culture can be combined and exploited so that the cells can function well in the necessary parts for bone formation and vascularisation.

1.2.4. Concluding remarks

Formulating novel hydrogels for BTE with tuneable properties has shown significant progress and great potential. However, as tissue engineering is an inter-disciplinary field, pivotal challenges remain in the areas highlighted in this review – BTE and hydrogel design. To create fully representative *in vitro* tissue models, which allow long-term, whole construct testing of potential therapeutics, researchers must identify the unmet requirements within these areas. The first is the dynamic and complex nature of the organ to be recapitulated. The current state-of-the-art in *in vitro* modelling of bone does not recapitulate the complex hierarchy of bone. This review highlights three main interlinked challenges in BTE, namely complexity, vascularisation, and organ-level simulation. These barriers can be overcome through synergistic developments in hydrogel formulations and utilisation of appropriate manufacturing methods. The second is the development and advancement of hydrogel formulations that can recapitulate the stem cell microenvironmental niche and direct the appropriate cell phenotype. Numerous hydrogel biophysical parameters, including stiffness, viscoelasticity, 3D architecture, and nanotopography, which have been successfully modified and controlled, directing stem cell fate, are presented. This literature review highlights the importance of developing novel hydrogels to bio-physicochemically cue cells over a time-scale mapping to key cellular processes in bone formation and remodelling.

1.2.5. Thesis aims

The aim of this thesis is to develop novel hybrid hydrogels using sol-gel processing for *in vitro* modelling of bone. To achieve this aim, this thesis has the following objectives:

1. Investigate the interaction of gelatin (organic) with polyol-modified silanes (inorganic) to create hybrid hydrogels. Characterise the chosen hydrogel systems in terms of phase separation, gelling properties, pH, and degradation properties.
2. Study the gelatin functionalisation reaction with epoxide electrophiles and develop improved methods for determining successful functionalisation of gelatin with 3-glycidyloxypropyl trimethoxysilane (GPTMS), including utilisation of a novel technique to purify reaction products.
3. Synthesise novel gelatin-based hybrid hydrogels using click chemistry and characterise the chosen hydrogel systems in terms of chemical composition, mechanical properties, and their ability to support cell growth and proliferation.

CHAPTER 2. INTERACTION OF GLYCOL-MODIFIED SILANES WITH GELATIN IN GELATIN-SILICA HYBRID HYDROGELS

2.1. Introduction

Naturally derived organic biopolymers, such as gelatin, collagen and chitosan, are a popular choice for hydrogels as they often have inherent biological activity, as well as being biocompatible (103–105). In addition to the numerous benefits discussed in Chapter 1, including mimicking the structure of the ECM, high water content, tuneable physicochemical properties, and supporting cell attachment and proliferation, naturally derived organic biopolymers are often readily and commercially available (11,104–107). Although the discussed benefits make naturally derived biopolymer hydrogels an outstanding choice for BTE, their employment is limited by their low mechanical strength, both compressive and tensile, uncontrolled degradation behaviour, and batch-to-batch variation (108–110). Incorporating other materials into these hydrogels provides a route to enhance the material chemistry to facilitate versatile use of hydrogels within more demanding tissue engineering applications.

2.1.1. Hybrid hydrogels

One strategy to improve the poor mechanical and degradation properties of naturally derived biopolymer hydrogels is to create hybrids; a ‘hybrid’ is defined as a molecular interpenetrating network of organic and inorganic moieties which interact at the nanoscale (111–114). Hybrid hydrogels can be classified into two classes. In Class I, the organic and inorganic matrices are embedded within one another through weak non-covalent interactions, such as hydrogen bonds, whereas in Class II, the organic and inorganic domains are covalently linked by a crosslinker (111) (Figure 5). Hybrid hydrogels often employ silica as the inorganic component because the physical network it can create includes covalent bonds which enhance the overall strength of the hydrogel, whilst also providing the scaffold with the ability to biomineralise (115,116). This integration of silica as the inorganic phase results

in synergy of the properties of these components (111,117). Therefore, the poor mechanical drawbacks associated with the organic biopolymer are addressed, while retaining the innate biological benefits. Additionally, manipulation of the proportion of both organic and inorganic provides a way to control biological and physical properties (112).

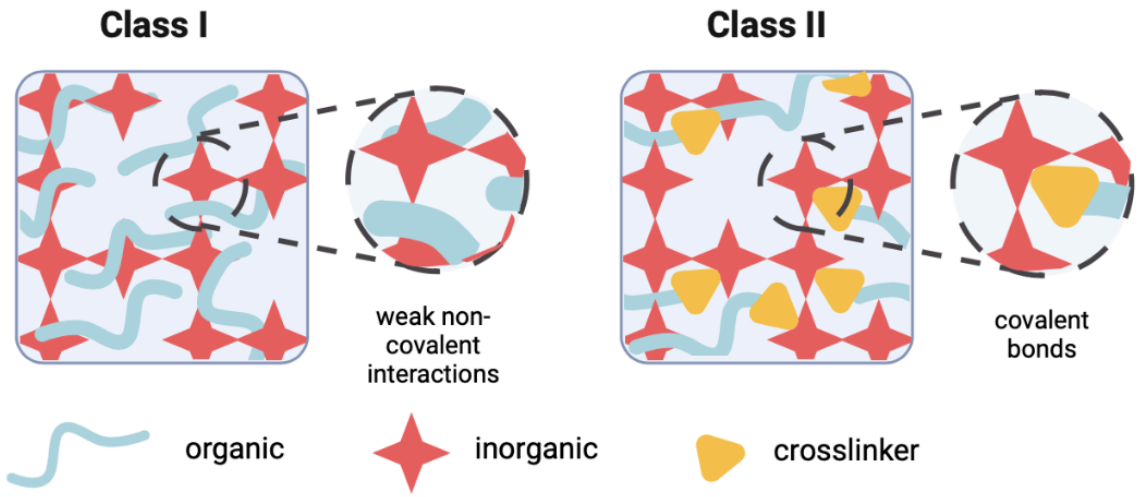


Figure 5. Classes of organic-inorganic hybrid hydrogels. Class I hydrogels have organic and inorganic components embedded within one another, with weak non-covalent interactions. Class II hydrogels have organic and inorganic networks linked by covalent bonds. Created on the BioRender website (https://biorender.com) by the author.

2.1.2. Sol-gel

Soft-chemistry sol-gel processing, an inorganic polymerisation, allows the development of organic-inorganic hybrid hydrogels for biomedical applications (112,117–121). The name 'sol-gel' is used to describe the transition between the two different states: a sol, a colloidal suspension, to a gel, an entangled solid network. During the sol-gel process, metal-containing molecular precursors, such as silicon alkoxides, form solid particles at the molecular level and react to construct a 3D network composed of a metal oxide, such as silica (111).

The formation of solid particles at the molecular level is driven by hydrolysis and condensation, resulting in an interconnected network in a continuous liquid phase. As the reaction progresses, an increase in viscosity of the system results in gelation (122,123).

Hydrolysis and condensation reactions are fundamental to sol-gel processing and so will be explored further in Section 2.1.2.1. The formation of an inorganic network via sol-gel processing, displaying the transition between sol to gel on a molecular level and macroscale, is presented in Figure 6.

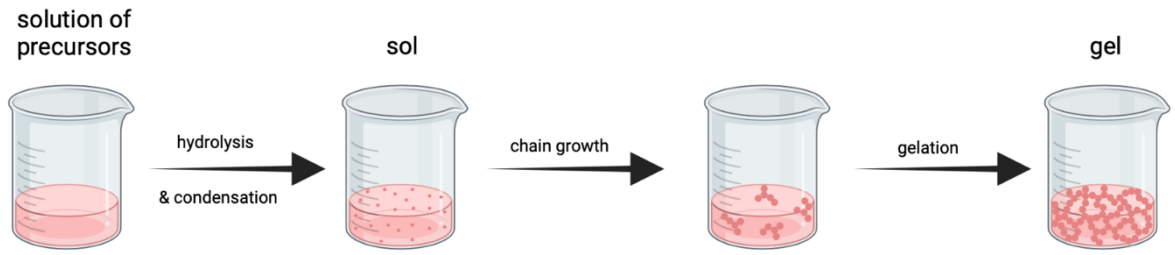


Figure 6. Representation of the sol-gel process. A solution of precursors containing a metal alkoxide and H_2O undergoes hydrolysis and condensation to result in chain growth, leading to gelation and a self-supporting gel through an increase in viscosity. Created on the BioRender website (https://biorender.com) by the author.

2.1.2.1. Hydrolysis and condensation

As part of the precursor solution, metal alkoxides are largely used, most commonly a silicon alkoxide. If the precursor is an alkoxysilane, such as tetraethyl orthosilicate (TEOS), the first step in the reaction is the hydrolysis of alkoxysilyl groups to form silanols (Si–OH) (Reaction 1) (111,124). As soon as an Si–OH has been formed, condensation can begin, and the two reactions will proceed to run simultaneously. Condensation can occur through two methods, as shown in Reaction 2 and 3, either by the reaction of two Si–OH with H_2O as a by-product (Reaction 2), or reaction between an Si–OH and an alkoxysilyl group, with an alcohol as the by-product (Reaction 3) (21); the former is often referred to as water condensation, as H_2O is produced, and the latter as alcohol condensation, as an alcohol is produced (125). Ultimately, polycondensation turns the formed monomers into oligomers, and finally, into polymers or colloidal nanoparticles (124).

$$(RO)_3Si-OR \quad + \quad H_2O \quad \rightarrow \quad (RO)_3Si-OH \quad + \quad ROH \qquad \text{(Reaction 1)}$$

$$(RO)_3Si-OH \quad + \quad (RO)_3Si-OH \quad \rightarrow \quad (RO)_3Si-O-Si(OR)_3 \quad + \quad H_2O \qquad \text{(Reaction 2)}$$

$$(RO)_3Si-OH \quad + \quad (RO)_3Si-OR \quad \rightarrow \quad (RO)_3Si-O-Si(OR)_3 \quad + \quad ROH \qquad \text{(Reaction 3)}$$

2.1.2.2. Application of sol-gel in hydrogels

Sol-gel processing is performed at low temperatures, neutral pH and in H_2O (111). The sol-gel process has been exploited within hybrid hydrogel development, as *in situ* formation of the network is desirable, and can be triggered by changes in environmental conditions such as changes in pH. Jeong et al. (126) state that sol-gel processing for hydrogels has multiple advantages over conventional hydrogels due to the simplicity and safety of the technique, and the potential to use low-temperature processing conditions. Consequently, it is a synthetic technique that occurs under mild conditions allowing the integration of an organic component and biologics, preserving any biological activity present, hence, the interest and focus on use of sol-gel as a method to create biocompatible hybrid hydrogels.

Characteristically, organic biopolymers are used in hybrid hydrogels as they can introduce biological functionality to the hybrid through innate bioactivity, for instance, RGD motifs that provide biochemical cues for cells (111,112,127–134). Where the organic biopolymer often lacks mechanical integrity, the inorganic part supplies mechanical strength and thermal stability (111). This approach is also highly promising for the integration of silica with organic biopolymer components. Sol-gel processing has utilised numerous biopolymers to produce hybrid hydrogels with enhanced mechanical properties and biological activity, which are reviewed below.

Lee et al. (135) integrated the organosilane tetramethyl orthosilicate (TMOS) into a 15% (w/v) hyaluronic acid (HA) hydrogel network and used *in situ* sol-gel of TMOS (2, 5 or 10% [v/v]) at 37 ^{o}C to form silica nanoparticles within the matrix. A structurally organised hybrid with an interconnected silica network was formed. Increasing silica content within the gel resulted in enhanced mechanical strength, specifically increasing the elastic modulus up to 160-fold to ~50 kPa, compared with that of pure HA; the storage modulus (G') increased by two orders of magnitude (1 to 160 kPa). Although the inclusion of silica increased G' and meant the physical properties could be varied for a wide range of soft and hard tissue applications, it was still far from the elastic modulus of bone, desirable for this thesis, which is on the scale of 15 to 20 MPa (136). The methanol (MeOH) produced from the hydrolysis and condensation of TMOS was removed through sequential washing of the hydrogels with 80%, 90%, and 100% ethanol, and subsequent washing with phosphate-buffered saline (PBS). Cellular responses were investigated using fibroblasts, seeded on the hydrogel surface. Inclusion of silica did not show any sign of toxicity and the hybrids had a significantly higher cell viability compared to the HA hydrogel (135).

Filipowska et al. (132) used sol-gel to prepare silica particles of two different sizes, (210 ± 1 nm [S1] and 438 ± 5 nm [S2]), from TEOS, and dispersed these into different biopolymers. Specifically, the method used H_2O dispersion of silica particles into collagen, chitosan, and collagen/chitosan hydrogels. The resulting hydrogels were washed with PBS, sterilised with ultraviolet (UV) light, and human bone marrow mesenchymal stem cells (hBMSCs) were seeded on top of the hydrogels. The choice of biopolymer, rather than size of the silica particles, influenced cell viability. The addition of silica particles to the hydrogels did not compromise the cytocompatibility of the resulting hybrids when compared with non-silica containing hydrogels. Specifically, cell viability was significantly higher for the chitosan and

collagen hydrogels, both silica and non-silica containing, compared with the collagen/chitosan composite. This observation reflected the collagen/chitosan composite's ability to promote osteogenic differentiation rather than proliferation, shown by significantly higher ALP activity. ALP activity was also significantly higher in the smaller particle silica-containing hydrogels compared to the native biopolymers, demonstrating high pro-osteogenic properties (132).

Hernández-González et al. (116) covalently coupled alginate with silica to form Class II hybrid hydrogels by functionalising oxidised alginate (alginate dialdehyde [ADA]) with (3-aminopropyl) triethoxysilane (APTES), and then reacted with TEOS. The synthesis parameters influenced the hydrolysis-condensation reactions of the silica precursors and altered how alginate interacted with them, resulting in hybrids with varying degrees of network connectedness and mechanical properties. Hybrids prepared with both APTES and TEOS generated longer silica chains and a higher degree of crosslinking, resulting in stronger materials than hybrids made with alginate/APTES or alginate/TEOS. Higher alginate concentrations (5 and 8%) resulted in a higher G' and loss modulus (G"), suggesting additional crosslinking from the added bridges of alginate ionic interactions, resulting in a stronger gel.

Improved mechanical properties resulting from sol-gel synthesised silica reinforcement within biopolymer hydrogels is widely recognised (112,117,137,138). Both Lee et al. (135) and Filipowska et al. (132) used sol-gel to create hybrid hydrogels, post-processing to remove toxic by-products, and then investigated two-dimensional (2D) cellular responses on the hydrogel surface. However, there are issues associated with sol-gel processing for hybrid

formation when cells are encapsulated for 3D culture, which will be discussed in the following section.

2.1.3. Issues with sol-gel for encapsulation of a protein/biomolecule

While alkoxysilanes, such as TEOS, provide numerous advantages as a precursor material for sol-gel processing, there are associated disadvantages when a cell or biomolecule-embedded product is desired. TEOS is the most prevalent alkoxide of silicon and is the most commonly used metal alkoxide in sol-gel experiments, however, this agent is limited for biomedical application for the following reasons:

i) TEOS undergoes hydrolysis and condensation to form ethanol as a by-product, which is a protein denaturant (139,140), and

ii) acidic or basic conditions are necessary to catalyse to the reaction, which can also affect protein stability (141).

For these reasons, novel silane precursors are required for the sol-gel process to form biocompatible hydrogels. Ideally TEOS would be substituted with an alternative alkoxide of silicon, which produces a biocompatible alcohol by-product (142). In addition, the reaction should be run under neutral conditions, without the need for an acid/base catalyst.

2.1.3.1. Polyol-modified silane precursors as alternatives to TEOS and TMOS

There has been intense effort to develop sol-gel techniques for the encapsulation of biologics, particularly to create silica-based materials with both inorganic and hybrid matrices (143–146). Gill and Ballesteros (145) produced polyglycerol silicate (PGS) through transesterification of polymethyl silicate (PMS; partially hydrolysed and condensed TMOS) with glycerol (GL), using a hydrochloric acid (HCl) catalyst. PGS retained 98% activity of encapsulated trypsin, when compared with the free enzyme, whereas PMS had only 34%

activity. The modification method was also used with metallosilicate, alkylsiloxane, and composite sol-gels, meaning a wide range of bio-doped polymers were created (145).

The transesterification method has also been used to synthesise ethylene glycol modified silane (EGMS) from TEOS and ethylene glycol by Patwardhan et al. (147). They investigated the reaction of EGMS with two macromolecules; polyallylamine hydrochloride (PAH) and poly-L-lysine (PLL). The reaction was performed under argon, at temperatures up to 150 ^{o}C and proceeded in the absence of a catalyst. Upon mixing the macromolecules with EGMS, a white precipitate was generated. Both EGMS and PAH, and EGMS and PLL showed the formation of well-defined spherical silica particles when imaged with scanning electron microscopy (SEM). Additionally, the PLL-containing gels formed non-uniform hexagonal sheet-like particles. In contrast, pure EGMS formed no precipitate, but instead a bulk amorphous gel was observed (147). The EGMS chemistry was further developed to synthesise numerous different ethylene glycol-based modified silanes based on organoalkoxysilanes such as methyl-, phenyl-, bridged ethylene, and phenylene, via transesterification. Although the hybrids were used in their monolith form, rather than as a hydrogel, this study demonstrates the versatility of the transesterification method for forming numerous different precursors for the synthesis of organosilica inorganic-organic hybrids with tailorable chemical functionalities (148).

Sorbitol, maltose, dextran and GL have been used to synthesise a variety of modified silanes from TEOS and TMOS, with different compositional ranges (sugar:silane) (140). The methoxy (TMOS) and ethoxy (TEOS) groups were directly replaced with the polyols using transesterification, in the absence of a catalyst. The resulting polyol-modified silanes had a greater solubility in H_2O, when compared to their unmodified counterparts, and proton

nuclear magnetic resonance (^{1}H NMR) and carbon-13 nuclear magnetic resonance (^{13}C NMR) spectroscopic analysis demonstrated release of only the polyol upon hydrolysis. It was possible to control the rates of hydrolysis and condensation in several ways. Increasing the polyol:silane ratio, using larger or more complex sugars, decreasing the ionic strength and introducing additional free polyols into the reacting solution all decreased the rate of gelation (140). Diglycerylsilane (DGS) monolith, made from GL and TEOS, was dissolved in H_2O and an enzyme, Factor Xa, was entrapped within the gel (149). Factor Xa activity was significantly higher in DGS than in TEOS, moreover its activity was almost unchanged over 60 days in DGS, compared to almost completely inactivated after seven days in TEOS. Additionally, residual entrapped GL was found to plasticise the gel and reduce the degree of shrinkage and cracking (149).

More recently, a glycerol-modified silane (GLMS) was synthesised from TEOS for use in silicon-containing chitosan hybrid hydrogels (120). The gelation characteristics over a range of pH (~pH 2 to ~pH 5) and temperatures (4, 20 and 37 ^{o}C) were studied. An increase in pH and temperature reduced the gelation time, demonstrating the reaction conditions are key sol-gel process factors (120). Jayash et al. (112) also created chitosan-silica hybrid hydrogels using GLMS. Chitosan was employed to provide biological activity and the incorporation of silica, synthesised through GLMS hydrolysis and condensation, to increase the mechanical properties. After 7 days of osteoblast cell culture, seeded on and encapsulated within the hydrogels, cell viability was >70% (112).

Modification of organosilanes to form non-harmful alternatives to TEOS and TMOS has evolved from solely the use of polyol-modified silanes for encapsulation of biologics, to incorporation of biopolymers and cells into the polyol-modified silane sol-gel process to

create hybrid hydrogels. The transesterification process can be used to synthesise a series of polyol-modified silanes, by varying the polyol and organosilane, to create precursors with tuneable properties and a gelation process compatible with bioencapsulation. This approach makes the use of polyol-modified silanes an attractive route for hybrid hydrogel creation for encapsulation of cells in tissue engineering approaches.

2.1.4. Aims and objectives

The aim of this chapter was to synthesise polyol-modified silanes for use in gelatin-silica hybrid hydrogels. The interactions between gelatin-based and silica-based materials were explored and discovered to be highly dependent on the components within the reaction.

The main objectives were to:

i. Modify organosilanes with polyols to create non-harmful silica precursor alternatives
    a. Use the transesterification reaction to modify TEOS with glycerol (GL) and propylene glycol (PG) to form glycerol-modified silane (GLMS) and propylene glycol-modified silane (PGMS), respectively
    b. Utilise the transesterification reaction to modify GPTMS with PG to form a polyol-modified organosilane crosslinker
    c. Characterise the polyol-modified silane reaction and products using ^{1}H NMR spectroscopy
ii. Develop a series of gelatin-based-silica Class I and Class II hybrid hydrogels using the synthesised polyol-modified silanes

a. Examine hybrid hydrogel component interactions by varying the type of gelatin, type of polyol-modified silane, inclusion of a crosslinker, ratio of gelatin to silica and choice of solvent
b. Test the degradation properties of the hybrid hydrogels to determine if the polyol-modified organosilane crosslinker contributes to more controlled dissolution

2.2. Methods

2.2.1. Transesterification of polyol-modified silane precursors

2.2.1.1. Materials

Tetraethyl orthosilicate (TEOS; reagent grade, 98.0%), glycerol (GL; for molecular biology, ≥99.0%), propylene glycol (PG; meets USP testing specifications, ≥99.5%) and 3-glycidyloxypropyl trimethoxysilane (GPTMS; ≥98.0%) were all purchased from Sigma-Aldrich. Experiments were carried out at the Institute of Translational Medicine Birmingham, University of Birmingham and Dental and Biomaterials Laboratory, Birmingham Dental Hospital, University of Birmingham.

2.2.1.2. Transesterification setup

The transesterification apparatus was a standard distillation set up within a fume hood (Figure 7). An argon atmosphere was supplied to the set-up to create an inert environment.

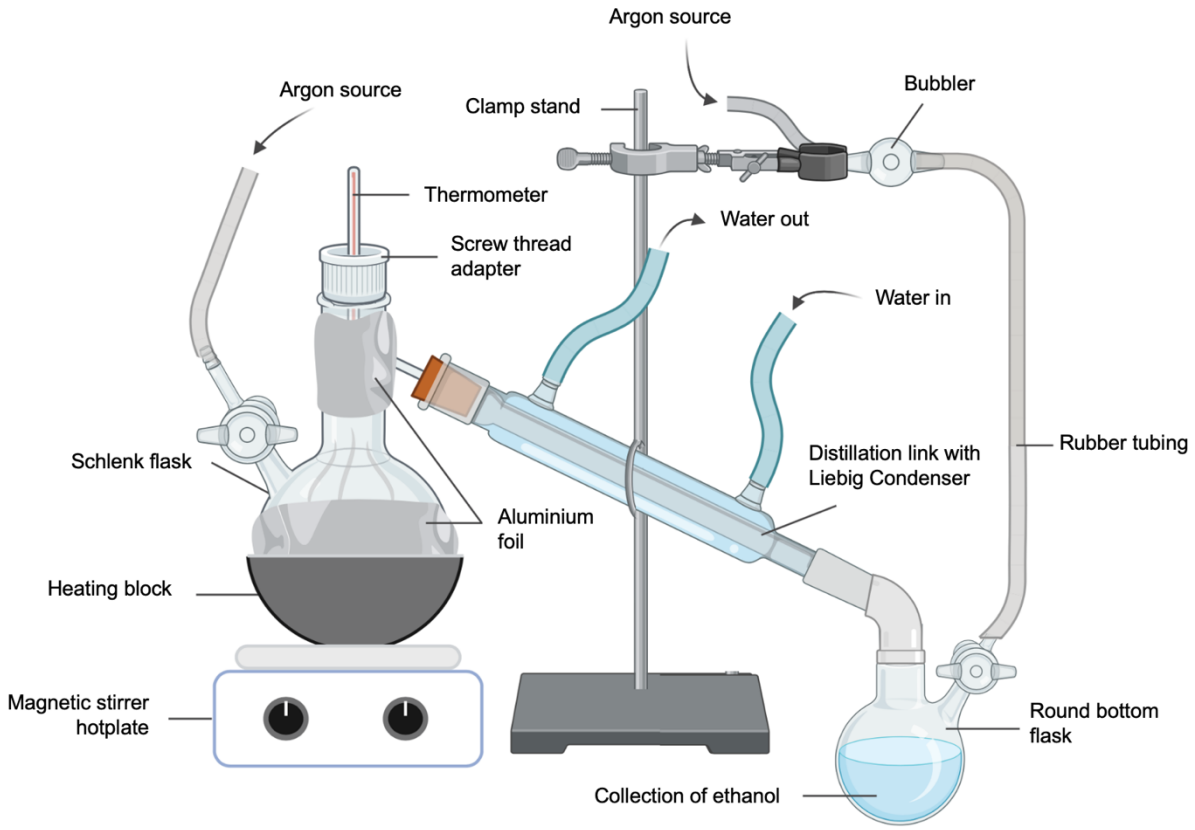


Figure 7. Transesterification apparatus set-up. Created on the BioRender website (https://biorender.com) by the author.

2.2.1.3. Transesterification protocol

GL and PG were used to modify TEOS to form GLMS (Reaction 4) and PGMS (Reaction 5), respectively.

Reagent preparation

The reactions to form GLMS and PGMS were as follows:

$$TEOS + GL \rightarrow GLMS + ethanol$$

$$Si(OC_2H_5)_4 + 4C_3H_8O_3 \rightarrow Si(C_3H_6O_3)_4 + 4C_2H_5OH \quad \text{(Reaction 4)}$$

$$TEOS + PG \rightarrow PGMS + ethanol$$

$$Si(OC_2H_5)_4 + 4C_3H_8O_2 \rightarrow Si(C_3H_8O_2)_4 + 4C_2H_5O \quad \text{(Reaction 5)}$$

For substitution of ethoxy-groups with GL or PG, a ratio of 1:4 (TEOS: polyol) of the reagents were prepared. First, TEOS (50 ml, 0.2 moles) was added to a 250 ml Schlenk flask, followed by either GL (66 ml, 0.9 moles) or PG (68 ml, 0.9 moles). A stirrer bar (40 mm, oval, FisherbrandTM Thermo Fisher Scientific) was placed in the Schlenk flask and then reconnected to the system. An argon atmosphere was maintained throughout, to prevent gelation of the mixture through contact with moisture in the air. The use of ground glass joints maintained an airtight system and joint clips were applied to all glassware connections to secure the glassware.

Reaction procedure

The H_2O source for the Liebig condenser was turned on, as well as the hotplate magnetic stirrer. The temperature of the hotplate was set to 120 ºC and the stirrer speed increased slowly until 200 rpm was achieved. The TEOS/polyol mixture was heated to 120 ºC, until it was homogeneous and appeared cloudy, steadily increasing the stirrer to ~250 rpm. Aluminium foil was added to the neck of the Schlenk flask to insulate the system. The hotplate temperature was increased in increments of 10 ºC until the thermometer read >70 ºC, at which point, ethanol was distilled from reacting mixture, and collected in the 50 ml round bottom flask. The reaction was stirred until either the temperature of the thermometer dropped <70 ºC or ethanol stopped collecting. At this point, the temperature of the hotplate was increased by further 10 ºC increments until the reaction commenced again – noted by ethanol beginning to collect. This process was continued until either ethanol stopped collecting (collecting approx. 50 mL) or 160 ºC was attained on the hotplate. At this point,

the apparatus was left to cool and the Schlenk flask removed and sealed with a bung, leaving the final product of either GLMS or PGMS.

2.2.1.4. Transesterification of polyol-modified organosilane crosslinking agent

GPTMS is a bifunctional organosilane with three methoxy groups on one side and an epoxy ring on the other. A transesterification reaction was also used to modify GPTMS to substitute the methoxy groups. In this reaction, PG was used to modify GPTMS and the product formed is referred to as propylene glycol-modified GPTMS (GPTPGS).

Reagent preparation and synthesis

The same experiment set-up was used as described in Section 2.2.1.2. The reaction to form GPTPGS was as follows (Reaction 6):

$$\begin{array}{ccccccccc} GPTMS & + & PG & \rightarrow & GPTPGS & + & methanol & & \\ Si(C_9H_{20}O_5) & + & 3C_3H_8O_2 & \rightarrow & Si(C_{15}H_{32}O_8) & + & 3CH_3OH & & \text{(Reaction 6)} \end{array}$$

A ratio of 1:3 (GPTMS: propylene glycol) of the solutions were prepared as follows: GPTMS (50 ml, 0.2 moles) was added to a 250 ml Schlenk flask, followed by PG (48 ml, 0.7 moles).

2.2.2. Interactions of gelatin- and silica-based components

The following work was conducted by undergraduate Leo Saturnino, under the supervision of the author.

2.2.2.1. Materials

Gelatin (porcine skin, gel strength ~175 g Bloom, Type A), dialysis tubing cellulose membrane (typical molecular weight cut-off = 14,000 Da), Dulbecco's Modified Eagle Medium (DMEM; high glucose), lithium phenyl-2,4,6-trimethylbenzoylphosphinate (LAP; ≥95%) and PBS were all purchased from Sigma Aldrich. All other reagents and kits are otherwise specified.

2.2.2.2. Preparation of gelatin-based solutions

Gelatin

Gelatin solutions (5.0 wt%) were prepared by adding 10 mM $HCl_{(aq)}$ (20 mL) to a sealed round bottom flask in a water bath at 40 °C. After 1 hour, gelatin (1.0 g) was added and the mixture stirred at 250 rpm for another 1 hour to ensure complete dissolution.

Gelatin methacryloyl (GelMA)

GelMA was prepared using the protocol outlined in Shirahama et al. (150). The GelMA solution was freeze-dried (Lablyo Mini, United Kingdom) for 3–4 days to generate a porous white foam, which was stored at –20 °C.

GPTPGS-functionalised polymer

GPTPGS-functionalised gelatin (Gel-GPTPGS) and GelMA-functionalised gelatin (GelMA-GPTPGS) were prepared by heating 10 mM $HCl_{(aq)}$ (10 mL) in a sealed round bottom flask at 40 °C for 1 hour. Next, 0.5 g of gelatin or GelMA (5.0 wt%) was added and the resulting mixture was stirred at 250 rpm for 1 hour. The pH of the solutions was adjusted to pH 5 using 0.1 M $HCl_{(aq)}$ and GPTPGS (2.3 g) was added to give a coupling factor (CF, molar ratio of gelatin:GPTPGS) of 500. The solution was stirred at 40 °C and 250 rpm for up to 24 hours

(gelatin) and 72 hours (GelMA), and then removed from the heat and used immediately for hydrogel preparation.

2.2.2.3. Preparation of Class I and Class II gelatin-silica hydrogels

The pH of all gelatin-based solutions (gelatin, GelMA, Gel-GPTPGS, and GelMA-GPTPGS) used was adjusted to pH 7.4 using 0.1 M sodium hydroxide ($NaOH_{(aq)}$). Predetermined volumes of gelatin-based solutions and DMEM/deionised H_2O (dH_2O) [Table 1] were vortexed in a universal tube for 15 seconds and the pH was recorded. Solutions containing GelMA also had the addition of LAP at 0.15 wt%. The following variables were investigated: gelatin type (gelatin, GelMA, Gel-GPTPGS or GelMA-GPTPGS), organic:inorganic ratio (O:I), solvent, and silica source. The O:I ratio reflects the contributions from gelatin and silica, but GPTPGS also contains both organic and inorganic components, and therefore, the contributions from GPTPGS were included in the calculations.

Table 1. Hydrogel formulations, varying gelatin type (gelatin, GelMA, Gel-GPTPGS or GelMA-GPTPGS), O:I, solvent (media or dH_2O), and silica source (GLMS or PGMS). Note, the contribution of organic and inorganic from GPTPGS was included in the O:I ratio.

Gelatin type	**O:I ratio**	**Volume of gelatin-based solution (mL)**	**Media/dH_2O**	**Volume of media/ dH_2O (mL)**	**Silica source**	**Mass of silica-source (g)**
Gelatin	100:0	5.00	DMEM	1.25	/	/
	80:20	5.00	DMEM	1.25	PGMS	0.34
	60:40	5.00	DMEM	3.33	PGMS	0.92
	60:40	5.00	dH_2O	3.33	PGMS	0.92
	60:40	5.00	dH_2O	3.33	GLMS	0.92
	40:60	5.00	DMEM	7.50	PGMS	2.05
	20:80	5.00	DMEM	20.00	PGMS	5.45
GelMA	60:40	5.00	DMEM	3.34	PGMS	0.91
	40:60	5.00	DMEM	7.49	PGMS	2.05
	20:80	5.00	DMEM	20.06	PGMS	5.49
Gel-GPTPGS	100:0	5.00	DMEM	15.40	GPTPGS + PGMS	0.00
	60:40	5.00	DMEM	15.40	GPTPGS + PGMS	1.36
	40:60	5.00	DMEM	25.72	GPTPGS + PGMS	4.16
	20:80	5.00	DMEM	55.83	GPTPGS + PGMS	12.38
GelMA-GPTPGS	60:40	5.00	DMEM	15.36	GPTPGS + PGMS	1.34
	40:60	5.00	DMEM	25.48	GPTPGS + PGMS	4.11
	20:80	5.00	DMEM	56.25	GPTPGS + PGMS	12.5

The gelatin and dH_2O/DMEM solution was then added to PGMS or GLMS, according to Table 1, and the mixture was vortexed for 15 seconds – after which time, the pH was measured. The time for gelation was recorded after vortexing using the inversion method, tilting the tube every 10 seconds, increasing to every 2 seconds when viscosity visibly increased. The gelation time was recorded when the hydrogel became self-supporting (151).

2.2.3. Synthesis of gelatin-silica hybrid hydrogels

Three hydrogel formulations were selected from the study of gelatin- and silica-based material interactions (Section 2.2.2); GelMA-Silica (Class I), Gel-GPTPGS-Silica (Class II), and GelMA-GPTPGS-Silica (Class II).

2.2.3.1. GelMA-Silica

GelMA solution (5.00 wt%) was prepared by dissolving GelMA (0.25 g) in 10 mM $HCl_{(aq)}$ (10.0 mL) at 40 ^oC and 250 rpm. After 1 hour, the temperature was increased to 70 ^oC and 0.15 wt% of LAP (0.02 g) was added to the solution. The resulting solution was stirred at 70 ^oC for 30 minutes.

To make the hydrogel, 2.80 mL of GelMA was added to 11.7 mL of DMEM, and the solution was vortexed for 15 seconds, and then added to 3.20 g of PGMS. Once vortexed for 15 seconds, the hydrogel solutions were immediately cast into a culture dish (60 mm), sealed with a lid and parafilm, and left to age for 4 hours. The cast hydrogel was irradiated for 2 minutes using a single peak of visible blue light from a single-wavelength array (SWA) platform (Loctite; Henkel-Loctite, Hemel Hempstead, UK) after 1 hour of ageing, with an average spectral irradiance of 190 mW/cm^2 and an irradiation distance set at 15.5 cm from the base of the culture dish (152).

2.2.3.2. Gel-GPTPGS-Silica and GelMA-GPTPGS-Silica

To make the hydrogels, 1.2 mL of Gel-GPTPGS or GelMA-GPTPGS solution was added to 13.5 mL DMEM and the solution was vortexed, followed by adding to 3.0 g PGMS. Once vortexed for 15 seconds, the hydrogel solutions were immediately cast into a culture dish, sealed with a lid and parafilm. The Gel-GPTPGS hydrogel was left to age for 4 hours. After 1 hour of ageing, the GelMA-GPTPGS hydrogel was irradiated for 2 minutes using an SWA platform and an irradiance of 190 mW/cm^2, with an irradiation distance set at 15.5 cm from the base of the culture dish (152). The GelMA-GPTPGS hydrogel was then aged for a further 3 hours.

2.2.4. Chemical characterisation

2.2.4.1. ^1H NMR spectroscopy

^1H NMR (Bruker Biospin AVANCE spectrometer, 400 Hz) was used to analyse how the transesterification reaction progressed and to determine successful exchange of the ethoxy/methoxy groups in TEOS and GPTMS, respectively.

During the transesterification reactions, aliquots were taken at specific time intervals: 20 minutes, and 1, 2, 6 and 8 hours and prepared for ^1H NMR analysis: a 200 µl aliquot was mixed with 800 µl of deuterated chloroform ($CDCl_3$). Methacryloyl functionalisation was also characterised using ^1H NMR spectroscopy using deuterium oxide (D_2O) as the solvent. Gelatin and GelMA ^1H NMR samples were made by dissolving 5.0 wt% of gelatin and GelMA, respectively, in D_2O (1.0 mL) and mixing 200 µl of the gelatin/GelMA solution with another 800 µl of D_2O.

^{1}H NMR data were collected by Siyun Liu (PhD Student) and all spectra were analysed with MRestNova x64 NMR software (version 14). For the transesterification samples, the resonance at δ_H = 3.55 ppm corresponding to the protons on the CH_2 group within PG was used as a standard integral, with a relative intensity of 1.00, for all transesterification data and the relative intensity of the signals within the collected spectra were analysed.

2.2.4.2. Fourier-transform infrared (FTIR) spectroscopy.

Hydrogels were dried in a 50 ºC oven for 24 hours and then ground into a fine powder using a pestle and mortar. Fourier-transform infrared (FTIR) spectroscopy was performed using a NICOLET 6700 spectrometer using 16 scans per sample with a resolution of 4 cm^{-1} over the range of 4000–650 cm^{-1}.

2.2.5. Hydrogel degradation properties

Hydrogel degradation behaviour was studied to assess how hydrogels degraded over time. Mass loss was monitored to test the degradation behaviour of the hybrid hydrogels.

2.2.5.1. Preparation

PBS (1 L) was made by dissolving 1 tablet per 200 mL in dH_2O. The pH was measured. PBS was pre-heated in an incubator to 37 ºC. After 4 hours of ageing, hydrogel cylinders were stamped out of the culture dish using a 5 ml syringe with the tip cut off. All hydrogel samples were weighed. To calculate the volume of PBS to add per 50 ml container, a ratio of 1.5 g:50 mL (hydrogel:PBS) was used.

2.2.5.2. Degradation assay

Hydrogel samples were placed in their respective PBS container and incubated at 37 ºC for the duration of the experiment. The hydrogel mass and pH of PBS were taken at the following time points: 1, 3 and 24 hours, and 2, 5, 7, 14, 21, and 28 days.

2.3. Results and discussion

The results present the steps taken to produce alternative silane precursors to TEOS and develop gelatin-silica hybrid hydrogels. TEOS was modified with GL or PG, and GPTMS was modified with PG. These modified alkoxysilanes were used to develop gelatin-silica hybrids. Numerous different hybrid compositions were created by varying the gelatin type, (gelatin or GelMA), O:I ratio, solvent (dH_2O or media), and silica source. The resulting hydrogels were investigated with respect to their gelation time, pH and degradation properties.

2.3.1. Chemical characterisation of polyol-modified silane structure and reaction kinetics

2.3.1.1. Polyol-modified silane precursors

GLMS

The kinetics of the transesterification reactions and structures of the products were evaluated by ^{1}H NMR spectroscopy.

A scheme showing the formation of GLMS is shown in Figure 8. After reaction of GL with TEOS for ~8 hours at 120–160 ^oC , ^{1}H NMR spectroscopic analysis of an aliquot showed a reduction in the relative area of the resonances for the protons on CH_2 and CH_3 ethoxy groups in TEOS, at δ_H = 3.75 ppm (a_1) and δ_H = 1.15–1.20 ppm (a_2), respectively (Figure 8). Both δ_H = 3.75 ppm (a_1) and δ_H = 1.15–1.20 ppm (a_2) signals were not present in the final sample taken at 8 hours (Figure 8), suggesting complete alcohol exchange of the ethoxy groups of TEOS with GL had taken place.

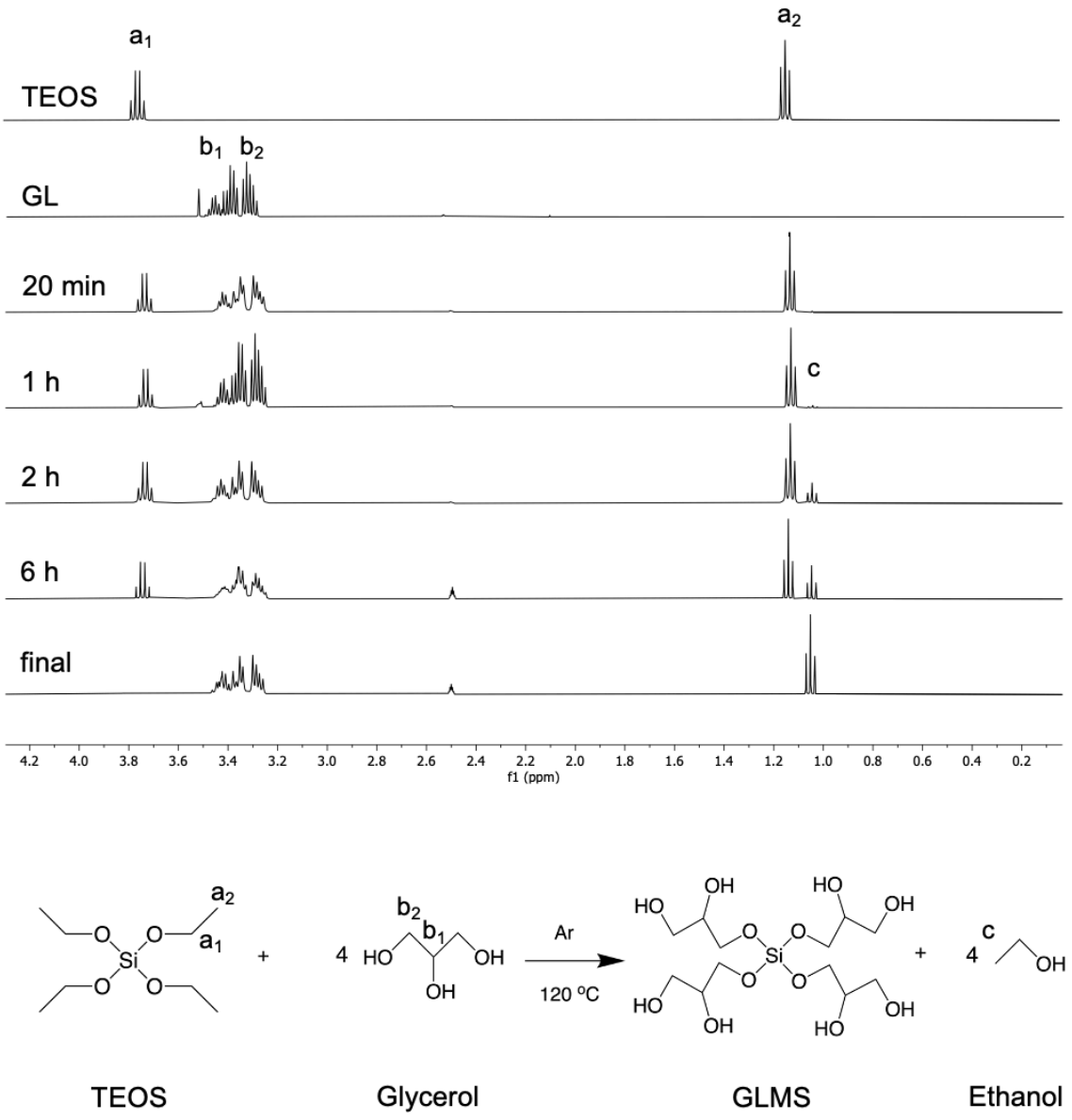


Figure 8. ^1H NMR spectra of starting reagents TEOS and GL (D_2O solvent), as well as GLMS after 20 minutes, 1, 2, and 6 hours, followed by the final sample at 8 hours ($CDCl_3$, 400 MHz). Both signals from TEOS at δ_H = 3.75 ppm (a_1) and δ_H = 1.15–1.20 ppm (a_2) for the protons on CH_2 and CH_3, respectively, are not present by the final sample. The GL resonances between δ_H = 3.20–3.45 ppm (b_1 and b_2) correspond to the protons in CH and CH_2 groups, respectively, which are present in the final sample. These changes in the resonances suggests that alcohol exchange of the ethoxy groups of TEOS with GL had occurred. The reaction scheme and a suggested chemical structure of GLMS is shown.

Additionally, by 1 hour a new triplet at δ_H = 1.05 ppm (c) for ethanol appeared, corresponding to the protons on the CH_3 group, which continued to increase in intensity over the duration of the reaction. This also supports that alcohol exchange is taking place as

ethanol is a by-product of the reaction. The spectrum shows that there is residual ethanol present in the final sample. This is backed up by the observation of ethanol collecting around the thermometer and where the Schlenk flask joined to the distillation link during the reaction (Figure 7), which when dismantled, resulted in residual ethanol collecting back into the flask containing the reaction product. The resonances between δ_H = 3.20–3.45 ppm (b_1 and b_2) correspond to the protons in the CH and CH_2 groups in GL, which remained present throughout the reaction. This was expected as the CH and CH_2 groups in GL are present within the starting reagent and are in the final product.

The relative intensity of the resonances δ_H = 3.75 ppm (CH_2, a_1) and δ_H = 1.15–1.20 (CH_3, a_2) were analysed using MestReNova; the protons from CH and CH_2 in GL giving rise to the resonances between δ_H = 3.20–3.45 ppm (b_1 and b_2) were used as the standard (Figure 9). Both resonance intensities followed a similar trend, observing a small initial decrease from ~0.16 arbituary units (a.u.) to ~0.12 a.u (δ_H = 3.75 ppm, a_1) and ~0.24 a.u to ~0.20 a.u (δ_H = 1.15–1.20, a_2). Between 1 hour and 2 hours, both resonance intensities increased to ~0.24 a.u (δ_H = 3.75 ppm, a_1) and ~0.35 a.u (δ_H = 1.15–1.20, a_2), followed by a decrease until a resonance intensity of zero was reached at 8 hours. The resonance intensity increase between 1 hour and 2 hours observed was unexpected and is unexplained. However, the similar trend observed between δ_H = 3.75 ppm, (a_1) and 1.15–1.20 (a_2) was expected as the ethoxy groups, containing both the CH_3 and CH_2, are removed as ethanol, and hence, would be exchanged at the same rate.

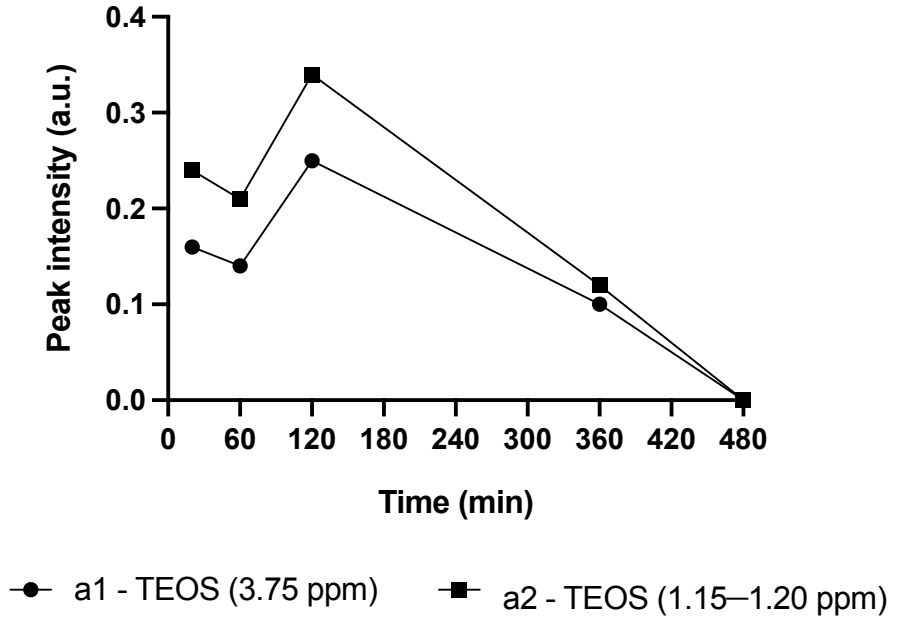


Figure 9. Resonance intensity (a.u.) of CH_2 (a_1, 3.75 ppm) and CH_3 (a_2, 1.15–1.20 ppm) in TEOS over time, using δ_H = 3.20–3.45 ppm GL resonance as 1.00 standard.

PGMS

The same conditions were used for the reaction of PG with TEOS and the ^{1}H NMR spectrum showed a reduction in the relative area of resonances at δ_H = 3.85 ppm (a_1) and δ_H = 1.20 ppm (a_2) in TEOS, which represent the protons on the CH_2 and CH_3 in the ethoxy groups, respectively (Figure 10). This reduction means that alcohol exchange was occurring during the reaction, however, residual ethoxy groups from TEOS were still detected within the sample as demonstrated by the remaining resonances at δ_H = 3.85 ppm (a_1) and δ_H = 1.20 ppm (a_2) in the final spectrum. When TEOS and PG were employed in a 1:4 molar ratio, as in this reaction, complete alcohol exchange has been previously reported (140,153). When running this reaction, the end point, and therefore the final sample, was noted as a time point when no further ethanol collection occurred when at a temperature of 180 °C. Consequently,

it can be suggested that the reaction had not run to completion, however, when repeated, similar results were obtained.

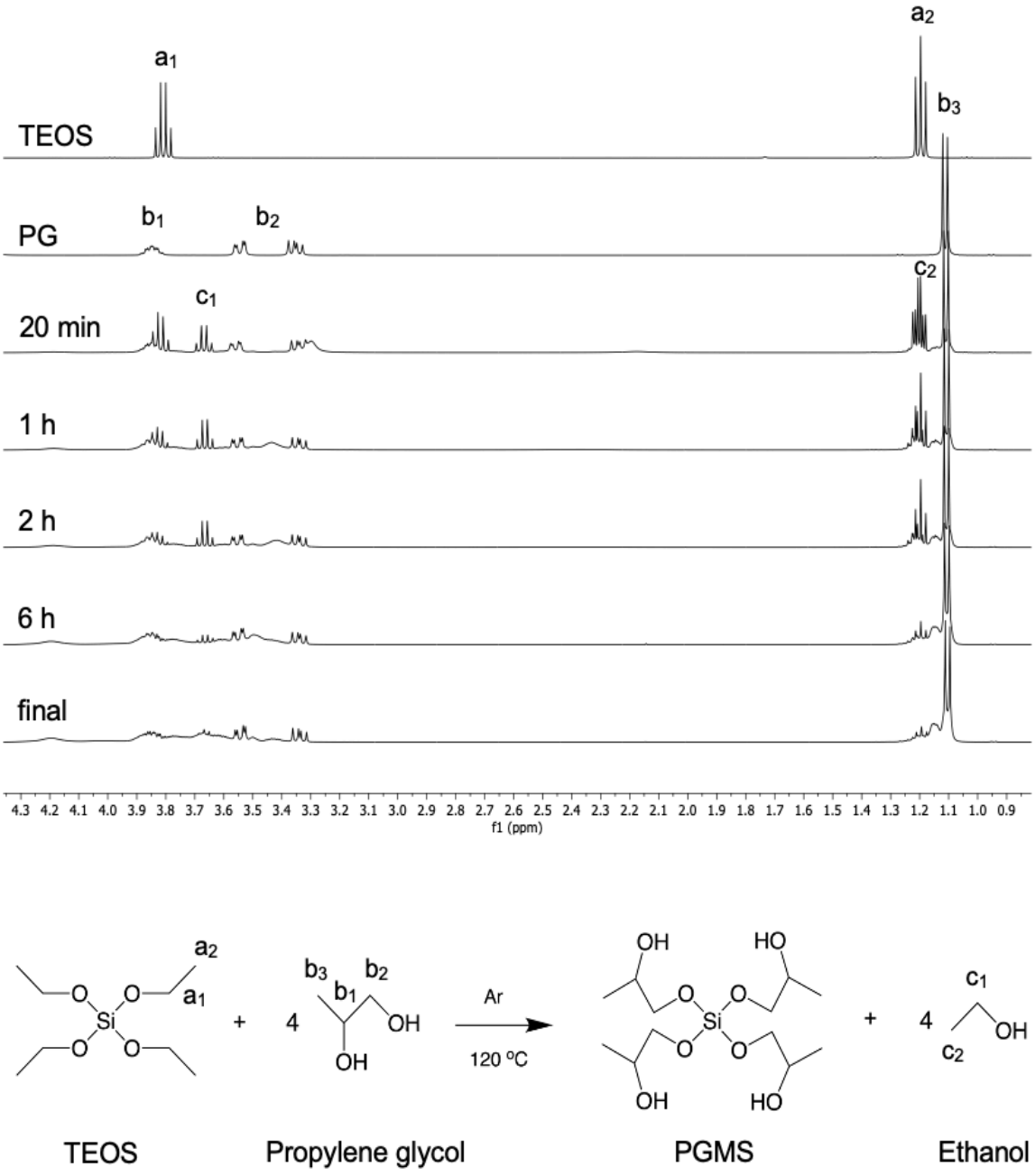


Figure 10. ^1H NMR spectra of starting reagents TEOS and PG (D_2O solvent), as well as PGMS after 20 minutes, 1, 2, and 6 hours, followed by the final sample at 8 hours ($CDCl_3$, 400 MHz). Both signals from TEOS at δ_H = 3.85 ppm (a_1) and δ_H = 1.20 ppm (a_2) for the protons on CH_2 and CH_3, respectively, reduced in relative area during the reaction. The signals at δ_H = 3.55 ppm (b_1), 3.35 ppm (b_2), and 1.10 ppm (b_3) correspond to the CH_3, CH_2 and CH groups in PG, respectively. which are present in the final sample. These changes in the resonances suggests that alcohol exchange of the ethoxy groups of TEOS with propylene glycol occurred. The reaction scheme and a suggested chemical structure of PGMS is shown.

A new quartet resonance was observed at 20 minutes at δ_H = 3.60–3.70 ppm (c_1) for the protons from CH_2 in ethanol. The relative area of this decreased over time, with a small relative area in the final sample – suggesting that similarly to GLMS, there was residual ethanol within the system. Additionally, a new low intensity triplet resonance corresponding to ethanol appeared at δ_H = 1.20 ppm (c_2) at 20 minutes, however, the overlap with δ_H = 1.20 ppm (a_2) for CH_3 of TEOS makes it difficult to distinguish if the resonances at δ_H = 1.20 ppm (a_2) in the final sample are residual ethanol or CH_3 from TEOS. The signals at δ_H = 3.55 ppm (b_1), 3.35 ppm (b_2), and 1.10 ppm (b_3) correspond to the protons in the CH_3, CH_2 and CH groups in PG, respectively. The relative intensity of the resonances the CH_3, CH_2 and CH protons in PG remained consistent throughout the reaction, which was to be expected as they were present in the starting reagents and final product.

The area of the resonances at δ_H = 3.85 ppm (CH_2, a_1) and δ_H = 1.20 ppm (CH_3, a_2) during the reaction were analysed using MestReNova and are shown in Figure 11. Both resonances intensity decreased over time and followed a similar trend. The ethoxy group, containing both the CH_3 and CH_2, is removed as ethanol, and hence, would be removed at the same rate. As previously discussed, it is challenging to assign the residual resonance intensity at δ_H = 1.20 ppm (a_2) to CH_3 in TEOS or CH_3 in ethanol, therefore, this presents as a limitation when interpreting the data and it is suggested that the intensity from the protons of the CH_2 resonance is representative of the residual ethoxy groups (Figure 10).

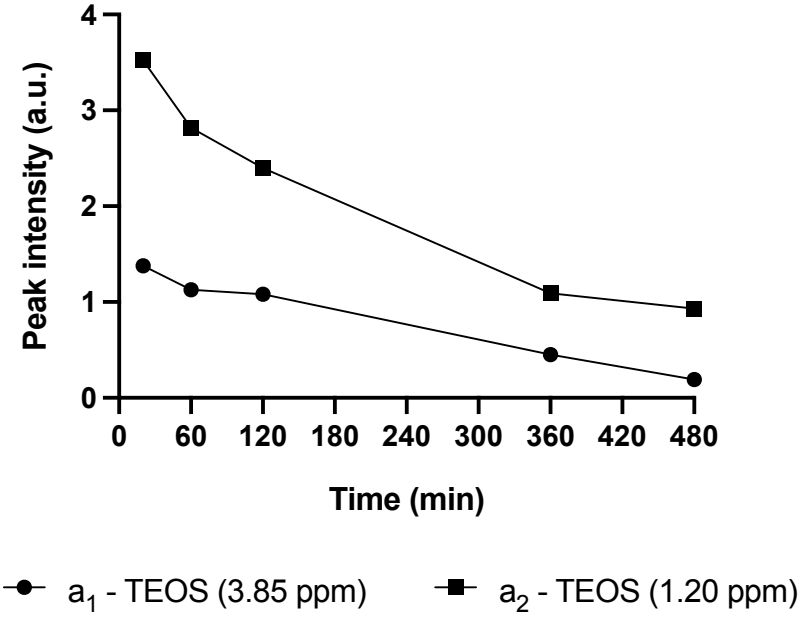


Figure 11. Resonance intensity (a.u.) of CH_2 (a_1) and CH_3 (a_2) in TEOS over time, using δ_H = 3.55 ppm PG resonance as 1.00 standard.

2.3.1.2. Polyol-modified silane crosslinker

GPTMS and PG were reacted for ~8 hours under an argon atmosphere at 120–150 °C and the structural evolution of the reacting reagents was evaluated by ^{1}H NMR spectroscopy. The notable resonances were monitored and are labelled in Figure 12. There was a reduction in the relative area of the singlet resonance at δ_H = 3.55 ppm (a_1), responsible for the methoxy protons in GPTMS; this was expected due to the exchange of methoxy groups and removal of MeOH. A small resonance remained in the final sample, suggesting that there was not complete exchange of the methoxy groups for PG in the reaction. The signals at δ_H = 3.85 ppm (b_1), 3.55 ppm (b_2) and 1.10 ppm (b_3) correspond to the CH_3, CH_2 and CH protons in PG, respectively. Their relative intensity remained consistent throughout the reaction, which was to be expected as they are present in the starting reagents and final product. A new resonance at δ_H = 3.35 ppm (c_1) was observed at 20 minutes for the CH_3 in MeOH. With respect to the resonances from the protons in GPTMS, δ_H = 3.15 ppm (a_2) from the CH proton in the

epoxide, δ_H = 2.55 and 2.75 ppm (a_3) from the CH_2 protons in the epoxide, and δ_H = 1.70 ppm (a_4) from the CH_2 protons adjacent to the silicon-bound carbon remained consistent throughout the reaction which suggests that these structures within GPTMS were retained as expected.

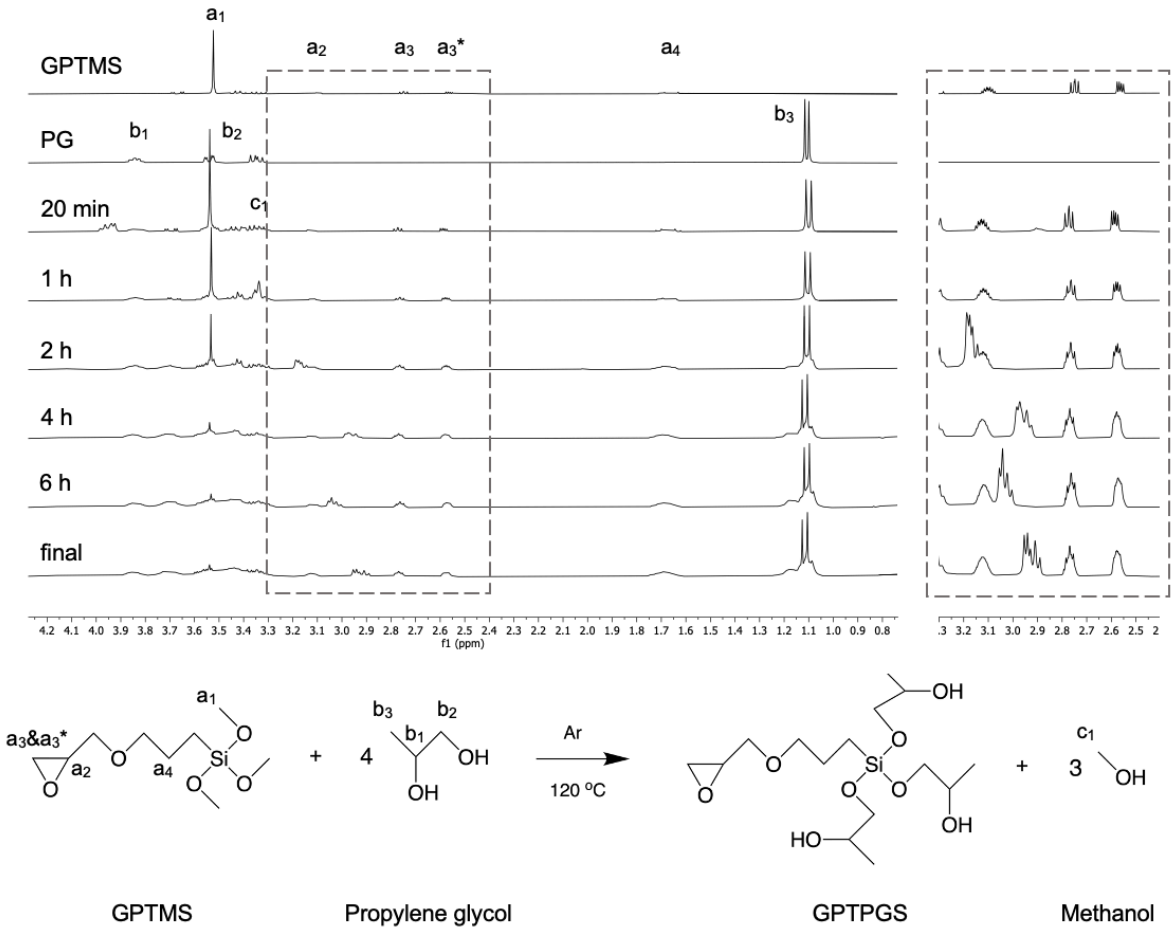


Figure 12. ^1H NMR spectra of starting reagents GPTMS and PG (D_2O solvent), as well as GPTPGS after 20 minutes, 1, 2, 4, and 6 hours, followed by the final sample at 8 hours ($CDCl_3$, 400 MHz). The reduction in δ_H = 3.55 ppm (a_1) for the protons on the CH_3 methoxy group of GPTMS suggests exchange of methoxy groups occurred. All other resonances from GPTMS and PG remained throughout the reaction. The reaction scheme and a suggested chemical structural of GPTPGS is shown.

The areas of the resonances from the GPTMS molecule were analysed over the course of the reaction using MestReNova and are shown in Figure 13. When quantified, the relative area of the resonance at δ_H = 3.55 ppm (a_1) from the methoxy groups in GPTMS decreased, which

confirmed the exchange of the methoxy groups and removal of MeOH. All other resonances quantified within the GPTMS structure; δ_H = 3.15 ppm (a_2), δ_H = 2.55 and 2.75 ppm (a_3), and δ_H = 1.70 ppm (a_4), remained at a consistent relative intensity throughout (Figure 12 and Figure 13). This demonstrates that the reaction conditions did not impact these structures within the GPTMS molecule. Additionally, the intensity of the new resonance at δ_H = 3.35 ppm (c_1) observed at 20 minutes for the CH_3 in MeOH increased at 1 hour and then decreased and plateaued throughout the reaction. However, it is challenging to interpret the residual resonance of MeOH due to its overlap with the resonance δ_H = 3.35 ppm (b_2) from PG (Figure 12).

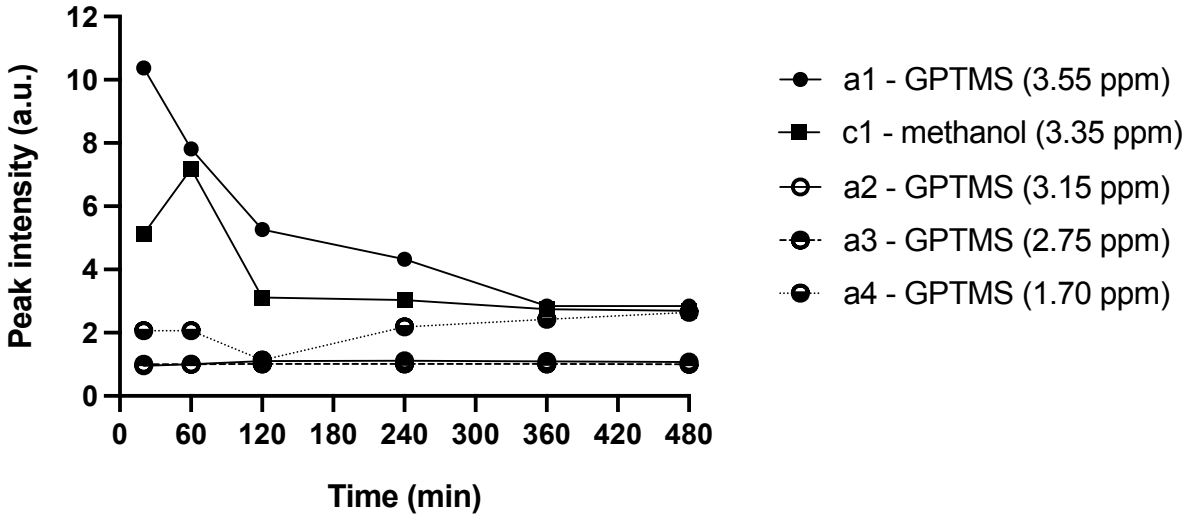


Figure 13. Resonance intensity (a.u.) of $a_{1, 2, 3,}$ and $_4$ in GPTMS and c_1 from the production of MeOH, using δ_H = 3.55 ppm PG resonance as 1.00 standard.

2.3.2. Chemical characterisation of GelMA

The functionalisation of methacryloyl groups to gelatin molecules was confirmed by the ^{1}H NMR spectra (Figure 14). This reaction is well described in the literature and is confirmed by

two characteristic changes to the spectra; the decrease in the resonance at δ_H = 2.90 ppm from the consumption of methylene protons of the lysine resonance during gelatin and methacryloyl conjugation and the appearance of resonances at δ_H = 5.40 and 5.70 ppm from the protons of methacrylate vinyl groups of methacrylic anhydride (MA) in the methacrylated product (154–156).

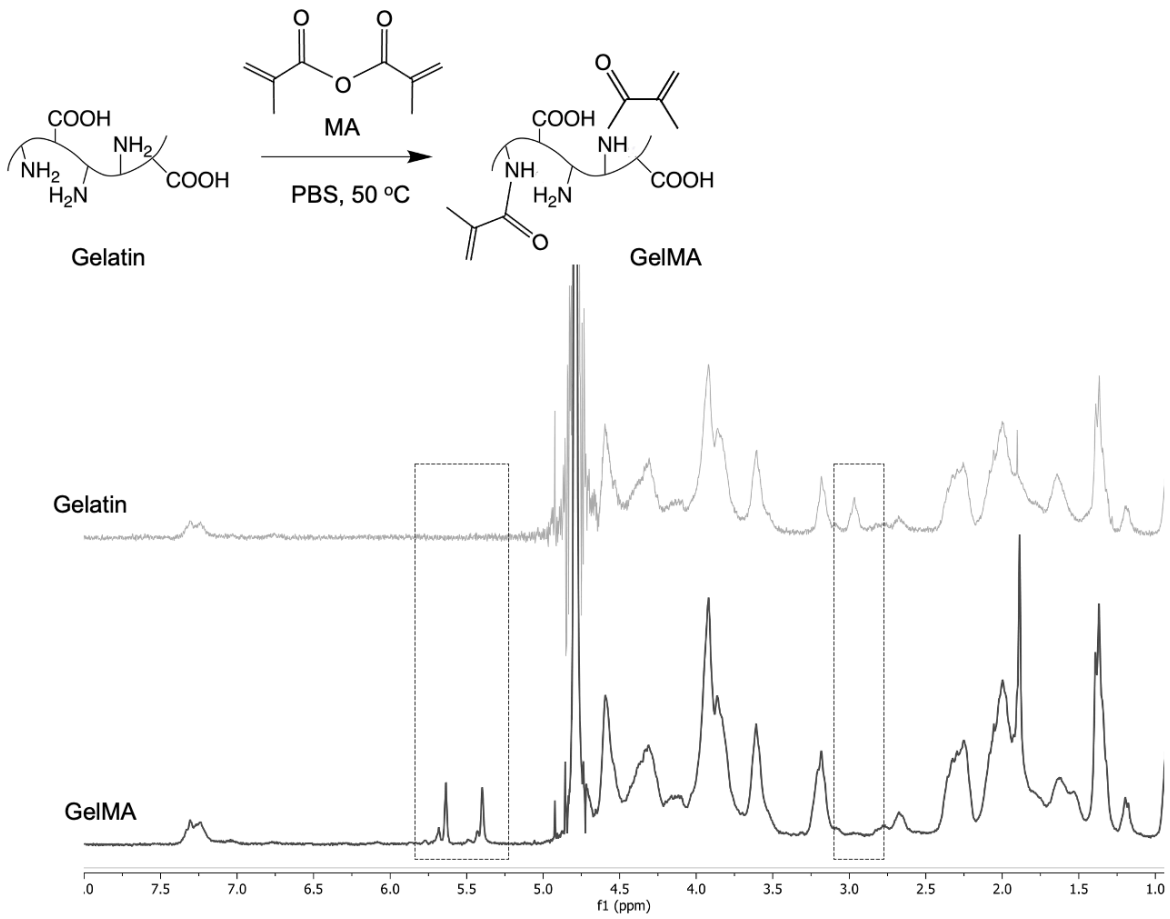


Figure 14. [1]H NMR spectra of unmodified gelatin (Gelatin) and methacryloyl functionalised gelatin (GelMA) (D_2O, 400 MHz).

2.3.3. Characteristics of hydrogels with varying compositions

Gelatin or GelMA were used as the organic portion in all hydrogel formulations and were chosen because gelatin is the hydrolysed form of collagen, a major component of the extracellular matrix of tissues (157). Gelatin also retains RGD sequences which are

recognised and adhered to by cells and can promote cell migration, proliferation and differentiation (158,159). However, there are difficulties associated with the use of pure gelatin hydrogels for functional materials; gelatin has poor mechanical properties and undergoes rapid degradation under physiologically relevant conditions due to its temperature sensitivity, rendering gelatin hydrogels unsuitable for applications such as BTE (159,160).

As gelatin is composed of different amino acids, it has numerous active side chains e.g. -COOH and -NH_2, which can be chemically modified (161). GelMA is an example of chemically modified gelatin, wherein a methacrylate group has been transferred to side chain lysine residues on the gelatin. Upon photopolymerisation in the presence of a photoinitiator, the methacrylate residues undergo covalent crosslinking to form a stable hydrogel (159). The mechanical properties of GelMA, such as the compressive modulus (5.0 wt%; ~3 kPa to 15.0 wt%; ~30 kPa), remain far off that of bone (15 to 20 MPa) limiting the application of GelMA in BTE (136,161–163).

This considered, both gelatin and GelMA were used to create gelatin-based-silica hybrids as there is the capacity to vary the crosslinking within the hybrid hydrogel on two levels. Firstly, ‘intra-crosslinking’ involving either non-covalently bonded gelatin chains versus covalently bonded GelMA chains. Secondly, ‘inter-crosslinking’ between gelatin/GelMA (organic) and a silica-precursor (inorganic) involving either non-covalent interactions in Class I hybrid or covalent bonds in a Class II hybrid. Therefore, the impact of combining different variations of ‘intra-crosslinking’ with ‘inter-crosslinking’ on the mechanical and degradative properties were investigated by comparing a:

- Class I hybrid hydrogel composed of non-covalently bonded gelatin chains with non-covalent interactions between gelatin and silica

- Class I hybrid hydrogel composed of covalently bonded GelMA chains with non-covalent interactions between GelMA and silica
- Class II hybrid hydrogel composed of non-covalently bonded gelatin chains with covalent bonds between gelatin and silica
- Class II hybrid hydrogel composed of covalently bonded GelMA chains with covalent bonds between GelMA and silica

2.3.3.1. Gelation characteristics

A sol-gel method was used to synthesise gelatin-based-silica hybrid hydrogels by mixing either gelatin, GelMA, Gel-GPTPGS, or GelMA-GPTPGS (organic source), with PGMS (inorganic source) and H_2O at physiologically relevant pH. PGMS was used in all hybrid formulations except one with GLMS; this was because the GLMS was more viscous than PGMS and often solidified after transesterification, and therefore was difficult to use.

Hydrogels were qualitatively assessed with respect to gelation characteristics, which included gelation time and appearance. Additionally, pH change was measured throughout gelation. Here, gelation time is noted as the time taken for the hydrogel to transition from liquid to solid and become 'self-supporting'. Upon gelation, hydrogel compositions were categorised as either translucent or opaque, if phase separation had occurred, and on their colour. The findings are presented in Table 2 with the corresponding hydrogel images in Figure 15.

Table 2. Gelation characteristics of 17 different compositions of gelatin-based-silica hybrid hydrogels. The following variables were altered to result in numerous different compositions; gelatin type (gelatin, GelMA, Gel-GPTPGS, or GelMA-GPTPGS), O:I ratio, solvent (DMEM or dH_2O), and silica source. When dH_2O was used, the same protocol as Section 2.2.3 was used to synthesise the hydrogels. Gelation time, phase separation, appearance, and pH change were investigated. Results were highlighted grey if the hydrogel gelled, did not phase separate, and was transparent in appearance as these properties were key for further use of the hydrogels. Gelation time and pH transition were performed in triplicate and the average is shown (n=3).

Gelatin type	**Composition No.**	**O:I ratio**	**Solvent**	**Silica source**	**Gelled (Y/N)**	**Phase separation (Y/N)**	**Appearance**	**Mean gelation time (min)**	**Mean pH transition**		
									Before	**After**	**Difference**
Gelatin	#1	100:0	DMEM	/	Y	N	Transparent	54:53	7.95	/	/
	#2	80:20	DMEM	PGMS	Y	N	Transparent	88:35	7.99	6.82	−1.17
	#3	60:40	DMEM	PGMS	Y	Y	Opaque	03:10	8.27	6.92	−1.35
	#4	60:40	dH_2O	PGMS	N	Y	Opaque	/	8.91	6.56	−2.35
	#5	60:40	DMEM	GLMS	N	Y	Opaque	/	8.09	7.25	−0.84
	#6	40:60	DMEM	PGMS	Y	Y	Opaque	01:05	8.05	6.78	−1.27
	#7	20:80	DMEM	PGMS	Y	Y	Opaque	05:12	8.05	6.79	−1.26
GelMA	#8	60:40	DMEM	PGMS	N	/	Transparent	/	6.79	5.94	−0.85
	#9	40:60	DMEM	PGMS	Y	Y	Opaque	02:35	7.31	6.66	−0.65
	#10	20:80	DMEM	PGMS	Y	Y	Opaque	01:30	7.64	6.85	−0.79
Gel-GPTPGS	#11	100:0	DMEM	GPTPGS + PGMS	N	/	Transparent	/	7.91	/	/

	#12	60:40	DMEM	GPTPGS + PGMS	N	/	Transparent	/	8.06	7.31	–0.75
	#13	40:60	DMEM	GPTPGS + PGMS	Y	Y	Opaque	01:32	8.03	7.07	–0.96
	#14	20:80	DMEM	GPTPGS + PGMS	Y	N	Opaque	04:48	7.96	7.02	–0.94
GelMA-GPTPGS	#15	60:40	DMEM	GPTPGS + PGMS	N	/	Transparent	/	8.09	6.96	–1.13
	#16	40:60	DMEM	GPTPGS + PGMS	Y	N	Opaque	01:15	7.87	6.70	–1.17
	#17	20:80	DMEM	GPTPGS + PGMS	Y	N	Transparent	02:42	7.95	7.03	–0.92

Phase separation and appearance

Phase separation occurred in hydrogels #3, 4, 5, 6, 7, 9, 10 and 13, also resulting in an opaque hydrogel (Figure 15). Phase separation is a thermodynamic phenomenon which results in two distinct phases from a homogenous mixture and was noted when any of the following occurred visually: inhomogeneity, precipitation, or particle agglomeration (164). Additionally, phase separation was often accompanied by syneresis, contraction of the gel network and expulsion of dH_2O/media from the hydrogel structure. Hydrogels #1, 2, and 17 gelled, were more transparent and did not phase separate. These hydrogels had a dissimilar O:I (e.g. 100:0, 80:20, 20:80). Additionally, when the organic and inorganic components were at a similar O:I ratio, e.g. 40:60 and 60:40, phase separation was more likely to occur, along with hydrogels appearing opaque.

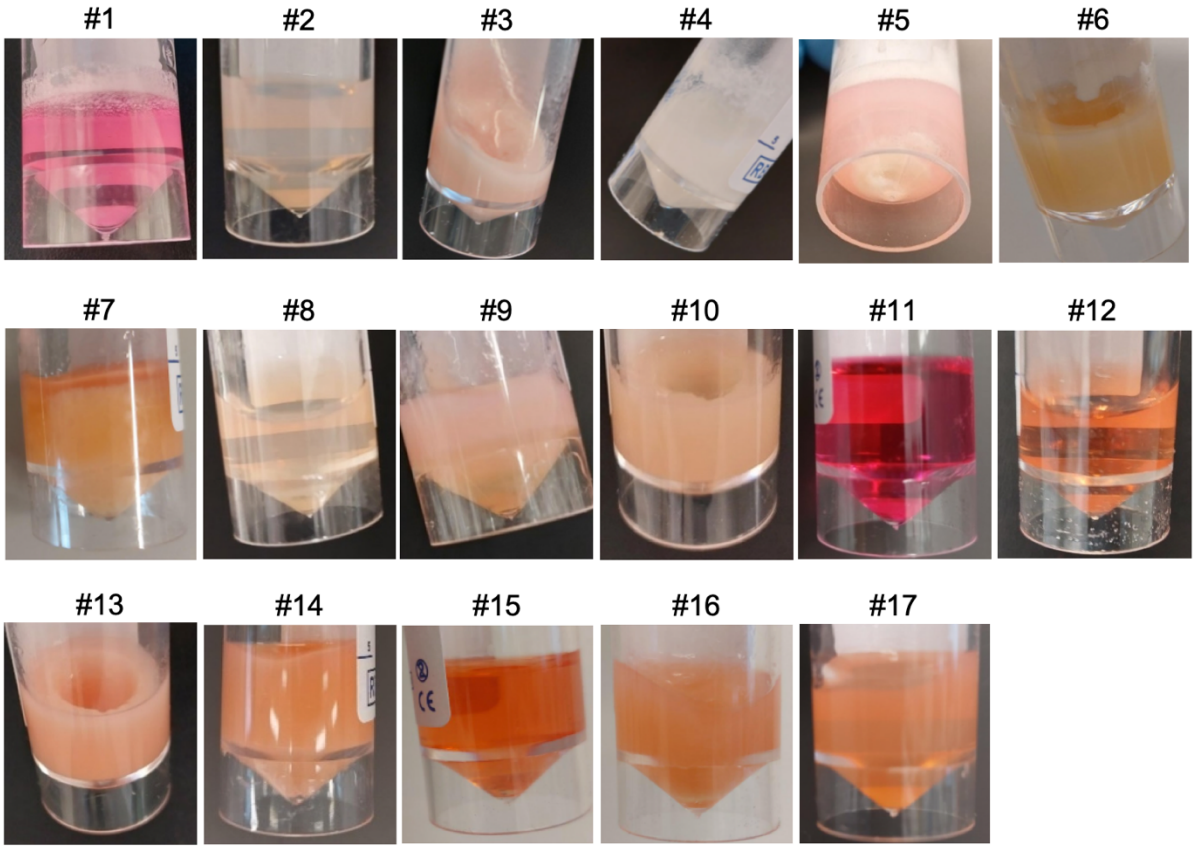


Figure 15. Visualisation of hybrid hydrogels. The following variables were altered to result in different compositions; gelatin type (gelatin, GelMA, Gel-GPTPGS or GelMA-GPTPGS), O:I ratio, media/water, and silica source with varying components, with numbers (#) corresponding to Table 2 . The variable colour is a result of different components used in the hydrogel formulation. Generally, hydrogels where the wt% of organic and inorganic a similar e.g. 40:60 and 60:40, precipitated, phase separated and were opaque, whereas all transparent hydrogels that gelled did not phase separate. For scale, diameter of the universal tube = 25 mm.

Within the hydrogels, there are three main phases: the gelatin-based organic, the silica-based inorganic, and the solvent aqueous phase. The organic and inorganic phases could be interacting intimately, leading to rapid agglomeration and phase separation from the aqueous phase; an interaction that has been reported in previous gelatin/silica mixtures (165,166). Scattering profiles from time-resolved small-angle X-ray scattering (SAXS) in a percolated gel have demonstrated that scattering intensities increased with time, indicating a more opaque and phase separated network, when compared to non-percolated gel (167).

Additionally, changes were reported in the dispersion of the condensed polymer segments, with a mixture of condensed regions and resultant sparse regions (167). Previous studies (168–170) have reported issues associated with unfavourable electrostatic interactions between composites containing organic polymers and other inorganic phases. When these unfavourable interactions happen, phase separation occurs which leads to difficulties dispersing the two phases, and therefore, particle agglomeration (171).

Other studies using organosilanes and their counterpart polyol-modified silanes detail the issue of hydrogel precipitation upon mixing with biologics (145,147). Precipitation/aggregation, premature/partial gelation and hydrogel syneresis, outcomes that were observed here, have all been reported, specifically in the hydrogels with more balanced O:I ratios (145,147). The hydrophobicity of the organosilane was highlighted by Gill et al. (145) as the cause for opaque, phase separated polymers. Furthermore, polyol-modified silane precipitated silica particles in the presence of biologics have demonstrated phase separation, which was rationalised by electrostatic interactions between the negatively charged silica and positively charged organic molecules, resulting in a change in the colloidal stability (147). Therefore, the hybrid hydrogels with more dissimilar O:I ratios may have one component that dominates the system, rather than enhanced intermolecular interactions in more similar O:I ratios, which leads to improved compatibility of the gelatin-based and silica components (168–170).

The compatibility of materials within a hybrid hydrogel is important to consider as it will often have a consequence on the mechanics of the hydrogel. For example, phase separation has been reported to provide hydrogels with favoured crack propagation direction (168), a phase with differing properties to the host bulk polymer (169), and lower stability than its

pure biopolymer counterpart (170). Another cause for phase separation could be that when gelatin is contained within solution near its isoelectric point (pI), 7.0–9.5 in Type A gelatin, there is an increased propensity for phase separation with certain solvents or counterions, and low transparency of the hydrogel (171,172). Table 2 shows that all hydrogels were mixed at a pH near gelatin's pI. Gelatin is naturally hydrophilic, however, at least 2/3 of the amino acid residues within the structure (e.g. alanine, proline, isoleucine, leucine, valine and phenylalanine) exhibit hydrophobic, non-polar properties (160,173), resulting in incompatibility of silica and gelatin. This means there is increased proximity of gelatin molecules when at a pH near gelatin's pI due to the net charge on the gelatin molecule being closer to zero. All of this results in gelatin self-aggregating to minimise its contact with H_2O and phase separation of the silica and gelatin.

Altering the pH and controlling reagent concentrations have both been shown to control phase separation (170,174). Precipitation and turbidity of protein-silica systems is lower in more acidic (below pH 4) and alkaline (over pH 10) pH because the aggregation of proteins and silica particles is occurring in the vicinity of the pI of the protein (174). As the aim of this thesis was to produce gelatin-based-silica hybrid hydrogels for the encapsulation of cells, the sol-gel reaction needed to occur at physiologically relevant pH, and so, altering the pH was not a potential route for controlling phase separation. The hybrid hydrogels that did not phase separate, were transparent, and gelled, were hydrogels #2 and #17. Both these formulations had a larger difference in O:I e.g. 80:20 and 20:80. Therefore, controlling the reagent concentration was deemed a more appropriate method to regulate phase separation.

Gelation time

Hydrogels were fixed at 5.0 wt %, which meant that the R-ratio (molar ratio of H_2O to inorganic content) changed between formulations. The R-ratio affects the transformation of silica-precursors to silica gels in the sol-gel process; the lower the R-ratio, the faster the gelation (175).

Hydrogels #4, 5, 8, 11, 12, and 15 did not form a gel. The 3D encapsulation of cells within hydrogels represents an increasingly important and popular technique for culturing cells. Gelation of a hydrogel is key for application within 3D scaffolds, and therefore, further analysis of hydrogels #4, 5, 8, 11, 12, and 15 was ruled out. Additionally, gelation time is an important factor for successful cell encapsulation, as a long gelation time can cause cell sedimentation and uneven distribution of cells due to gravity. This presents a big obstacle and can restrict a hydrogel's application.

For the hydrogels that gelled, all compositions took <10 minutes, excluding hydrogels #1 and 2. Interestingly, these two hydrogels did not experience phase separation and were translucent, whereas all gels that appeared opaque with phase separation experienced rapid gelation. It is suggested that the observed 'gelling' when mixing these formulations could be a transient state formed immediately after phase separation (176,177). The transient state, which is observed as a gel-like structure, is potentially driven by the entanglement or weak physical crosslinking of gelatin molecules (178). As the phase separation process progresses, the gel experiences shrinkage which can expel the 'fast' component, the component that has high mobility, which is not stabilised and integrated within the gel (177). This component is likely to be the solvent, as seen by the expulsion of media from the structure which is particularly visible in hydrogel #7 (Figure 15).

As previously mentioned, a lower R-ratio in sol-gel is associated with a quicker gelation time due to higher hydrolysed degree of the silica-precursor and more primary particles (individual, non-agglomerated particles) in the solution (179). However, for all 60:40, 40:60, and 20:80 hydrogel formulations, except those containing GelMA, a lower R-ratio yielded a shorter gelation time. Gelation time for 60:40 (hydrogel #3; 3 minutes 10 seconds), 40:60 (hydrogel #6; 1 minute 5 seconds), and 20:80 (hydrogel #7; 5 minutes 12 seconds) hydrogel formulations was significantly shorter when compared to 100:0 (hydrogel #1; 54 minutes 53 seconds) and 80:20 (hydrogel #2; 88 minutes 35 seconds) (Figure 16). This supports that the observed phenomena of 'gelling' is actually a transient gel due to phase separation.

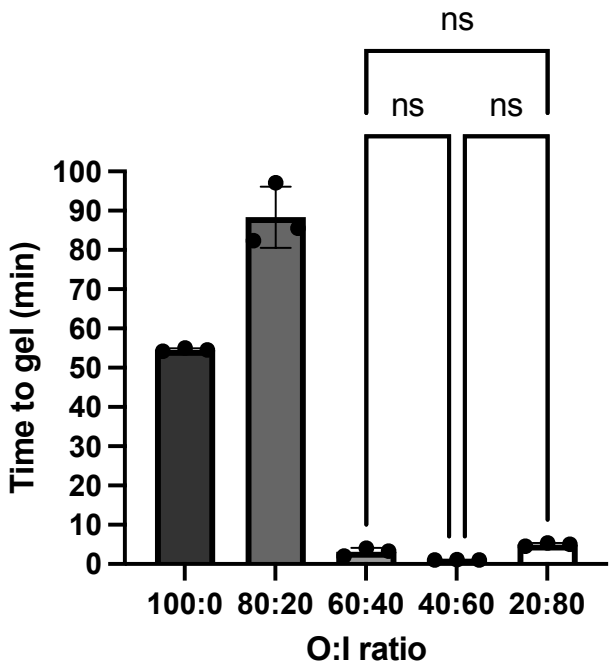


*Figure 16. Gelation time of Gel-Silica hydrogels with varying O:I. The points plot on each bar represent a repeat measure and errors bars represent the SD (n=3). Ns is shown for clarity, all other comparisons were statistically significant (****; p≤0.0001) [ns = non-significant].*

Upon PGMS addition, an increase in the gelation time was observed for formulations #1 and 2, a pure gelatin formulation and then with the addition of silica (Figure 16). This increase in

gelation time with the addition of silica is likely due to the solution being depleted of protein molecules and the silica particles hindering the build-up of the gelatin network (170,180). In fact, it has been reported that the minimum gelatin concentration for gel formation in the presence of a precipitate is larger than the concentration necessary for the protein alone – the minimum concentration required for aqueous gelatin gelation is 1 wt% (170,180). This is supported by hydrogel #11, Gel-GPTPGS 100:0 (Table 2), not achieving gelation, which can be suggested again to be owed to the addition of GPTPGS hindering gelatin molecule proximity and the hydrogen bonding intermolecular interactions that are required for the formation of the typical collagen-like structure for gelation (173,181–183).

As previously discussed, transparency and phase homogeneity are desirable features to give optimum properties. Therefore, focussing on Class II hydrogels that gelled, as well as appeared transparent and did not phase separate, hydrogel #14 was the only Gel-GPTPGS formulation to fulfil these criteria. Additionally, its GelMA-GPTPGS counterpart hydrogel #17 yielded the same results.

Based on the results, three hydrogel formulations were selected for further analysis: GelMA-Silica (#10; Class I), Gel-GPTPGS-Silica (#14; Class II), and GelMA-GPTPGS-Silica (#17; Class II), all at 20:80 (O:I). These were selected as both Class IIs were transparent, did not experience phase separation and gelled through sol-gel mechanism; the Class I counterpart was also selected for comparison.

2.3.4. Chemical characterisation of hybrid hydrogels

2.3.4.1. FTIR

Samples were oven-dried and FTIR spectra were taken to examine functional groups and bonds, such as siloxane (Si–O–Si) stretching vibrations that would be expected to be observed due to the silica network. FTIR spectra obtained from the three different hydrogel formulations are shown, as well as their starting reagents, in Figure 17. The presence of siloxane/Si–O–Si bands in the FTIR spectra at 1150–1020 cm^{-1} is a good indicator that a silica network has been formed by PGMS within the hydrogels (184). A strong band appeared in all three hydrogel formulations at 1050 cm^{-1}, confirming siloxane/Si–O–Si network condensation. There is conflicting evidence in the literature as to where the vibration for Si–OH non-bridging oxygen bond is seen; 970–940 cm^{-1}, 950 cm^{-1}, and 920 cm^{-1} (112,184,185). Here, the results suggest that the small shoulder band arising at 960–900 cm^{-1} may correspond to Si–OH bands, suggesting the small presence of uncondensed network.

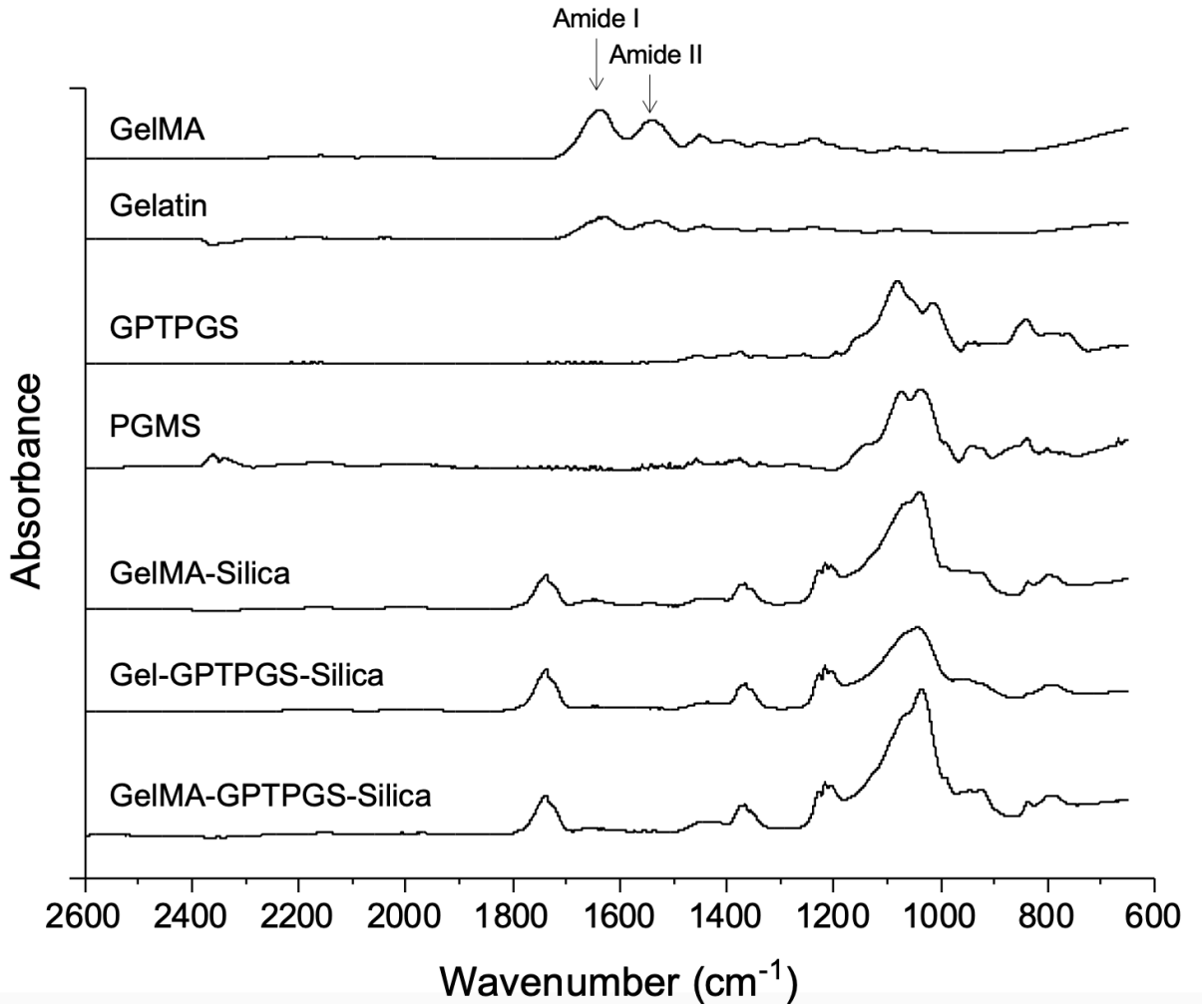


Figure 17. FTIR spectra of a GelMA-Silica hydrogel (Class I), Gel-GPTPGS-Silica (Class II) and GelMA-GPTPGS-Silica (Class II) hydrogels and their starting components GelMA, gelatin, GPTPGS, and PGMS (n=3).

A strong peak is visible at 1750 cm^{-1} in all three hydrogels. Based on literature, it is theorised that the carboxylic groups (114,187) of gelatin/GelMA will react with the epoxide in GPTPGS via nucleophilic attack and result in the formation of an ester (114,186). A band for an ester linkage is typically visible at 1750–1725 cm^{-1}. However, it is unlikely that an ester linkage is responsible for this peak as an ester linkage would not be present in the Class I GelMA-Silica but the peak is visible in this spectrum. This suggests that the peak at 1750 cm^{-1} does not correspond to ester bonding being present and is instead a consequence of an issue with the FTIR and the force applicator absorbing IR in the range.

The high ratio of silica to gelatin/GelMA in the hydrogels is evident as notable bands on the gelatin and GelMA starting reagent spectra, such as 1700–1600 cm^{-1} (Amide I), 1580–1510 cm^{-1} (Amide II), and ~1400 cm^{-1} (Amide III), have lower intensity in the hydrogels. This could also be a reason for why it is difficult to find the ester band. These FTIR analyses only give an indication of the final product composition, it is not possible to discern the mechanism for the functionalisation of gelatin with GPTPGS. These data would suggest the confirmation of a condensed silica network forming within the hydrogels.

2.3.5. Degradation behaviour of gelatin-based-silica hybrid hydrogels

To investigate their degradation behaviour, the hybrid hydrogels were submerged in PBS and hydrogel degradation was analysed by measuring mass and pH change over 28 days.

For tissue engineering purposes, hydrogels must have the ability to be constructed into strong scaffolds with an open, interconnected pore network, with adaptable mechanical properties. Ideally, these hydrogels should display regulated degradation in order to preserve mechanical properties, but also facilitate neotissue ingrowth (187). Gelatin has uncontrolled degradation when at physiologically relevant temperatures due to its thermoreversible nature in aqueous media, with a sol-gel transition of ~27 ºC, due to an increase in temperature breaking down the triple helices structures (180,188,189). Numerous gelatin-silica hybrid studies have reported precise control of dissolution properties upon hybridisation (117,184,190). Here, a degradation assay was used to determine if the hybridisation processes with the incorporation of a silica component would lead to more controlled degradation of the gelatin-silica hydrogels.

2.3.5.1. Change in mass

Over 28 days, hydrogels were removed from PBS and weighed. Mass remaining (%) of the three hydrogel formulations as a function of time across the 28 days is shown in Figure 18. Overall, there was no significant difference in the mass of hydrogel remaining between any of the formulations at any time points. The results indicate that all three formulations experienced a similar rate of dissolution until 7 days, whereafter GelMA-Silica progressed to decrease in mass at a higher rate than the two Class II formulations. This suggests that the Class II formulations provide more control over long term degradation, compared to GelMA-Silica, a Class I hybrid hydrogel.

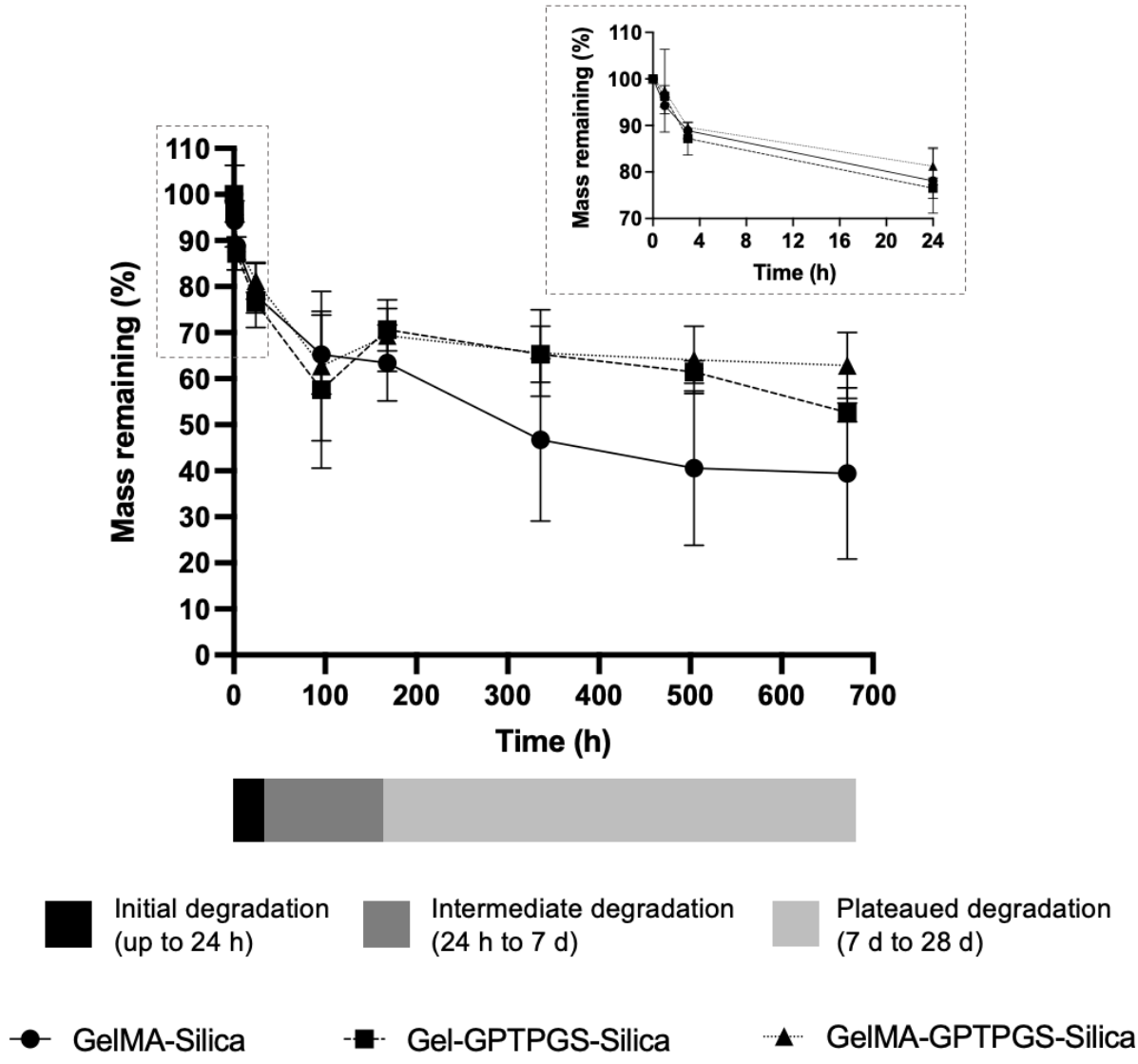


Figure 18. Mass remaining (%) of GelMA-Silica, Gel-GPTPGS-Silica, and GelMA-GPTPGS-Silica hybrid hydrogel formulations immersed in PBS at 37 °C over a 28 day time period (n=3). Degradation trend has been split into three distinctive regions; initial, intermediate and plateaued degradation. There was no significant difference in the mass of hydrogel remaining (%) for each formulation at any time point throughout the assay. Inset shows the first 24 hours. Error bars represent the SD (n=3).

Overall, there was no significant difference between the degradation rate per hour of any of the formulations (Appendix Section A.2.3.5). The lack of difference between GelMA-Silica and Class II formulations indicates that the use of GPTPGS as a coupling agent with gelatin and PGMS is not effective. This could be due to numerous reasons, including, unsuccessful

functionalisation of gelatin/GelMA with GPTPGS, which would mean no covalent bonds between the organic and inorganic phase. Alternatively, if the gelatin/GelMA is successfully functionalising, it may not be providing enough crosslinks between the organic and inorganic phase to yield a beneficial effect on properties. This suggests that GPTPGS does not have the same effect as GPTMS, the native coupling agent that is used to synthesise GPTPGS. Literature investigating the coupling reaction of GPTMS with biopolymers is extensive, although in all of these studies, the hybrid is used in its monolithic form, the crosslinking yielded benefits such as tailorable properties by varying fraction of GPTMS, the ability to create membranes with patterned surfaces with contact guidance ability and the capacity to 3D print, retaining high levels of coupling and sol-gel network condensation (117,128,130,131,133,184,190,191). The coupling reaction between GPTPGS and gelatin/GelMA should in theory be the same as if GPTMS were used. The gelatin-GPTMS reaction involves the reaction of the epoxide group of GPTMS with the nucleophilic functional groups of gelatin, such as a carboxylic acid (-COOH) or amine ($-NH_2$), under in mildly acidic conditions (pH 5) (129,130,190–193). GPTPGS also has the epoxide functionality and so is expected to undergo the same nucleophilic substitution reaction. Therefore, future work will investigate the coupling reaction between GPTMS with gelatin in more detail.

2.3.5.2. Change in pH

Incubation of all three hydrogel formulations resulted in an overall reduction in pH of the PBS, which began to plateau and eventually reach pH 6.6 after 28 days (Figure 19). The rapid decrease in pH observed after 24 hours until 7 days (intermediate region) can be attributed to the release of silica as silicic acid (194). However, from 7 days onwards, GelMA-Silica PBS pH was significantly lower than the Class II hybrids. As the GelMA-Silica hydrogel was

formulated as a Class I hybrid, the GelMA and silica components are simply embedded within one another, associated through weak, non-covalent interactions, such as hydrogen bonds. Therefore, the continual decrease in pH could be a consequence of weakly bonded silica within the network that is released from the hydrogel in the form of silicic acid.

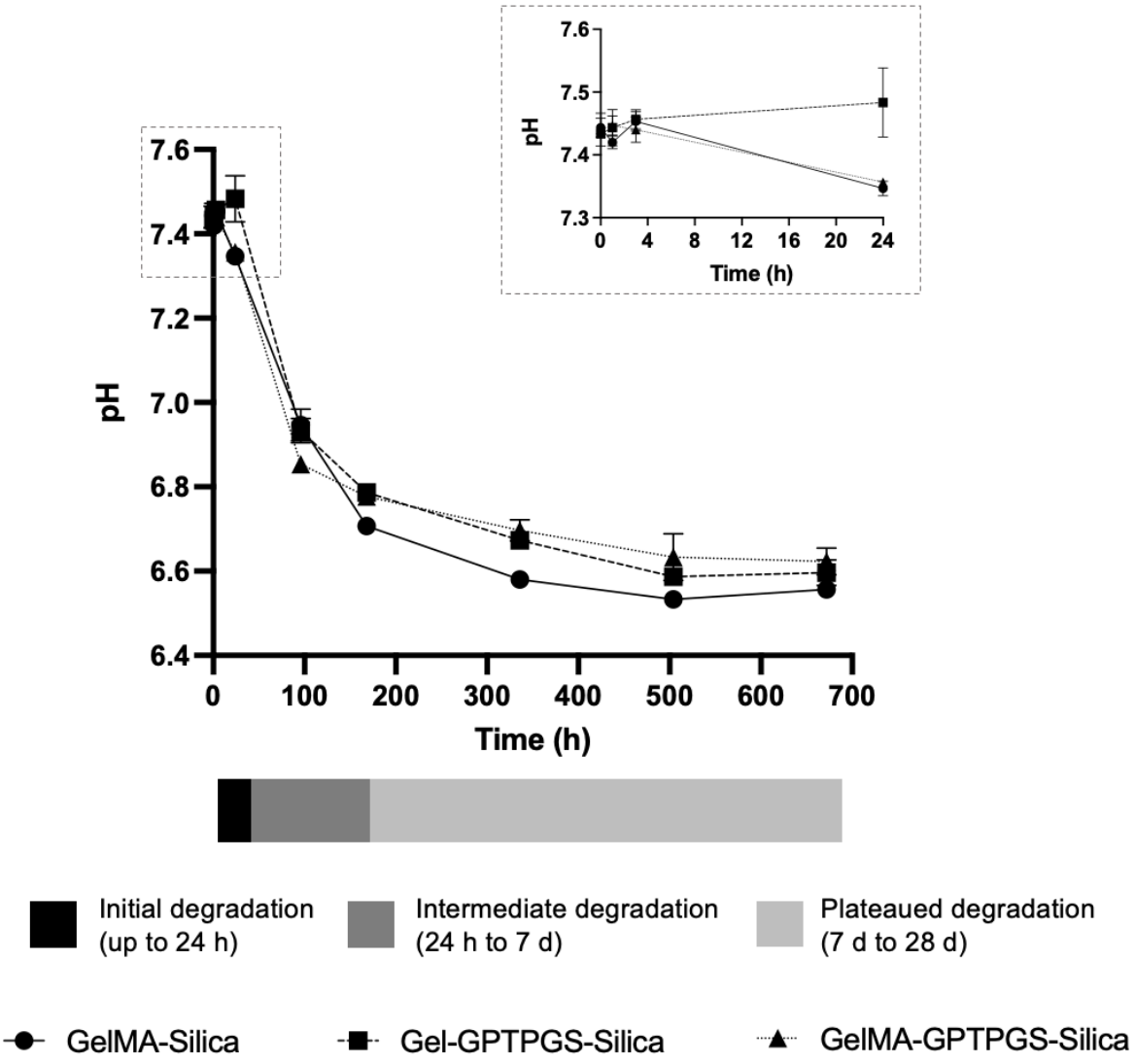


Figure 19. pH of PBS, with GelMA-Silica, Gel-GPTPGS-Silica, and GelMA-GPTPGS-Silica hybrid hydrogel formulations immersed at 37 °C over a 28 day time period. pH change has been split into three distinctive regions; initial, intermediate and plateaued degradation. Inset shows the first 24 hours. Error bars represent SD (n=3).

The pH of the environment as a result of hydrogel dissolution is an important parameter to consider as pH must stay within the range that osteoblasts and osteoclasts would encounter *in*

vivo to aid bone remodelling. Osteoclasts have the capacity to resorb bone between pH 6.8 to 7.2, although it is optimal at pH 7.0. Beyond pH 7.4, bone-resorbing capacity sharply declines. Bone nodules are best formed by osteoblasts at pH 7.4; capacity to create bone nodules declines with decreasing pH (195). Therefore, the capability of bone cells to form bone nodules should decrease with increased dissolution due to the increasing acidity of the environment. Specifically, it can be assumed that after 96 hours, osteoblast cell viability would decrease as the pH <6.8. In fact, low pH media (pH 6.4–6.8) has been shown to induce autophagy in osteoblasts (196).

2.4. Summary

Glycol-modified silane precursors and coupling agents have been synthesised for the preparation of gelatin-based compatible silica hybrid hydrogels. Using conditions similar to previous functionalisation reactions, functionalisation of gelatin and GelMA with a novel PG-modified silane coupling agent, GPTPGS, was attempted for the first time. An in-depth study was conducted to probe the interactions of gelatin and GelMA with polyol-modified silanes PGMS and GLMS, to form hydrogels using a sol-gel reaction. Hydrogels that experienced phase separation were found to be opaque in appearance and were typically formulation from similar proportions of the organic and inorganic components, i.e. 40:60 or 60:40. It was difficult to obtain hydrogels that underwent full gelation without phase separation. Phase separation led to hydrogels with a low load-bearing capability. Additionally, phase separation seemed to highly influence 'gelation time', although it is thought that the hydrogels were not gelling but experiencing a 'transient', gel-like structure state as a consequence of phase separation. A 28-day dissolution study in PBS showed that there was no difference in degradation rate with respect to mass loss between the three formulations. This indicates there was either low or no functionalisation between gelatin/GelMA and GPTPGS, meaning a lack of linkages between the organic and inorganic domains. This work highlights the issues around interactions of gelatin and silica when wanting to produce a hybrid hydrogel, including phase separation and precipitation. More importantly it confirms the need to investigate the functionalisation reaction between a gelatin-based biopolymer with an epoxide-based coupling agent, a reaction used widely by the scientific community, in more detail.

CHAPTER 3. INVESTIGATING AND OPTIMISING GELATIN FUNCTIONALISATION WITH EPOXIDE ELECTROPHILES

3.1. Introduction

Gelatin-silica hybrids, particularly Class II hybrids, which contain covalent linkages between the two components, are frequently investigated for biomedical applications. These materials have been thoroughly researched owing to their distinctive characteristics and numerous biomedical applications. They have enormous potential for tissue engineering, drug administration, and regenerative medicine because these hybrid materials combine the biocompatibility of gelatin with the tuneable qualities of silica. GPTMS is an epoxide-based organosilane that has been used to form the covalent linkages in biopolymer-containing hybrid hydrogels (112,114,117,133). In this study, coupling was performed with GPTMS, as despite its widespread use, it is still unclear how gelatin and GPTMS react, and this is something we wanted to study. "Coupling" in this study refers to the procedure of covalently joining gelatin and GPTMS to produce an inorganically modified gelatin hybrid structure. We hypothesised that a Class II gelatin-silica hybrid employing GPTMS would display improved degradation stability, when compared to Class I gelatin-silica hybrids, and make it more appropriate for BTE applications.

3.1.1. GPTMS as a coupling agent

GPTMS is a bifunctional organosilane comprising a trimethoxysilyl group at one terminus and a terminal epoxide at the other (Figure 20). It has been used extensively as a silane coupling agent for covalently crosslinking and functionalising biopolymers (114,130,133,184,190,191). Due to the variety of natural biopolymers and the flexibility of organosilane chemistry, hybrid materials hold promise as a route for improving hydrogel properties. The dual functionality of GPTMS, as well as its reaction with nucleophiles that occurs during biopolymer functionalisation, will be further discussed.

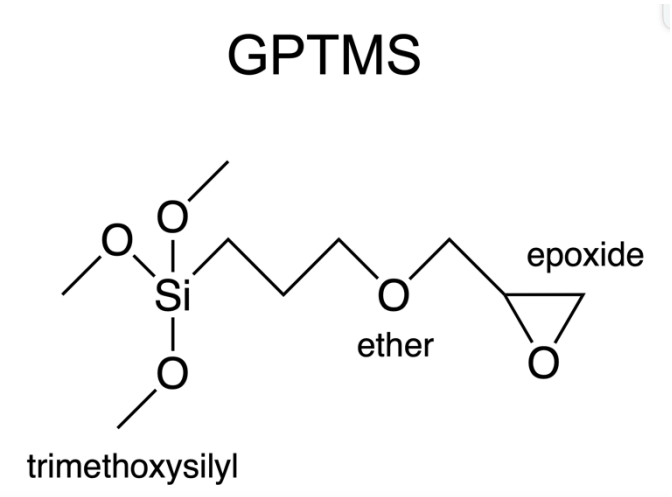


Figure 20. Structure of GPTMS.

3.1.1.1. Silyl functionality

The trimethoxysilyl functional group in GPTMS is key for the formation of silica-based hybrids. In the presence of H_2O, hydrolysis results in the formation of Si–OH, with MeOH as the by-product (Figure 21). The Si–OH groups can undergo condensation reactions with other Si–OH groups resulting in the production of Si–O–Si and the formation of a 3D silica network (Figure 21). These hydrolysis and condensation reactions are essential for generating the inorganic silica component in biopolymer-silica hybrids.

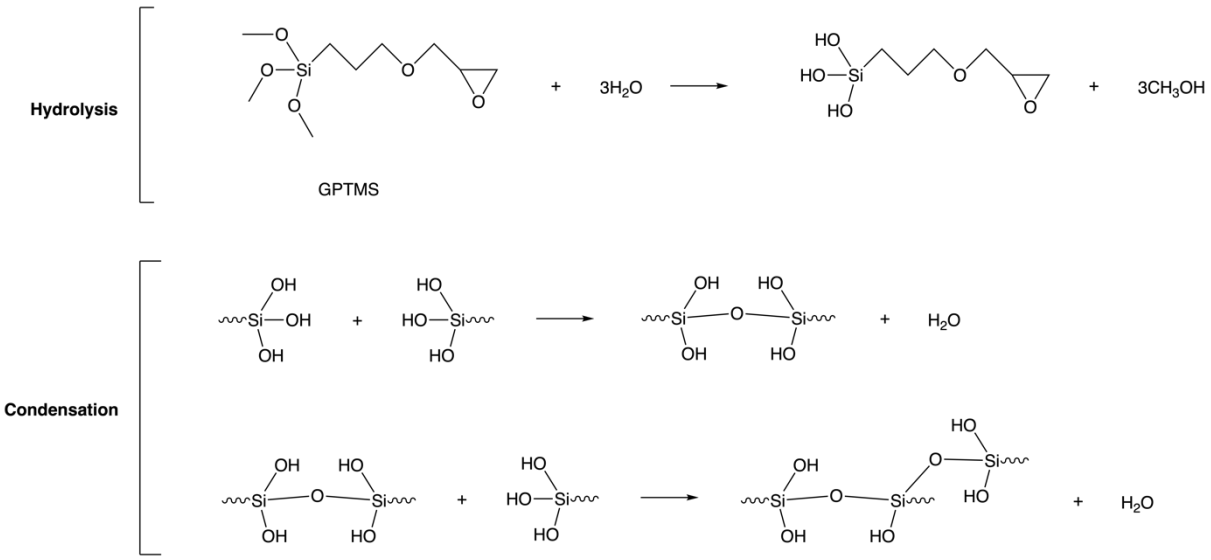


Figure 21. Hydrolysis of the trimethoxysilyl functional group in GPTMS to form Si–OH and subsequent condensation to form Si–O–Si and ultimately a silica network.

3.1.1.2. Epoxide functionality

GPTMS contains an epoxide. An epoxide is a three-membered cyclic ether consisting of an oxygen atom linked to two carbon atoms (197). Whilst ethers are generally not electrophilic, epoxides are particularly susceptible to nucleophilic ring-opening reactions owing to the release of ring strain upon ring opening. Nucleophilic ring-opening is typically regioselective, usually occurring at the less substituted terminus of the epoxide. Amines, alcohols, carboxylic acids, and thiols are examples of typical nucleophiles that can react with epoxides (198). These functional groups are also frequently found in biopolymers. Typically, coupling of GPTMS with a biopolymer proceeds through reaction of nucleophilic amino acid side-chain residues, such as the primary amine ($–NH_2$) groups of lysine residues on chitosan (112,199–201) and the carboxylic acid (–COOH) residues present in glutamic and aspartic acid of gelatin (117,190,202) (Figure 22).

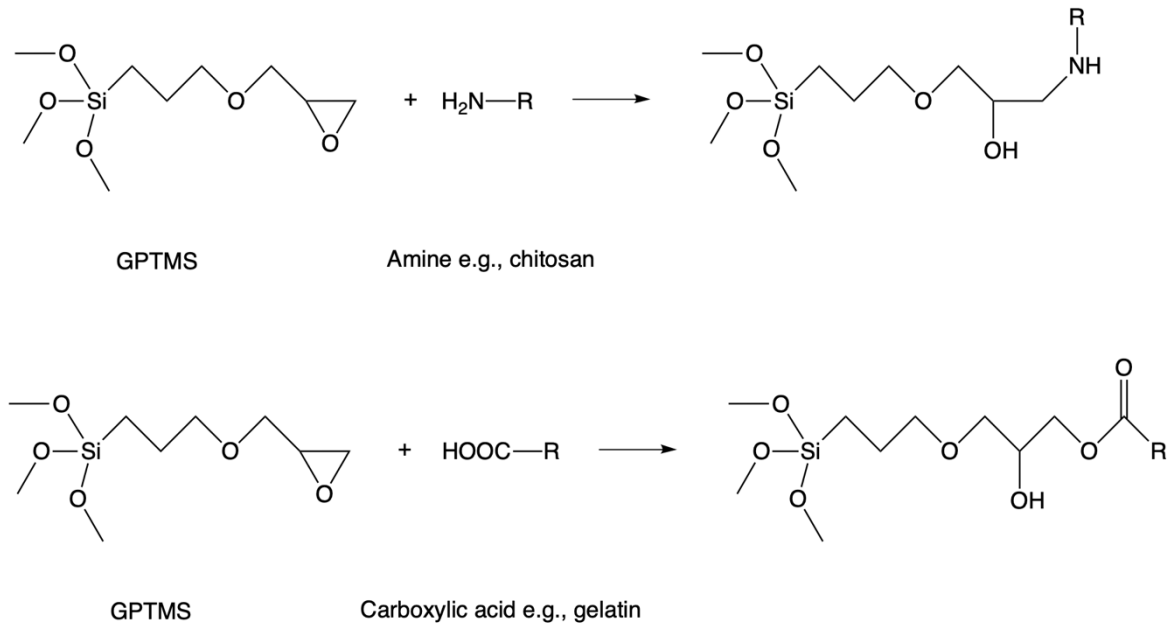


Figure 22. Epoxide ring opening of GPTMS allows functionalisation of amine-containing and carboxylic acid-containing biopolymers.

3.1.2. Formation of GPTMS-functionalised gelatin

The availability of amino acid side-chain functionality in gelatin, such as amine (-NH_2) and carboxylic acid (-COOH) groups, potentially allows for chemical modification. To enable the covalent coupling of the organic and inorganic components to form Class II hybrids, gelatin can be chemically modified with a bifunctional coupling agent prior to preparation of the hybrid – this modification step is often referred to as functionalisation (184,190).

Having discussed the nucleophilic ring-opening of the epoxide in GPTMS with diverse nucleophiles that are present in biopolymers in the previous section, it is now important to understand the reaction conditions employed, in the case of this thesis, to prepare GPTMS-functionalised gelatin. The relationship between reaction pH and the ionisation state of

functional groups on the biopolymer has a substantial impact on the outcome and attributes of the GPTMS-gelatin functionalisation reaction.

3.1.2.1. Gelatin-GPTMS functionalisation conditions

The functionalisation of gelatin with GPTMS is a reaction marked by significant variability in the methods that have been reported in the existing literature (Appendix Table B.1). Researchers use a variety of approaches, introducing variables at different stages of the reaction (Figure 23). The choice of gelatin source (bovine vs porcine), the Bloom (100–300), and reaction concentration (5–10 wt%) vary widely (114,117,184,185,190,191,193,203). Typically, gelatin is dissolved in a mildly acidic (pH 5) aqueous solution using HCl ($HCl_{(aq)}$) as a solvent (117,184,190,191). However, the reaction is not always done under mildly acidic conditions as other solvents previously used include PBS, D_2O and dH_2O (114,185,193,203). The reaction stoichiometry also varies significantly, with the molar ratio of GPTMS to gelatin (C-factor; CF) ranging from 250–2000 (117,184,190). Reaction times vary from 3 hours to 48 hours, with ~14 hours being the most common (114,117,184,190,193,203). Whilst the reaction temperature is most commonly 40 ^{o}C, the functionalisation reaction has also been performed at 50 ^{o}C and 70 ^{o}C (114,185,190,191,193,203).

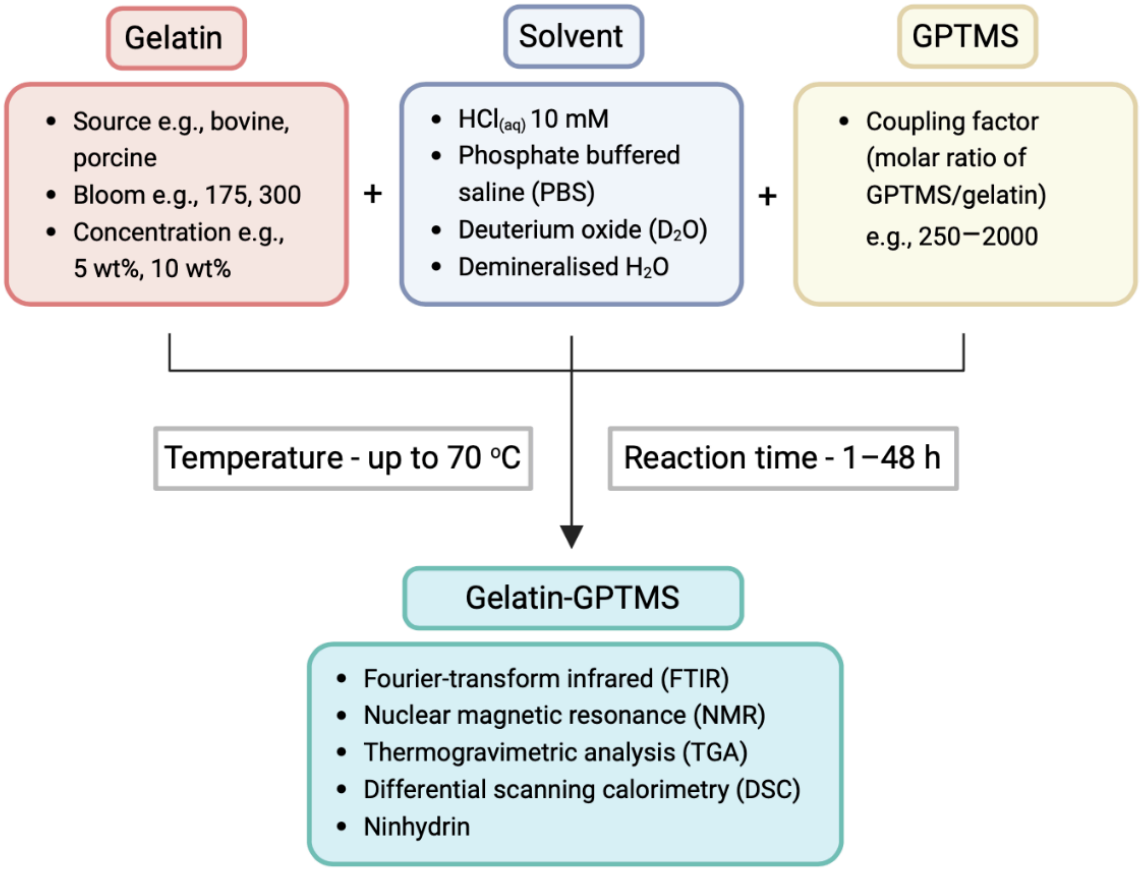


Figure 23. Gel-GPTMS functionalisation reaction, showing the sources of variation and uncertainties within the reaction reagents, conditions, and characterisation pipeline. Created on the BioRender website (https://biorender.com) by the author.

The gelatin functionalisation reaction is commonly run at pH 5 as the mildly acidic conditions making the carboxylic acid (-COOH) group on the biopolymer its more nucleophilic carboxylate (COO^-) (114). The degree of ionisation of an acid at a particular pH value can be determined by its pK_a according to the Henderson-Hasselbalch equation. The pK_a of a carboxylic acid is ~5 and the two predominant carboxylic acid containing side chain residues of gelatin, glutamic acid and aspartic acid, have a pK_a of ~4.3 and ~3.7, respectively (204). When pK_a ~ pH, the acid is approximately 50% ionised, thus at ~pH 5, we can assume approximately 50% of the carboxylic acid residues in glutamic acid of gelatin should exist in their more nucleophilic carboxylate form (205). There are two mechanisms by which the

epoxide can react with gelatin: the carboxylate, facilitating the nucleophilic epoxide ring-opening on GPTMS to form an ester, and via a protonated carboxylic acid, which can activate the epoxide towards ring-opening by H-bond activation (Figure 24). Additionally, there are a number of competing processes; hydrolysis of the epoxide on GPTMS into the corresponding 1-2 diol, as well as hydrolysis of the methoxy groups into Si–OH, and further condensation of Si–OH. All of these potential reactions have different rates and can potentially be impacted by changes in pH.

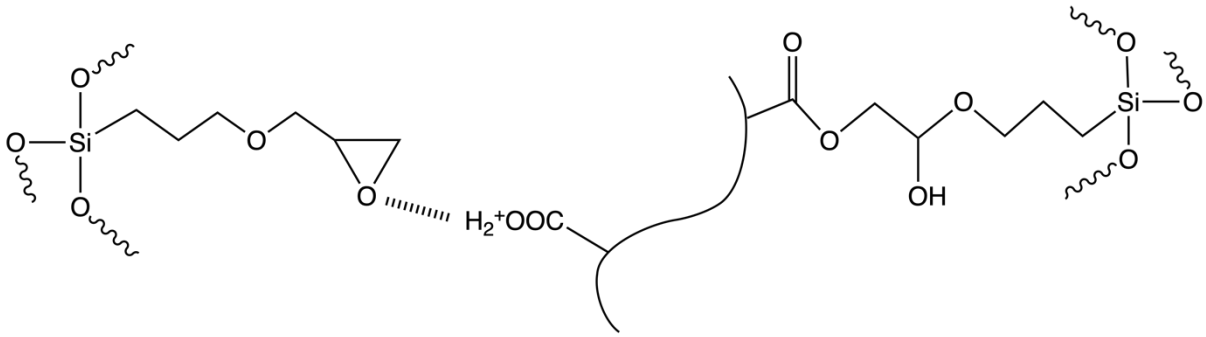


Figure 24. Two mechanisms by which the epoxide of GPTMS can react with gelatin; via hydrogen bonding of a protonated carboxylic acid which activates the epoxide (left) or via a carboxylate to form an ester (right).

Although there is more nucleophilic carboxylate form of carboxylic acid at pH 6, the reaction between the epoxide and carboxylate group is slow relative to pH 5, and instead, hydrolysis of the methoxy groups of GPTMS competes (198). Therefore, pH 6 is not used. Connell et al. (114) found that performing the reaction at pH 6 caused gelation, while reactions performed above pH 7 promoted the formation and gelation of a silicate network. An observed increase in pH also led to unwanted gelation at ~pH 7. Preliminary functionalisation of gelatin with GPTMS experiments were run, using the method from Mahony et al. (184), but adapting it to use an 8 hour reaction time due to laboratory access constraints. The pH was monitored throughout the reaction and results showed a deviation from pH 5 over the course of the

reaction, with a continual increase to ~pH 7.5 over the 8 hours reaction time. Additionally, premature gelation of the reacting solution was often observed. This increase in pH level over the course of the reaction is potentially important as pH plays a key role in controlling the reaction kinetics of the gelatin and GPTMS functionalisation reaction.

A range of characterisation techniques have been employed to validate the gelatin-GPTMS functionalisation process (Appendix Table B.2), including FTIR and NMR spectroscopy, thermogravimetric analysis (TGA), differential scanning calorimetry (DSC) and a ninhydrin assay (114,117,184,185,191,203,206). Researchers use FTIR and NMR to reveal information about the chemical structure of the product from functionalisation, using the techniques to identify functional groups and the formation of new bonds from the reaction (114,117,184,185,191,203). A ninhydrin assay is used to quantify the number of primary (1°) and secondary (2°) amines in a solution (117,203). Whereas TGA and DSC have been used compare the thermal degradation profile and glass transition temperature of unmodified versus functionalised gels, respectively (117,191). NMR is the only technique that will provide information about the selectivity of functionalisation. Techniques such as TGA and DSC are used to indicate the successful crosslinking of gelatin and GPTMS, but do not provide information about the selectivity of functionalisation. FTIR spectroscopy has been used to observe the formation of new functional groups in the reaction between gelatin and GPTMS (185,191,203). This technique, however, lacks the sensitivity to detect low levels of coupling. Again, this reflects the lack of standardisation in characterisation of gelatin and GPTMS functionalisation selectivity.

3.1.3. Issues with GPTMS functionalisation reactions

Even though GPTMS is extensively used, the functionalisation of biopolymers using GPTMS is potentially problematic as both the epoxide and alkoxysilane functionalities are susceptible to side-reactions. Epoxides are susceptible towards hydrolytic ring-opening, to provide a 1,2-diol by-product. This side-reaction not only reduces the amount of epoxide available for reaction with the biopolymer, but the diol side-product can also prevent the desired crosslinking reaction between gelatin and GPTMS (Figure 25a). Reduced epoxide availability as a consequence of hydrolysis is one reason why GPTMS is typically used in super-stoichiometric amounts in biopolymer functionalisation reactions. That said, at pH 5, Gabrielli et al. (192) found hydrolytic ring-opening of the epoxide in GPTMS was found to be slow, at just 13% conversion after 3 days.

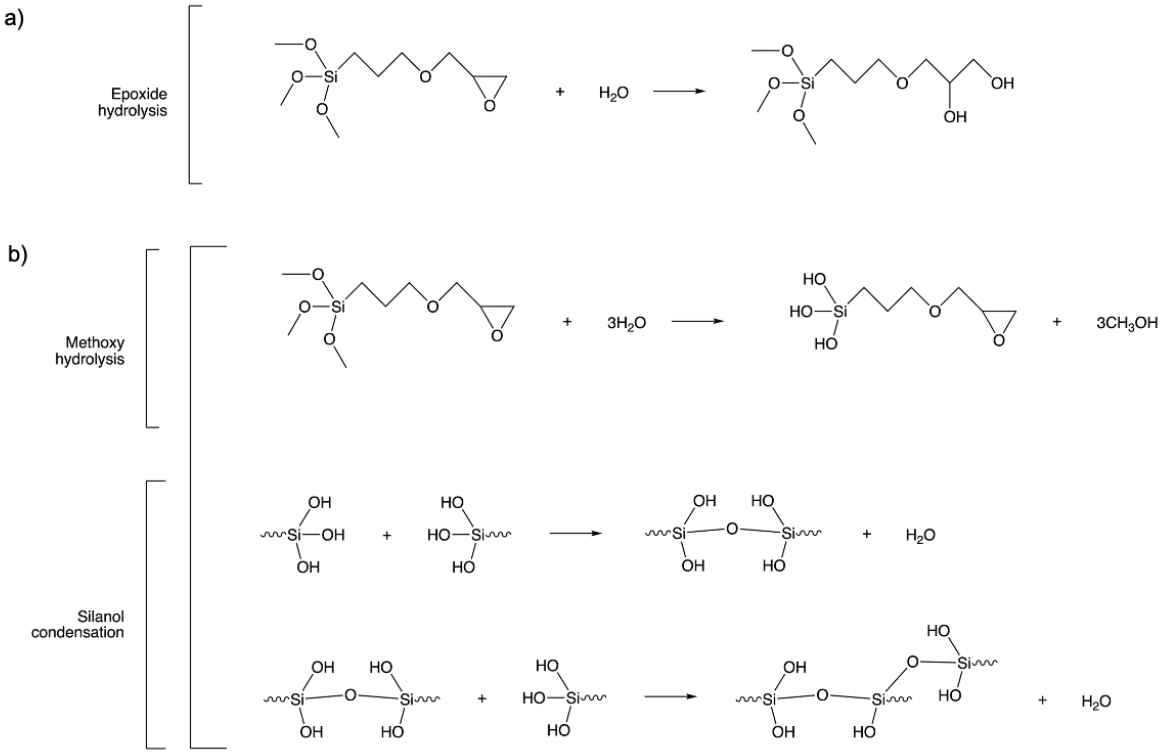


Figure 25. Competing reactions occurring during reaction of gelatin and GPTMS in aqueous solution; a) hydrolytic ring opening of the epoxide in GPTMS to form a 1,2-diol and b) hydrolysis of the methoxy groups to form MeOH, and condensation of Si–OH to form a silica network.

When the trimethoxysilyl groups on GPTMS undergo hydrolysis, MeOH is formed as a by-product (Figure 25b). MeOH release during the reaction could potentially damage or denature proteins and cells, resulting in cytotoxicity (207). As trimethoxylsilyl groups will always be employed when using GPTMS as a crosslinker, ideally the gelatin-GPTMS product should undergo processing to remove the MeOH generated during the functionalisation reaction. However, processing to remove MeOH generated from hybrid hydrogel synthesis upon further hydrolysis and condensation of trimethoxysilyl groups is beyond the scope of this study.

The functionalisation process is further complicated by the fact that hydrolysis of the alkoxysilane and condensation of the resulting Si–OH can result in the reaction solution becoming more viscous and eventually lead to a gel through the formation of an Si–O–Si silica network and GPTMS oligomers (Figure 25b) (192). Long functionalisation times have been reported to be detrimental to the hybrid formation, as prolonged exposure of the trimethoxylsilyl groups and epoxide ring to reaction conditions can lead to unwanted side reactions occurring (184). Gabrielli et al. (192) hypothesised that GPTMS oligomer formation is unfavourable for hybrid formation as it limits the level of biopolymer functionalisation, and thus crosslinking that can occur. Work by Nelson et al. (117), observed that by 22 hours of GPTMS and gelatin functionalisation, the solution had gelled. A compromise therefore has to be found between allowing long enough for biopolymer functionalisation whilst avoiding the detrimental effects of GPTMS oligomer formation and potential gelling. Ideally, both issues need to be avoided in order to extend the functionalisation time to increase the crosslinking that can occur between GPTMS and the biopolymer.

In the gelatin-GPTMS functionalisation reactions, CF is used to describe the molar ratio of GPTMS:gelatin. GPTMS is often used in up to 500–750x (CF500–750) excess of gelatin, and in some cases, up to 2000x (CF2000) (117,184,190). This means there is a relatively higher concentration of GPTMS compared to gelatin in the reaction. Furthermore, the excess GPTMS that remains within the functionalised solution, either as oligomers or diols (from hydrolytic ring-opening of the epoxide), is a problem and attempts to remove the excess are yet to be considered in literature investigating the gelatin-GPTMS functionalisation reaction. A separation step to remove the unreacted GPTMS is usually not performed, thus, it – or hydrolysed diol products – is still present in the product, increasing the amount of

trimethoxysilyl groups which form MeOH upon hydrolysis, which as previously discussed can result in cytotoxicity, thus, limiting the application of the hybrid material for cell encapsulation (208,209). Previous work by Mahony et al. (190) and Nelson et al. (117) using GPTMS-functionalised biopolymers within sol gel inorganic polymerisation formed a monolith hydrogel, where the sol is first transferred into moulds and further condensation of the silica network is allowed to occur. The hydrogels are then aged and dried to form hybrid monoliths. This processing will trap excess GPTMS-species within the formed structure. However, if the hybrid was not dried and instead used in its hydrogel state, as aiming to in this study, it can be suggested that excess GPTMS would be more easily released when submerged in solution.

The discussed issues with the gelatin-GPTMS functionalisation reaction leave scope for improvement in the functionalisation protocol in four main areas:

- Reaction pH – maintaining pH 5 throughout functionalisation
- Gelatin functionalisation time – extending the length of the reaction whilst avoiding gelling
- Post-processing – removal of unreacted GPTMS and other small-molecule by-products
- Cell encapsulation – removal of MeOH as a by-product

3.1.4. Aims and objectives

The aim of this chapter was to better understand how gelatin and GPTMS react with the aim of improving the functionalisation reaction process.

The main objectives were to:

i. Investigate the impact of reaction pH for biopolymer functionalisation
    a. Study pH change over the functionalisation reaction between gelatin and two different epoxide electrophiles, namely GPTMS and allyl glycidyl ether (AGE)[1] as a simplified model for GPTMS
    b. Analyse the functionalisation reaction between gelatin and GPTMS or AGE using ^{1}H NMR spectroscopy
ii. Carry out post-processing to purify the gelatin-GPTMS functionalisation reaction product
    a. Use dialysis to remove excess epoxide crosslinker and functionalisation reaction by-products
iii. Improve the efficiency and extent of the functionalisation reaction between gelatin and GPTMS by extending the reaction duration
    a. Vary the functionalisation solvent to increase functionalisation reaction duration and investigate the impact on extent of gelatin-GPTMS coupling
    b. Investigate and use ^{1}H NMR spectroscopy, ninhydrin assay and titration as verification techniques to determine position of conjugation of GPTMS on gelatin

[1] AGE was selected as it shares the epoxide structure of interest but has a relatively inert alkene instead of the trimethoxysilyl groups. Therefore, use of AGE removes a layer of complexity from the reaction as it will avoid hydrolysis and condensation of these groups, allowing for a more focused investigation.

3.2. Methods

Initially, GPTMS was used in this study to determine epoxide reactivity with gelatin (Figure 26). AGE was also investigated. This compound retains the terminal epoxide functionality present in GPTMS but replaces the trimethoxysilyl group with an unreactive double bond and so would allow study of epoxide reactivity without concern for hydrolysis of the trimethoxysilyl group (Figure 26).

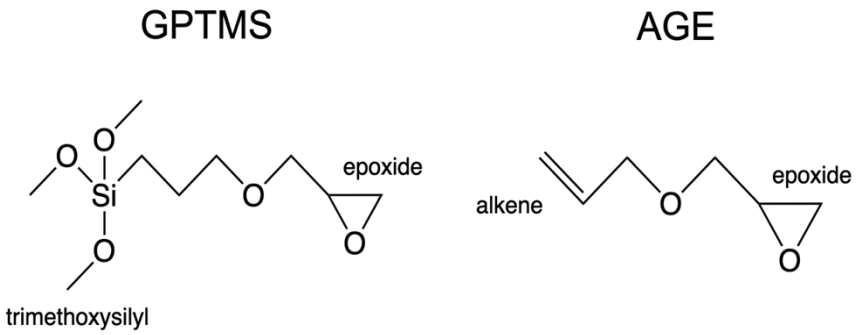


Figure 26. Structure of GPTMS and AGE.

The gelatin functionalisation reactions were carried out using a CF of 500, where CF describes the molar ratio of GPTMS:gelatin (190,206). Therefore, the functionalisation reaction was run at 500:1 (epoxide (AGE or GPTMS):gelatin) using 40 kDa as the average molecular weight of gelatin.

3.2.1. Materials

Gelatin (type A from pig [~175 g Bloom]), allyl glycidyl ether (AGE, ≥99%), 3-glycidyloxypropyl)trimethoxysilane (GPTMS; ≥98%), formamide (≥99.5%), ninhydrin reagent (2% solution), and dialysis tubing cellulose membrane (typical molecular weight cut-off = 14,000 Da) were purchased from Sigma-Aldrich and used as purchased. Deuterium

oxide (D_2O) was purchased from Goss Scientific and dimethyl sulfoxide (DMSO, ≥99%) from Fisher Scientific.

3.2.2. Attempted preparation of GPTMS functionalised gelatin (Gel-GP)

For the functionalisation of gelatin with GPTMS (Figure 27), gelatin (0.50 g, 1.25 x 10^{-2} mmol) was added to $HCl_{(aq)}$ (10 mL of 10.0 mM solution) contained in a 50 ml round-bottom flask. The flask was covered, and the mixture stirred at 250 rpm for 1 hour at 40 °C to achieve a gelatin solution with a concentration of 50 mg ml^{-1}. After 1 hour, GPTMS (1.40 mL, 6.25 mmol) was added to give a reaction CF of 500. After 5 min of mixing, the pH was measured using a pH meter and probe, and adjusted if necessary to pH 5, using either 0.2 M $HCl_{(aq)}$ or 0.2 M $NaOH_{(aq)}$. The solution was stirred for 8 hours at 40 °C and the pH of the solution measured hourly. Aliquots (500 µl) were taken at the following time intervals: 1, 2, 3, 4, and 8 hours. Each aliquot was added to D_2O (500 µl) and the resulting solution was analysed by ^1H NMR spectroscopy.

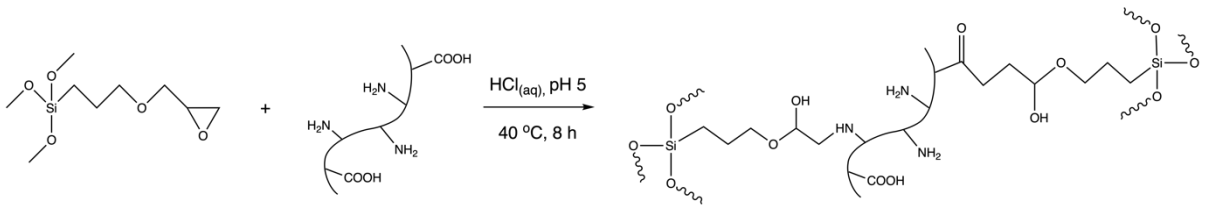


Figure 27. Reaction of GPTMS with both amine and carboxylic acid groups on gelatin backbone.

3.2.2.1. Effect of pH on functionalisation of gelatin with GPTMS

Three different experiments, numbered 1–3 below, were used to investigate how changes in pH of the functionalisation reaction affected the functionalisation reaction. Experiments 2 and 3 were used in an attempt to address the increase in pH of the reaction mixture over the time course of the reaction observed in Experiment 1.

Experiment 1: reaction solvent = 10 mM $HCl_{(aq)}$ with no intervention measures taken to control the reaction pH. The reaction was run for 8 or 72 hours as described in Section 3.2.2 following a literature procedure (190,206).

Experiment 2: reaction solvent = 10 mM $HCl_{(aq)}$ with intervention measures made at specific times to manually change the pH. Specifically, the pH of the reaction mixture was readjusted to pH 4.9 ± 0.02 using 2 M $HCl_{(aq)}$ every hour for the first 8 hours, and then at 24, 48 and 72 hours. In between these readjustment time points, the reaction was left to run with no intervention measure. The reaction was performed as described in Section 3.2.2.

Experiment 3: reaction solvent = potassium dihydrogen phosphate buffer (PB). The reaction was performed for 8 or 72 hours, as described in Section 3.2.2, only PB was used in place of 10 mM $HCl_{(aq)}$ as the solvent. The buffer was prepared by dissolving PB (6.8 g, 50.0 mmol) in dH_2O (750 mL). Once dissolved, the solution was made up to 1 L using dH_2O. Reactions were performed for 8 or 72 hours.

3.2.3. Attempted preparation of AGE functionalised gelatin (Gel-AGE)

For the functionalisation of gelatin with AGE (to prepare Gel-AGE) (Figure 28), the same protocol was followed as detailed in Section 3.2.3, only AGE (0.74 mL, 6.23 mmol) was added in place of GPTMS to give a CF of 500. After 5 min of mixing, the pH was measured using a pH meter and probe, and adjusted if necessary to pH 5, using either 0.2 M $HCl_{(aq)}$ or 0.2 M $NaOH_{(aq)}$. The solution was stirred for 72 hours at 40 ^{o}C, taking aliquots (500 µl) for analysis by ^{1}H NMR spectroscopy at 1, 2, 3, 4, 8, 24, 48 and 72 hours as described in Section 3.2.3. The pH of the reaction mixture was measured at the same time intervals, and every

hour during the first 8 hours. Post-reaction processing as described in Section 3.2.4 was also performed, however, no dilution with dH_2O was performed.

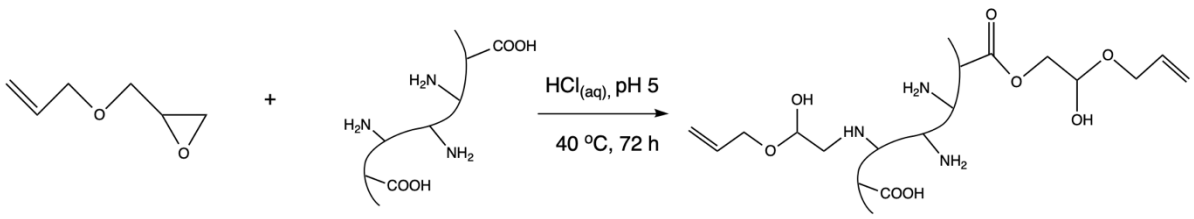


Figure 28. Reaction of AGE with both amine and carboxylic acid groups on gelatin backbone.

3.2.3.1. Effect of pH on functionalisation of gelatin with AGE

The same experiments as detailed in Section 3.2.2.1 were performed using AGE in place of GPTMS to investigate the effect of solution pH on functionalisation of gelatin with AGE.

3.2.4. Post-reaction processing – removal of unwanted small molecules

At the end of the reaction, the resulting solutions from the gelatin functionalisation reactions were dialysed at 40 °C for up to 120 hours against dH_2O (800 mL) through a dialysis tubing cellulose membrane, gently stirring throughout. DH_2O was refreshed daily. In the case of the reactions involving GPTMS, the solutions were diluted by a 2x factor with dH_2O to prevent gelling of the solution within the tube. Every 24 hours, aliquots (500 µl) were taken from the tubing and added to 500 µl D_2O. The resulting solutions were analysed by ^1H NMR spectroscopy.

3.2.4.1. Freeze drying

Dialysed GPTMS-functionalised gelatin solutions were freeze-dried for 48 hours using a Christ 1-2LDplus freeze dryer.

3.2.5. Hydrogel formulation: formation of Class I and Class II hybrids

Three hybrid hydrogel formulations were made, a Class I gelatin-silica (Gel-Silica) hybrid and two Class II GPTMS functionalised gelatin-silica (Gel-GP-Silica) hybrids, one made with dialysed Gel-GP and one with undialysed Gel-GP. From the pH study results (Section 3.3.1), the functionalisation product synthesised from the $HCl_{(aq)}$ gelatin-GTPMS reaction was selected for use. Hydrogels were made so that the final O:I was 20:80.

Preparation of organic component: 5.0 wt% gelatin solution was made by dissolving gelatin (0.50 g, 0.13 mmol) in DMEM (10.0 mL). The gelatin solution was mixed at 250 rpm for 1 hour at 40 ^{o}C prior to use in hydrogel formation.

Preparation of a Class I Gel-Silica hybrid

Gelatin solution (5.0 mL) was added to DMEM (20 mL) and the resulting mixture vortexed for 10 seconds, followed by the addition of propylene glycol modified silane (PGMS) (5.33 g, 16.7 mmol).

Preparation of Class II Gel-GP-Silica hybrids

The same protocol was followed for the preparation of Gel-GP-Silica hydrogels, only gelatin solution was substituted for either dialysed or undialysed Gel-GP solution (5.0 wt%). The hybrid hydrogel solutions (15 mL) were cast into a culture dish (60 mm) and left to gel overnight, covered and at room temperature.

3.2.6. Hydrogel degradation properties

3.2.6.1. Degradation assay

A degradation assay was used to determine the change in mass and silica release over time. The method was as described in Section 2.2.5, however, the degradation profile was observed over 7 days, using the following time points: 1, 3 and 24 hours, and 2, 5 and 7 days. At these time points, the hydrogels were weighed, and a 1 mL PBS sample was taken from the PBS container. After, 1 mL of fresh PBS was used to replenish the removed PBS. Inductively Coupled Plasma Optical Emission spectroscopy (ICP-OES) was performed on the samples to determine silicon concentration.

3.2.6.2. ICP-OES

ICP-OES analyses a sample for its elemental content. In this case, the element of interest was silicon. A serial dilution (20x, 200x) was performed on the samples taken during the degradation assay. First, 500 µl of sample was diluted with 9.5 mL of dH_2O to perform a 20x dilution. Then, 1 mL of 20x dilution was diluted with 9 mL of dH_2O to result in a 200x dilution. ICP-OES was run by Christopher Stark, Division of Environmental Health and Risk Management School of Geography, Earth and Environmental Sciences, University of Birmingham. The concentration obtained from the ICP-OES measurement was multiplied by 200 to account for dilution of the samples.

3.2.7. Alternative functionalisation reaction conditions

In efforts to extend the functionalisation time of gelatin with GPTMS, the reaction solvent, gelatin concentration and reaction pH were varied. Unless stated otherwise, all other reaction variables were kept the same as the functionalisation reaction in 10 mM $HCl_{(aq)}$ (Section 3.2.2).

For reactions performed in DMSO, gelatin was dissolved in DMSO 24 hours before the start of the functionalisation reaction to ensure complete dissolution. The reaction pH was not adjusted in this case in order to avoid introducing H_2O into the system and minimise hydrolysis. For aqueous reactions, the effect of pH was investigated by adjusting the pH to 3 from 5 before addition of GPTMS. Finally, in the 0.5 wt% condition, 0.25 g of gelatin was dissolved in 50 mL of 10 mM $HCl_{(aq)}$, to give a final concentration of 0.5 wt%.

3.2.8. Characterisation of Gel-GP

3.2.8.1. Ninhydrin assay

An aliquot (0.5 mL) from the functionalisation reaction was added to a centrifuge tube and diluted 10-fold by adding dH_2O (9.5 mL). An aliquot (0.5 mL) of this solution was added to a different centrifuge tube and further diluted by the addition of dH_2O (1.0 mL). The mixture was heated at 80 °C in a water bath. After 30 minutes, 2% ninhydrin reagent solution (0.5 mL) was added. The mixture was heated at 80 °C for a further 30 minutes, after which time, the mixture was removed from the water bath and cooled to room temperature over 30 minutes. Ethanol (95%, 2.5 mL) was added. An aliquot (100 µl) was pipetted into a 96 well-plate and the absorbance at 570 nm was read using a microplate reader (TECANSPARK). For each functionalisation condition, a gelatin control (solution of gelatin in $HCl_{(aq)}$/DMSO/formamide) was also measured. These solvent 'blanks' were subtracted from the experimental values.

The percentage of available primary/secondary amines, where A_{bc} is the optical absorbance measurement before functionalisation and acts as the control, was calculated (Eq. 1). Whereas A_{ac} is the optical absorbance measurement after functionalisation.

Available primary/secondary amines (%) = (A_{ac} / A_{bc}) x 100% (Equation 1)

3.2.8.2. Titration

A titration was performed for each gelatin functionalisation reaction, and gelatin in a solution of $HCl_{(aq)}$/DMSO/formamide (blank) as a control: 6 M $HCl_{(aq)}$ was added dropwise to the gelatin solution (25 mL), whilst gently stirring, to achieve a pH of 1.5 (measured using a pH probe [Fisherbrand accumet AE series single junction gel pH electrode]). Next, 0.1 M $NaOH_{(aq)}$ (titrant) was then added to produce increments in the pH of the solution of the order of 0.2–0.4 up to a maximum value of pH = 11.5. Upon every addition of titrant, the volume of titrant was noted, as well as the resulting pH.

3.2.8.3. FTIR spectroscopy

FTIR was performed using a NICOLET 6700 spectrometer with a resolution of 16.000, at wavenumber ranging of 4000–400 cm^{-1}. All spectra were plotted using OriginPro.

3.2.8.4. ^{1}H NMR spectroscopy

^{1}H NMR spectra were recorded in D_2O on a Bruker Biospin AVANCE spectrometer, at 400 Hz, and used to analyse the functionalisation reaction, determine the extent of functionalisation, and success of post-processing to remove excess GPTMS or AGE. All spectra were processed and analysed with MRestNova x64 NMR software (version 14).

3.2.9. Statistical analysis

GraphPad Prism v5 was used to test the statistical difference using mean ± standard deviation (SD), and n=3 where possible.

3.3. Results and Discussion

The initial aim of this study was to couple GPTMS with gelatin to prepare gelatin–silica hybrid hydrogels. First, the reactivity of the epoxide in GPTMS with the amino acid side-chain groups of gelatin was investigated. A pH control study was performed to investigate the effect of different reaction solutions and their influence on pH during the gelatin functionalisation reaction. Numerous challenges arose with the GPTMS-gelatin functionalisation reaction, which will be discussed. Consequently, AGE was used in place of GPTMS to simplify the reaction. The products from both GPTMS- and AGE-gelatin functionalisation reactions were purified using dialysis. The products from the GPTMS-functionalised reactions were used to create Class I and (assuming functionalisation) Class II hybrid hydrogels, which were investigated with respect to their degradation profile, to determine the effect of functionalisation on degradation properties.

3.3.1. GPTMS-gelatin functionalisation study

GPTMS was used as a coupling agent and the reactivity of the epoxide with gelatin was investigated. Hydrolysis of the trimethoxysilyl groups in the functionalised gelatin, to provide Si–OH, can then enable crosslinking with an inorganic component, silica, in a sol-gel reaction to provide a Class II hybrid hydrogel.

Other processes that occur in the functionalisation included competing hydrolysis of the epoxide in GPTMS, providing a 1,2-diol side-product (Figure 25a). The trimethoxysilyl groups present mean that the GPTMS is able to oligomerise, forming further potential products – oligomerised GPTMS (Figure 25b).

3.3.1.1. Preliminary GPTMS-gelatin functionalisation study

The initial focus of these experiments was to investigate the functionalisation of gelatin with GPTMS, hypothesising that coupling would occur between the epoxide of GPTMS and the carboxylic acid of gelatin (114,190,191,198,210). Reactions of gelatin with GPTMS were studied at 40 ^{o}C over 8 hours, in 10 mM $HCl_{(aq)}$. The reaction was started at pH 4.9 (± 0.02) and was monitored hourly. The progress of the functionalisation reaction was investigated by ^{1}H NMR spectroscopic analysis of aliquots taken from the reaction mixture at time points, in combination with FTIR to study the end product of these reactions.

The preliminary results of the study, presented in more detail within the following section (Section 3.3.1.2) did not show any significant indication of gelatin functionalisation. The lack of a clear functionalisation reaction raised serious concerns about the underlying issues. Importantly, the results highlighted an issue with pH control during the functionalisation reaction. Notably, the pH increased from 4.9 to ~7.0 over the course of the reaction.

pH is a key factor in GPTMS-gelatin functionalisation reaction. Epoxides can undergo ring-opening with nucleophiles under both acidic and basic conditions and has been found to be dependent on the pH of the reaction (192). A previous study has investigated the reactivity of GPTMS with nucleophiles (198). It highlighted that carboxylic acid (-COOH) groups are able to perform nucleophilic ring-opening of the epoxide ring (198).

Carboxylic acid residues are often present along protein/polypeptide chains, such as in gelatin, as they are found in amino acids glutamic acid and aspartic acid, and thus, they present an opportunity for gelatin functionalisation for hybrid synthesis (211). Whilst the neutral carboxylic acid can function as a nucleophile, its conjugate base, the negatively

charged carboxylate ($RCOO^-$) is more nucleophilic. Thus, when functionalising gelatin with GPTMS, slightly acidic conditions will cause it to be in its more nucleophilic state as a carboxylate ($-COO^-$). This is because carboxylic acids have pK_a's near 5, and when pK_a ~ pH, the acid is approximately 50% ionised (192,205). The reaction of gelatin with GPTMS is commonly reported in literature and typically uses 10 mM $HCl_{(aq)}$ to achieve the mildly acidic conditions (114,117,184,190). However, the previous work fails to address the increase in pH within the solution that occurs throughout the duration of the reaction that is observed here, and the subsequent effect that this has on the functionalised product.

Gabrielli et al. (192) investigated the effect of reaction pH on epoxide ring opening and silica condensation during sol-gel hybrid synthesis and highlighted important considerations when using GPTMS to functionalise biopolymers. Epoxy-ring hydrolysis is kinetically more favourable under slightly acidic conditions, whereas, in contrast, the major reaction that occurs under basic circumstances is silicon condensation (192). Additionally, if the pH is too acidic, it can result in the hydrolysis of the epoxide ring to the corresponding diol being the prevalent reaction. This highlights the critical role that pH plays on the reactivity of GPTMS and the impact it can have on the functionalisation process. However, the study did not monitor, or at least report, whether pH changed over the course of the reaction, but the findings imply the implications this could have on the resulting functionalised product.

It became clear that the functionalisation process was not progressing as planned, necessitating a closer look at the factors behind these challenges. A pH study involving different ways to control the pH in the GPTMS-gelatin functionalisation reaction was investigated.

3.3.1.2. pH control in GPTMS-based functionalisation reactions

It was hypothesised that being able to control the pH within the GPTMS-gelatin functionalisation would impact the reactivity of GPTMS within the reaction. To investigate influence of pH on the functionalisation reaction, three different experiments were conducted: experiment 1 (10 mM $HCl_{(aq)}$ run as per literature, $HCl_{(aq)}$), experiment 2 (10 mM $HCl_{(aq)}$ with manual pH changes at specific time intervals, $HCl_{(aq)}$ pH), and experiment 3 (PB).

In the GPTMS-gelatin reactions, $HCl_{(aq)}$ (experiment 1) (+ pH 2.18) had the largest pH change at the end of the 8 hours, followed by PB (experiment 3) (+ pH 0.98), and then $HCl_{(aq)}$ pH (experiment 2) (+ pH 0.23) (Figure 29).

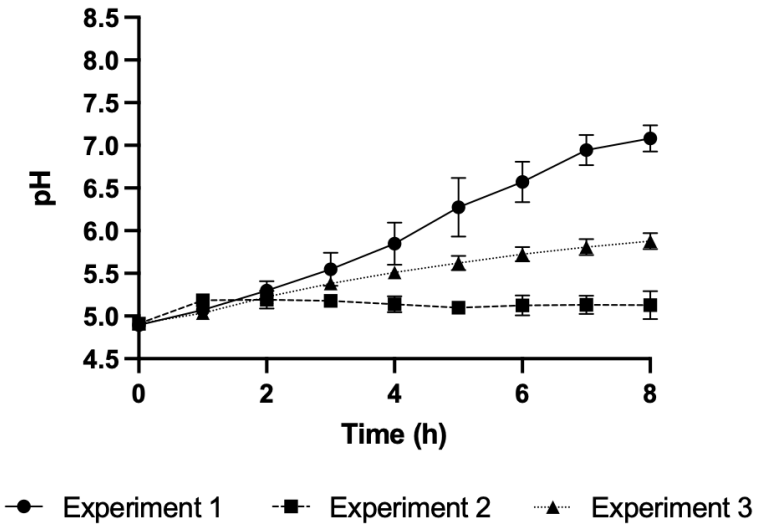


Figure 29. pH as a function of time for reaction of GPTMS and gelatin in, experiment 1: 10 mM $HCl_{(aq)}$ reaction solvent with no intervention measures taken to control the reaction pH; experiment 2: 10 mM $HCl_{(aq)}$ reaction solvent with intervention measures made to manually change the pH to pH 4.9 every 1 hour; and experiment 3: PB reaction solvent. Starting pH of all reactions was 4.9 ± 0.02 (n=3).

PB lost its buffering capacity, which can be suggested to be owed to the need to lower the pH of the potassium dihydrogen PB at the beginning of the reaction to pH 4.9 through addition of

2 M $HCl_{(aq)}$. PB systems present as more complicated than simple ones such as those involving acetic acid-sodium acetate, and because of this, it is more difficult to keep the ionic strength constant and often results in a large ionic strength variation (212). Manually readjusting the pH every 1 hour was more effective in controlling the pH compared to the use of PB.

PB was introduced in this study to investigate if this buffer would be able to control the pH of the reaction and maintain it at the desired pH 5. Buffers work by neutralising any H^+ or OH^- ions to maintain a particular pH. Any buffer will lose its effectiveness if too higher concentration of acid or base is added, and in this case, it also must not react with the reactants in the solution it is buffering. PB was chosen as a buffer in this system due to predicted lack of reactivity with the reagents, specifically the epoxide in GPTMS, unlike citrate or trisaminomethane (TRIS), two other common buffers. However, different buffers operate within an effective pH range, for example, PB can be adapted to a variety of pH levels from pH 5.5 to 7.4 (213). Although a lower pH range would have been desirable, due to the reaction commencing at pH 5, avoiding reactivity of the reagents with the buffer was prioritised over a perfectly effective pH range in this study.

It should also be noted that from a macroscopic point of view in the GPTMS reaction in experiment 1, that the solution went cloudy and began to gel. The cloudiness was observed between 5 and 6 hours and coincided with a change to a pH >7. This finding strongly supports a link between cloudiness and the creation of a silica-based network. The cloudiness in the solution could be caused by hydrolysis and condensation processes between the Si–OH groups in GPTMS, resulting in the creation of a 3D silicate-based network.

As a result, the transition to a pH >7 observed during our experiment is consistent with the findings of Gabrielli et al. (192), who discovered that at more basic conditions, the creation and gelation of a silicate network is promoted within the reaction. This was evidenced by ^{13}C NMR resonances showing a new product was formed, as the new resonances did not correspond to the ones observed upon diol formation but still resonate closely with the resonances from GPTMS (192). Additionally, there were no changes in the epoxide region of the GPTMS spectrum when in basic conditions which strongly suggests the epoxide ring structure is retained and other moieties are involved in the formation of the silicate network. Nelson et al. (214) also found when using a 22-hour functionalisation time, the solution gelled. When this finding is coupled with the pH increase over time observed in this study, it can be suggested that the gelation experienced could be as a consequence of exceeding pH 7, however, Nelson did not explore this finding any further (214).

It is suggested that this pH increase can be attributed to several chemical reactions occurring within the system. Firstly, epoxide hydrolysis (Reaction 8) will release hydroxide ions (OH^-) into the solution as a result of ring-opening reactions. Diol formation as a consequence of the epoxide hydrolysis reaction will also contribute to pH increase as diols can accept protons (H^+) from the solution as they are weak bases. Finally, MeOH formation (Reaction 9) upon hydrolysis of trimethoxysilyl groups in GPTMS will contribute to a pH increase as MeOH has a pH of 7 to 8 (215).

$$GPTMS + H_2O \rightarrow diol + OH^- \quad \text{(Reaction 8)}$$

$$GPTMS + H_2O \rightarrow methanol + Si - OH \quad \text{(Reaction 9)}$$

With reference to maintaining pH 5 during the functionalisation reaction, this work supports the use of a PB over long time periods, but that manually altering the pH is also effective if it can be done at regular intervals.

3.3.2. Gelatin and GPTMS ^{1}H NMR spectra

It was expected that the epoxide of GPTMS would undergo a nucleophilic ring opening reaction with the carboxylic acid residues of gelatin (114,190,191,198,210). Rodin et al. (216) assigned the chemical shift of amino acids present in gelatin and these have been used to assign the ^{1}H NMR spectra of gelatin. Based on literature precedent, it was expected that the epoxide of GPTMS would undergo a regioselective nucleophilic ring-opening reaction, either with the side-chain carboxylic acid or amine amino-acid residues of gelatin to form an ester or secondary amine linkage, respectively (114,190,191,198,210). By combining assigned resonances (Table 3) and the ^{1}H NMR of gelatin (Figure 30), determining the precise site of reaction becomes possible.

Table 3. Identification of the amino acids in gelatin and their respective chemical shift in ^{1}H NMR spectrum in D_2O. Modified from (216).

No.	Chemical shift (ppm)	Amino acid
1	3.92	Glycine, Hydroxyproline
2	3.62	Proline
3	3.20	Arginine, Histidine
4	2.99	Lysine
5	2.30	Glutamic acid, Hydroxyproline
6	2.00	Proline, Methionine
7	1.40	Alanine
8	0.90	Valine, Leucine, Isoleucine

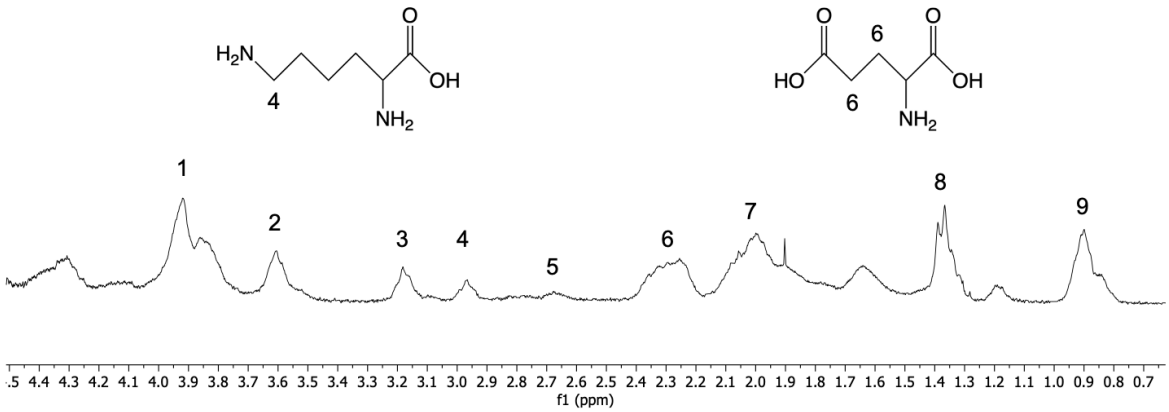


Figure 30. ^{1}H NMR spectrum of gelatin, with amino acid residues labelled. The resonances correspond to the follow amino acid (type of protons): 1: glycine (α-CH_2), hydroxyproline (γ-CH); 2: proline (δ-CH_2); 3: arginine (δ-CH_2), histidine (β-CH_2); 4: lysine (ε-CH_2); 5: aspartic acid (β-CH_2); 6: glutamic acid (β- and γ-CH_2), hydroxyproline (β-CH_2); 7: proline (β-, γ- and δ-CH_2), methionine (β-CH_2 and CH_3); 8: alanine (CH_3); 9: valine (γ- and δ-CH_2), leucine (γ- and δ-CH_2), isoleucine (γ- and δ-CH_2) [D_2O, 400 MHz]. The structure of lysine (left) and glutamic acid (right) is shown with corresponding protons labelled (216).

The resonance at δ_H = 2.99 ppm (resonance 4) corresponds to the protons on the epsilon (ε) carbon of lysine and δ_H = 2.30 ppm (resonance 6) to the beta and gamma protons (β- and γ-CH_2) of glutamic acid within gelatin (Figure 30) (216). If GPTMS reacts with the side-chain functionality in either of these two amino acid residues, it should affect (most significantly) the chemical shift of the resonances for these hydrogens in the ^{1}H NMR spectrum. The reaction between gelatin and GPTMS will also result in new resonances arising from the ring-opened GPTMS unit. Their position in the resulting ^{1}H NMR spectrum will depend on the nucleophile that opens the epoxide. Thus, mindful of resonance overlap potentially complicating analysis, the ^{1}H NMR spectrum of the reaction product might allow the site of conjugation to be identified. Additionally, aspartic acid has a carboxylate side-chain functionality of which GPTMS could react with, however, the resonance at δ_H = 2.70 ppm (resonance 5) corresponding to the beta protons (β-CH_2) in aspartic acid is only present at low intensity and so identifying resonance changes were difficult (216).

Additionally, specific protons in GPTMS have been assigned to a ^{1}H NMR spectrum (Figure 31). The resonances at δ_H = 2.50 and 2.35 ppm (a_3 and a_3*, respectively) correspond to the protons on the epoxide. Nucleophilic ring-opening at this site should result in a decrease in signal intensity of these resonances and the appearance of new resonances at lower fields, approximately δ_H = 3.75–4.00 ppm, whose position will depend on the nature of the nucleophile and would be indicative of a reaction (198). Further changes to native gelatin ^{1}H NMR resonances must be observed and analysed.

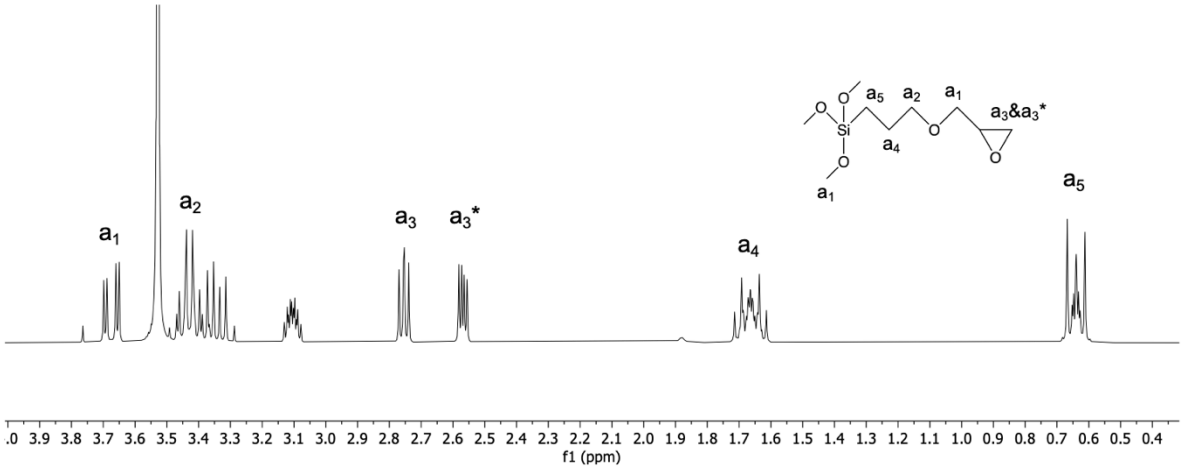


Figure 31. ^{1}H NMR spectrum of GPTMS, with key resonances labelled on the chemical structure ($CHCl_3$, 400 MHz).

There are two mechanisms by which the epoxide can react with gelatin: via a carboxylate, such as glutamic acid, facilitating the nucleophilic epoxide ring-opening on GPTMS to form an ester, and via an amine, such as lysine, facilitating the nucleophilic epoxide ring-opening on GPTMS to form a secondary amine (Figure 32) (130,217). The resonances of the different products formed will have characteristic chemical shifts, δ_H ~4.1 ppm for the methylene protons on the ester alkoxy chain and δ_H ~3.5 ppm for the secondary amine (112,114,199). Hydrolytic ring opening of the epoxide is a competing reaction and would also result in a decrease in intensity of the resonances associated with the terminal epoxide. Therefore,

epoxide consumption does not alone confirm successful functionalisation. Resonances for the other protons in GPTMS (δ_H = 3.65 ppm (a_1), δ_H = 3.45 ppm (a_2), δ_H = 1.70 ppm (a_4), and δ_H = 0.65 ppm (a_5)) as demonstrated in Figure 31 should not change significantly upon functionalisation so the appearance of resonances at these approximate chemical shifts will also indicate successful reaction (Figure 32).

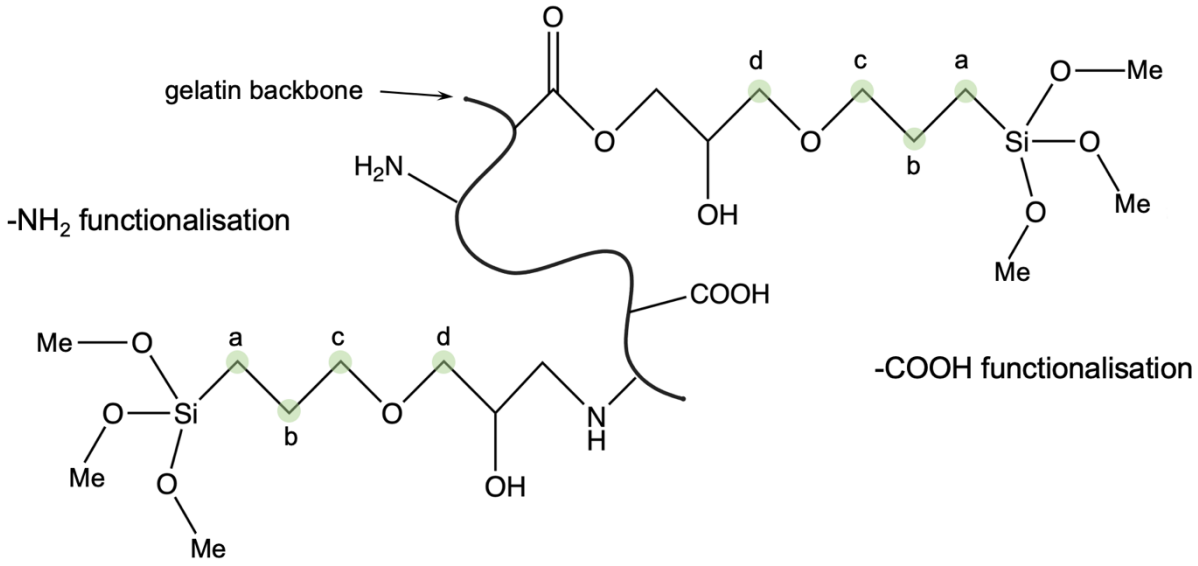


Figure 32. Schematic showing possible sites of functionalisation – amine (-NH_2) and carboxylic acid (-COOH), with salient groups with for analysis by ^{1}H-NMR spectroscopy highlighted in green with corresponding resonances labelled from Figure 31.

3.3.2.1. GPTMS epoxide ring opening as a function of time

The ^{1}H NMR spectra for Gel-GP from the $HCl_{(aq)}$ reaction (experiment 1) is shown in Figure 33, with time points only up to 3 hours due to gelation of the reaction mixture beyond this point. The $HCl_{(aq)}$ pH and PB reactions (experiment 2 and 3, respectively) were comparable, however, the reaction time could be extended to 8 hours as in these two cases and gelation was not observed (Appendix Figure B.1 and Figure B.2).

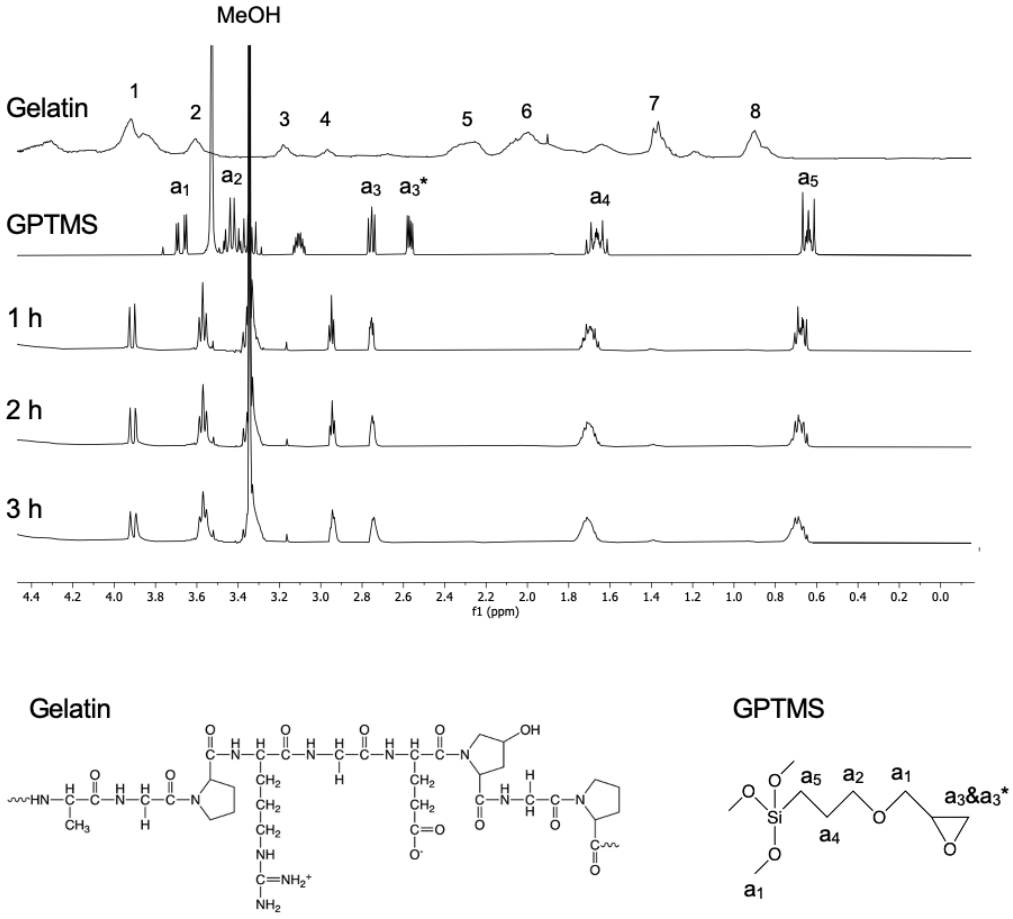


Figure 33. [1]H NMR spectra of starting reagents gelatin (D_2O, 400 MHz) and GPTMS ($CDCl_3$, 400 MHz), and the progressing reaction at 1, 2, and 3 hours in $HCl_{(aq)}$ (D_2O, 400 MHz). Note, the reaction had gelled at 4 and 8 hours and so it was not possible to take a sample. Chemical structures are shown. See Table 3.1 to assign gelatin amino acid structure.

^{1}H NMR spectroscopy showed a small reduction in the relative area of the epoxide resonances a_3 and a_3* at δ_H = 2.50 and 2.35 ppm (shifting to δ_H = 2.95 and 2.80 ppm). This was expected due to ring opening of the epoxide through reaction with gelatin or H_2O (hydrolysis).

GPTMS resonances, a_1 δ_H = 3.65 ppm (shifting to δ_H = 4.90 ppm), a_2 δ_H = 3.45 ppm (shifting to δ_H = 3.55 ppm), a_4 δ_H = 1.70 ppm, and a_5 δ_H = 0.65 ppm, remained at a consistent intensity

throughout which shows that the reaction conditions do not affect the core structure of the GPTMS molecule and that the only reactions taking place were at the trimethoxysilyl/alkoxy and epoxide functionality (Figure 33). The spectra were dominated by the GPTMS resonances, making it difficult to investigate any changes in the structure of gelatin due to functionalisation.

MestReNova was used to quantify the process of epoxide ring opening through measuring the relative area of the epoxide resonances in the ^{1}H NMR spectra (a_3 and a_3*) (Figure 33, Appendix Figure B.1 and Figure B.2). The degree of epoxide ring opening was calculated by dividing the relative area of the epoxide resonance at a specific time point by the relative area of the epoxide resonance in the starting reagent and multiplying by 100 to obtain the percentage of epoxide remaining. The formation of solid materials at 4 and 8 hours for $HCl_{(aq)}$ GPTMS, assumed to be as a consequence of alkoxysilane hydrolysis and condensation, prevented the accurate evaluation of epoxide ring opening (198).

For Gel-GP, epoxide opening was 14% in $HCl_{(aq)}$ pH (experiment 2) reaction and 12% in PB (experiment 3) by 8 hours (Figure 34).

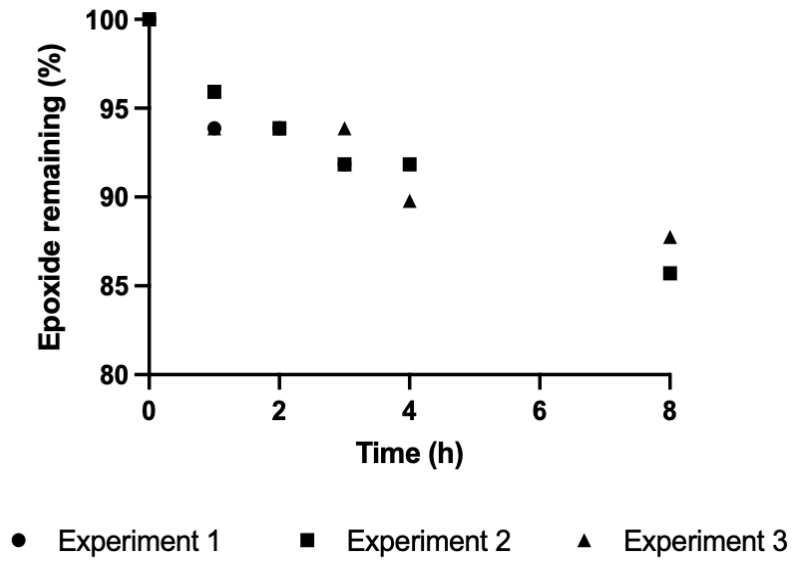


Figure 34. Epoxide remaining (%) calculated from relative area of resonances a_3 and a_3 at δ_H = 2.50 and 2.35 ppm (shifting to δ_H = 2.95 and 2.80 ppm) in Gel-GP, reacted in experiment 1, 2 and 3.*

As there is more than one potential product of epoxide ring opening in both reactions, when discussing 'epoxide ring opening' in the following section it includes both nucleophilic ring opening for functionalisation and hydrolytic ring opening when forming diols.

The highest rate of ring opening was where pH increase was lowest, in the $HCl_{(aq)}$ pH solution (experiment 2) and then PB (experiment 3) (Figure 34). When using ^1H NMR to quantify epoxide hydrolysis in solutions with different pH, Gabrielli et al. (192) found epoxide hydrolysis was very slow at neutral pH with only a 5% conversion after three days, compared to 13% conversion at pH 5.

This agrees with the conclusion that manually readjusting the pH is the best method to control pH in an 8-hour gelatin-GPTMS functionalisation reaction. As previously mentioned, total epoxide ring opening does not equal just nucleophilic ring opening for gelatin

functionalisation, and it is key that diol formation through hydrolytic ring opening is also considered in the future. Unfortunately, the considerable resonance overlap in the ^{1}H NMR spectra means it is difficult to directly quantify diol formation.

3.3.2.2. Summary of initial GPTMS-gelatin functionalisation study

As the experiments progressed, the primary aim of investigating the reactivity of the epoxide end of the GPTMS with gelatin amino acid residues faced numerous hurdles. Notably, the hydrolysis and condensation of trimethoxysilyl groups over the duration of functionalisation created an unforeseen issue, eventually leading to gelation, preventing any further functionalisation efforts and ruled out the material's further use. This also led to the issue of a restricted functionalisation window as a result of GPTMS-induced gelation, which needs consideration, as it significantly shortened the available time for epoxide ring opening reactions, resulting in reduced epoxide ring opening.

Furthermore, the analysis revealed a significant pH elevation during the experimental processes, necessitating alternative control measures, such as manually readjusting the pH or the use of a buffer. The presence of excess GPTMS in the solution, while key in the development of silicate networks within the next stage of hydrogel formation, inhibited the determination of effective functionalisation using ^{1}H NMR spectroscopy due to the prominent GPTMS resonances.

These complications highlighted the need for a simpler epoxide-based molecule, one that would allow an easier understanding of epoxide-gelatin interactions.

3.3.3. AGE-gelatin functionalisation study

As a consequence of the Gel-GP results and the difficulties surrounding hydrolysis and condensation of trimethoxysilyl groups, it was decided to use AGE to functionalise gelatin (Gel-AGE) to simplify the reaction by replacing trimethoxysilyl with an inert double bond. This was done in an attempt to remove a variable to simplify analysis of the reaction product, to focus on determining the chemoselectivity of the reaction. The only two reaction products using this epoxide should be Gel-AGE and the 1,2-diol resulting from hydrolytic ring-opening of the epoxide. Silicate network formation is therefore not possible, eliminating the potential issue of this when characterising materials.

3.3.3.1. pH control in AGE-based functionalisation reactions

Reactions of gelatin with AGE were studied at 40 °C over 72 hours. All reactions were started at pH 4.9 (± 0.02). The progress of the functionalisation reaction was investigated by ^{1}H NMR spectroscopic analysis of aliquots taken from the reaction mixture at specific time points.

To investigate influence of pH on the functionalisation reaction, three different experiments were conducted: experiment 1 (10 mM $HCl_{(aq)}$ run as per literature, $HCl_{(aq)}$)), experiment 2 (10 mM $HCl_{(aq)}$ with manual pH changes at specific time intervals, $HCl_{(aq)}$ pH), and experiment 3 (PB).

In the first 8 hours of the AGE-gelatin reactions (Figure 35), the $HCl_{(aq)}$ (experiment 1) had the largest pH change (+ pH 2.12), followed by PB (experiment 3) (+ pH 0.75), and finally $HCl_{(aq)}$ pH (experiment 2) (+ pH 0.25). After 72 hours, the largest pH change was still $HCl_{(aq)}$

(experiment 1) (+ pH 2.97), but then followed by $HCl_{(aq)}$ pH (experiment 2) (+ pH 2.55), and finally, PB (experiment 3) (+ pH 1.56).

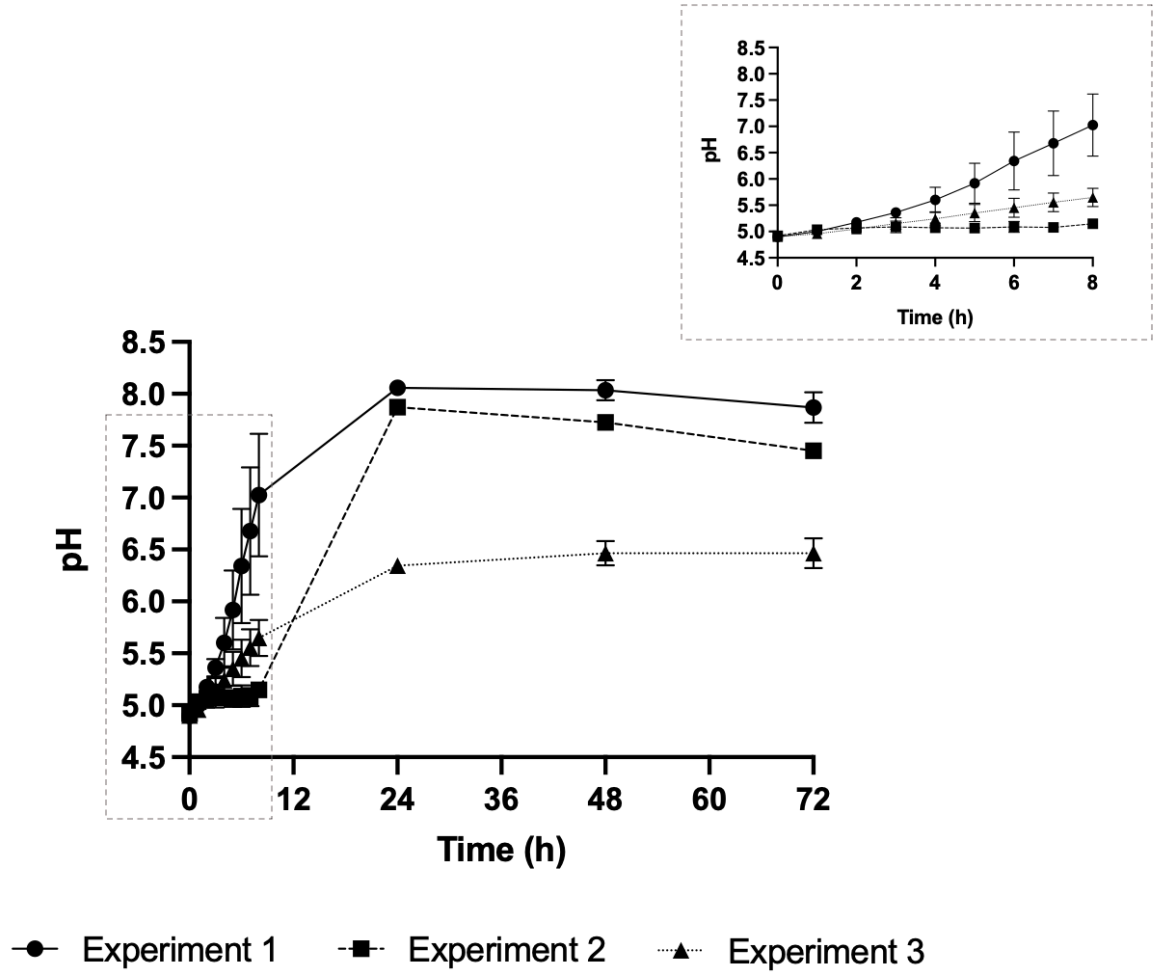


Figure 35. pH as a function of time for reaction of AGE and gelatin in, experiment 1: 10 mM $HCl_{(aq)}$ reaction solvent with no intervention measures taken to control the reaction pH; experiment 2: 10 mM $HCl_{(aq)}$ reaction solvent with intervention measures made to manually change the pH to pH 4.9 every 1 hour for 8 hours, and then at 24 hour intervals until 72 hours; and experiment 3: PB reaction solvent. Starting pH of all reactions was 4.9 ± 0.02 (n=3).

The pH increase was significantly lower in the PB reaction (experiment 3) compared to $HCl_{(aq)}$ and $HCl_{(aq)}$ pH (experiment 1 and 2, respectively). However, within the first 8 hours of AGE and GPTMS reactions, manually readjusting the pH every 1 hour was more effective in controlling the pH. PB was able to buffer but was limited in its ability. Similarly, to the

GPTMS functionalised gelatin reactions, PB lost its buffering capacity, which again can be suggested to be owed to the need to lower the pH of the potassium dihydrogen PB at the beginning of the reaction. Therefore, there is difficulty in keeping the ionic strength constant which often results in a large ionic strength variation (212).

It is proposed that this pH increase is due to epoxide hydrolysis (Reaction 7), which will release hydroxide ions (OH^-) into the solution as a result of ring-opening processes. Diol production as a result of the epoxide hydrolysis reaction will also contribute to pH increase since diols are weak bases and can receive protons (H^+) from the solution.

$$AGE + H_2O \rightarrow diol + OH^- \qquad \text{(Reaction 7)}$$

In terms of maintaining pH 5 during the functionalisation reaction, this work supports the use of a PB over long time periods, but that manually adjusting the pH is also successful if done at regular intervals.

3.3.3.2. AGE epoxide ring opening as a function of time

A representative spectrum of a Gel-AGE reaction is shown in Figure 36, other experiments were comparable (Appendix Figure B.3 and Figure B.4). ^{1}H NMR spectroscopy showed a decrease in the relative integration of the epoxide resonances a_3 and a_3* at δ_H = 2.50 and 2.35 ppm (shifting to δ_H = 2.95 and 2.80 ppm). This suggests that epoxide ring opening was occurring, however, epoxide ring opening is not solely synonymous with functionalisation as hydrolysis of the epoxide ring into the corresponding 1,2-diol is a competing reaction. Multiple resonances arose within 1 hour of reaction, at δ_H = 3.50–3.70 ppm (b), becoming particularly obvious by 24 hours. These resonances correspond to the formation of diols,

supporting that at least some of the epoxide ring opening is responsible for diol formation. Resonances at $\delta_H = 5.95$ (a_1) and $\delta_H = 5.30$ (a_2) correspond to the protons on the alkene of AGE and remain consistent throughout the experiment, suggesting that the reaction conditions do not affect the alkene on AGE. The spectra of the reaction mixture were dominated by the AGE resonances (as it was used in such large excess), making it difficult to investigate any changes in the structure of gelatin due to functionalisation.

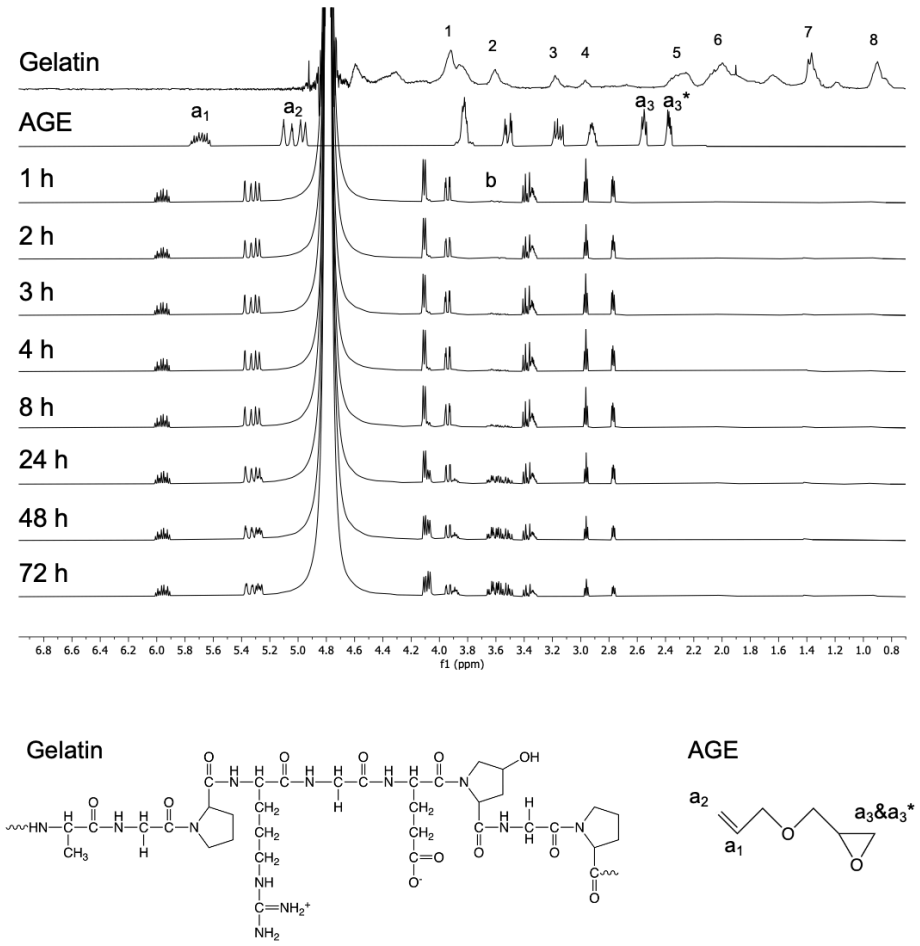


Figure 36. ^1H NMR spectra of starting reagents gelatin (D_2O, 400 MHz) and AGE ($CHCl_3$, 400 MHz), and the progressing reaction at 1, 2, 3, 4, 8, 24, 48 and 72 hours in $HCl_{(aq)}$ (D_2O, 400 MHz). Chemical structures are shown. See table 3.1 to assign gelatin amino acid structure.

MestReNova was used again to quantify the process of epoxide ring opening through measuring the relative area of the epoxide resonances (a_3 and a_3*) in Figure 36, Appendix

Figure B.3 and Appendix Figure B.4. For Gel-AGE, the degree of epoxide ring opening over 72 hours increased for reactions functionalised in $HCl_{(aq)}$ pH and PB solution, with 71% and 69% of the epoxide rings opened by 72 hours, respectively, compared to 59% in $HCl_{(aq)}$ (Figure 37). The epoxide ring hydrolysis was significantly higher in AGE reactions, with an average of 67% epoxide ring opening in AGE functionalised reactions, compared to 13% in GPTMS (Figure 34). It is suggested that this is due to length of time allowed for reaction, with 72 hours (AGE) compared to 8 hours (GPTMS).

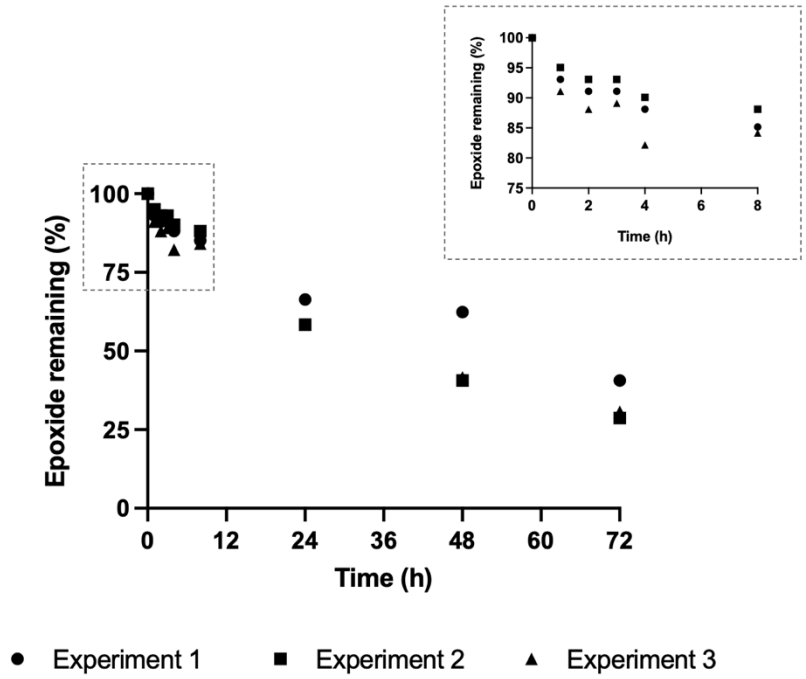


Figure 37. Epoxide remaining (%) calculated from relative area of resonances a_3 and a_3 at δ_H = 2.50 and 2.35 ppm (shifting to δ_H = 2.95 and 2.80 ppm) in Gel-AGE, reacted in experiment 1, 2 and 3.*

Results from Gel-AGE show there is a negative relationship between pH and epoxide ring opening; a lower pH of reacting solutions is associated with higher epoxide ring opening (192). More specifically, the epoxide ring opening was higher in $HCl_{(aq)}$ pH and PB solutions (experiment 2 and 3, respectively) compared to $HCl_{(aq)}$ (experiment 1). This demonstrated the

negative relationship between pH and epoxide ring opening as $HCl_{(aq)}$ (experiment 1) had a significantly higher pH than both the $HCl_{(aq)}$ pH and PB solutions (experiment 2 and 3, respectively) throughout the reaction. As mentioned earlier, Gabrielli et al. (192) found epoxide hydrolysis conversion after three days at neutral pH to be slower (5%) compared to pH 5 (13%).

This supports the conclusion that manually regulating the pH is the best way to manage pH in gelatin-based functionalisation reactions during the first 8 hours, after which PB functions as the best pH controller.

3.3.4. Dialysis: a post reaction processing method

3.3.4.1. Dialysis of GPTMS-based functionalisation products

Effort was made to remove excess, unreacted epoxide (GPTMS) and the hydrolysed diol by-product from the reaction mixture. If GPTMS is in excess and unreacted, once submerged in solution, it would be at risk of burst release (an uncontrolled, high rate of release) and higher concentrations of GPTMS are associated with induced cytotoxicity (191). It was hypothesised that dialysis would allow the removal of low-molecular-weight impurities, including unreacted epoxide species and hydrolysis products, thus, preventing the issue of cytotoxicity. Dialysis enables the separation and exchange of substances by employing a semipermeable cellulose membrane that lets small molecules, such as ions and nutrients, pass through, whilst preventing the passage of larger molecules, such as proteins (218).

An example of a successful dialysis and representative spectra are presented for gelatin reacted with GPTMS in $HCl_{(aq)}$ pH (experiment 2) (Figure 38). Resonances present at δ_H = 2.95 (a_3) and δ_H = 2.80 ppm (a_3*), corresponding to the protons in the epoxide ring, were

absent in the ^{1}H NMR spectrum of Gel-GP product from $HCl_{(aq)}$ pH (experiment 2) after 96 hours dialysis. This result demonstrates that unreacted epoxide had been removed. Additionally, the resonance at δ_H = 3.35 ppm corresponding to MeOH, a by-product of GPTMS trimethoxysilyl hydrolysis and condensation, was also absent by 72 hours, indicating the removal of this small-molecule alcohol. The spectra from the dialysis of Gel-GP synthesised in the PB reaction (experiment 3) was comparable (Appendix Figure B.5).

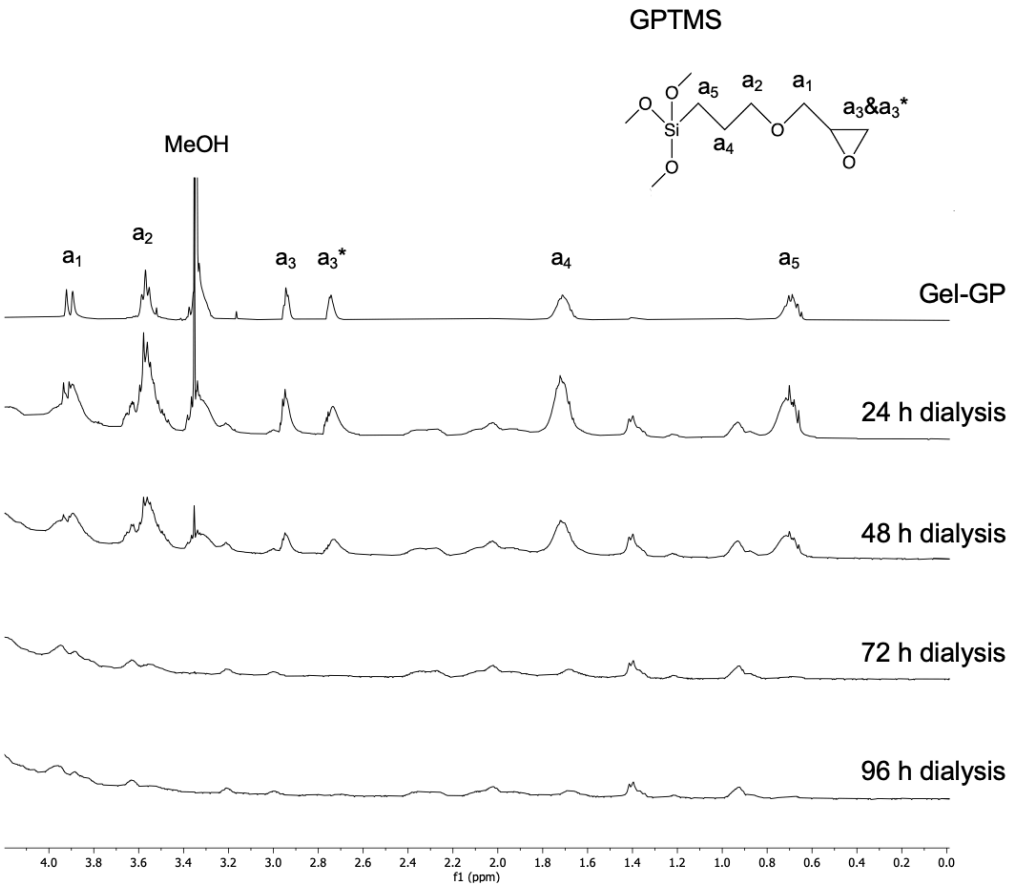


Figure 38. ^{1}H NMR spectra of (a) the Gel-GP product from $HCl_{(aq)}$ pH reaction conditions and further dialysis for 96 hours, with key resonances for GPTMS noted (D_2O, 400 MHz). The spectra show the removal of resonances a_3 and a_3, as well as the MeOH resonance. Other resonances present from GPTMS are difficult to examine due to the complexity of the spectra and resonance overlap.*

The Gel-GP solution from the $HCl_{(aq)}$ reaction (experiment 1) continued to gel and solidify during dialysis. This meant that after 72 hours of dialysis, excess unreacted GPTMS and by-

products remained (Figure 39). This was observed as resonances remained at δ_H = 2.95 and 2.80 ppm, corresponding to the protons in the epoxide ring, as well as MeOH at δ_H = 3.35 ppm. It was not possible to take a 96 hour sample due to the sample solidifying.

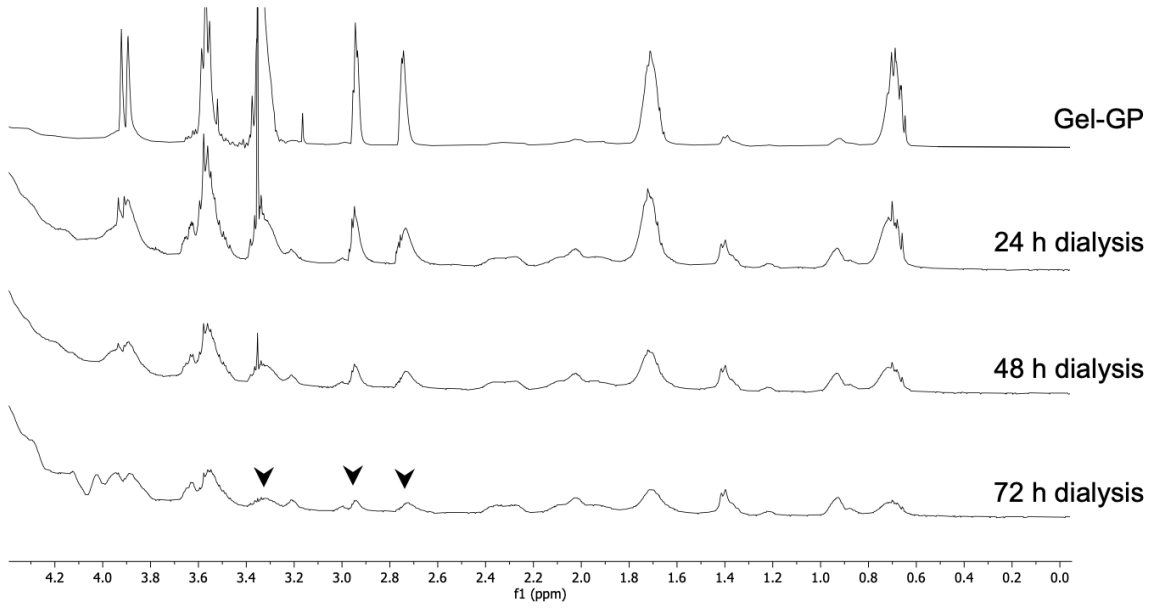


Figure 39. ^1H NMR spectra of (a) the Gel-GP product from $HCl_{(aq)}$ reaction conditions and further dialysis reaction for 72 hours, with residual GPTMS and MeOH labelled (arrow) (D_2O, 400 MHz).

Taken together, these results suggest it is not possible to remove all of the unreacted GPTMS and unwanted low molecular weight by-products using dialysis in the $HCl_{(aq)}$ reaction (experiment 1) because of silica network formation due to an increase in pH. If dialysis is to be effective, significant effort should be made to reduce the hydrolysis and condensation of alkoxysilyl groups during the gelatin functionalisation reaction. The following strategies could be considered as ways to achieve this: temperature; using a reaction temperate <40 ^oC as higher temperatures can promote the hydrolysis of trimethoxysilyl groups and condensation of the resulting Si–OH, H_2O content; minimising the H_2O within the reaction by selecting reagents and solvents that are anhydrous or contain controlled amounts of H_2O,

and reaction time; shorten the reaction time to limit exposure of trimethoxylsilyl groups to H_2O (219,220). However, a shorter reaction time may also affect the degree of functionalisation achieved; an ideal reaction involves fast gelatin functionalisation and a slower rate of hydrolysis.

Analysis of Gel-GP reacted in $HCl_{(aq)}$ (experiment 1) by FTIR spectroscopy further confirms the presence of a silica network as absorbance peaks at 1093 and 1035 cm^{-1}, and 907 cm^{-1}, corresponding to Si–O–Si and Si–OH, respectively, are present (Appendix Figure B.6). This is consistent with the observation of the reaction mixture becoming very viscous at 4 hours and eventually gelling at 8 hours for $HCl_{(aq)}$ (experiment 1).

The results from the ^1H NMR of dialysis products support the use of dialysis as a post-processing step in pH controlled GPTMS-functionalisation reactions.

3.3.4.2. GPTMS-gelatin functionalisation

With successful use of dialysis to remove unreacted GPTMS and small-molecule reaction by-products, ^1H NMR spectroscopy was used to investigate the effect of pH-controlled reactions on the functionalised products. Changes to the structure of native gelatin were investigated to assess if successful functionalisation was occurring.

Schematic illustrations of the preparation of the Gel-GP hydrogels are presented in Figure 40. The proposed mechanism of the reaction between GPTMS and gelatin involves ring opening of the epoxide of GPTMS by nucleophilic attack of amino acid side-chain carboxylic acid groups (-COOH) and formation of an ester. This functionalisation is proposed as previous evidence from Connell et al. (114) demonstrates changes to the glutamic acid resonance in

gelatin using ^{1}H NMR, suggesting that the epoxide ring reacts with the carboxylic acid group. Additionally, Gabrielli et al. (198) confirmed the reaction of the epoxide ring of GPTMS with a carboxylic acid in mildly acidic conditions to form an ester, demonstrating an intensity decrease of the epoxide and propanoic acid protons using ^{1}H NMR and using Heteronuclear Multiple Bond Correlation (HMBC) experiments, to confirm the ester formation. Mahony et al. (184) and Balavigneswaran et al. (191) state that functionalisation occurs with carboxyl groups, however, experimental evidence is not provided. If GPTMS is reacting with carboxyl groups, an ester linkage would be formed, which would be evidenced by the appearance of a new resonance at δ_H ~4.1 ppm for the methylene protons on the ester alkoxy chain (* in Figure 40).

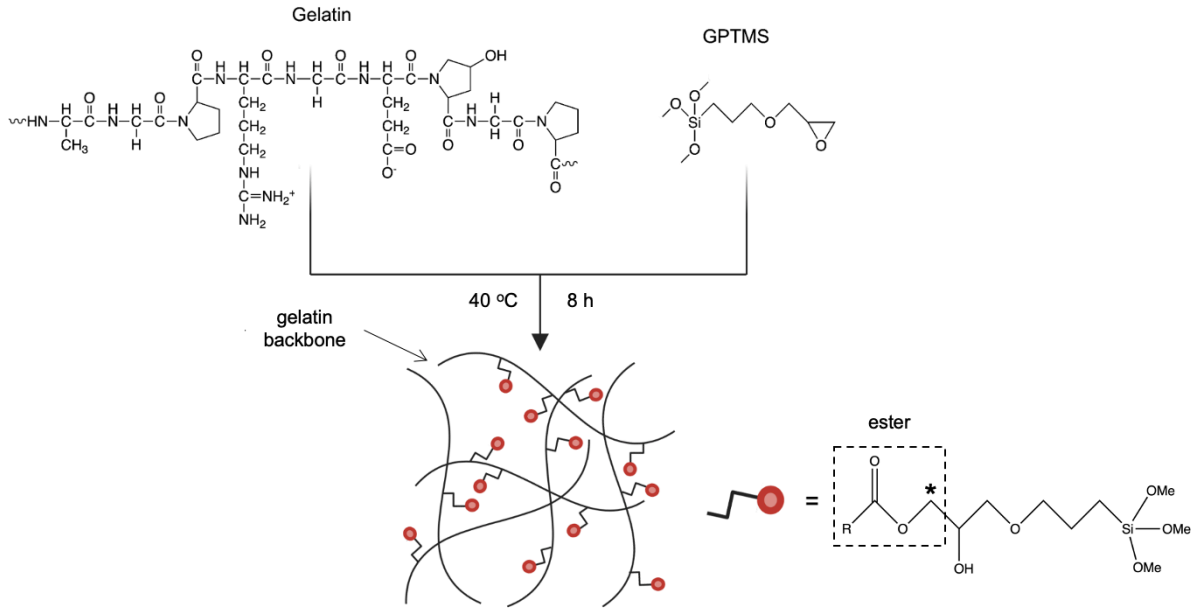


*Figure 40. Schematic illustration of preparation of Gel-GP. GPTMS undergoes ring opening of the epoxide to form an ester (RCOOR'). * represents the protons on the carbon attached to the alkoxide that would have a characteristic downfield chemical shift in the ^{1}H NMR spectrum (h = hours). Part of this figure was created on the BioRender website (https://biorender.com) by the author.*

The final spectrum of the GPTMS functionalisation reaction after dialysis shows differences compared with native gelatin, with resonances δ_H = 3.55 ppm and δ_H = 0.65 ppm (Figure 41)

which can be attributed to positions a_2 and a_5 in GPTMS (Figure 38). The presence of these resonances indicates successful functionalisation of gelatin with GPTMS as the protons responsible for these resonances would remain essentially unchanged in the functionalised gelatin product. The low intensity of the resonance at δ_H = 0.65 ppm suggests that the functionalisation is not extensive.

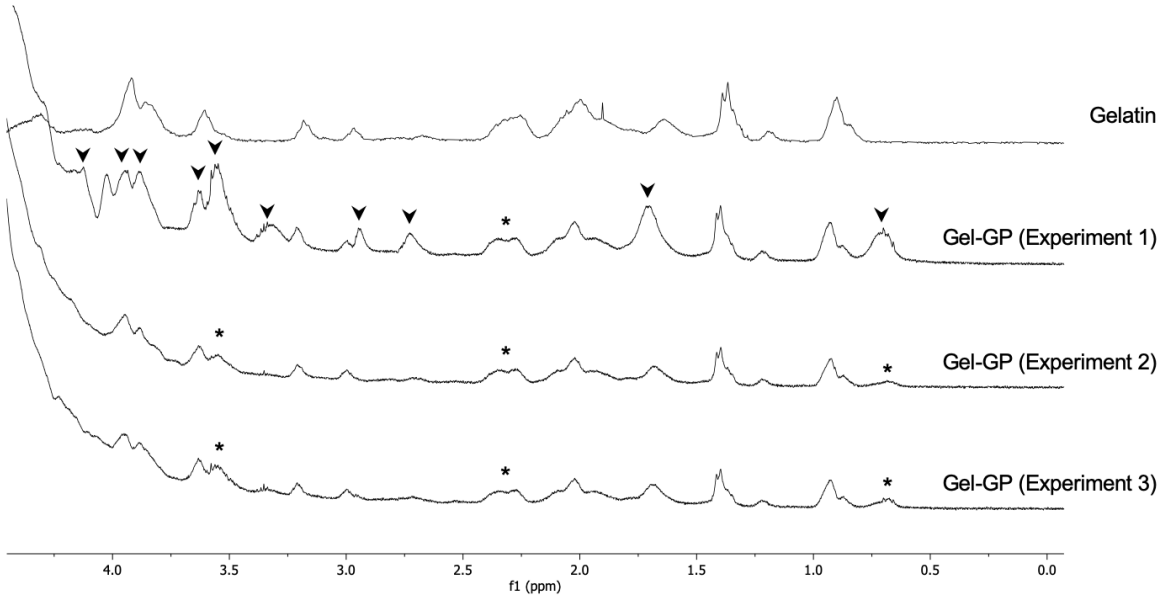


*Figure 41. ^{1}H NMR spectrum of native gelatin compared with the dialysed Gel-GP products from experiment 1, 2 and 3 (D_2O, 400 MHz). Differences in spectra are indicated with *. Arrows identify resonances for unreacted GPTMS and by-products.*

Unfortunately, the large H_2O resonance in the ^{1}H NMR spectra means that it is difficult to examine the region around ~δ_H = 4.10 ppm where a resonance characteristic of an ester would be expected to appear. Differences to the native structure of gelatin were seen elsewhere in the ^{1}H NMR spectrum in the form of an increased intensity of the resonance at δ_H = 2.30 ppm, which was observed in the ^{1}H NMR spectra of the products from the reactions performed under the three sets of functionalisation conditions. Specifically, an increased left shoulder on the broad δ_H = 2.25–2.40 ppm resonance (Figure 42). This

resonance has been assigned to the alpha protons (α-CH_2) of glutamic acid (114,221). The shoulder is proposed as a result of the α-CH_2 of glutamate that have ring-opened the epoxide in GPTMS (114).

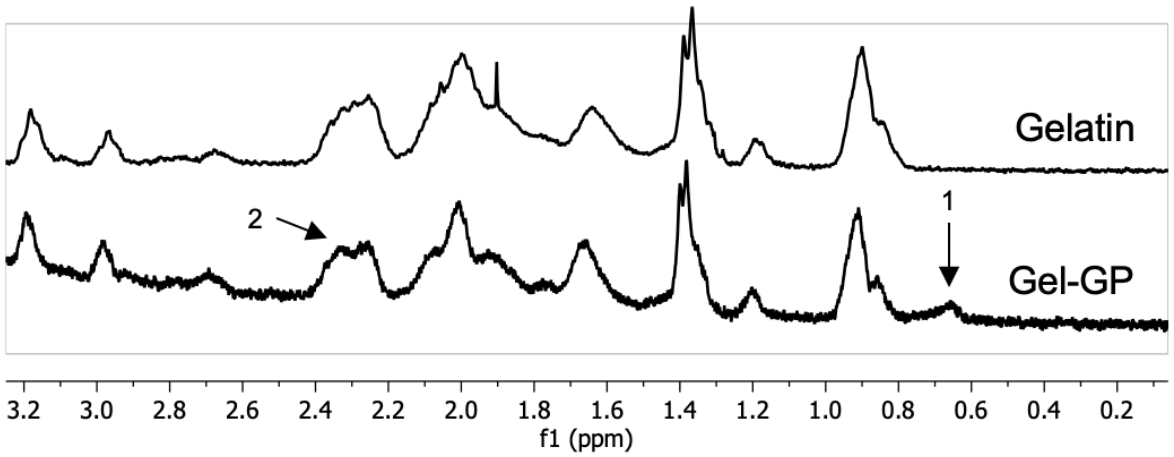


Figure 42. ^1H NMR spectrum of gelatin and Gel-GP after reaction with GPTMS for 8 hours in $HCl_{(aq)}$ (experiment 1) to form Gel-GP and dialysed for 120 hours. Differences in the spectra are indicated with arrows at 1) δ_H = 0.65 ppm and 2) δ_H = 2.35 ppm corresponding to -CH_2 next to the Si on GPTMS and glutamic acid group on gelatin, respectively (D_2O, 400 MHz).

The resonance for the lysine residue at δ_H = 2.99 ppm remains (Figure 41 and Figure 42). This can be suggested to be explained by the reaction pH. In the GPTMS-gelatin functionalisation reaction run in $HCl_{(aq)}$ (experiment 1), the pH reached ~pH 7 at the end of the reaction, whereas $HCl_{(aq)}$ pH and PB (experiment 2 and 3) remained below pH 6. Therefore, below pH 7, lysine will still mainly be in its protonated state within the Gel-GP reactions as the pKa of lysine is ~10 and so lysine is less likely to behave nucleophilic in the epoxide ring-opening reaction (222). This observation highlights the significance of the equilibrium of the acid and base conjugate during functionalisation. emphasising how reaction pH conditions can affect system reactivity. Finally, the arrows represent excess unreacted GPTMS and diols within the spectrum of Gel-GP reacted in $HCl_{(aq)}$ (experiment 1) after 72 hours of dialysis (Figure 38). This finding is potentially significant because it

suggests that even after an extended period of dialysis, it was not possible to remove completely unreacted GPTMS, potentially due to the formation of a silicate-network and partial gelation as a result of pH increase resulting in trapping of small molecules within the network. Understanding the presence of unwanted or unreacted components is crucial for optimising the reaction conditions for functionalisation of gelatin to ensure that the desired modifications are achieved.

Whilst we tentatively suggest the epoxide ring of GPTMS reacts with carboxylate side-chain residues in gelatin, this protein is a complex polypeptide containing other nucleophilic side-chain residues. The amino acids with highest relative abundance in bovine gelatin, that contain side-chain residues that could potentially undergo reaction with GPTMS, are glutamic acid (6.19 g/100 g protein), aspartic acid (4.62 g/100 g protein) and lysine (3.13 g/100 g protein) (223). However, gelatin varies according to source, and so, these values are an approximation. The relatively low abundance of amino acids that are able to undergo reaction with GTPMS supports the low presence of bound GPTMS, as observed at δ_H = 0.65 ppm (resonance 1) (Figure 42).

3.3.5. Dialysis of AGE-based functionalisation products

An example of successful dialysis is presented for Gel-AGE $HCl_{(aq)}$ (experiment 1) in Figure 43. Complete removal of excess AGE from the $HCl_{(aq)}$ reaction product was confirmed by the disappearance of resonances at δ_H = 2.95 (a_4) and 2.80 ppm (a_4*) and diol resonance disappearance at δ_H = 3.65 and 3.45 ppm. Additionally, the relative intensity of the resonances present at δ_H = 5.95 (a_1) and 5.30 ppm (a_2), which correspond to the protons on the alkene in AGE, decreased throughout dialysis but a small relative area remained in the final spectrum (Figure 43). The spectra from the dialysis of Gel-AGE reacted in $HCl_{(aq)}$ pH

and PB (experiment 2 and 3, respectively) were comparable (Appendix Figure B.7 and Figure B.8).

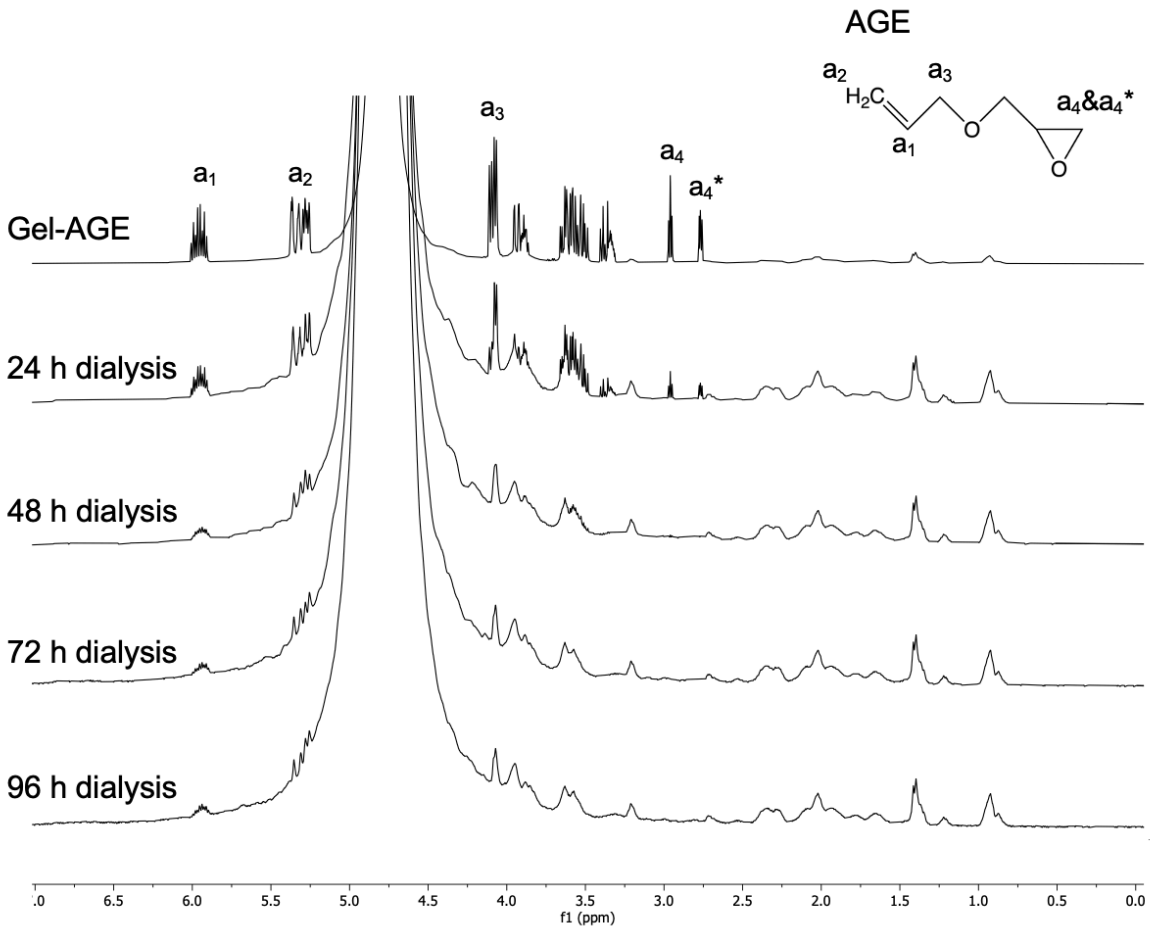


Figure 43. [1]H NMR spectra of (a) the Gel-AGE final product from experiment 1 and dialysis reaction for 96 hours, with key resonances for AGE noted (D_2O, 400 MHz). The spectra shows the retention of resonances at a_1, a_2, and a_3, but removal of resonances a_4 and a_4, corresponding to the epoxide protons in AGE.*

Dialysis was noted as complete, dependent on both of the following:

i. when the relative integration for resonances a_1, a_2 and a_3 no longer changed, and

ii. resonances a_4 and a_4* were no longer visible.

These resonances were chosen to assess the efficiency of gelatin functionalisation and dialysis because resonances a_1 and a_2 should correspond to the protons from AGE that would still be visible in the functionalised gelatin. Resonances a_4 and a_4* correspond to the protons

from the epoxide, which if dialysis works, would be removed. By these criteria, dialysis for AGE functionalisation was complete after 72 hours. These findings verify the use of dialysis as a post-processing step to remove unreacted small-molecule epoxide species and unwanted reaction by-products in AGE-functionalisation reactions.

3.3.5.1. AGE-gelatin functionalisation

Schematic illustrations of the preparation of the Gel-AGE solution are presented in Figure 44. Similar to the GPTMS-gelatin functionalisation, the proposed functionalisation mechanism involves ring opening of the epoxide in AGE by nucleophilic attack of amino acid side-chain carboxylic acid groups (-COOH) and formation of an ester, which would be evidenced by the appearance of a new resonance at δ_H ~4.1 ppm for the methylene protons on the alkoxy group (* in Figure 44).

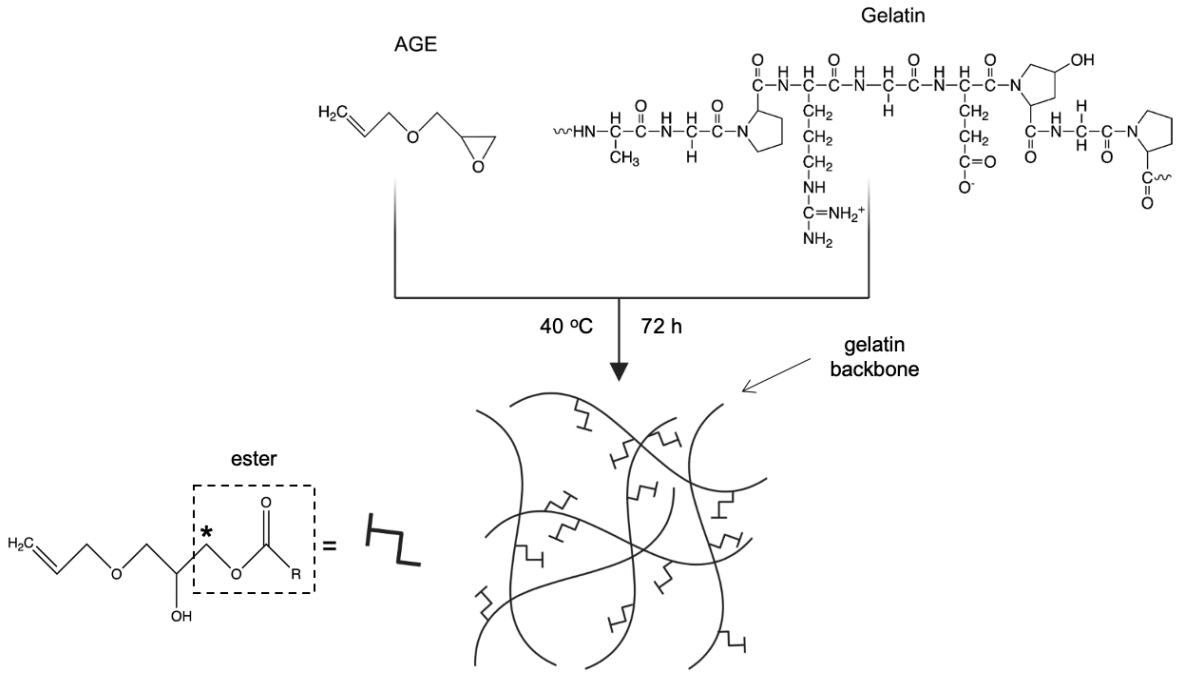


*Figure 44. Schematic illustration of preparation of Gel-AGE. AGE undergoes ring opening of the epoxide to bond with gelatin backbone, forming an ester (RCOOR'). * represents the protons on the carbon of the ester alkoxy group (h = hours). Part of this figure was created on the BioRender website (https://biorender.com) by the author.*

The ^{1}H NMR spectrum of the AGE-gelatin functionalisation revealed new resonances (*) at δ_H = 5.30 and 5.95 ppm, corresponding to the protons on the alkene in AGE (Figure 45). The new resonance at δ_H = 4.10 ppm also indicates ester formation (114). Taken together, these results confirm the presence of AGE in the final sample after dialysis, which supports successful functionalisation of gelatin.

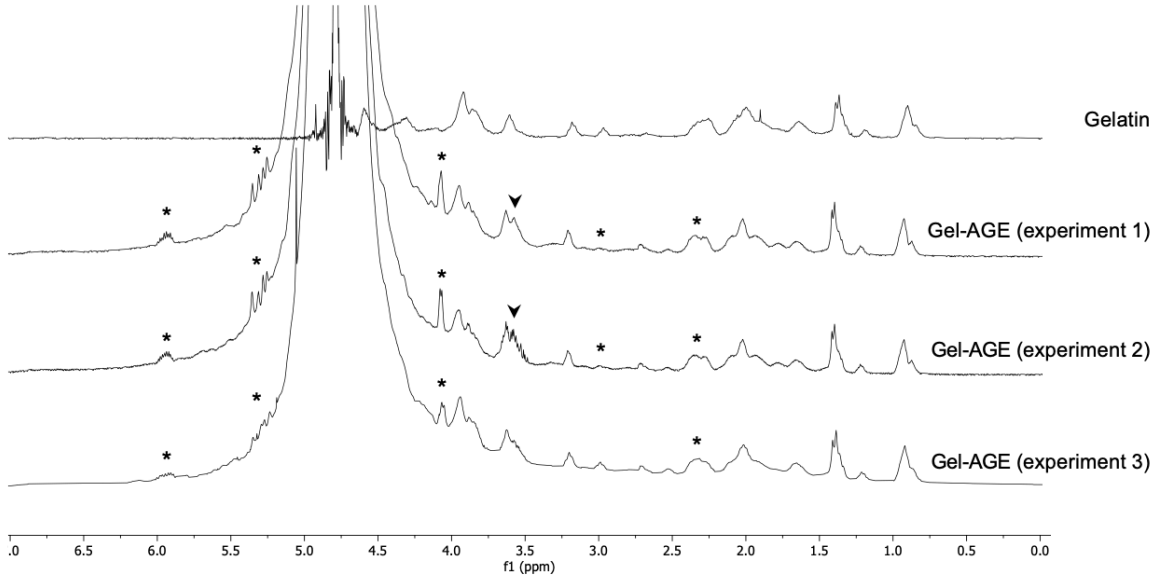


*Figure 45. ^{1}H NMR spectrum of native gelatin compared with the dialysed Gel-AGE products from experiments 1, 2 and 3 (D_2O, 400 MHz). Differences in the spectra are indicated with *. Arrows show unremoved, unreacted AGE and by-products.*

Further differences to the native structure of gelatin were seen in the form of an increased intensity of the resonance at δ_H = 2.30 ppm in the products from the reactions performed under the three sets of functionalisation conditions. Specifically, the broad resonance δ_H = 2.25–2.40 ppm shows an increased left shoulder. Therefore, the same conclusions can be drawn as with the GPTMS functionalisation reaction, specifically, that this change is proposed due to the glutamic acid ring-opening the epoxide (114). However, it is not possible to determine the extent of the reaction.

Additionally, in both $HCl_{(aq)}$ based reactions (experiment 1 and 2), the resonance δ_H = 2.99 ppm corresponding to the methylene (CH_2) protons in the lysine side chain on gelatin disappears, but not in the PB reaction (experiment 3) (224). If the amine in the lysine side-chain effects epoxide ring-opening with the AGE, then the protons responsible for the resonances at δ_H = 2.99 ppm should still be present in the product but may appear in a different position in the spectrum. New resonances are found in both $HCl_{(aq)}$ based reactions (experiment 1 and 2) product's NMR spectra at δ_H = 1.80 ppm, therefore, it is hypothesised that a change in the chemical environment of these lysine protons is as a result of the reaction with AGE.

This is an important finding in the understanding of reactivity of these systems and modification of gelatin, as these results suggest that AGE can react with both the carboxylic acid (glutamic acid) and amine (lysine) groups in gelatin when reacted in $HCl_{(aq)}$. Therefore, in the context of gelatin reactivity with these two different epoxides, a key question arises: why does gelatin react differently with the epoxides in AGE and GPTMS?

It is important to consider pH of the reaction here, as when pH varies, the protonation state of acidic and basic amino acid side-chain residues on gelatin will also change, which may affect the chemoselectivity of reaction with AGE. In the AGE functionalisation reactions run in $HCl_{(aq)}$ (experiment 1) and $HCl_{(aq)}$ pH (experiment 2), the reactions were carried out starting at ~pH 5, but both proceeded to continue to react up to ~pH 8 (Figure 35). Whereas a smaller pH increase was observed in the GPTMS functionalisation reactions; the pH remained at ~pH 5 in the reactions run in $HCl_{(aq)}$ pH and PB (experiment 2 and 3) and increased to ~pH 7 in the $HCl_{(aq)}$ pH (experiment 1) (Figure 29). At pH 5, carboxylic acid-containing amino groups, such as glutamic acid, will exist significantly in their (more nucleophilic) carboxylate form

whereas amine-containing amino groups, such as lysine, will be almost fully protonated. Therefore, it can be expected that the nucleophilic ring opening of GPTMS and therefore functionalisation reaction will occur primarily on the more nucleophilic carboxylic acid-containing amino groups (114,130,184,190). However, the increase in pH over the course of the reaction will affect these equilibria. At higher pH, a higher concentration of amine groups could open up a second functionalisation site for the reaction with the epoxide in AGE. The reaction of lysine in gelatin is commonly cited in methacrylation protocols, where the resonance at δ_H = 2.99 ppm corresponding to the methylene (CH_2) protons in the lysine side chain is also seen to decrease or disappear (150,181). Furthermore, the PB solution (experiment 3) did not see a pH increase past ~pH 6.5, and thus, the lysine resonance at δ_H = 2.99 ppm remained. This finding indicates that maintaining the reaction at a lower pH may help retain the lysine resonance by potentially restricting the reactivity of lysine with the epoxide in AGE. This is relevant because the presence or absence of this resonance can provide information on the degree of lysine modification and the chemoselectivity of the functionalisation reaction, both of which are important for understanding the overall structural changes in gelatin during the functionalisation process.

Together, these findings indicate that under mildly acidic conditions (<pH 6.5), the side-chain carboxylic acid groups of glutamic acid residues are predominantly acting as nucleophiles in ring-opening the epoxide in AGE. However, the increase in pH over the course of the reaction, opens up the potential for a competing functionalisation reaction involving the amine functionality of lysine residues.

In the cases of GPTMS- and AGE-based functionalisation reactions, dialysis allowed for the removal of excess epoxide-based molecules and reaction by-products, to indicate the

functionalisation within the systems was not extensive. AGE was used to remove a layer of complexity within the epoxide-gelatin functionalisation reaction; however, it cannot be used to create the silica-based hybrids of interest here due to the relatively inert alkene. Therefore, further characterisation was carried out on Gel-GP.

3.3.6. Degradation behaviour of gelatin-silica hybrid hydrogels

The prepared gelatin-silica hydrogels were submerged in PBS at 37 °C to study hydrogel degradation over a 7-day period. A degradation study was conducted to determine if the use of GPTMS as a crosslinker in Class II hybrid hydrogels lead to more controlled degradation when compared to Class I hybrids. In particular, this assay was used to investigate the impact of dialysis and presence of GPTMS on the degradation behaviour of the hydrogels. A change in degradation could indicate the extent of covalent bonds formed by the Class II hybrid hydrogels between Gel-GP and Silica, as it is predicted that the degradation profile will be more controlled, avoiding burst release, in the hydrogels with covalent coupling present. Therefore, it should help to indicate the effectiveness of GPTMS coupling at improving unpredictable degradation (110,112,161,181). Degradation behaviour of hybrids is commonly studied in literature and used to better understand how material formulation can impact the rate of *in vitro* hydrogel dissolution (112,184,225).

The degradation profile of the hydrogels was investigated, focusing on (a) the change in mass of hydrogels, shown as mass remaining and (b) silicon concentration in the PBS solution, shown as silicon release. The % mass loss of hydrogels and release of silicon is indicative of degradation due to the loss of bulk H_2O, as well as network breakdown through hydrolytic degradation which leads to the dissolution of gelatin molecules and silica, and ultimately, structural disintegration (226–228).

3.3.6.1. Change in mass

To investigate the hydrogel mass degradation profile, hydrogels were removed from the PBS solution and weighed at time intervals over a 7-day period. The results demonstrate that there was significantly more mass remaining, and thus a slower degradation rate, in the Gel-GP-Silica (undialysed) hydrogel (100.8%) when compared to Gel-Silica (96.4%) and Gel-GP-Silica (dialysed) (95.0%) in the first 3 hours of being submerged in PBS (Figure 46a). A mass remaining value >100% indicates that the hydrogel had become swollen through H_2O uptake (108,229). The dialysed hydrogel from 3 hours onwards continued to have a higher degradation rate, shown as less mass remaining, compared to the undialysed hydrogel.

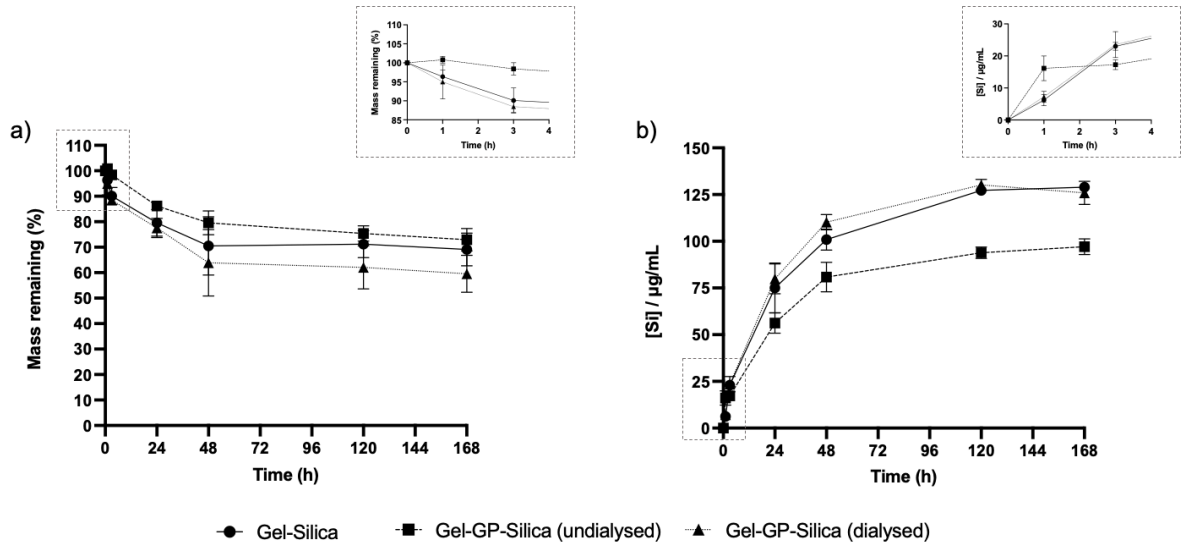


Figure 46. a) Change in mass of Gel-Silica, Gel-GP-Silica undialysed, and Gel-GP-Silica dialysed hydrogels over a 7-day period in PBS. b) Si species release in PBS, giving Si concentration (µg/ml) in PBS over a 7-day period. Insets of both show the 0–4 hours (n=3).

The mass change results suggest that the improved hydrogel properties observed in the literature in Class II hybrids (133,184,190), such as a more desirable controlled degradation rate, could be attributed to the presence of excess GPTMS within the system that has not been removed post-functionalisation; the excess GPTMS within the system and the silica network

it ultimately forms, helps to control the degradation rate. This finding is consistent with the ^{1}H NMR characterisation study that suggests the degree of functionalisation is low. As a result, the low concentration of trimethoxysilyl groups present post-dialysis means that covalent crosslinking within the hybrids between Gel-GP and silica is not extensive, and accounts for the lack of any improved degradation properties in the Gel-GP-Silica (dialysed).

3.3.6.2. Silicon (Si) species release

Samples were taken from the PBS hydrogels were submerged in at time intervals over the 7-day degradation assay and subjected to ICP-OES analysis to determine Si species concentration in solution, and therefore, Si release over time.

There remains a lack of understanding of how Si species influence cell behaviour, however, it is thought to be dependent on the form (soluble versus insoluble), concentration and Si species (e.g. ortho-, di- or polysilicates) (230). Nonetheless, Si has been found to have several beneficial effects on osteoblast cells; some of these effects include increased osteoblast growth and proliferation, stimulation of osteogenic differentiation, as well as promotion of mineralisation, thereby influencing bone formation (231–235). Level of Si has also been associated with bone metabolism, homeostasis and higher bone strength and bone mineral density (233,236). Additionally, silicic acid, a soluble form of Si, is present at active calcification sites during bone formation (237). Although Si can have beneficial impact, Si concentration may play a dose-dependent role in impacting cell behaviour on a material (231). For example, Gough et al. (238) found that apoptosis occurred in 50% of osteoblasts cultured in high ion concentration extracts (8.19 mM). Therefore, studying Si release from the Gelatin-Silica-based hydrogels is crucial as to understand how released Si could be impacting cells during cell culture.

There was significantly less Si release in the Gel-GP-Silica (undialysed) hydrogel compared to Gel-GP-Silica (dialysed) and Gel-Silica hydrogels (Figure 46b). An explanation for this could be that the trimethoxysilyl groups from the excess GPTMS are forming a highly condensed silicate network with the inorganic silica, essentially condensing the formed silica within the network, and preventing its release. Whereas, in the Gel-GP-Silica (dialysed) and Gel-Silica hydrogels, there is no difference between Si release, again supporting a low degree of gelatin functionalisation. A more controlled release profile observed over the assay duration would suggest that GPTMS has effectively established covalent bonds between the gelatin and silica phases. These covalent bonds, when compared to weak non-covalent interactions when GPTMS is not present, prevent the rapid or burst release of silicon, which is a favourable outcome in this context.

The main difference between this study and those in the literature by Mahoney et al. (184,190), Ravarian et al. (239), Negahi Shirazi et al. (203) and Reyes-Peces et al. (240) is how the end hydrogel products are used. This study involves hybrids used in their hydrated form, whereas those described in the literature use hybrids in their monolith form (184,190,203,239,240). Formation of monolithic hybrids would involve polycondensation of the network, meaning any unreacted GPTMS would be locked into the network – incorporating toxic molecules into the scaffold which would have controlled release as the scaffold degrades (191,241).

Thus, the incorporated hydrolysed excess GPTMS network could have an influence on the mechanical properties of the resulting hydrogel. However, only Nelson et al. (117) acknowledge the excess GPTMS within the hybrid system, and all fail to account for the presence of low-molecular-weight impurities, including unreacted epoxide species and diols.

Questions around the efficiency of the GPTMS-gelatin functionalisation reaction remain and the presence of only a small amount of bound GPTMS after dialysis and the lack of improvement in degradation highlights the need to improve this process. Furthermore, since dialysis is not a routinely performed purification method, the role of residual GPTMS (and hydrolysis products), given it is often employed in large excess, on the final hydrogel system should be considered. This led to additional investigations of the gelatin-GPTMS functionalisation reaction in an attempt to increase the reaction duration to improve degree of functionalisation.

3.3.7. Extending reaction time in an attempt to increase extent of gelatin functionalisation

Previous studies have highlighted the hydrolysis and condensation of methoxysilyl groups and the subsequent formation of GPTMS oligomers in a silicate network during the gelatin-GPTMS functionalisation as unfavourable for hybrid formation, as it often results in precipitation and premature gelation (117,192).

Several reaction parameters were selected (solvent, pH, and gelatin concentration) in an attempt to extend the functionalisation reaction time with the aim to increase the degree of gelatin functionalisation. $HCl_{(aq)}$ (10 mM, pH 5) was used as a control solvent to investigate the optimal functionalisation time before gelation occurred.

Formamide and DMSO were selected as alternative reaction solvents. Polar aprotic solvents, such as formamide and DMSO, are commonly used when nonaqueous solvents are needed in reactions (242,243). Removing H_2O from the reaction would reduce the GPTMS hydrolysis and condensation which often results in gelation. Using these solvents, the functionalisation time was extended to 48 hours and 72 hours for formamide and DMSO, respectively.

The reaction was next performed using 0.5 wt% gelatin, a 10-fold lower concentration than normal. This also had a 10-fold lower concentration of GPTMS to maintain CF500. Performing the functionalisation reaction at this lower concentration extended the reaction to 96 hours (and beyond) as gelation was not observed.

Above pH 7, the formation and gelation of the silicate network is promoted (192). Therefore, as the pH of the reaction mixture increases throughout the reaction, by starting the reaction at pH 3 it extended the time before gelation occurred and thus, time for functionalisation was increased from 8 hours to 14 hours. However, at pH 3, the carboxylic acid side-chain residues are protonated and therefore less nucleophilic, so even though starting the reaction at pH 3 extended the time for functionalisation, a balance needs to be struck attempting to increase functionalisation time but maintaining conditions appropriate for functionalisation to occur. The impact of reaction conditions on degree of functionalisation will be discussed in the following section.

3.3.7.1. Gel-GP characterisation

Ninhydrin assay – a focus on amine functionalisation

Researchers have used a ninhydrin assay to study the reaction between gelatin and GPTMS (117,203,244); this assay is used to quantify the number of primary and secondary amine units in solution, and thus, justified as ‘degree of crosslinking’. The use of this method in these studies suggests the reaction takes place at least in part on the amine, and in some cases, purely the amine, due to the sole use of this verification method and the absence of one for carboxylic acid reaction. Nelson et al. (117) investigated the effect of C-factor (CF) on crosslinking by using a ninhydrin assay to optically quantify the levels of free primary and

secondary amines before and after crosslinking. The degree of crosslinking increased linearly as CF increased from CF0 to CF500 (117).

The ninhydrin assay was used to determine the extent of reaction between gelatin and GPTMS in the different reaction conditions. The assay works by ninhydrin reacting with a primary amine to form Ruhemann's Purple and with a secondary amine to form a yellow-orange complex (245,246). Therefore, this assay should allow quantification of lysine residues before and after functionalisation of gelatin with GPTMS, as the secondary amine product from the reaction of lysine would deliver a yellow product. Zatorski et al. (245) investigated the use of a ninhydrin assay on norbornene and methacryloyl functionalised gelatin reactions to determine extent of amine-based functionalisation. It was determined that the assay enabled quantification of fractional functionalisation as an indicator of reaction completeness (245).

To determine the fraction of primary amines remaining in the Gel-GP samples, they were normalised to their control (gelatin + solvent). The control represented untreated gelatin within the same reaction condition. Note that pH 5 functionalisation condition only had a value for control and 8 hours as it was not possible to run the reaction for longer than 8 hours.

Gel-GP reacted in DMSO for 72 hours (full functionalisation time) was the only reaction where there was a significant decrease in the available primary amine groups ($p<0.01$) (Figure 47). However, in the other three reactions (pH 5, pH 3 and 0.5 wt %), all carried out in $HCl_{(aq)}$, the ninhydrin results showed no significant decrease in available primary amines on the functionalised gelatin when compared to untreated gelatin, suggesting a lack of primary amine functionalisation.

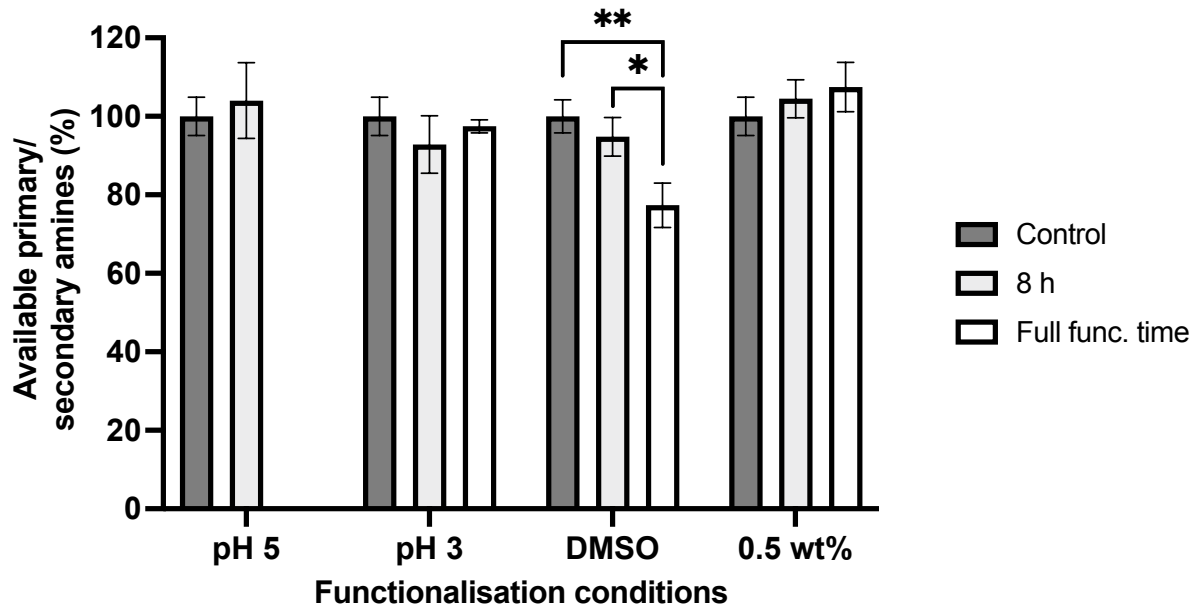


*Figure 47. Available primary/secondary amines for Gel-GP after four different functionalisation reactions with varied conditions; pH 5, pH 3, DMSO, and 0.5 wt%. The results were normalised against the control, with the control representing native gelatin within the same solvent, without GPTMS (n=3; * p≤0.05; ** p<0.01).*

After investigation, formamide was not a compatible solvent for this assay and so was not explored further. It is suggested that formamide undergoes hydrolysis during the ninhydrin reaction (as H_2O is introduced), to result in the production of ammonia (247). As ninhydrin is also used to detect ammonia, it is not possible to determine the change in absorbance owed to functionalisation. Future work should explore the use of dialysis, freeze drying, and ^{1}H NMR to analyse the product of this reaction.

Solution pH influences the protonation state of side-chain amino-acid residues on gelatin, and therefore, should affect the location of functionalisation with the epoxide of GPTMS. It should be noted that the DMSO reaction occurred at pH 9–10, i.e. under basic conditions. However, pK_a values are solvent dependent and are typically higher in DMSO than in H_2O; the pK_a of an ammonium species in DMSO at neutral pH is ~20, meaning it is likely to be

protonated in DMSO at neutral pH but will begin to deprotonate as the pH increases (248). Therefore, the protonation state of an acid and its conjugate base at equilibrium will be solvent dependent. These results highlight the importance of solvent and pH in the functionalisation reaction.

Ninhydrin results also show that reaction time is a key factor that influences extent of functionalisation in mildly basic reaction conditions, with a significant increase in the DMSO functionalisation when comparing 8 hours functionalisation time with 72 hours ($p \leq 0.05$). This supports the need to extend reaction time in gelatin epoxide-based reactions.

Titration – a focus on carboxylic acid functionalisation

Titration curves have been used to determine the carboxylic acid content in gelatin, demonstrating the region between pH 1.5 to 6.5 is characteristic of carboxyl groups; this means at ~pH 1.5 carboxyl groups begin to deprotonate and are sensitive to pH changes (249,250). The change in shape of the curve between pH 1.5 to 6.5 can determine the number of carboxylic acid groups, e.g. if the curve has shifted left and a smaller portion of the curve is within this region, it suggests that there is a lower number of free carboxylic acid groups, and vice versa (Figure 48) (251).

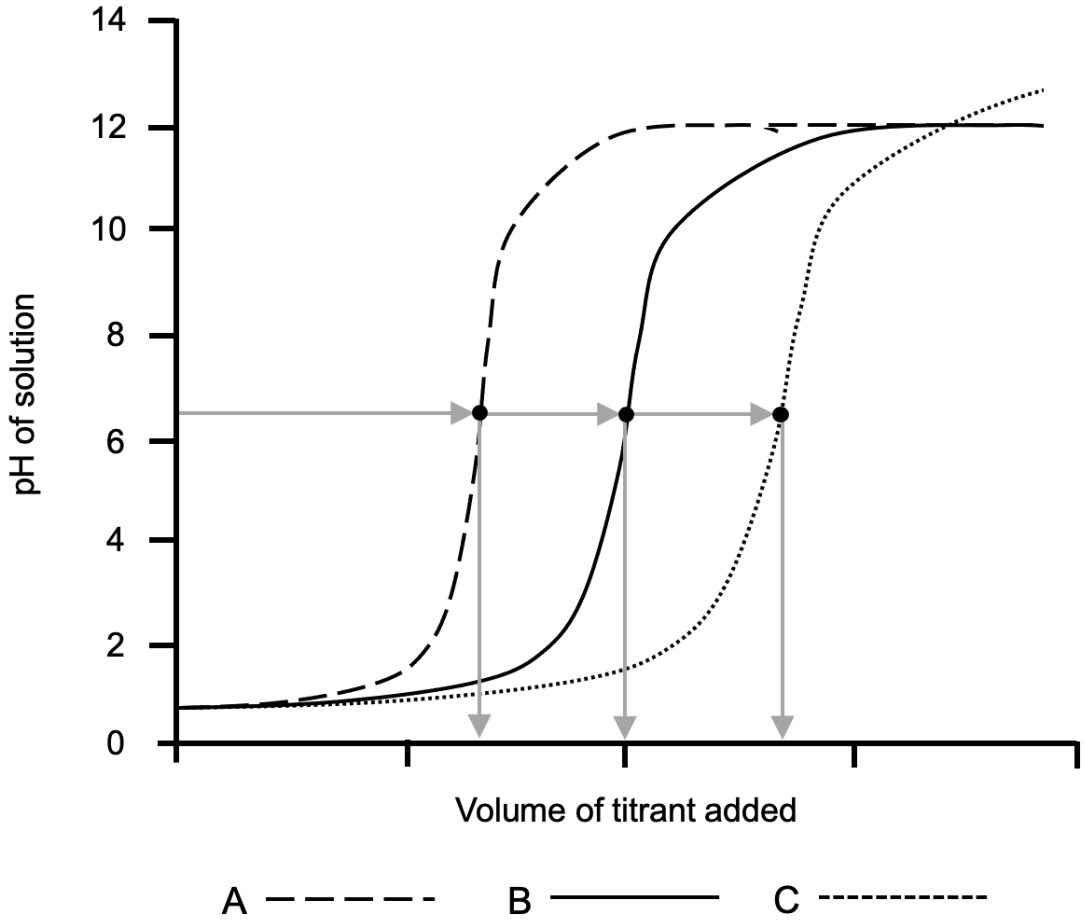


Figure 48. Graphical representation of a titration curve of three solutions: A, B and C. The grey arrows represent where the carboxyl region ends at pH 6.5 on the different solutions. Solution A would have the least free carboxylic acid groups as a shorter portion of the curve is within the carboxyl region, followed by B and then C. The left shift of the curve occurs because the solution requires a lower volume of titrant to be added to cause the carboxyl groups to deprotonate, demonstrating there are less free carboxyl groups in solution (251).

Titration is a technique that in this context will allow for exploitation of the ionisable nature of carboxylic acid groups and how this will change if native gelatin has been modified via reaction through carboxylate side-chain residues. Kuijpers et al. (251) used titration curves to quantify the number of carboxylic acid residues in gelatin from two different sources; gelatin A (porcine skin) and gelatin B (bovine skin). Differences in titration curve shape signified changes in the number of free carboxylic acid groups in the different types of gelatin,

specifically, there was a lower number of carboxylic acid groups in gelatin A as a lower proportion of the titration curve was in the carboxyl region compared to gelatin B.

Titrations were performed to investigate the change in carboxylic acid group residues within the Gel-GP compared to native gelatin. To our knowledge, this is the first time that titration curves have been used to analyse the products of the Gelatin-GPTMS functionalisation reaction. Titrations were performed on the reactions performed in $HCl_{(aq)}$, DMSO and formamide; however, titrations on the reactions performed in DMSO and formamide were not reproducible and so are not reported or discussed here.

The titration curve for the gelatin control (5 wt%) (Figure 49a) exhibits a gradual increase in pH initially between pH 1.5 and pH 5, followed by a sharp increase between pH 5 and pH 10. The sharp pH increase started to occur when approximately 10.00 mL of titrant (0.2 M $NaOH_{(aq)}$) had been added. The resultant titration curves for the Gel-GP products (pH 5 and pH 3) had the same shape as the control but had shifted to the left. Therefore, the Gel-GP curves required less volume of titrant to reach the equivalence point. As carboxylic acid residues are titrated between pH 1.5 and 6.5, this leftward shift indicates a decrease in required volume of titrant (0.2 M $NaOH_{(aq)}$) between pH 1.5 and 6.5 to cause a pH increase. The quicker pH increase results in a leftward shift, potentially reflecting a decrease in free carboxylic groups in Gel-GP compared to native gelatin due to functionalisation (250,251). There was minimal difference in the titration curves for Gel-GP from pH 5 and pH 3 reaction conditions, suggesting a comparable extent of alteration in free carboxylic acid groups (Figure 49a).

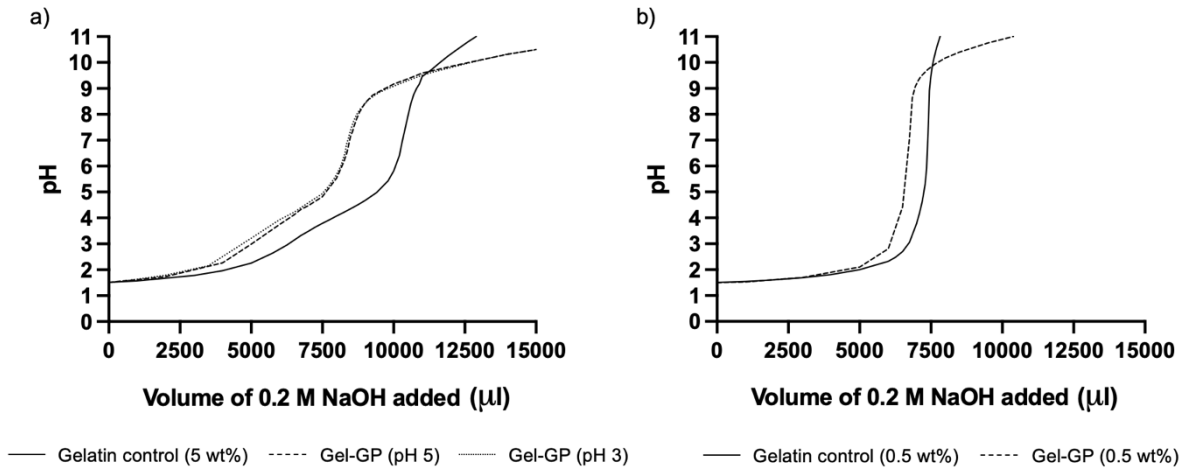


Figure 49. Titration curves of a gelatin control compared to different HCl-based functionalisation reactions; a) gelatin control (5 wt%), Gel-GP (pH 5) and Gel-GP (pH 3), and b) gelatin control (0.5 wt%) and Gel-GP (0.5 wt%). Focussing between pH 1.5 and 6.5 (the carboxylic acid region), both titration curves demonstrate a left shift and so decrease in available carboxylic acid groups.

A similar trend was observed with the gelatin control (0.5 wt%) and the Gel-GP (0.5 wt%) product (Figure 49b). In the control, an initial plateau period between pH 1.5 and 2.0 was followed by a sharp increase at pH 2.0, when approximately 6.25 mL of titrant had been added. The Gel-GP product saw the same increase at pH 2.0 but the increase started after approximately 5.00 mL of titrant had been added, again, suggestive of a decrease in free carboxylic acid groups in Gel-GP (0.5 wt%).

The lower level of carboxylic acid groups present in the Gel-GP products is consistent with carboxylic acid functionalisation with the epoxide on GPTMS. These titration curves support the conclusions drawn from interpretation of the ^{1}H NMR spectra of Gel-GP (Figure 42). However, the small changes in the titration curves suggest that functionalisation is not extensive, which is also in line with conclusions drawn in the NMR study.

3.4. Summary

This study set out to investigate the reactivity of GPTMS with gelatin, and how GPTMS-functionalised gelatin can be used to create gelatin-silica hybrid hydrogels. The functionalisation process was carried out with $HCl_{(aq)}$ and PB under various pH conditions. The results indicated side-chain carboxylic acid groups in gelatin effect GPTMS epoxide ring-opening, although the degree of functionalisation with GPTMS is low.

During the course of this study, significant challenges emerged. The GPTMS-gelatin functionalisation method proved to be complex with problems associated with GPTMS hydrolysis and condensation of trimethoxysilyl groups, as well as pH increase of the reacting solution over time. Furthermore, there were doubts about the degree of GPTMS functionalisation, implying that the procedure was not as efficient as hoped.

These difficulties forced a shift in emphasis towards a different epoxide-gelatin functionalisation method, involving AGE. By substituting the trimethoxysilyl groups with an inert double bond, AGE was investigated to simplify the functionalisation process. In both GPTMS and AGE reactions, epoxide ring opening was discovered to be influenced by reaction time and pH, with longer reaction times observing more epoxide ring opening and higher pH values resulting in slower epoxide ring opening. The results of the AGE pH-controlled studies revealed important insights on gelatin functionalisation, particularly the successful reaction of side-chain carboxylic acid groups in gelatin, and side-chain amine groups with AGE when reacted across a larger pH range – spanning acidic through to basic pH.

This work highlights the need to remove such impurities to be able to conclude definitively that functionalisation has occurred. Dialysis was an effective technique to remove excess and undesirable small-molecule by-products in both AGE and GPTMS functionalised gelatin reactions. However, it was not possible to completely remove all of the excess GPTMS and small-molecule by-products from the Gel-GP $HCl_{(aq)}$ product due to the formation of a silicate network as a result of pH increase.

Hydrogel degradation profiles were examined to investigate the influence of dialysis on the properties of the hydrogels. As functionalisation of gelatin was on a relatively low level, it was not to an extent to impart improved properties on Class II hydrogels when compared to Class I. It was found that the Class II hydrogel made with undialysed Gel-GP degraded at a slower rate than the Class II with dialysed Gel-GP and there was no difference between the dialysed hydrogel with the Class I hybrid. These observations raised questions around the efficiency of the gelatin-GPTMS functionalisation reaction and support a low degree of functionalisation. It is predicted that the excess GPTMS in the undialysed products creates a silicate network that is highly condensed and reduces the release of silica from the hydrogel.

A series of characterisation techniques, namely ^{1}H NMR, a ninhydrin assay, and titrations, were used to support the conclusions drawn within this work. ^{1}H NMR spectroscopy was used pre- and post-dialysis to analyse the chemical structure of Gel-GP and compare it to a baseline of untreated gelatin, finding small changes in the structure at the glutamic acid residue of gelatin suggesting functionalisation through this side-chain residue. A ninhydrin assay and titration experiments were used in an attempt to confirm the position of conjugation of GPTMS on gelatin, focusing on amine and carboxylic acid functionalisation, respectively. Both techniques were used on Gel-GP products from a variety of different reaction solvents

and reaction lengths. A key finding from the ninhydrin assay was that amine functionalisation seemed to occur in the 72 hour DMSO-based reaction, which was carried out at basic pH. The titration curves showed that there was a lower number of free carboxylic acid groups in Gel-GP after functionalisation at acidic pH (synthesised in $HCl_{(aq)}$), when compared to untreated, native gelatin, supporting carboxylic acid functionalisation. This work shows the important role that solvent and pH plays, and also shows that reaction time is a key factor that influences extent of functionalisation.

Finally, the efficiency of the epoxide-based gelatin functionalisation reaction is still an issue. Ultimately, this study would make the following recommendations for researchers wanting to use this reaction:

- Use of dialysis – if GPTMS is used in excess within the reaction
- Use of different solvents – to extend functionalisation time whilst focusing on minimising methoxysilyl hydrolysis and condensation
- Use of numerous verification techniques to confirm the extent and position of functionalisation

CHAPTER 4. NOVEL SYNTHESIS OF GELATIN-BASED HYBRID HYDROGELS FORMED VIA THIOL-NORBORNENE CLICK CHEMISTRY

4.1. Introduction

Previous attempts at functionalisation of gelatin-based materials with an organosilane crosslinker are dominated by GPTMS (114,117,184,185,190,191,193,203), and have been the focus of Chapters 2 and 3. As previously highlighted in this thesis, the epoxide-based reaction efficacy is bought into question due to numerous issues associated with the reaction. There is the need to develop faster, more efficient functionalisation processes to inorganically modify gelatin. Thiol-ene chemistry has emerged as a popular alternative crosslinking approach in gelatin-based materials as it is fast, light-initiated and occurs under mild reaction conditions (252,253).

4.1.1. Thiol-ene click chemistry

A thiol-ene organic reaction involves photo-mediated reaction of a 'thiol' (-SH) functionality and an 'alkene' (C=C), via a radical-mediated mechanism to form a thioether (R-S-R) (Figure 50) (36). The reaction is initiated upon exposure to a photoinitiator, such as LAP, and light (252,254,254–257).

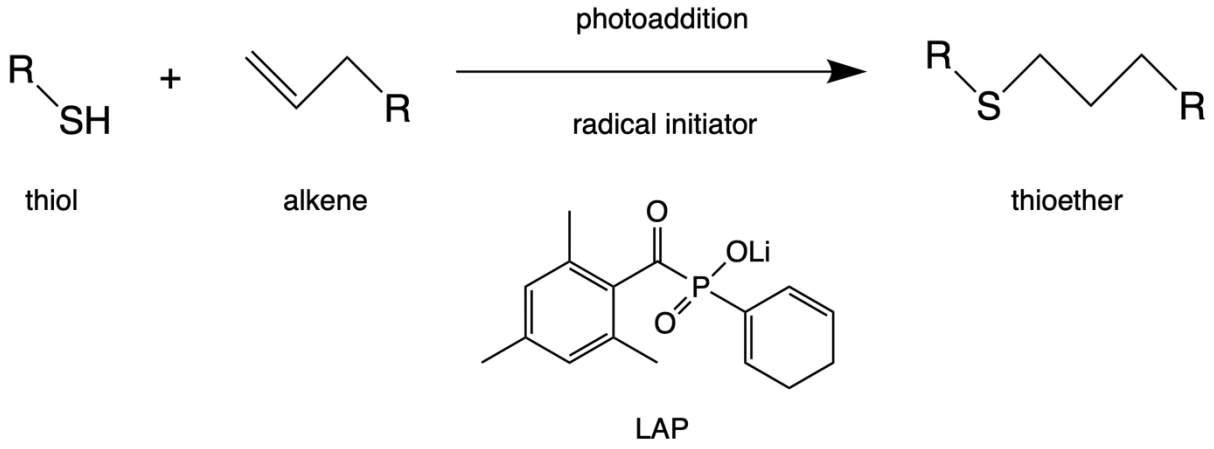


Figure 50. Scheme of a photoaddition thiol-ene reaction with an LAP photoinitiator, to form a thioether.

The thiol-ene reaction has many attractive features, including availability of a range of thiol and alkene functionalities, mild reaction conditions, fast reaction rates, efficiency and high chemoselectivity (258–260). Additionally, *in situ* hydrogel formation via thiol-ene click chemistry photopolymerisation reactions represents one of the most widely adopted synthetic methods (261–263).

4.1.1.1. Reaction conditions employed

There are numerous experimental parameters that can be varied to impact the thiol-ene kinetics, including thiol and -ene stoichiometry, diffusion and solvent (264). Varying reaction conditions has been demonstrated to impact alkene conversions in some cases from effectively 0% to 99% (265). Additionally, a study investigating the stereoselective thiol-ene reaction of glycals with numerous thiols, found that lower temperatures (in some cases down to –80 ^{o}C) increased the yield and were beneficial to the efficacy, and in the majority of reactions significantly raised the stereoselectivity (266).

Varying light source (365 nm vs visible light [455 nm]) and irradiation time (2, 5 or 10 minutes) have been shown to impact the rate of thiol-ene photopolymerisation of norbornene functionalised 8arm-PEG with a dithiol functionalised crosslinker (267) (Figure 51). After 2 minutes of 365 nm light irradiation nearly 100% conversion of norbornene groups was observed, compared to ~40% with visible light. Longer irradiation times were needed when using visible light; at 5 minutes ~70% conversion occurred and 100% at 10 minutes. After 5 minutes of visible light irradiation the moduli of the hydrogels did not increase even though full conversion was not achieved. The different reaction kinetics achieved with different light sources and irradiation time provides a way to control the resulting hydrogel modulus (267).

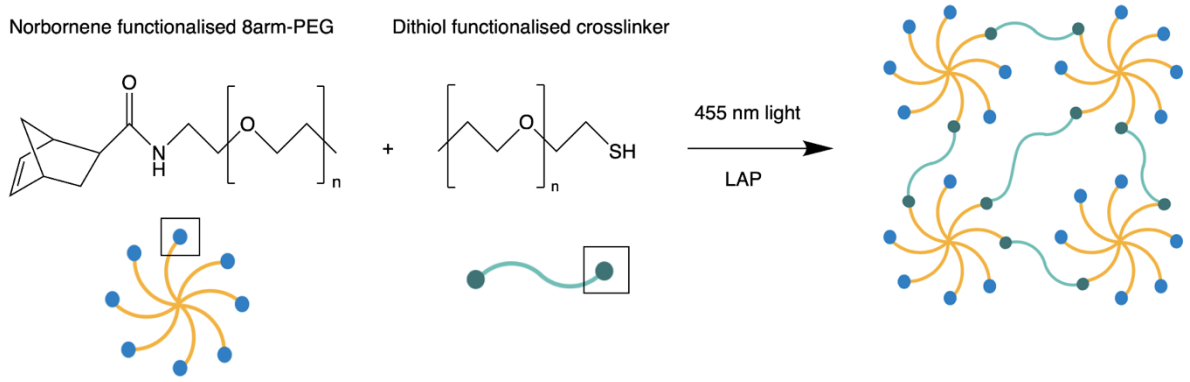


Figure 51. Thiol-ene reaction of norbornene functionalised 8arm-PEG with a diothiol functionalised linker to form a synthetic thioether crosslinked hydrogel. The black square represents the chemical structure shown and the bridged cyclic hydrocarbon is the norbornene group. Adapted from Wiley et al. (267). *Part of this figure was created on the BioRender website (https://biorender.com) by the author*.

The choice of photoinitiator species in thiol-ene reaction is important. Irgacure (2-hydroxy-4′-(2-hydroxyethoxy)-2-methyl- propiophenone) and LAP are two photoinitiators often employed in photopolymerisation reactions due to their cytocompatibility and sufficient polymerisation rate to facilitate gelation (268–270). However, preferential use of LAP over Irgacure has been suggested when improved mechanical properties are desirable, due to faster G' evolution and improved Z stability in printed constructs (271). Additionally, using a higher concentration of LAP has been demonstrated to significantly increase the modulus of a norbornene-containing PEG hydrogel (267).

4.1.1.2. Types of alkenes

Thiol-ene kinetics have been studied to understand the influence of different alkene functionalities on the energetics of the reaction. Methyl mercaptan, an organosulfur compound, was used as the model thiol and its reactivity was studied with a variety of 12 alkenes, including propene, norbornene, methyl acrylate and butadiene. Norbornene was found to have the highest reactivity due to alleviation of ring strain leading to a low

propagation barrier (264). This is supported in other literature, which also found that the most reactive alkenes are norbornene and electron-rich alkenes, for example allyl ether, and the least reactive are conjugated and electron-poor alkenes, for example butadiene (265,272–274).

4.1.1.3. Types of thiol

There is far less published on the reactivity of thiols when compared to the literature on the reactivities of alkenes (265). Thiol-containing compounds with a carbonyl positioned in immediate proximity to the -SH group, such as in mercaptopropionate, react more quickly than those that do not, such as mercaptoacetate, due to the carbonyl destabilising the sulfur-hydrogen bond (273). The impact of using a primary, secondary or tertiary thiol on the thiol-ene reaction kinetics has been studied, demonstrating that changing from a primary to a tertiary thiol led to a 10-fold decrease in polymerisation rate (275). It is thought that steric hindrance as a result of increasing substitution is responsible for the decrease in reaction rate (275).

4.1.1.4. Thiol-ene hydrogels

PEG-based macromers are commonly used to form hydrogels via thiol-ene reactions due to their solubility in organic and aqueous media, tissue-like elasticity, tuneable properties, and well-characterised chemistry (265,276). Anderson et al. (277) synthesised peptide-containing 4arm PEG-norbornene thiol-ene crosslinked hydrogels (Figure 52).

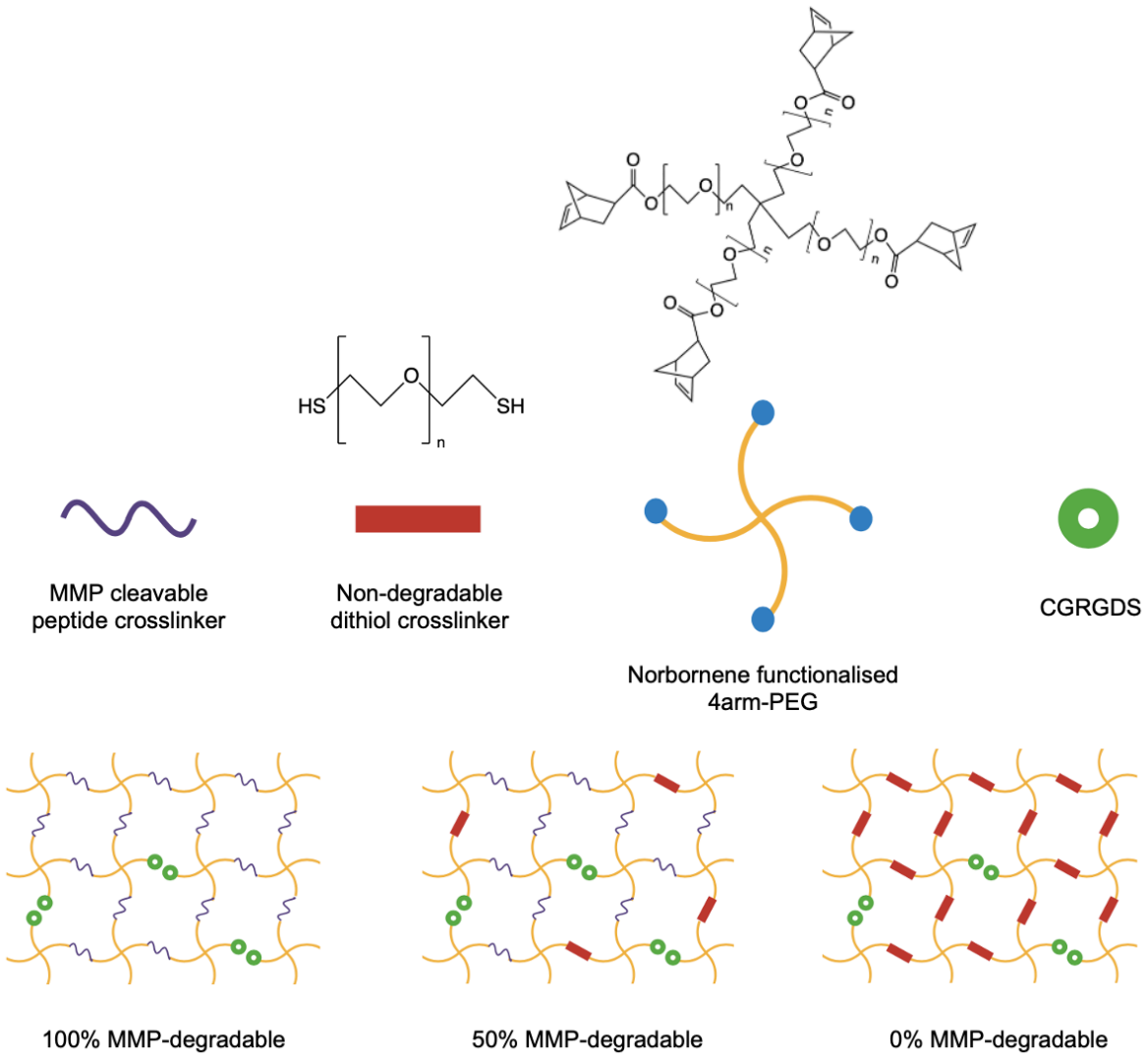


Figure 52. Scheme of thiol-ene hydrogels with variable degradability, created from controlling the proportions of a MMP cleavable peptide crosslinker and a non-degradable dithiol crosslinker in a norbornene functionalised 4arm-PEG polymer network with CGRGDS (a pendant fibronectin-binding sequence for cell adhesivity). Adapted from Anderson et al. (277). *Created on the BioRender website (https://biorender.com) by the author.*

The thiol-ene chemistry employed to synthesise these hydrogels permitted gel polymerisation that could be controlled spatially and temporally, occurring at a neutral pH in less than 2 minutes, with the ability to integrate bioactive peptides to promote osteogenic differentiation (277). By varying the levels of an MMP-degradable peptide crosslinker with a non-degradable PEG-dithiol crosslinker within the networks, the hydrogels had variable cell-

directed degradabilities: 100% cell-degradable (MMP-degradable peptide), 50% cell-degradable (both MMP-degradable peptide and non-degradable PEG-dithiol crosslinker), and 0% cell-degradable (non-degradable PEG-dithiol crosslinker). Encapsulation of hMSCs and culture in osteogenic media showed that cell survival was not impacted by the different degradability of the gels, with similar cell density observed between the formulations over a 14-day culture period (~600–1000 cells/mm^3) (277). ALP, a marker of osteogenic differentiation, was significantly higher in 100% cell-degradable hydrogels after 7 and 14 days of culture. Additionally, deposition of mineralised matrix, analysed by Alizarin Red S staining, occurred in all three hydrogel formulations after 14 and 21 days of culture (277). Poly(ethylene) glycol diacrylate (PEGDA) has been grafted onto silk fibroin (SF) molecules via native disulfides in silk, to form a PEGDA-biopolymer hydrogel, using a thiol-ene reaction (278). Prior low temperature treatment, consisting of refrigeration at 4 ^{o}C, increased the compressive modulus of the hydrogels from ~3 kPa to ~80 kPa after 2 minutes of irradiation (405 nm) and ~4 kPa to ~120 kPa after 3 minutes of irradiation (405 nm). An MTT assay demonstrated that after 24 hours of culturing human embryonic kidney (HEK) 293 cells, the cell viability was 102% and not significantly different from the blank, indicating the PEGDA-SF hydrogel was non-cytotoxic (278).

More recently, alkene or thiol-functionalised biopolymers have been developed (279–281). Holmes et al. (280) created collagen-PEG hydrogels via thiol-ene click chemistry by reacting thiol-functionalised collagen with PEG-norbornene. The type and concentration of photoinitiator impacted human osteosarcoma G292 cell viability following 24 hours of culture. Increasing photoinitiator concentration from 0.1% to 0.5% (w/v) led to a decrease in cell viability from 86 to 8% with LAP and 62 to 2% with Irgacure 2959 (I2959). Additionally, the use of LAP led to a significantly higher cell viability when compared to I2959. Gelation

kinetics were also impacted by photoinitiator choice as LAP-containing hydrogels reached gelation 8x faster (279 ± 11 seconds [0.1% w/v] and 187 ± 6 seconds [0.5% w/v]) than I2959-containing hydrogels (1496 ± 43 seconds [0.1% w/v] and 1683 ± 33 seconds [0.5% w/v]), regardless of photoinitiator concentration. Altering the PEG content within the hydrogels from 2% (w/v) to 4% (w/v) increased G' in curing time sweep measurements from 500 Pa to 4800 Pa and decreased swelling equilibrium time from 360 minutes to 10 minutes, demonstrating that it was possible to form hydrogels with tuneable mechanical and physical properties.

Ooi et al. (279) synthesised norbornene-functionalised alginate (AlgNb) to provide improved crosslinking control to the alginate-based hydrogel, something that is lacking in the native ionotropic crosslinking chemistry of alginate (279). By varying the stoichiometry of alginate and norbornene, the degree of functionalisation could be reproducibly controlled from 4 to 12%. A series of thiol-containing PEG chains of varying molecular weights (1500 and 5000) and number of arms (2 and 4) were used to crosslink the AlgNorb hydrogels. A higher concentration of crosslinker, longer PEG dithiol crosslinkers, and higher number of arms all led to an increased hydrogel modulus (279). This study demonstrates the tailorability of the mechanics of the hydrogel systems, which is important for tissue engineering as matrix elasticity plays a key role in directing cell behaviour (1). The integration of biopolymers within thiol-ene click chemistry hydrogels presents an attractive route for synthesising biologically active and mechanically tuneable hydrogels for tissue engineering purposes. The biopolymer gelatin has been the focus of this thesis and therefore, the following section discusses its current and potential use within thiol-ene reactions to form hydrogels.

4.1.1.5. Gelatin norbornene (GelNB) hydrogels formed via thiol-ene reaction

Gelatin hydrogels are a popular choice for biomedical applications for several reasons. Firstly, their innate advantageous biological properties; gelatin contains RGD motifs which help in cell adhesion, proliferation and differentiation (282). It is also possible to chemically modify gelatin via amino acid side groups. For example, it can be modified with additional side groups such as norbornene, to form GelNB, for use in a thiol-ene reaction.

Gelatin hydrogels produced from GelNB and crosslinked with thiol-containing molecules have received a lot of attention as potential replacements for GelMA. This is due to quick and controllable step-growth photopolymerisation (the reaction of two chemically different monomers), significantly lower reactive oxygen species (ROS) accumulation during the reaction and lower radical concentrations required for the photochemical initiation step (252,254,256,257,283–288). Lower cell toxicity is also associated with the use of GelNB instead of GelMA when cells are encapsulated within the solutions, as the methacrylate-based reaction involves a radical chain-growth mechanism which can increase intracellular oxidative stress, compared to step-growth polymerisation in GelNB which needs lower concentration of photoinitiator and generates fewer radicals (254,256,286).

Using different thiol and GelNB concentrations in the precursor solution, as well as crosslinker functionality, has been shown to vary the degree of crosslinking in GelNB hydrogels (256). Additionally, random chain-growth photopolymerisation and step-growth thiol-ene photopolymerisation are the crosslinking mechanisms in GelMA and GelNB (Figure 53), respectively, and the impact of the crosslinking mechanisms on hMSC viability and spreading have been demonstrated by Muñoz et al. (256). hMSC viability, analysed through LIVE/DEAD staining, was significantly higher in 4 wt% (~97%) and 8 wt% (~91%) GelNB

hydrogels, compared to their counterpart 4 wt% (~85%) and 8 wt% (80%) GelMA. Orthogonal, referring to the formation of crosslinks with 100% selectivity and no cross-reactivity, step-growth thiol-ene crosslinks in GelNB hydrogels promoted a faster and higher degree of cell spreading in GelNB hydrogels, shown by increased cell length, when compared to the random chain-growth of GelMA hydrogels (256,289). The decrease in hMSC viability and lower degree of cell spreading in chain-growth GelMA hydrogels could be a consequence of a higher initial radical concentration, which has elsewhere been demonstrated to cause a significant reduction in encapsulation protein activity (290). Additionally, the different polymerisation mechanisms and the resulting network nanostructure of the hydrogel could prevent cell spreading due to matrix constrictions; it is suggested that GelMA forms heterogeneous kinetic chains which could lead to a higher degree of chain entanglements, preventing cells from spreading within the network (256,291).

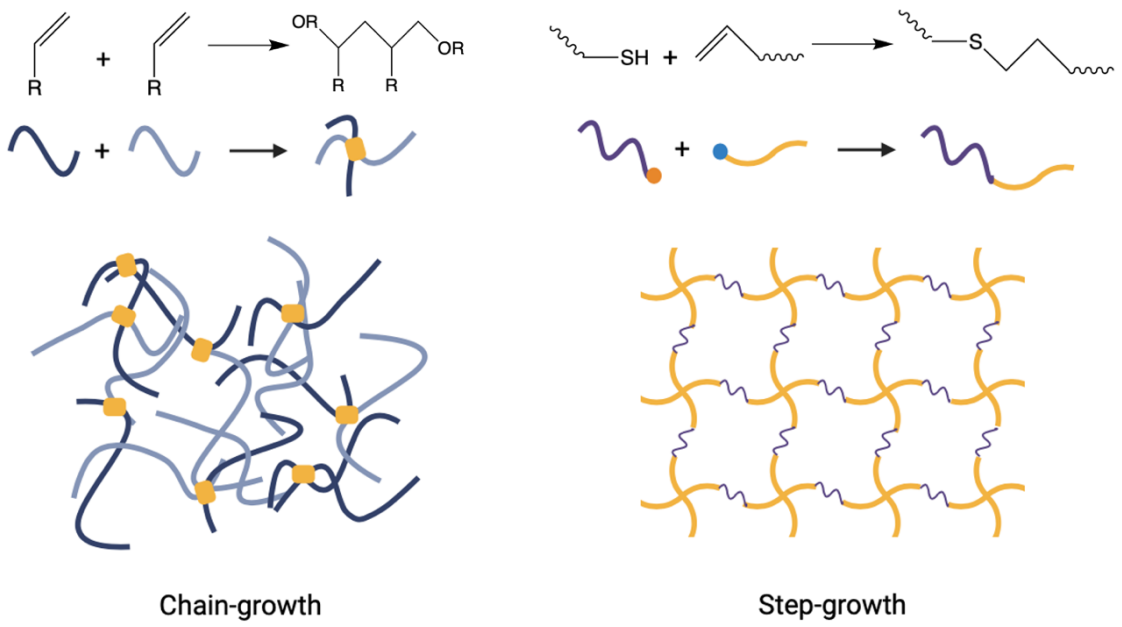


Figure 53. Light-mediated polymerisation, demonstrating random chain-growth based on methacrylate prepolymers, such as GelMA, and structurally uniform step-growth based on click reactions such as thiol-ene (PI = photoinitiator; UV = ultraviolet; Vis = visible light) (256). *Created on the BioRender website (https://biorender.com) by the author.*

Burchak et al. (254) investigated the reaction of GelNB with thiolated gelatin (GelSH) to produce hydrogels for 3D bioprinting. Using various crosslinking densities (low, medium and high) and by changing the equivalence of groups (norbornene and thiol) able to crosslink, hydrogels with varying elastic moduli from 206 Pa (low) to 1383 Pa (high) were produced. All hydrogel formulations supported the viability and proliferation of adipose-tissue derived mesenchymal stem cells (ASCs) to a similar ability. Regulating the hydrogels' mechanical properties influenced the differentiation fate of ASCs, as the elastic moduli in stiffer hydrogels directed ASC differentiation towards an osteogenic lineage (254). Photopolymerisation of the hydrogels took between 140–160 seconds, again demonstrating the benefit of the 'ultrafast' photocurable GelNB system (254). Notably, improved photocuring kinetics have been demonstrated in GelNB, compared to GelMA, due to thiol-ene chemistry exhibiting faster reaction kinetics compared to chain-growth polymerisation (271,276).

Wang et al. (292) selected the gelatin-based norbornene-thiol system due to the ability of the reaction to occur efficiently under light irradiation. The physical and biological properties of a GelNB hydrogel were altered by modifying GelNB with thiol-containing peptides that promote vascularisation and osteoinduction (angiogenic vascular endothelial growth factor (VEGF) and parathyroid hormone (PTH) 1−34). Dual-peptide-functionalised GelNB was fabricated via an *in situ* covalent functionalisation method by exposing a GelNB and thiol-containing peptide solution to blue light (420–480 nm). The ability to covalently include these active peptides within the hydrogel system via light irradiation led to an increase in *in vitro* and *in vivo* angiogenic and osteogenic processes (292). Arkenburg et al. (293) used GelNB as the backbone of numerous crosslinked hydrogels, with thiolated crosslinkers including PEG-thiol and thiolated HA. The resulting hydrogel maintained the biological

activity of gelatin but allowed for the creation of tuneable mechanical properties by adjusting the thiol crosslinker content. For example, the G' increased from ~1.5 to ~3.5 kPa when the crosslinker concentration was increased by 0.8 wt% (0.6 to 1.4 wt%). Varying the crosslinking density also modulated the behaviour of encapsulated induced pluripotent stem cells (iPSCs), as a higher concentration of crosslinker resulted in higher cell death, irregularity in cell size, and cell aggregation. These cell behaviours were attributed to the hydrogel matrix stiffness, from the high crosslinking density, being greater than the encapsulated iPSCs (293).

4.1.2. GelNB hydrogels formed via thiol-ene reaction for sol-gel processing

GelNB was selected in this study for its alkene functionality on the norbornene and the potential for a thiol-ene reaction (Figure 54).

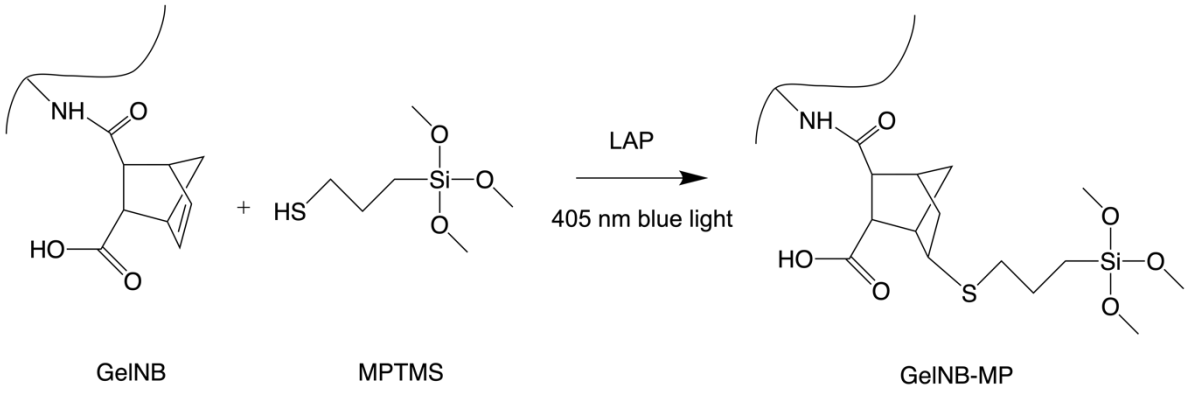


Figure 54. Scheme representation of the proposed thiol-ene reaction of GelNB and MPTMS.

When considering the requirements of the inorganic crosslinker used for GelNB functionalisation, dual functionality is necessary. One functionality must be the thiol for the thiol-ene reaction, and another functionality must provide a precursor to Si–OH groups for

inorganic polymerisation. Therefore, 3-mercaptopropyl trimethoxysilane (MPTMS) was selected, as this organosilane fulfils both requirements (Figure 54).

To our knowledge, this study is the first attempt to produce thiol-norbornene gelatin with the crosslinker MPTMS. Therefore, numerous reaction variables were investigated to optimise this new reaction. In the last few years, studies have focussed on crosslinking GelNB with dithiothreitol (DTT), a di-thiol, at various thiol/ene stoichiometric ratios – ranging from 1:1 to 1:4 (256,285,287). However, reports have shown full conversion at an equimolar thiol-ene ratio (284). Additionally, concentration of LAP has been studied, including 0.1%, 0.045%, 0.03% (w/v), as well as 2 mol% (252,254–257). Therefore, in this study, both thiol/ene stoichiometric ratio (GelNB:MPTMS) and photoinitiator concentration (LAP) were studied.

4.1.3. Aims and objectives

This chapter investigated the use of an alternative reaction to the traditional gelatin-GPTMS functionalisation reaction to synthesise an organosilane-functionalised gelatin-based material. To achieve this, click chemistry via a photoinitiated thiol-ene reaction was used, with focus on MPTMS (thiol) and GelNB (-ene). The effect of varying reaction conditions was investigated using ^{1}H NMR spectroscopy, and the subsequent hydrogels were characterised using mechanical testing and biological assays.

The main objectives of the chapter were to:

i. Develop a robust and efficient method to functionalise gelatin that overcomes the challenges posed in gelatin and GPTMS reactions (Chapter 3)
    a. Establish a protocol for a thiol-ene click chemistry-based reaction to functionalise GelNB with a thiol-containing organosilane crosslinker, MPTMS

b. Determine and optimise the thiol-ene reaction between GelNB and MPTMS

ii. Create organic-inorganic hybrid hydrogels with the functionalised GelNB as the organic component and silica as the inorganic component to result in enhanced mechanical properties and tailorable degradation

a. Test the degradation properties of the hybrid hydrogels to determine if the organosilane crosslinker in Class II GelNB hydrogels contributes to more controlled degradation compared to Class I hydrogels

b. Investigate the compressive mechanical properties of the hybrid hydrogels using uniaxial, constant cyclic and incremental cyclic testing

c. Examine the rheological properties of the hybrid hydrogels using a frequency sweep, amplitude sweep and single frequency sweep

d. Use cryogenic scanning electron microscopy (CryoSEM) to characterise the architectural properties of the hybrid hydrogels

iii. Examine the biological properties of the GelNB-silica-based hybrid hydrogels through 2D cell studies

a. Test the cell viability of the hybrid hydrogels using a LIVE/DEAD and PrestoBlue assay

b. Test the capacity of the hydrogels to promote cell spreading with actin and 4′,6-diamidino-2-phenylindole (DAPI) stain and mineralisation using Alizarin Red S

c. Measure the extent of cell migration within the hydrogel over time using light sheet fluorescence microscopy

4.2. Methods

MPTMS functionalised GelNB (GelNB-MP) was synthesised and chemically characterised and used to create three compositions of hydrogel. The three hydrogel compositions were examined for their mechanical and biological properties.

4.2.1. Materials used for functionalisation and hydrogel preparation

Norbornene-modified gelatin (GelNB) with 65% degree of substitution (DoS) was supplied by Claro™. Lithium phenyl-2,4,6-trimethylbenzoylphosphinate (LAP, ≥95%), 3-mercaptopropyl trimethoxysilane (MPTMS, 95%), dithiothreitol (DTT, =97%), Dulbecco's Modified Eagle Medium (DMEM; high glucose) and phosphate buffered saline (PBS) were all supplied by Sigma Aldrich UK. Deuterium oxide (D_2O, 99.9%) was supplied by Goss Scientific and degassed using a sonicating bath and argon source.

4.2.2. GelNB functionalisation preliminary study

GelNB was synthesised and supplied by Claro™, but in short, GelNB is synthesised by reacting gelatin with carbic anhydride at 50 ^oC (Figure 55a) (256). LAP (0.30 wt%, 15.0 mg) and GelNB (5.00 wt%, 250 mg) were measured into a glass vial. A magnetic stirrer was added and the top secured tightly with a septum. An argon atmosphere was created within the glass vial by inserting an argon fed needle through the septum, and an outlet needle. Using a syringe and needle, degassed D_2O (previously degassed for 10 minutes using a sonicator; 5.0 mL) was added to the glass vial through the septum. The glass vial was then covered in foil and placed in a 40 ^oC water bath and left for 10 minutes, stirring at 250 rpm.

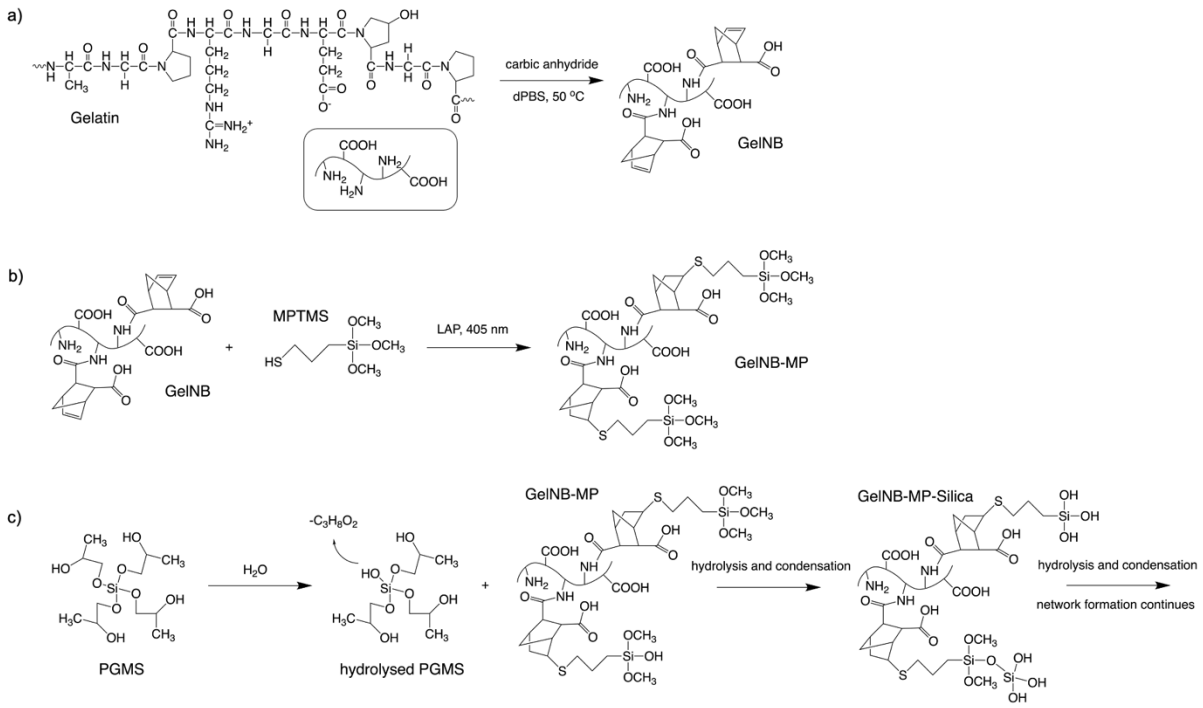


Figure 55. Schematic of a) GelNB synthesis, conducted by Claro™, b) thiol-ene reaction of GelNB with MPTMS to form GelNB-MP, c) GelNB-MP-Silica hybrid hydrogel synthesis through the condensation of Si–OH groups on the MPTMS of GelNB-MP with Si–OH groups on PGMS.

Using a Hamilton syringe, MPTMS (50 µl, 2.5 mmol) was added to the GelNB + LAP solution in a 1:4 ratio[2] (GelNB:MPTMS). The covered solution was stirred at 1000 rpm for 10 minutes at room temperature to generate a homogeneous solution. At this point a 300 µl aliquot was taken for ^{1}H NMR spectroscopic analysis. The uncovered solution was irradiated for 30 minutes, using 405 nm light (Form Cure, Formlabs; Figure 56). The thiol-ene reaction of GelNB with MPTMS to form GelNB-MP is shown in Figure 55b. Light irradiation was paused at 5, 15 and 30 minutes and aliquots (200 µl) were taken and added to D_2O (500 µl). The solution was then analysed by ^{1}H NMR spectroscopy. For control reactions see Appendix Section C.4.2.2.

[2] 1 (-ene): 4 (SH)

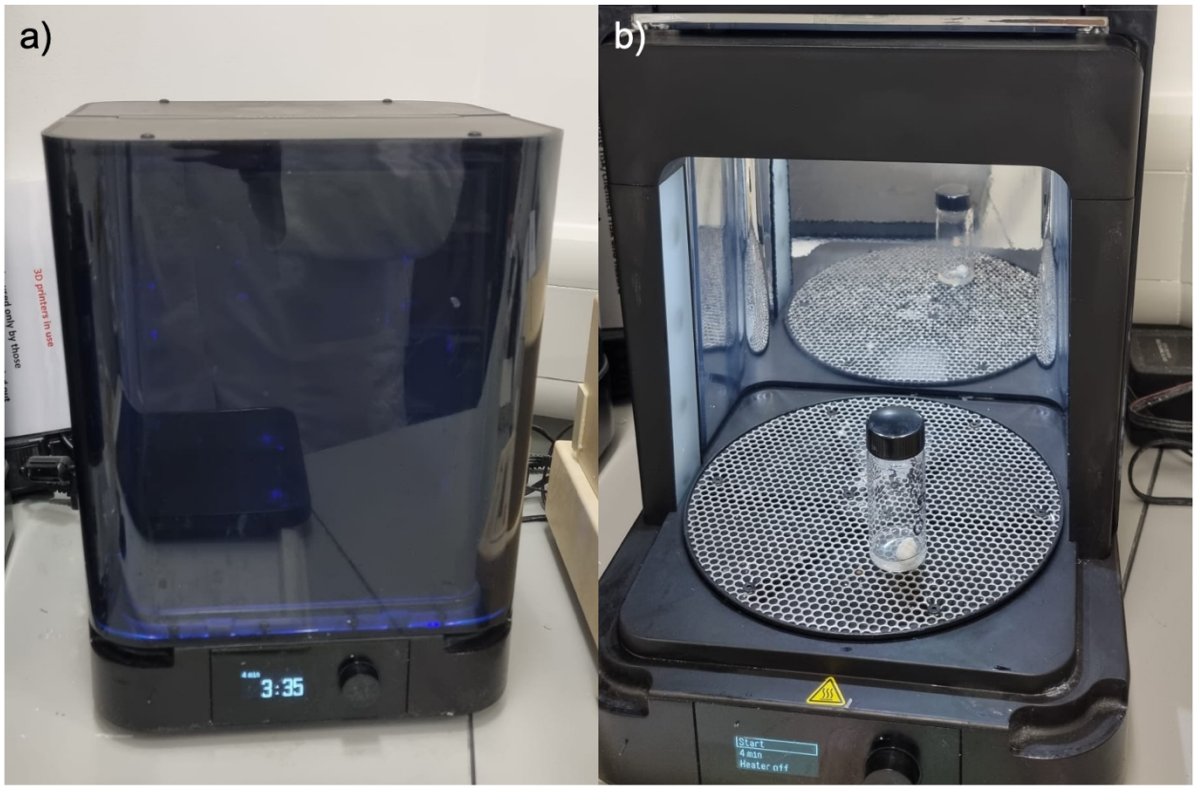


Figure 56. Form Cure set-up a) closed and b) open for 405 nm light irradiation of the GelNB-MPTMS solution.

5-Norb is an organic compound with a C=C, and thus, removes the complex resonances associated with the polymer structure that is seen in a GelNB ^{1}H NMR spectra (Figure 57). The same method as in Section 4.2.2 was followed but substituting GelNB for 5-Norb at the same 1:4 ratio.

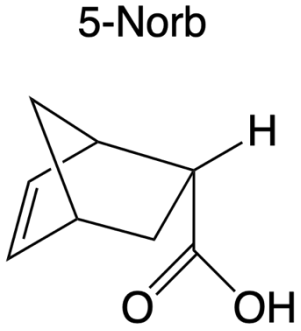


Figure 57. Chemical structure of 5-Norb.

4.2.3. GelNB functionalisation optimisation study

The following experiments were conducted in the sequence discussed, and once optimal conditions for each variable was identified, this condition was maintained throughout the remaining experiments.

4.2.3.1. Ene:thiol ratio

Preliminary GelNB and MPTMS functionalisation reactions were run at a 1:4 ene:thiol ratio. This ratio was calculated based on the amount of free NH_2 per 10 g gelatin being 3.8 mmol and the DoS of 65% for the GelNB (norbornene groups), meaning 2.47 mmol of norbornene was present in 10 g GelNB. The reaction of GelNB with DTT was investigated by varying the ratio of DTT to GelNB (Figure 58). This was done by following the same protocol as described in Section 4.2.2, but substituting MPTMS for DTT and mixing it with LAP (0.30 wt%, 15.0 mg) and GelNB (5.00 wt%, 250 mg) at the following ene:thiol ratios: 1.00:0.25 (DTT; 3.10 mg, 0.16 mmol), 1.00:0.5 (DTT; 6.20 mg, 0.31 mmol) and 1.00:1.00 (DTT; 12.4 mg, 0.62 mmol).

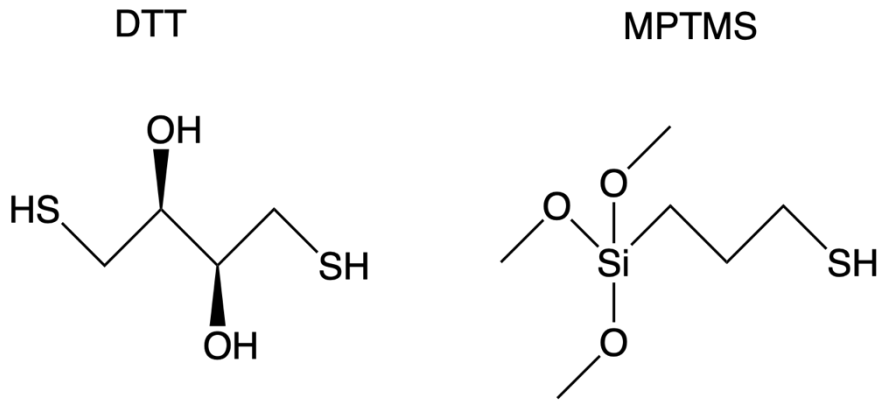


Figure 58. Chemical structure of DTT and (3-mercaptopropyl)trimethoxysilane (MPTMS).

The method was run as stated in Section 4.2.2, but 25 µl of MPTMS was added to achieve a 1:2 ratio of GelNB:MPTMS.

4.2.3.2. LAP concentration

LAP concentration was varied between 0.03 wt%, 0.15 wt% and 0.30 wt% within the GelNB-MPTMS (1:2) reaction.

4.2.3.3. Dialysis

Dialysis was carried out to remove the excess MPTMS and any side reaction by-products to confirm the thiol-ene reaction was successful via observing resonances for MPTMS within the ^{1}H NMR spectrum of the thiol-ene product. It was hypothesised that the intensity of resonances from MPTMS within the spectrum would decrease as unreacted MPTMS is removed via dialysis.

A GelNB functionalisation reaction was run as described in Section 4.2.2 using the following conditions: 1:2 (GelNB:MPTMS), 0.03 wt% LAP, and 405 nm irradiation for 4 min. MPTMS-functionalised GelNB (GelNB-MP) was placed inside dialysis tubing cellulose membrane (typical molecular weight cut-off = 14,000). The tube was placed in 40 ^{o}C dH_2O in a 250 mL beaker, gently stirring, and the dH_2O was replenished every 24 hours. Every 24 hours, a 500 µl aliquot was taken for ^{1}H NMR spectroscopic analysis to determine at which point dialysis was complete.

4.2.4. Fabrication of GelNB-Silica hydrogels

Hydrogels were fabricated using 5.00 wt% GelNB (with or without functionalisation) and PGMS as the silica source at an O:I weight ratio of 40:60. The two components were mixed

together with dH_2O and media (DMEM) to form the desired hydrogel formulations. Three formulations were produced: Class I GelNB-Silica, Class II GelNB-MP-Silica with a 1:1 DMEM:dH_2O ratio, and Class II GelNB-MP-Silica with a 1:2 DMEM:dH_2O ratio (Table 4). The DMEM-dH_2O solution was produced by mixing DMEM and dH_2O (pH 7.4) at either 1:1 or 1:2 volume ratio.

Table 4. Different hydrogel formulations developed, with varying GelNB source (GelNB or GelNB-MP) and DMEM:dH_2O content.

Formulation	GelNB source	GelNB concentration (wt%)	LAP concentration (wt%)	Silica source	GelNB:silica (Organic:inorganic)	DMEM: dH_2O
GelNB-Silica	GelNB	5.00	-	PGMS	40:60	1:1
GelNB-MP-Silica (1:1)	GelNB-MP	5.00	0.03	PGMS	40:60	1:1
GelNB-MP-Silica (1:2)	GelNB-MP	5.00	0.03	PGMS	40:60	1:2

4.2.4.1. Fabrication of Class I GelNB-Silica hydrogels

A 5 wt% GelNB solution was made by dissolving GelNB (500 mg, 0.13 mmol) in dH_2O (pH = 7.4) (10.0 mL). The solution was stirred at 250 rpm for 1 hour, at 40 ^oC. PGMS (0.42 g) was added to a 1:1 DMEM-dH_2O solution (1.60 mL) and the mixture vortexed for 15 seconds. The solution was left to go transparent (~15 seconds), at which point, GelNB solution (1.0 mL) was added continuously dropwise to the PGMS solution, whilst being vortexed (Figure 59). This solution was then poured into moulds and allowed to gel. Hydrogels were moulded dependent on the characterisation technique to be performed.

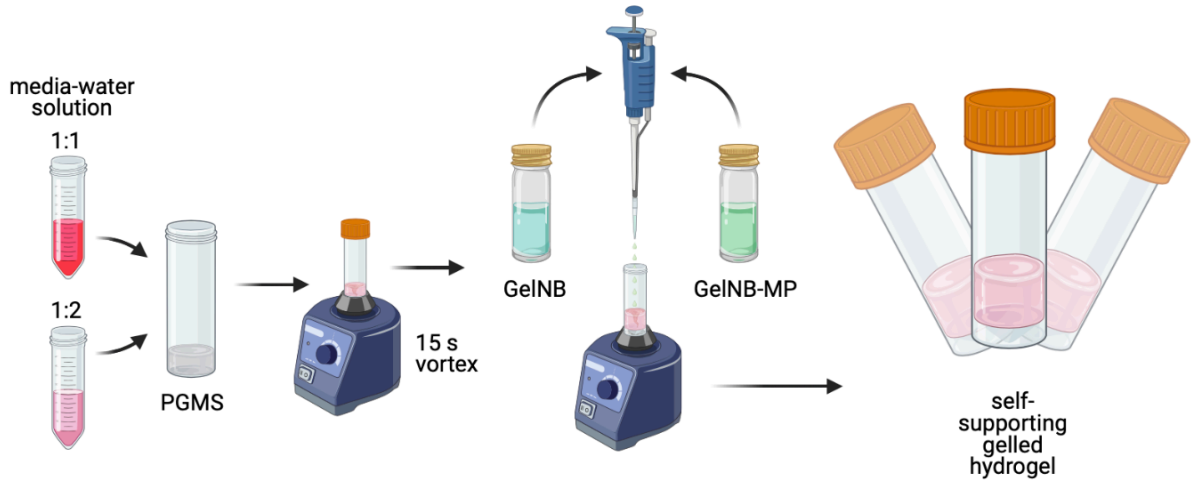


Figure 59. Schematic diagram of the hydrogel preparation and manufacturing methods, involving the mixture of DMEM-dH_2O solution (1:1 or 1:2) with PGMS and vortexing for 15 seconds. GelNB-based solution was then added to the PGMS solution and left to gel and form a self-supporting hydrogel (s= seconds). Created on the BioRender website (https://biorender.com) by the author.

4.2.4.2. Fabrication of Class II GelNB-MP-Silica hydrogels

For the Class II hybrids, the same protocol was followed as in Section 4.2.4.1, however, GelNB-MP was used instead of GelNB to form a Class II 1:1 formulation (GelNB-MP-Silica [1:1]). Additionally, a 1:2 DMEM-dH_2O solution was used to form a Class II 1:2 formulation (GelNB-MP-Silica [1:2]) (Figure 59). The schematic of the overall reaction of GelNB-MP with PGMS is shown in Figure 55c.

4.2.5. Hydrogel degradation properties

4.2.5.1. Hydrogel preparation

For the degradation samples, 1.6 mL of hydrogel solution was cast into 24 well plates and left to age (Figure 60). Gel ageing here refers to the length of time the hydrogels were left to undergo gelation.

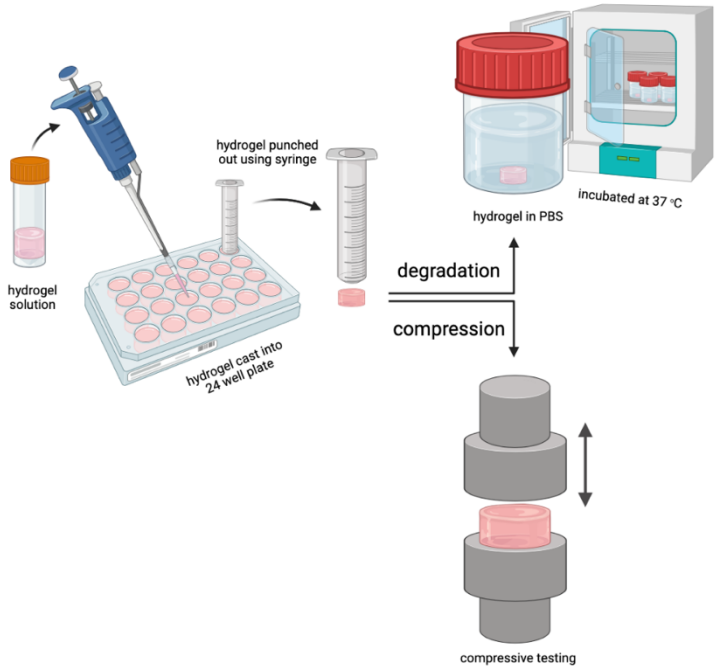


Figure 60. Schematic diagram of hydrogel preparation for degradation assay and compression tests. Created on the BioRender website (https://biorender.com) by the author.

Three well repeats were cast for each hydrogel formulation, as well as each ageing condition (1 day vs 7 days). When the appropriate ageing time was reached, hydrogel cylinders were stamped out of the well plates using a 5 ml syringe with the tip cut off (Figure 60). All hydrogel samples were weighed, and the mass noted. The hydrogels were submerged in either PBS with or without collagenase (25 u/mL) for the degradation assay.

PBS, both with and without collagenase, was pre-heated in an incubator to 37 ºC and then added to 50 ml containers. To calculate the volume to add, a ratio of 1.5 g:50 mL (hydrogel:PBS) was achieved, with the volume of PBS altered dependent on the mass of the hydrogel sample. The pH of the PBS, with and without collagenase, was recorded.

4.2.5.2. Degradation assay

The degradation assay, including ICP-OES, was run as stated in Section 2.4.5. Additionally, a bicinchoninic acid (BCA) assay was run to quantify gelatin release.

4.2.5.3. BCA assay

A BCA assay is used for colorimetric detection and quantitation of total protein. It is used to quantify gelatin release from the hydrogels as a consequence of degradation over the duration of the experiment (184,190,294). A Pierce™ Rapid Gold BCA Protein Assay Kit (ThermoFisher) was used for the BCA assay. Albumin (BSA) standards were prepared from 2 mg/mL albumin at the following concentrations: 0 (blank), 25, 125, 250, 500, 750, 1,000, 1,500, and 2,000 µg/mL using PBS as the diluent.

Next, 20 µl of each BSA standard (triplicates) and 20 µl of unknown (degradation) samples (triplicates) were transferred via pipette into a 96 well plate. Using a multi-channel pipette, 200 µl of working reagent (WR) was added to the well plate. The well plate was placed on a plate shaker for 30 seconds, followed by 5 minutes at room temperature. Using a microplate reader (Spark® Tecan), absorbance was read at 480 nm. The mean blank value was subtracted from the respective experimental and standard plate readings. A standard curve was produced from the BSA standards and the concentration of 'gelatin' release calculated.

4.2.6. Mechanical characterisation – compressive properties of hybrid hydrogels

Hydrogel preparation

For compression testing, 1.6 mL of hydrogel solution was cast into individual wells in a 24 well plate and left to gel. Five repeats were used for each ageing condition: 1, 3, 7, and 14 days. When the appropriate ageing time was reached, hydrogel cylinders were removed from

the well plates using a 5 ml syringe with the tip cut off (Figure 60). The diameter of the syringe was noted, as well as the height of the hydrogel sample.

4.2.6.1. Uniaxial compression testing

Uniaxial compression testing was performed on cylindrical samples approx. 10 mm (h) x 12 mm (d) in air, using a 0.1 mm/s strain rate and 250 N load cell with 2.04 mV/V sensitivity (MTS Criterion, Model 42).

At least three independent measurements were taken for statistical significance, and in some cases up to five, providing the hydrogels did not break during sample extraction. Crosshead (mm) position was converted to strain (ε) (Eq. 2) and load (N) was converted to stress (Pa) (Eq. 3).

$$strain\ (\varepsilon) = \frac{crosshead\ travel\ (mm)}{initial\ height\ of\ hydrogel\ sample\ (mm)} \qquad \text{(Equation 2)}$$

$$stress\ (Pa) = \frac{load\ (N)}{surface\ area\ of\ hydrogel\ sample\ (mm^2)} \qquad \text{(Equation 3)}$$

Stress-strain curves

Stress-strain curves were plotted for each individual repeat, removing the initial lag phase. From each stress-strain curve repeat, the yield stress, Young's modulus and toughness (AUC; area under curve) were determined as described below. The stress-strain repeats were then averaged to plot one stress-strain curve per hydrogel and condition.

Yield stress

Yield stress was calculated using the stress strain data in the elastic region with the =max function on Excel to determine the highest point on the stress-strain curve before the yield point – the point at which elastic deformation of a material ends and plastic deformation begins (Figure 61). Yield stress values were calculated for all repeats and averaged.

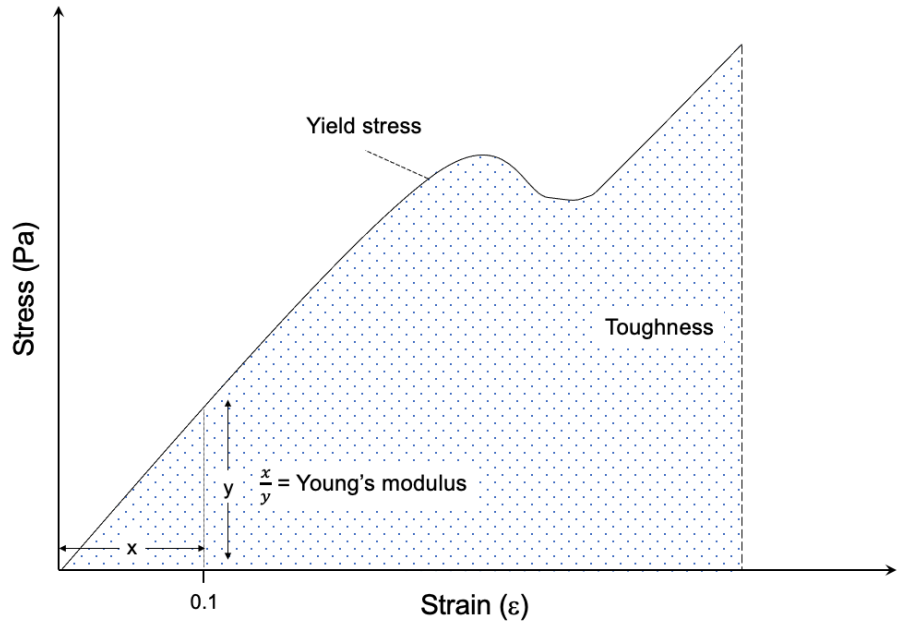


Figure 61. Example stress strain curve with the following shown: yield stress; the point at which elastic deformation of a material ends and plastic deformation begins, Young's modulus; stiffness calculated from two points in the linear region at zero tangent, and toughness; the area under the stress strain curve.

Young's modulus

Using the data from compression testing, the Young's modulus of the hydrogels was calculated using an approach which was developed for silica hydrogels by Krupa et al. (295), and thus, is applicable here. On each independent stress-strain curve, the gradient was calculated from two selected points in the linear region at low deformation; a tangent at zero

deformation was used, and so, relative deformation was ε<0.1 (Figure 61). Using the following equation (Eq. 4), where σ is stress and ε is strain, modulus was determined:

$$E = \frac{\sigma}{\varepsilon} \qquad \text{(Equation 4)}$$

Toughness

Toughness was calculated by determining the AUC; this was computed from the stress strain curves by calculating the area under each individual trapezoid under the curve (296). The sum of these values was then calculated. The AUC values of each hydrogel repeat were averaged for each formulation and time point (Figure 61).

4.2.6.2. Cyclic compression testing

The following cyclic compression testing of hydrogels aged for 7 days was conducted by undergraduate Georgios Mikalef, under supervision from the author.

Constant cyclic compression testing:

Constant cyclic compressive testing was performed using a Bose ElectroForce 5500 Test Instrument equipped with a 200 N load cell (Bose, United States). Before beginning the test, the height and diameter of the cylindrical hydrogel sample was measured using a Vernier calliper. The machine was programmed to compress the hydrogel sample to 20% of original height for 20 cycles. The hydrogel sample was placed on the stage and the test started, using a strain rate of 0.1 s^{-1} at a frequency of 0.1 s^{-1}. The following parameters were enforced on the Bose testing software: maximum force exertion limit of 1.67 N, scan time: 900, scan points: 1000, and number of scans: 1.

Incremental cyclic compression testing:

For incremental compressive testing Bose ElectroForce 5500 Test Instrument (Bose, United States) was used. The height and diameter of the hydrogel samples were measured using a Vernier calliper and used to calculate the displacements during each increment. The machine was programmed so that samples were compressed at incremental stresses as a percentage of the hydrogel sample height using 2% increments, starting at 5% of the hydrogel height, up to 45%, at a strain rate of 0.1 s^{-1}.

4.2.7. Rheological properties of hybrid hydrogels

Hydrogel preparation, frequency sweep shear strain controlled and amplitude sweep strain controlled of hydrogels aged for 7 days were conducted by undergraduate Georgios Mikalef, under supervision from the author. Three independent samples (n=3) were tested for statistical significance, however, the number of samples for GelNB-MP-Silica (1:2) aged for 1 day was 2 as samples broke during extraction. The mean of the repeat runs was calculated.

Hydrogel preparation – gelled state

For rheology, acrylic moulds were used to create shallow cylinders for the rheometer geometry (Figure 62). Transparent polyester sheets were coated with cling film, and then the polymer moulds were attached using a Vaseline grease to create a seal between the mould and cling film. Then, 3.2 mL of hydrogel solution was pipetted into polymer moulds and left to gel. This formed hydrogel with 40 mm (d) x 1.5 mm (h) which could be directly placed on the rheometer.

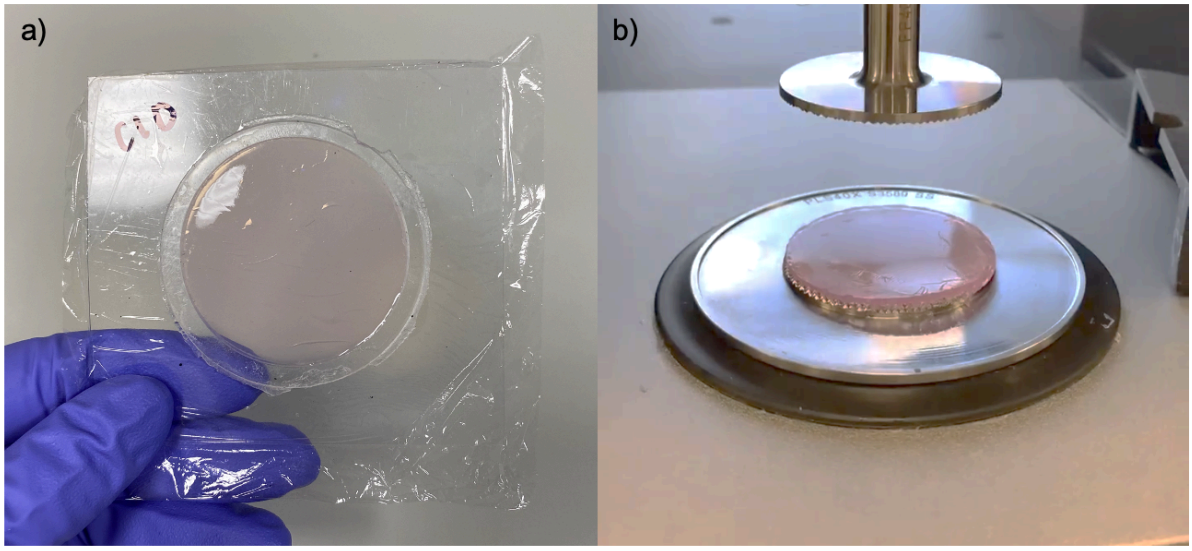


Figure 62. a) hydrogel sample preparation in acrylic moulds and b) extracted onto a rheometer plate for rheological testing.

Rheometer settings

A parallel plate (40 mm diameter, 1.5 mm gap) oscillation rheometer (Kinexus DSR-III Rheometer Bundle) was used to measure the viscoelastic properties of the gelled and liquid hydrogels. The temperature of the plates was fixed at 25 ºC.

4.2.7.1. Frequency sweep shear strain controlled

Frequency sweeps were first performed, selecting a predicted strain (%) within the linear viscoelastic (LVE) region, with sweeps performed without plastically deforming the samples. The cylindrical mould was loaded onto the bottom parallel plate and the frequency sweep was performed at a constant deformation of 0.5% strain and frequency sweep from 100 to 0.1 Hz, taking 5 samples/decade. A frequency sweep determines the storage modulus (G') and loss modulus (G").

4.2.7.2. Amplitude sweep strain controlled

After the frequency sweep, amplitude sweep strain tests were performed on the same samples. Measurements were taken from 0.01% to 100% strain at a constant frequency of 1 Hz, taking 5 samples/decade.

4.2.7.3. Constant frequency and strain time sweeps – gel point

To determine the gel point for the hybrid hydrogels, a single frequency strain sweep was performed. Hybrid preparation followed Section 4.2.4, mixing the PGMS and DMEM-dH_2O solution outside of the rheometer. When both organic and inorganic solutions were vortexed, a stopwatch was started. After 15 seconds, 2 mL of hydrogel solution was pipetted onto the parallel plate. The time at which the test began was noted, so that the mixing and transfer time could be included within the test time to ascertain the time to gel formation.

4.2.8. Structural characterisation

4.2.8.1. CryoSEM

CryoSEM (Cryo: Quorumtech-Cryo stage PP3010; SEM: FEI-FIB Quanta 3D) was used to image hydrogels, including GelNB-DTT, PGMS-derived silica gels and the three hybrid hydrogel formulations aged for 1 day and 7 days. Gelled GelNB aged for 1 day was created following the protocol in Section 4.2.3.1, using DTT as the thiol-containing molecule at 1:1 molar ratio of ene:thiol. Silica made from hydrolysed and condensed PGMS aged for 1 day was made by following the GelNB-Silica protocol in Section 4.2.4, but only using DMEM-dH_2O and no GelNB. Hydrogel formulations were made as described in Section 4.2.4.

Each material was plunged into liquid nitrogen to rapidly freeze the sample (called cryofixation) before imaging. Cryofixation is performed to preserve the sample structure and

minimise ice crystal formation. The sample was quickly transferred to the cryoSEM chamber, where it was put under vacuum to maintain its frozen state and a knife fixed within the chamber was used to cut the tip off the sample to create a fracture point to image. The chamber was cooled to cryogenic temperatures of around –150 ºC. Different times for removing vitrified ice on, or within, the sample was investigated using 30 seconds, 1-, 2- or 6-minute sublimation time. The images were taken at ~4.0 mm WD and 5.00 kV accelerating voltage.

4.2.9. Biological characterisation

4.2.9.1. Hydrogel preparation and cell seeding

Samples were prepared as explained in Section 4.2.4, only using 30 µl of hydrogel solution per well in a 96 well plate, with 4 repeats per condition. The well plate was organised as demonstrated in Figure 63, with the conditions in the centre of the plate to avoid evaporation issues associated with seeding around the edge of the plate. PBS was added to all empty wells to help with evaporation.

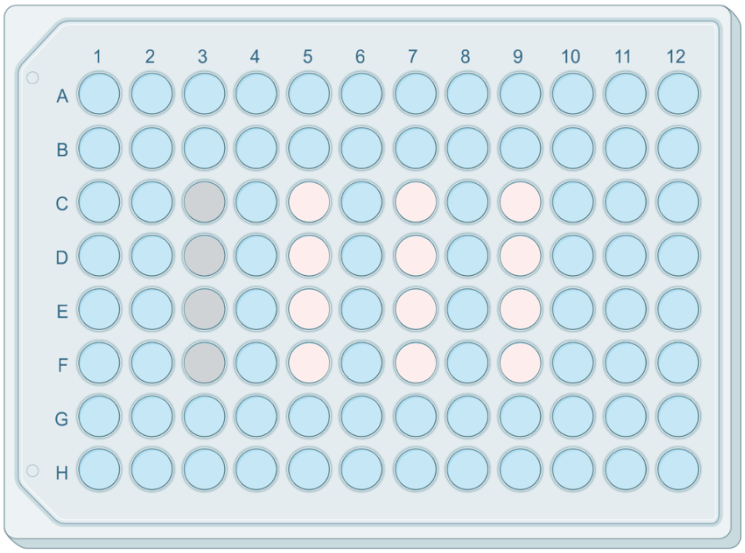


Figure 63. 96 well plate layout for cell culture experiments; 3CDEF – control (represented as grey), 5CDEF – GelNB-Silica, 7CDEF – GelNB-MP-Silica (1:1), and 9CDEF – GelNB-MP-Silica (1:2). All other wells were filled with PBS to help with evaporation. Created on the BioRender website (https://biorender.com) by the author.

The hydrogels were aged for 1 day and covered with the well plate lid, at room temperature. After 1 day the hydrogels were sterilised using UV irradiation (UV Crosslinkers, CL-508, Thistle Scientific, UK) for 1 hour prior to seeding. Sarcoma osteogenic (Saos-2) cells were seeded at 2.5 x 10^3 in 200 µl for all plates and cultured in McCoys 5A Medium modified with L-glutamine and sodium bicarbonate ($NaHCO_3$) (Sigma Aldrich) supplemented with 10% fetal bovine serum (FBS) and 1% penicillin/streptomycin.

4.2.9.2. Cell viability

LIVE/DEAD assay

The LIVE/DEAD assay was conducted by undergraduate Sophie Birch, under supervision from the author. Saos-2 cell viability was determined by performing a LIVE/DEAD assay at 1, 3, 5 and 7 days. The LIVE/DEAD viability/cytotoxicity kit (Fisher Scientific, UK) was allowed to reach room temperature (20–22 ºC) before using it. After removing the media

from the 96 well plate, 200 µl of Dulbecco's phosphate-buffered saline (dPBS) was used to wash the samples. The LIVE/DEAD staining was prepared using 4 mL of dPBS, 8 µl of calcein-AM and 8 µl of ethidium homodimer-1, and the mixture vortexed for 3 seconds. It was immediately applied (200 µl) to the hydrogels and incubated for 30 min. Saos-2 cell viability and spreading on the hydrogels was visualised by a confocal microscope (Zeiss LSM 700) at 10x objective, using 494/517 nm (excitation/emission [calcein; live]) and 528/617 nm excitation/emission [ethidium homodimer-1; dead]). Ten images were taken per technical repeat.

Cell viability (%) was calculated using ImageJ (version 1.53t) [n = 3] by counting the green and red cells in an image and adding the number of both together to obtain a total cell count, and then dividing the live cell count by the total cell count and multiplying by 100. This was repeated for the other 9 images, and an average cell viability calculated. This was repeated for biological repeats, averaging the final values.

PrestoBlue assay

A PrestoBlue assay was performed on 1-, 4-, 7- and 14-day cultured Saos-2 cells to assess cell viability. The assay was also performed on hydrogel blanks and a calibration plate including the following cell seeding density: 1.0×10^3, 2.5×10^3, 5.0×10^3, 10×10^3, 25×10^3, 50×10^3, and 100×10^3.

For the assay, a 10% PrestoBlue cell viability reagent (Thermo Fisher Scientific, UK) was made by mixing PrestoBlue with HBSS [Hanks Balanced Salt Solution, modified with $NaHCO_3$, without phenol red, Sigma, UK], and placed in an incubator at 37 ^oC for 30

minutes. After the cell culture media was removed from the well plates, the hydrogels were washed with dPBS and 200 µl of the 10% PrestoBlue was added.

Fluorescence of the PrestoBlue reagent from the experimental, calibration, and blank well plates was measured 2 hours after using a microplate reader (Spark® Tecan) at 560/590 nm (excitation/emission). Additionally, measurements were continued for the calibration plate for 3 hours and 4 hours. The mean blank value was subtracted from the respective experimental plate readings to determine the true cell viability fluorescence value.

4.2.9.3. Cell morphology and matrix deposition

For the following biological characterisation methods, cells were cultured for 14 days and fixed as follows: all media was removed from the well plates, and the hydrogels were washed with dPBS. Next, 100 µl of 3.7% paraformaldehyde (PFA) in PBS was added to each well and the hydrogels were left to fix at room temperature for 15 minutes. PFA was removed and hydrogels and cells washed with dPBS prior to the addition of 200 µl of dPBS for storage at 2–4 ^{o}C. Cell-free blanks of all hydrogels followed the same protocol.

Alizarin Red staining

Fixed Saos-2 cells were stained with Alizarin Red S solution to observe extracellular calcium deposition. A 1% (w/v) Alizarin Red S (Sigma, UK) staining solution was created using dH_2O and was then filtered using filter paper (0.45 µm pore). The dPBS was removed from the wells using a pipette and thoroughly rinsed with dH_2O. Each well received 100 µl of the Alizarin Red staining solution before being left at room temperature for 30 minutes. This was repeated on a plate of blanks. The stain was removed after 30 minutes, and the plate received two washes with dH_2O.

Calcium deposition was imaged using a fluorescent microscope (Nikon ECLIPSE TE300) at 10x magnification for qualitative analysis. After imaging, de-staining solution (200 µl), composed of 20% MeOH and 10% acetic acid in dH_2O was added to stained wells and left at room temperature for 30 minutes, agitating the samples periodically to ensure stain removal. Absorbance of the experimental and blank was measured at 405 nm using a microplate reader (Spark® Tecan). The mean blank value was subtracted from the respective experimental plate readings. Following readings, the de-staining solution was discarded, and the wells were rinsed thoroughly with dH_2O.

Actin and nuclei staining

An actin and nuclei staining was performed using Phalloidin (Green - cytoplasm) and DAPI (Blue - nucleus) to evaluate the structure of the cytoskeleton. Well plates were cleared of dPBS using a pipette and to permeabilise cells, 100 µl of 0.5% Triton X-100 solution prepared in dPBS was added. This was removed after 30 minutes at room temperature. The wells were rinsed with dPBS and a drop of actin stain (ActinGreen 488, Thermo Fisher, UK) was added. After 20 minutes at room temperature, the wells were again washed with dPBS to ensure removal of the excess actin stain. Cell nuclei were then stained with DAPI reagent (Abcam, UK) and left at room temperature for 10 minutes. After, the wells were washed with dPBS to remove excess stain. Additional dPBS was added for imaging. Wells were imaged using a confocal microscope (Zeiss LSM 700, Germany) using a 20x objective. The following excitation/emission values were used; 495/518 nm (actin) and 358/461 nm (DAPI).

4.2.10. Cell location

Light sheet fluorescence microscopy was performed by Dr Robert Lees with supervision from Dr Gowsihan Poologasundarampillai, at the Central Laser Facility (CLF), Rutherford

Appleton Laboratory, Harwell Science and Innovation Campus. Data processing was conducted by Dr Benjamin Davis, also part of the CLF, Rutherford Appleton Laboratory, Harwell Science and Innovation Campus.

4.2.10.1. Light sheet fluorescence microscopy

To determine cell migration, light sheet fluorescence microscopy was used to image cells within the hydrogel after 7 days. Samples were prepared in agar poured into a culture dish (35 mm) and left to set. Once set, sections of agar were removed from the centre of the culture dish to the base of the culture dish, to make a well approximately 10 mm (l) x 3 mm (w). Hydrogel solutions were made as in Section 4.2.4 and were cast into the well in the culture dish (Figure 64).

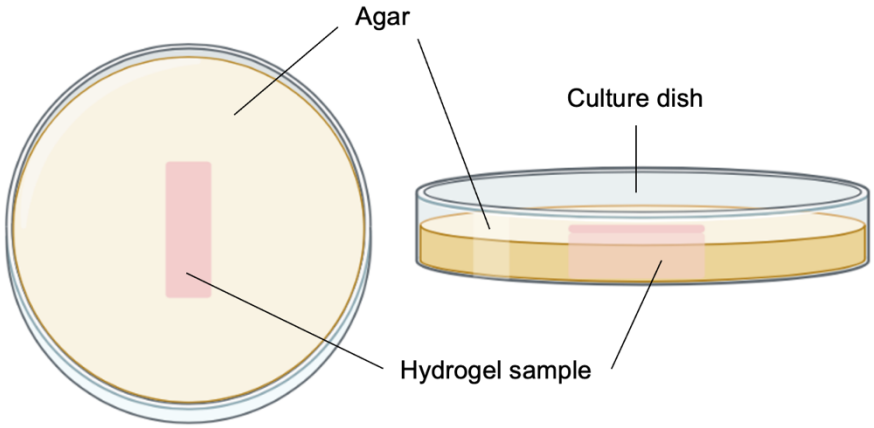


Figure 64. Culture dish filled with agar, with a cuboid hydrogel sample in a middle well. Created on the BioRender website (https://biorender.com) by the author.

The hydrogels were left to age for 1 day, after which time they were sterilised using UV irradiation (UV Crosslinkers, CL-508, Thistle Scientific, UK) for 1 hour prior to seeding. Saos-2 cells were seeded at the same seeding density per volume used in Section 4.2.9 (2.5 x 10^3 / 200 µl) for all hydrogels. Cells were cultured on the surface of the hydrogels for 7 days,

changing the McCoys media every 48 hours. At 7 days, the cells were fixed with PFA as stated in 4.2.9.3 and Alexa Fluor™ 647 Phalloidin staining was performed by Dr Sam Moxon, University of Birmingham as described in Section 4.2.9.3.

Hydrogels were then cut out of the culture dishes in small rectangular sections, with some agar still surrounding the hydrogel. The hydrogel was clamped in the sample holder spoon and immersed in PBS inside the sample chamber. The samples were imaged using the Cleared Tissue LightSheet (CTLS) from Intelligent Imaging Innovations, using a scanned light sheet, at Harwell Science and Innovation Campus. The air illumination objective used to create the light sheet was 5x/0.14 numerical aperture (NA) and a 1.5x/0.37 NA air detection objective was used to image the sample on to a Hamamatsu Flash 4.0 camera, with a 4.33x optical zoom.

For Alexa Fluor 647™, the 640 nm laser line was used for illumination (at ~150 mW at the laser head). The final step size for the full resolution raw data was 10 µm and the lateral pixel size was 1 µm/pixel. Z-stacks sizes (1–3 mm) were varied to fit regions until cells were no longer visible. Stitching was carried out using the SlideBook software (version 6.0) that controls the microscope, using zero shifts (i.e. merging based on stage position alone).

Using ImageJ (version 1.53t), 3D cell positions were extracted from the hydrogels. The ImageJ Macro ‘Cell_extraction_macro.ijm’ was used to isolate cells. A masked manual pre-evaluation of the datasets by two independent observers was carried out which recognised the existence of two populations of objects in the hydrogels that were distinguishable by eye, and therefore, were evaluated independently. These two objects were termed 'cells' and non-cell 'particles'. The particles were agreed to be substantially larger and rounder than cells based on

prior knowledge of the cell type under investigation (297). Using this information, cells were separated from ‘particle’ data based on Area (<200 μm) and Circularity (>0.7) criteria. This was completed prior to subsequent consideration of the spatial distribution of cell objects in advance of dataset analysis and the same thresholds were applied to all datasets.

4.2.11. Statistical analysis

GraphPad Prism (version 10.2.0 [335]) was used for statistical analysis of all experimental data. Prior to the statistical tests, normality tests were run to determine if the data was parametric or non-parametric. Consequently, a t-test, one-way analysis of variance (ANOVA), or two-way ANOVA was used if the data was parametric, whereas an ANOVA followed by a Tukey post-hoc test was run for non-parametric data.

4.3. Results and discussion

The results present the journey taken to form GelNB-silica hybrid hydrogels for application within bone tissue engineering. Firstly, reaction parameters and conditions were established for a thiol-ene click reaction to functionalise GelNB with MPTMS. The product was characterised using ^{1}H NMR spectroscopy. GelNB in both unfunctionalised (Class I) and functionalised (Class II) form was then combined with a silica-precursor, PGMS, to form hybrid hydrogels, which were tested to assess their mechanical, structural, and biological properties.

4.3.1. GelNB functionalisation preliminary study

The use of a thiol-ene reaction to crosslink GelNB using small-molecule thiols has previously been shown feasible by Göckler et al. (286), Mũnoz et al. (256), Zhao et al. (257), Yao et al. (255), and Perera et al. (283). In this study, it was necessary to deploy a functionalised thiol with an organosilane to enable crosslinking with silica. GelNB was reacted with MPTMS, a thiol-containing organosilane crosslinker, and the reaction was monitored using ^{1}H NMR spectroscopic analysis.

4.3.1.1. GelNB and MPTMS ^{1}H NMR spectra

It was expected that a thiol-ene reaction would occur when MPTMS (thiol-) and GelNB (-ene) were irradiated with blue light. Therefore, the signal of interest within the GelNB ^{1}H NMR spectrum was δ_H = 6.15 ppm as this has previously been assigned to the alkene (C=C) within NB (257,298). It would be expected that the intensity of this signal would decrease as the alkene is consumed within the thiol-ene reaction. To identify the alkene (C=C) in GelNB, a ^{1}H NMR spectrum was obtained and the singlet resonance at δ_H = 6.15 ppm was attributed to the two alkene protons of norbornene (resonance a, Figure 65) (245). Addition of a thiol to

this alkene, to form a thioether bond, would result in a new signal for the sulfide (CH-S) appearing between δ_H = 2.25–2.70 ppm within the ^{1}H NMR spectrum of the functionalised GelNB (GelNB-MP) product (299–301).

4.3.1.2. GelNB functionalisation with MPTMS

The GelNB-MPTMS reaction was photoinitiated using 405 nm (Form Cure, FormLabs) irradiation for 30 minutes, at a 1:4 ratio (ene:thiol), and aliquotes were taken for analysis by ^{1}H NMR spectroscopy at 5, 15 and 30 minutes. Preliminary results showed consumption of the norbornene double bond proton resonance at δ_H = 6.15 ppm within 5 minutes of irradiation, suggesting the reaction was complete at a point within this range (Figure 65). Reduction in the relative integration of the alkene proton resonance in a norbornene-thiol reaction has been shown by Nguyen et al. (302), specifically focussing on different ene:thiol ratios, showing a linear relationship between thiol-norbornene ratio and norbornene consumption. Additionally, in Figure 65, a new resonance was observed at δ_H = 2.70 ppm by 10 seconds, assigned to the protons in the new bond created upon thiol-ene conjugation and formed in concordance with the consumption of the alkene. This resonance is attributed to the CH proton attached to the thioether (300).

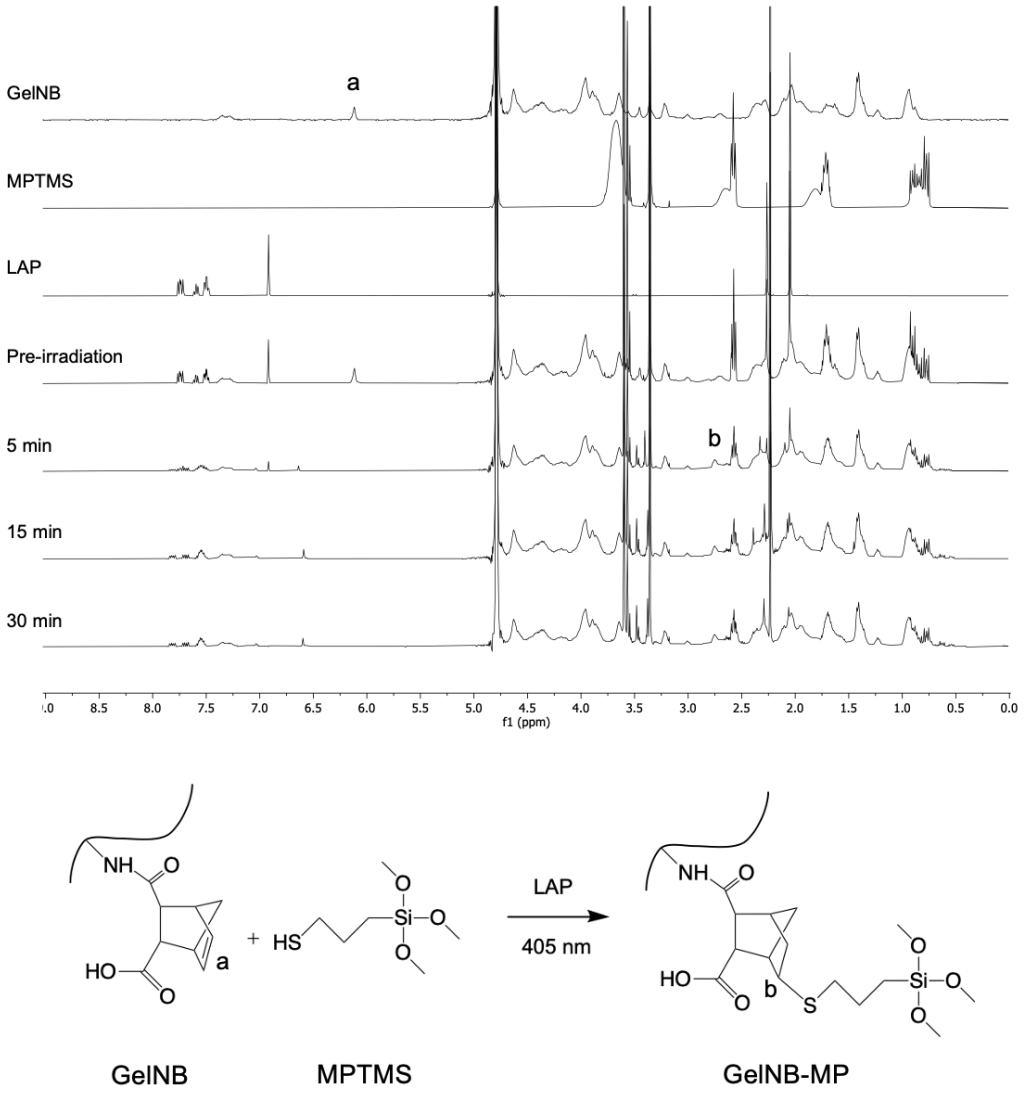


Figure 65. [1]H NMR spectra of GelNB-MPTMS (1:4) reacted with LAP (0.3 wt%) for 30 minutes, 405 nm light. Spectra shown for starting reagents, samples taken pre-irradiation, and 5, 15 and 30 minutes of irradiation (D_2O, 400 MHz). Reaction chemistry is shown with notable resonances δ_H = 2.70 ppm (b) and δ_H = 6.15 ppm (a) labelled.

From the preliminary investigation, the reaction was repeated, however, samples were taken for ^{1}H NMR spectroscopic analysis at 10 and 30 seconds, and 1, 2 and 4 minutes. A decrease in intensity of the resonance at δ_H = 6.15 ppm, corresponding to the norbornene double bond protons, by 10 seconds and disappearance of this resonance by 30 seconds was observed (Figure 66) (252). Again, a new resonance corresponding to -CH attached to the product was

observed at δ_H = 2.70 ppm by 10 seconds (299,300). Both of these findings indicate that the thiol-ene reaction is occurring between GelNB and MPTMS and that the reaction was complete within 4 minutes. However, it should be acknowledged that GelNB produces a complex ^{1}H NMR spectrum, particularly between δ_H = 0.5–5.0 ppm, and so it is easier to investigate the norbornene double bond proton resonance compared to the formation of the thioether.

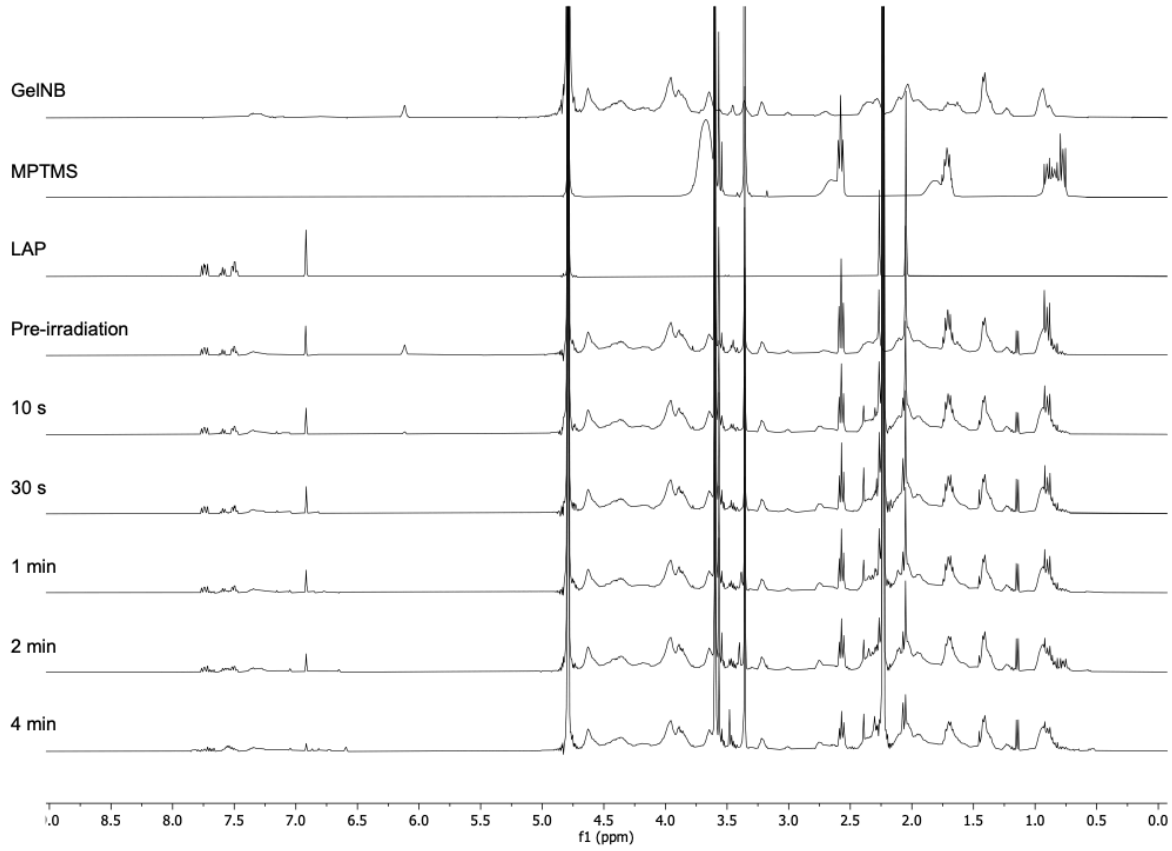


Figure 66. ^{1}H NMR spectra of GelNB-MPTMS (1:4) reacted with LAP (0.3 wt%) for 4 minutes, 405 nm light. Spectra shown for starting reagents, samples taken pre-irradiation, and 10 and 30 seconds, and 1, 2 and 4 minutes of irradiation (D_2O, 400 MHz).

4.3.1.3. 5-Norb functionalisation with MPTMS

To determine if the high molecular weight gelatin-based molecules were having an impact on the thiol-norbornene reaction, as well as selecting a molecule that was less complex than GelNB, GelNB was replaced with 5-Norb, a small alkene containing molecule, and reacted with MPTMS. The reaction was run using a 1:4 (ene:thiol) ratio, 0.3 wt% of LAP and irradiated with 405 nm light for 4 minutes. ^{1}H NMR spectra of samples taken during the reaction are shown in Figure 67. Similarly, to the beforementioned GelNB-MP reactions, a new resonance appeared at δ_H = 2.60 ppm, suggested to correspond to the new -CH attached to the formed thioether (299,300). Again, the alkene resonance at δ_H = 6.15 ppm in the starting material was consumed within 10 seconds.

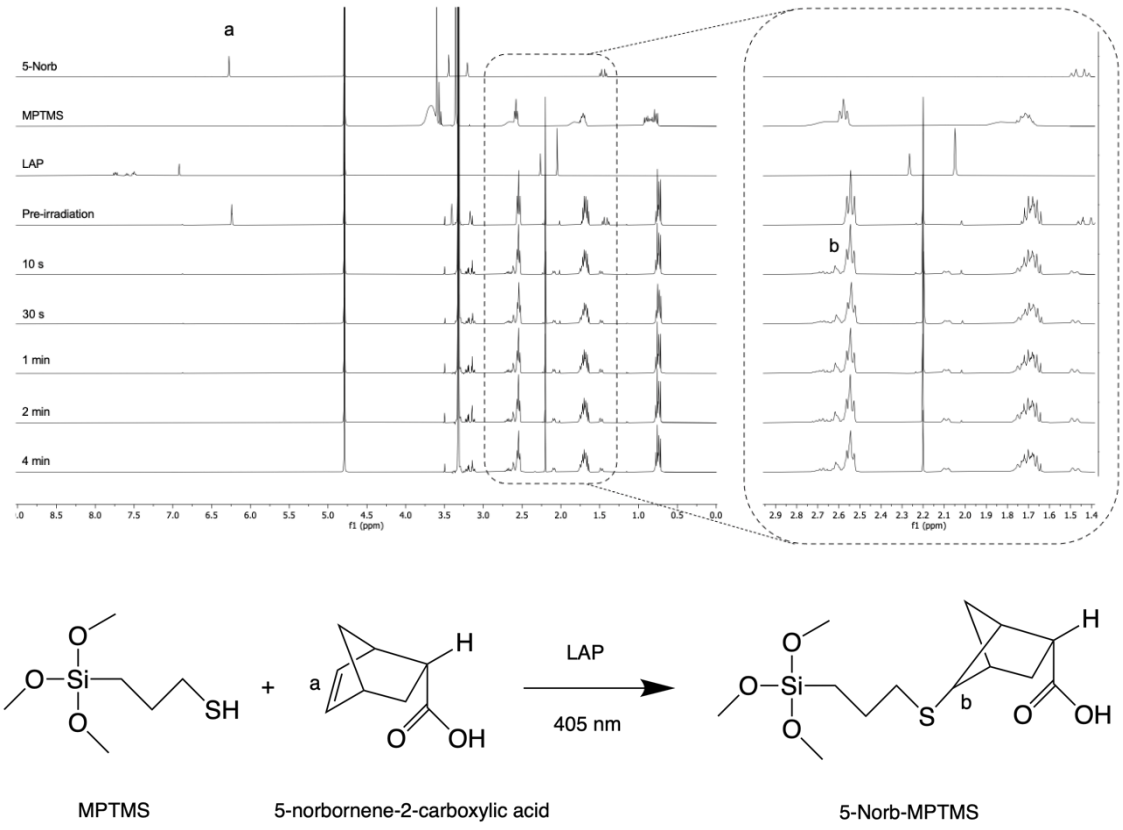


Figure 67. ^{1}H NMR spectra of 5-Norb-MPTMS (1:4) reacted with LAP (0.3 wt%) for 4 minutes, 405 nm light. Spectra shown for starting reagents 5-Norb, MPTMS, and LAP, as well as samples taken pre-irradiation, and 10 and 30 seconds, and 1, 2 and 4 minutes of irradiation (D_2O, 400 MHz). Reaction chemistry is shown with notable resonances δ_H = 2.70 ppm (b) and δ_H = 6.15 ppm (a) labelled.

The thiol-ene reaction reached completion, noted as consumption of the alkene δ_H = 6.15 ppm resonance, within 1 minute in all thiol-norbornene reactions investigated. Norbornene has been reported to be a reactive alkene with thiols resulting in exceptionally rapid rates of reaction (273). This is because the insertion of the thiyl radical across the double bond, and the accompanying quick hydrogen-abstraction rate of a thiol hydrogen by the carbon-centred radical, significantly reduces the ring strain (273). This supports the selection of GelNB for functionalisation, especially when considering previous functionalisation work in this thesis required up to 96 hours of reaction when selecting other crosslinkers (GPTMS).

4.3.2. GelNB functionalisation optimisation study

4.3.2.1. Ene:thiol ratio

As prior results had confirmed the thiol-ene reaction between GelNB and MPTMS occurs efficiently, different reaction variables were studied to further optimise the process. Firstly, the ene:thiol ratio was investigated, selecting 1:2. Double the number of moles of MPTMS are needed compared to DTT due to there being one thiol group on MPTMS, meaning it would be stoichiometrically balanced at 1:1 ratio of GelNB:MPTMS. However, decreasing the ratio to 1:1 was decided against due to practical considerations, as the reaction was run with low volumes. Therefore, the 1:4 ene:thiol ratio originally investigated was decreased to a 1:2 ene:thiol ratio to mitigate the excess of MPTMS within the system but still ensuring practical feasibility.

Results showed complete disappearance of the resonance at δ_H = 6.15 ppm by 30 seconds and appearance of a new product at δ_H = 2.70 ppm, corresponding to the new -CH attached to the product thioether (Figure 68) (300). Previous reports involving the reaction of GelNB with the low-molecular-weight DTT have been performed in the presence of 0.5 equivalents of

DTT corresponding to an equimolar thiol/norbornene ratio (284). A study of ene:thiol ratio of GelNB-DTT was carried out to confirm this, with two key findings: the rate of reaction increased with increasing ratio and 1.00:0.25 did not show full conversion after 2 minutes (Appendix Figure C.4). At a 1.00:0.25 ratio, the thiol- and -ene components are not equimolar, therefore, for full conversion of the alkene to take place another reaction must be occurring. This is in line with the findings in Appendix Section C.4.3.1.4. suggesting that in the presence of LAP, the alkenes in GelNB could potentially react together to form long chain GelNB polymers.

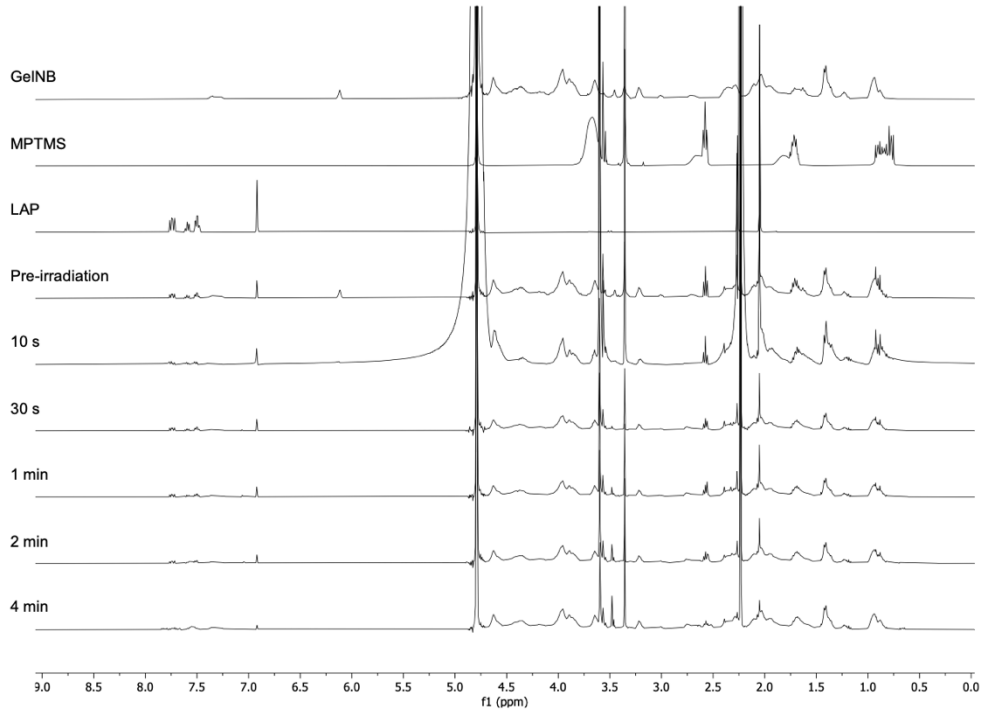


Figure 68. ^{1}H NMR spectra of GelNB-MPTMS (1:2) reacted with LAP (0.3 wt%) for 4 minutes, 405 nm irradiation. Spectra shown for starting reagents GelNB, MPTMS and LAP, as well as samples taken pre-irradiation, and 10 and 30 seconds, and 1, 2 and 4 minutes of irradiation (D_2O, 400 MHz).

Studies are often run reacting GelNB with DTT, a molecule with a thiol group present on each end (256,285,287). To initiate the step-growth photopolymerisation of GelNB hydrogels in the presence of LAP, 0.5 mmol of DTT is required per mmol of norbornene. DTT is a

dithiol, and therefore when considering MPTMS, it can be hypothesised that a 1:1 ratio of GelNB:MPTMS would show full conversion. However, a 1:2 ratio was selected due to the speed of functionalisation compared to a 1:1 ratio, as well as to avoid the difficulties of measuring low volumes (<50 µl) of MPTMS that would be needed in a 1:1 ratio within these thiol-ene reactions as they were carried out on a low volume scale. For all future experiments, a 1:2 ratio was used.

4.3.2.2. LAP concentration

Next, the effect of concentration of the LAP photoinitiator was investigated. All reactions until this point had been run using 0.30 wt% LAP. Similar to Göckler et al. (286) a photoinitiator concentration of 0.30 wt% was taken as the starting point, as when LAP is used in GelMA crosslinking reactions it is used at ~0.30 wt% (303,304). A 2-fold and 10-fold decrease were investigated, using 0.15 and 0.03 wt %. ^{1}H NMR spectra showed full disappearance of the alkene at δ_H = 6.15 ppm by 30 seconds for 0.15 wt%, similarly to 0.30 wt%, whereas full disappearance took place by 1 minute for 0.03 wt% (Figure 69).

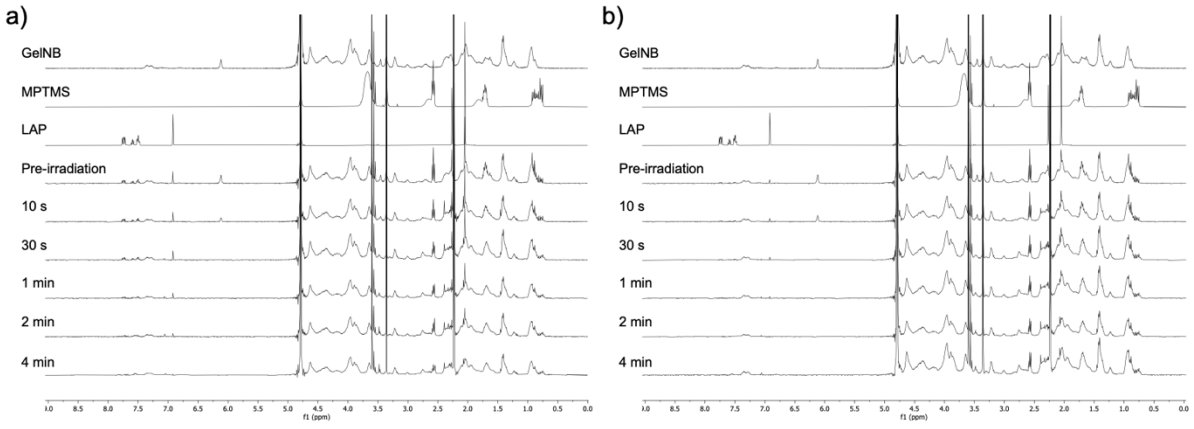


Figure 69. ^{1}H NMR spectra of GelNB-MPTMS (1:2) reacted with LAP a) 0.15 wt% and b) 0.03 wt% for 4 minutes, 405 nm light. Spectra shown for starting reagents GelNB, MPTMS and LAP, as well as samples taken pre-irradiation, and 10 and 30 seconds, and 1, 2 and 4 minutes of irradiation (D_2O, 400 MHz).

Therefore, it can be suggested that a higher concentration of LAP led to an increased rate of reaction, demonstrated with 23%, 62%, and 85% of C=C remaining after 10 seconds for 0.3 wt%, 0.15 wt% and 0.03 wt%, respectively (Figure 70). By 30 seconds, full disappearance of C=C had taken place in both 0.3 wt% and 0.15 wt%, but 8% of C=C remained in 0.03 wt%. Full conversion in 0.03 wt% was achieved by 60 seconds. Therefore, in order to minimise the mass of reagent used, 0.03 wt% was selected as the photoinitiator concentration for the remaining experiment.

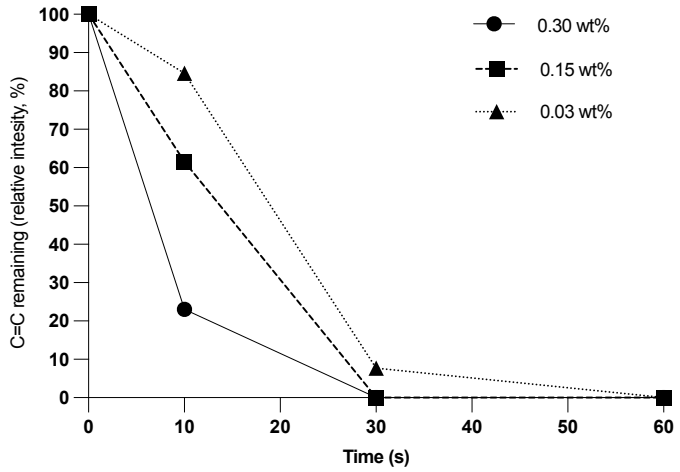


Figure 70. C=C remaining over time with varying LAP wt% in a GelNB-MPTMS (1:2) thiol-ene reaction irradiated for 4 minutes with 405 nm light. Measured as relative intensity of δ_H = 6.15 ppm corresponding to the two vinyl protons of norbornene.

4.3.2.3. Dialysis

Dialysis was performed to remove excess MPTMS and reaction by-products from the Gel-MP product. After 48 hours of dialysis of the GelNB-MP solution, changes were observed to the unmodified GelNB spectra, specifically, the loss of the resonances at δ_H = 3.45 ppm and 3.30 ppm. These two resonances were also present in the ^{1}H NMR spectrum of 5-Norb (Figure 67), which suggests that they are a consequence of the norbornene in the starting

material in Figure 71, but disappear when thiol-ene conjugation occurs. This is further confirmed by Zatorski et al. (245), where an increased intensity of resonances at δ_H = 3.45 ppm and 3.30 ppm occurred when the ratio of norbornene reagent, carbic anhydride, was increased in GelNB synthesis. This is another finding that demonstrates the successful reaction of GelNB with MPTMS.

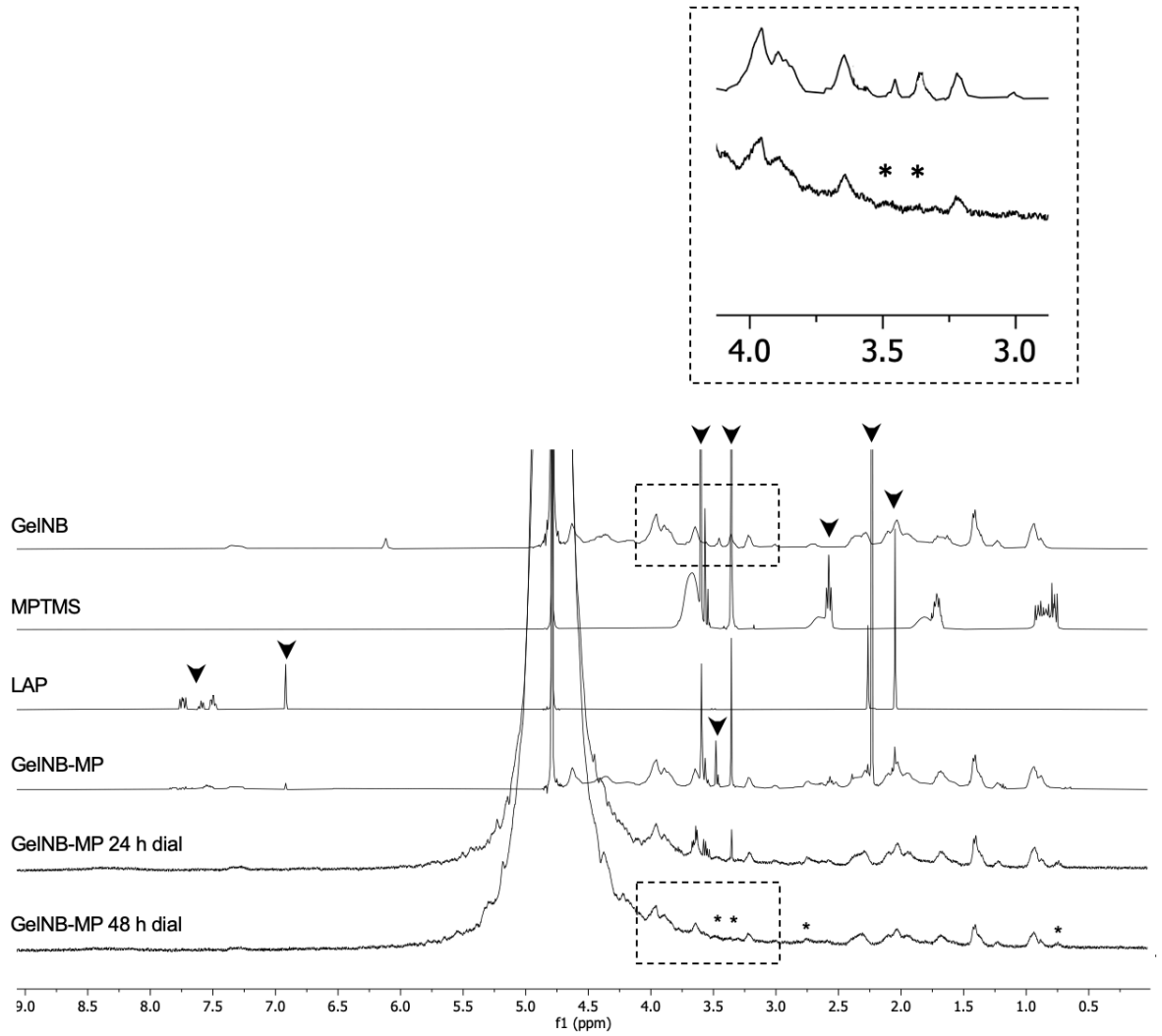


*Figure 71. [1]H NMR spectra of GelNB, MPTMS, LAP and GelNB-MP product, as well as GelNB-MP dialysed for 24 and 48 hours (D_2O, 400 MHz). Differences in GelNB-MP spectra compared to native GelNB are labelled with *. Signals, corresponding to excess starting reagents and reaction by-products removed with dialysis are labelled with an arrow. Inset shows the disappearance of the resonances at δ_H = 3.45 ppm and 3.30 ppm from GelNB to GelNB-MP dialysed (d = dialysis; h = hours).*

Additionally, the new resonance observed at δ_H = 2.70 ppm, corresponding to the new -CH attached to the formed thioether, was present in the undialysed and dialysed Gel-MP. A new resonance at δ_H = 0.75 ppm, which can be suggested to be the protons (-CH_2-) adjacent to the silicon atom in MPTMS, was also observed (305). These two changes to the GelNB spectrum present after dialysis indicate successful conjugation of MPTMS to GelNB. Additionally, the new resonance at δ_H = 0.75 ppm and disappearance of the resonances at δ_H = 3.45 ppm and 3.30 ppm that were not visible without dialysis show the importance of post-processing to identify masked ^{1}H NMR spectral changes.

4.3.3. GelNB-silica hydrogels

Work described in Chapter 2 explored the often-unfavourable interaction between gelatin and silica in terms of phase separation and precipitation. Preliminary work within this chapter identified that replacing part of the media (DMEM) with dH_2O in the hydrogel solvent led to an increase in homogeneity of the gelled hydrogel (Appendix Figure C.5). Therefore, drawing on findings summarised in Chapter 2, it can be suggested that DMEM increased phase separation and precipitation in GelNB-silica hydrogels. It is hypothesised that DMEM might increase phase separation in this context due to its complex composition. DMEM contains salts, such as calcium chloride ($CaCl_2$), with various ionic strengths that could influence the electrostatic interactions between gelatin and silica (306). Gelatin hydrogels are sensitive to variations in ionic strength, and salts are known to influence the gelation of gelatin due to its polyampholyte behaviour (ability to develop cationic and anionic interactions) (307,308). Therefore, the addition of salts and changes in electrostatic interactions with the gelatin molecule have the potential to impact the stability of the hydrogel structure.

An increase in the dH_2O-to-media ratio was observed to result in a prolonged gelation time, as visually assessed. When dH_2O was used alone, the hydrogel did not gel. Therefore, to achieve gelation, whilst avoiding phase separation and precipitation, a DMEM-dH_2O mix at various ratios (1:1 and 1:2) were used as the hydrogel solvent.

Three hydrogel formulations were investigated, a Class I hydrogel; GelNB-silica (1:1), and two Class II hydrogels with varied DMEM-dH_2O ratios; GelNB-MP-Silica (1:1) and GelNB-MP-Silica (1:2) (Figure 72).

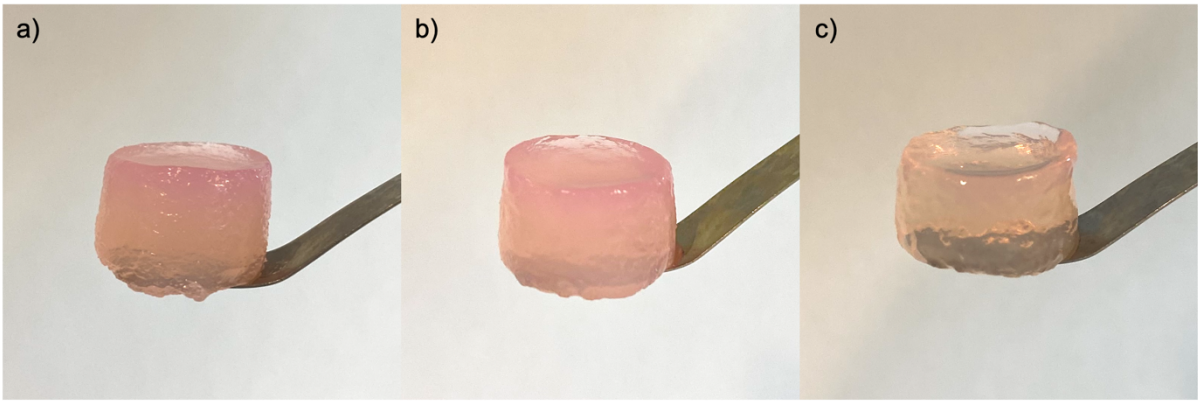


Figure 72. Images of the three hydrogel formulations investigated: a) GelNB-Silica (Class I), b) GelNB-MP-Silica (1:1) [Class II] and c) GelNB-MP-Silica (1:2) [Class II], where the ratio represents DMEM:dH_2O.

Hydrogel gelation time was assessed using the tilt method, as previously described by Scelsi et al. (151), and gelation was recorded when the hydrogel became self-supporting. GelNB-Silica and GelNB-MP-Silica (1:1) gelled significantly faster at ~12 minutes when compared to GelNB-MP-Silica (1:2) which took 40 minutes (both; $p \leq 0.0001$) (Figure 73).

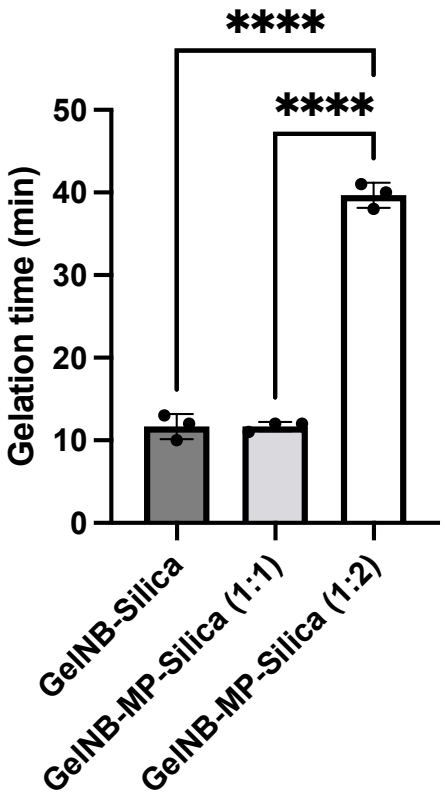


*Figure 73. Gelation time of three hydrogel formulations; GelNB-Silica (Class I), GelNB-MP-Silica (1:1) [Class II], and GelNB-MP-Silica (1:2) [Class II], demonstrating a higher ratio of media results in a shorter gelation time. Individual plots are repeat measures and error bars represent SD (n=3; **** p≤0.0001).*

This demonstrates that a higher proportion of media increased the rate of gelation, whereas the inclusion of MPTMS did not impact gelation time (125). Previous research has demonstrated metal ions, including Ca^{2+}, Mg^{2+} and Na^{+}, lower the gelation time in sol-gel synthesis and as previously mentioned, the media used here (DMEM) contains inorganic salts such as $CaCl_2$ and magnesium sulfate ($MgSO_4$) (309,310). Additionally, Dolinina et al. (311) previously demonstrated that faster gelation of sol-gel silica hydrogels resulted in less condensed and more flexible structures, with lower density and higher porosity. Therefore, it

is hypothesised that inorganic salts in the media formulation are resulting in an increased rate of condensation and faster gelation of the hydrogels, as gelation is achieved through condensation. To test the degree of condensation within the hydrogels, future work should involve the use of ^{29}Si magic angle spinning (MAS) NMR to analyse the connectivity of the silicate network.

It is also hypothesised that the difference in hydrogel formulation with respect to media proportion, and subsequently gelation time, and the resulting hydrogel network structure will impact the properties of the hydrogel. Therefore, hydrogels were also analysed for their degradation, mechanical, architectural and biological properties.

4.3.4. Degradation behaviour of GelNB-silica-based hydrogels

4.3.4.1. Change in mass

In vitro degradation of the three hydrogel formulations, aged (left to gel) for either 1 day or 7 days, was studied by monitoring mass and pH change, as well as analysing substances released into PBS with and without collagenase over time. All hydrogel formulations, irrespective of ageing time and presence of enzyme, followed a similar trend (Figure 74). An initial period of rapid mass loss of the hydrogels was observed up to 24 hours, this was followed by a slower, intermediate degradation period up to 7 days, and finally a plateau period where mass loss stabilised up to 28 days. The similar trend suggests that neither collagenase nor hydrogel ageing time impacted the degradation rate of the hydrogels.

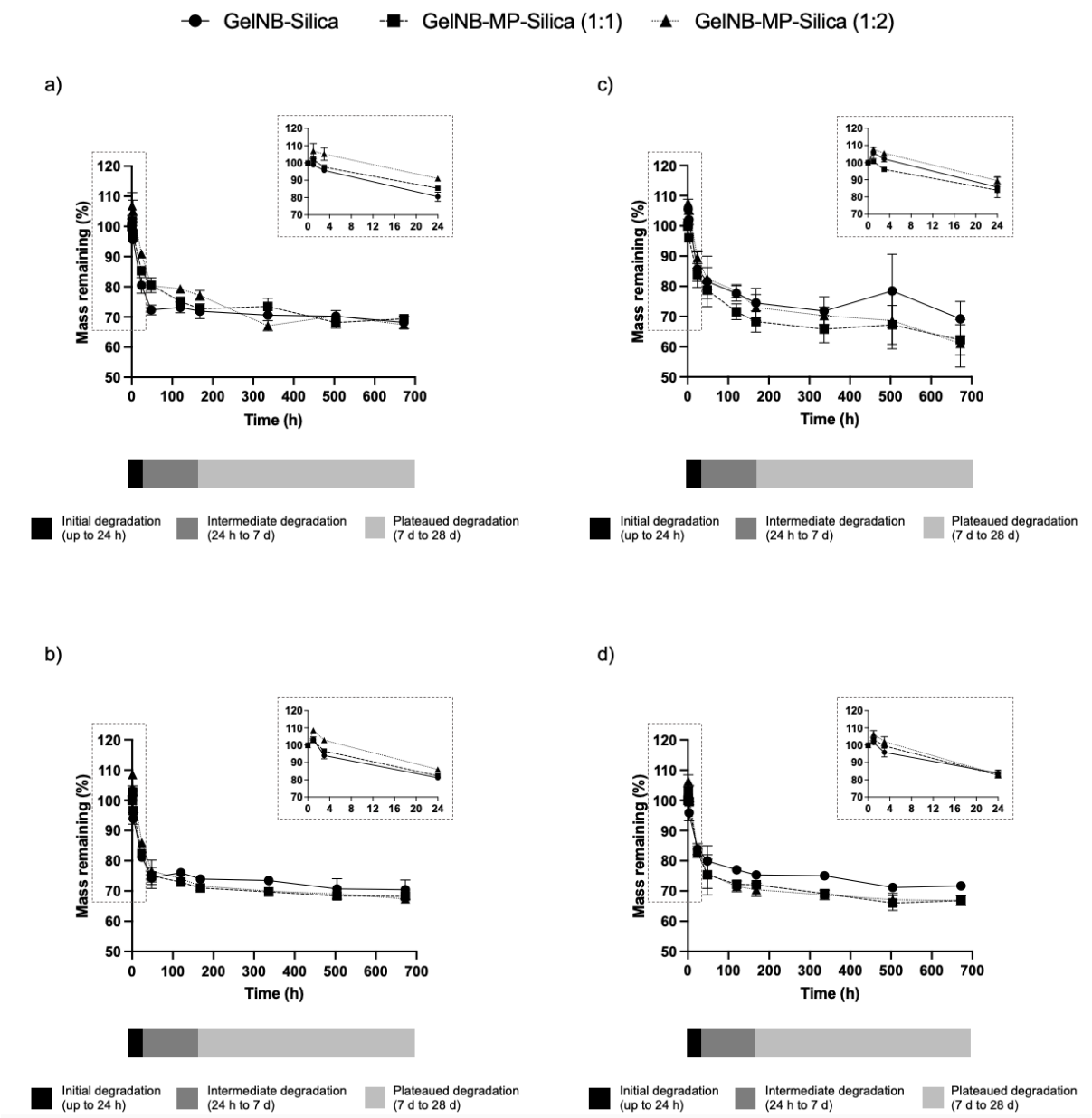


Figure 74. Mass remaining after a degradation assay of three hydrogel formulations aged for 1 day and incubated in a) PBS and b) PBS with collagenase, and 7 day aged hydrogels incubated in c) PBS and d) PBS with collagenase at 37 °C over a 28 day time period. Insets show the first 24 hours of the degradation assay. Error bars represent the SD (n=3).

For 1-day aged hydrogels in PBS, the GelNB-MP-Silica (1:2) had significantly more mass remaining after 24 hours of degradation, compared to the other two hydrogel formulations (Figure 74a). This was the same for GelNB-MP-Silica (1:2) in PBS with collagenase (Figure 74b). Overall, after 28 days of degradation, all hydrogel formulations had ~70% mass

remaining in both the PBS and the PBS with collagenase. Controllable biodegradability and bioresorption are key for the overall performance of hydrogels (70). For tissue engineering purposes, hydrogels should degrade at an equivalent rate of cell aggregation and the formation of new bone tissue (70). It is crucial that an initial period of degradation occurs to allow for infiltration of MSCs and other progenitor cells to begin to differentiate into various cell types, including osteoblasts. Bone nodule mineralisation has been shown to occur as early as 21 days (312). As ~70% of the hydrogel mass remained by 28 days, this indicates that the hydrogel may be able to provide temporary support during the initial stages of bone growth, although this would require testing.

Biomaterials are subject to enzymatic degradation within a normal physiological environment by MMPs, such as collagenase, which are present in human ECM (226). The incorporation of collagenase better mimics physiological conditions to which the hydrogel would be exposed to *in vivo* and allows evaluation of whether the hydrogel will undergo controlled degradation within this environment for tissue remodelling (313). To better understand the contributions of enzymatic degradation, hydrogel samples were incubated in PBS with collagenase, utilising a concentration of collagenase (25 u/mL) previously used in literature (314,315) (Figure 74b and d). There was no difference in the degradation rate of the hydrogels with the addition of collagenase, compared to PBS alone. The degradation remained at around 30% degradation after 28 days. However, it has been noted in the literature that the collagenase solutions should be replaced during the experiment to maintain constant enzyme activity, suggesting that the lack of difference in mass loss could be attributed to lack of enzyme activity over the duration of the assay (316). Therefore, this presents as a limitation and the results should be interpreted with caution. The degradation assay should be repeated in future work, refreshing the collagenase to maintain its activity over time.

4.3.4.2. Si species and gelatin release

Degradation products, namely Si species and gelatin were further analysed. As previously mentioned in Section 3.3.6.2, it is important to quantify Si release as it can have both a positive impact on osteoblasts, including increased growth and proliferation, leading to enhanced mineralisation, but can also exert negative effects, such as apoptosis, at high concentrations (231–234,238). Understanding the dynamics of Si release from the GelNB-Silica hydrogels is therefore essential for optimising their potential to promote mineralisation, while mitigating any potential drawbacks or adverse effects on cell behaviour.

The Si ion concentration was variable, with large error bars for 1 day-aged hydrogels in PBS (Figure 75a). Therefore, these results were deemed unreliable and will not be further analysed. However, overall, burst release of Si ions was observed within the first 2 days of incubation in PBS with and without collagenase, for all hydrogel formulations (Figure 75b, c and d). After the initial Si burst release up to 2 days of immersion, the concentration of Si release plateaued until 28 days. A difference in Si release was observed in the 1 day-aged hydrogels immersed in PBS with collagenase (Figure 75b). The concentration of Si release was lower in the GelNB-MP-Silica (1:2) from 24 hours onwards, compared to GelNB-MP-Silica (1:1) and GelNB-Silica, suggesting that the crosslinking effect of MPTMS was more impactful for GelNB-MP-Silica (1:2).

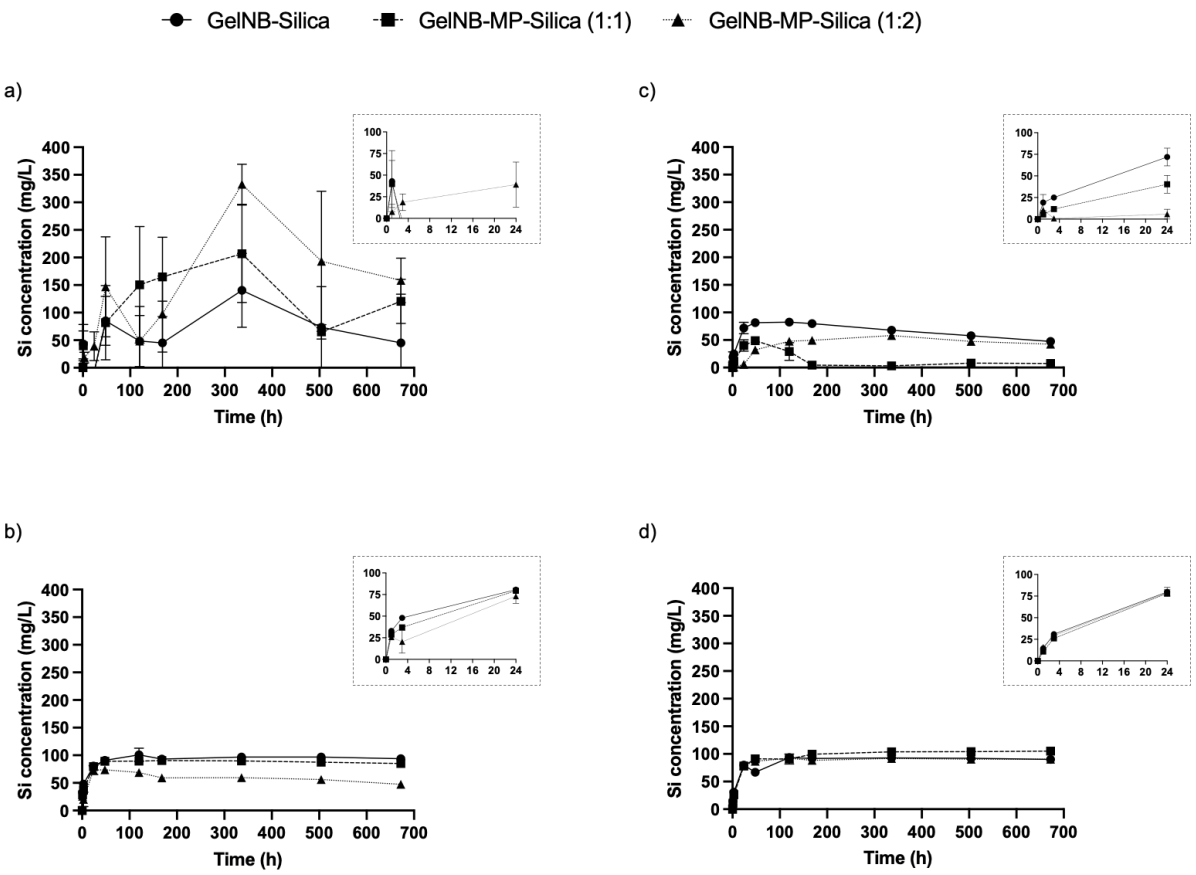


Figure 75. Release profile of silicon from a degradation assay of three hydrogel formulations aged for 1 day and incubated in a) PBS and b) PBS with collagenase, and 7-day aged hydrogels incubated in c) PBS and d) PBS with collagenase at 37 °C over a 28-day time period. Insets show the first 24 hours of the degradation assay. Error bars represent the SD (n=3).

Similarly, a difference in Si release was seen in the 7 day-aged hydrogels incubated in PBS alone, specifically that the Si release was more controlled in the Class II hydrogels (GelNB-MP-Silica (1:1) and (1:2)) within the first 2 days, compared to the Class I hydrogel (GelNB-Silica) (Figure 75c). This suggests that the MPTMS covalent crosslinking in the Class II hydrogels was successful and led to a more extensively connected network, compared to the Class I, resulting in slower Si release. Therefore, in some cases, the degradation rate was found to be dependent on the inclusion of MPTMS crosslinker. Finally, there remains dispute over the appropriate concentration of Si for beneficial effects on cell behaviour (231). Therefore, by using cell viability (e.g. Live/Dead and PrestoBlue) and proliferation (e.g.

Alamar Blue® and MTT) assays, as well as Alizarin Red S staining to observe osteoblast mineralisation, the impact of Si release on cells can be studied (231,317,318).

The rate of gelatin release increased with the addition of collagenase in the hydrogels aged for 1 day, with ~250–500 μg/L of gelatin released from the three formulations at 7 days of degradation without the presence of collagenase, compared to ~1000–1250 μg/L of gelatin released at 7 days in PBS with collagenase (Figure 76a and b). Therefore, in the hydrogels aged for 1 day, gelatin release was accelerated in the presence of collagenase. This behaviour was expected and is attributed to the fact that collagenase is an enzyme found in the body that degrades hydrogels made from a gelatin backbone, as gelatin is a form of hydrolysed collagen (319). In PBS without collagenase, the two Class II hydrogels aged for 1 day released a lower amount of gelatin compared to GelNB-Silica, whereas all three formulations followed similar gelatin release profiles with collagenase (Figure 76a and b). In contrast, gelatin release was higher in PBS without collagenase for the 7 day-aged hydrogels. This finding was unexpected and unexplained, although, the gelatin release rate was particularly high for GelNB-Silica and GelNB-MP-Silica (1:1) in Figure 76c which suggests that these results may not be reliable and should be repeated in future work. Interestingly, when comparing the release rate of gelatin in PBS with collagenase for hydrogels with different ageing conditions, the highest concentration of gelatin release within the degradation period was in the 1 day-aged hydrogels (~1250–1600 μg/L at 14 days) compared to the 7 day-aged hydrogels (~800–1000 μg/L at 7 days) [Figure 76b and d]. The lower gelatin release associated with a longer ageing time could be as a result of gelatin being entrapped within a more highly condensed and extensive silica network. Further work, such as ^{29}Si MAS NMR, would give an insight into the connectivity of the silica network.

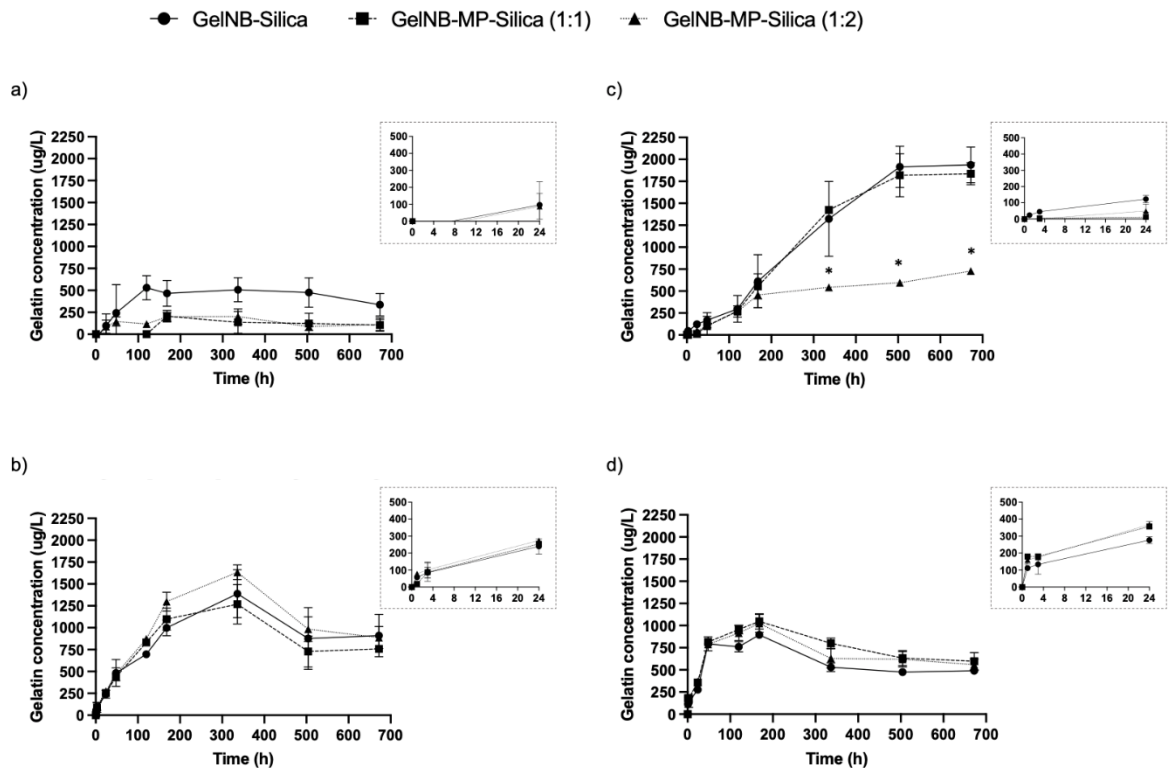


*Figure 76. Release profile of gelatin from a degradation assay of three hydrogel formulations aged for 1 day and incubated in a) PBS and b) PBS with collagenase, and 7 day aged hydrogels incubated in c) PBS and d) PBS with collagenase at 37 °C over a 28 day time period. Insets show the first 24 hours of the degradation assay. Error bars represent the SD (n=3), where * is used n=2.*

4.3.5. Mechanical characterisation – compressive properties of hybrid hydrogels

The mechanical properties of a hydrogel are crucial when being used in a tissue engineering application due to a number of reasons. Firstly, the mechanical properties of a hydrogel would be expected to mimic those of the native tissue, which here is bone, to be representative of the *in vivo* environment, and secondly, the mechanical properties play a major role in controlling and directing the local environment and growth of the adhered cells on the hydrogel for neotissue formation (1,320). Therefore, it is important to analyse and understand a variety of mechanical properties when designing a material for BTE.

4.3.5.1. Uniaxial compressive testing

The uniaxial compressive mechanical properties were tested for the three hydrogel formulations – GelNB-Silica, GelNB-MP-Silica (1:1), and GelNB-MP-Silica (1:2) – aged for 1, 3, 7 and 14 days (Figure 77), to investigate the influence of hydrogel formulation, as well as ageing time, on mechanical properties.

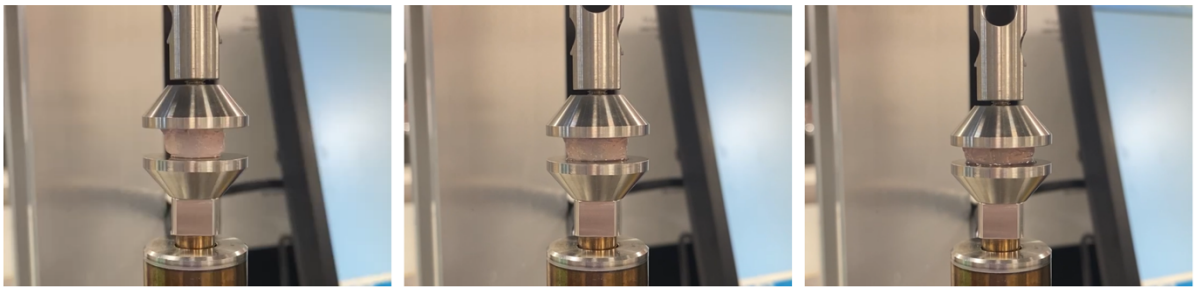


Figure 77. Uniaxial compressive test of hydrogel samples using Bose ElectroForce 5500 Test Instrument equipped with a 200 N load cell.

When evaluating the stress-strain responses qualitatively, the hydrogels showed that the yield point (yield stress, where the curve transitions from elastic to plastic behaviour) and slope of the curve (Young's Modulus) were similar for GelNB-Silica hydrogel, irrespective of ageing time (Figure 78a-i). Whereas, in the Class II hydrogels, the stress-strain curves varied depending on ageing time – generally showing that a longer ageing time led to a higher yield point and steeper curve (Figure 78b-i and c-i).

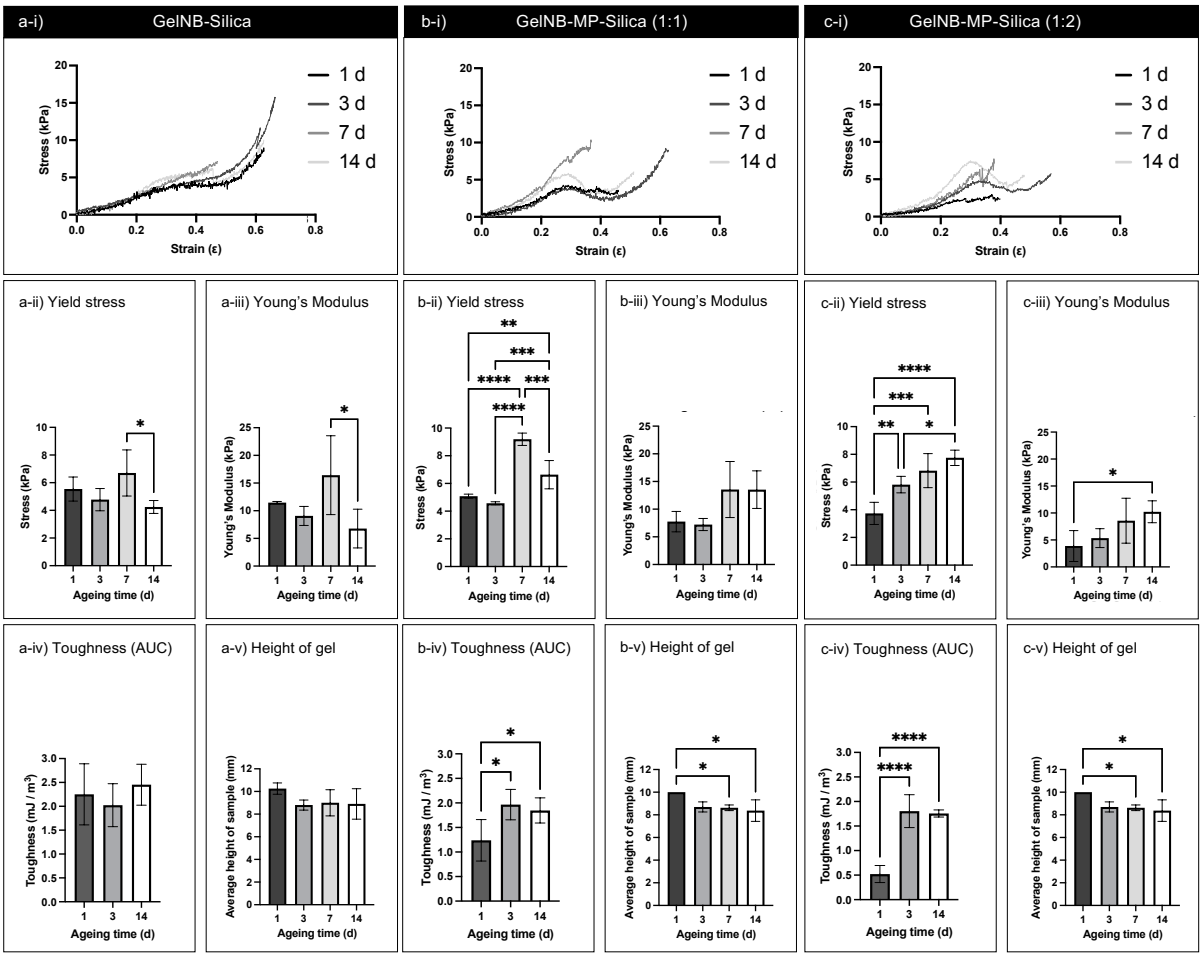


Figure 78. Uniaxial compressive data for three hydrogel formulations a) GelNB-Silica, b) GelNB-MP-Silica (1:1), and c) GelNB-MP-Silica (1:2) aged for 1, 3, 7 and 14 days (d: day). Results presented include i) Stress-strain curve, ii) Yield stress, iii) Young's Modulus, iv) Toughness (AUC), and v) Height of gel (d = day). Note, toughness values are not shown for 7 days because of issues with the quality of data. Error bars represent the SD and non-significance is not shown, p≤0.05 (*), p≤0.01 (**), p≤0.001 (***), and p≤0.0001 (****).

Yield stress, taken as the highest point of the curve before elastic to plastic deformation occurred, did significantly depend on the ageing time in both of the Class II hydrogels (Figure 78b-ii and c-ii). Specifically, both Class II hydrogels had the highest yield stress after 7 days of ageing (~9 kPa [1:1] and ~7 kPa [1:2]), with a significant increase in yield stress between 1 and 7 days (p≤0.0001; [1:1] and p≤0.001; [1:2]). There was no significant increase in yield stress from 7 to 14 days in GelNB-MP-Silica (1:2), however, a significant decrease in yield stress was observed for GelNB-MP-Silica (1:1) from 7 to 14 days. In GelNB-silica, no significant increase in yield stress was observed over any ageing periods, however, the yield

stress significantly decreased from 7 to 14 days ($p \leq 0.05$) (Figure 78a-ii). Yield stress is a measure of the material's resistance to permanent deformation and a higher yield stress means a material can withstand loads without undergoing excessive plastic deformation (321). The results for yield stress indicate that a change occurred within the Class II hydrogels over the ageing period. It is suggested that the hydrogel network, including covalent crosslinks facilitated by MPTMS as well as polycondensation of the silica network, continue to develop and result in a material with increased strength over time. Krupa et al. (295) studied silica hydrogels in compression and also found that after 7 days of ageing, the maximum strength of gels was reached, and Jayash et al. (112) also found that chitosan-silica-based hybrid hydrogels demonstrated increased G' as a result of ageing and the continued polycondensation of the silica network. It was not possible to find ageing studies on similar hydrogel systems in the literature, however, ageing dynamics in the microstructure of gelatin hydrogels has been reported. Tosh et al. (322) demonstrated the structure of gelatin (up to 5 wt%) hydrogels was found to be dynamic and continues to evolve over time as a result of the structure rearranging into more stable, energetically favourable conformations. Using dynamic light scattering (DLS), it was suggested that in the gelation of gelatin, two concurrent processes occur; firstly, growth and aggregation of polymer clusters, followed by, restructuring of the gel network. Additionally, the G' was found to increase over time, suggested to be owed to continued formation of the triple helices in the network and fibril rearrangement (322). However, the experimental techniques used were DLS and rheology, and the ageing time was shorter (hours), and so, this must be interpreted with caution.

The increased yield stress was not observed in the Class I hydrogel which can be suggested to be due to this material only having non-covalent interactions between the GelNB and silica phases. The significant decrease in yield stress observed between 7 and 14 days for GelNB-

Silica and GelNB-MP-Silica (1:1) can be suggested to be due to a number of factors, such as changes in the network structure from degradation of the gelatin backbone or crosslinks, or changes in the H_2O content of the hydrogel due to evaporation (323,324).

Young's Modulus was calculated as it directly characterises the stiffness of the hydrogels. A similar trend as seen in yield stress was observed for the Young's Modulus (stiffness) of GelNB-Silica hydrogels, with no significant change in stiffness between 1 and 7 days, with a significant decrease in Young's Modulus between 7 and 14 days (~15 kPa to ~7 kPa; $p \leq 0.05$) (Figure 78a-iii). The Young's Modulus did not change significantly throughout the ageing period in GelNB-MP-Silica (1:1) hydrogels (Figure 78b-iii). The GelNB-MP-Silica (1:2) was the only formulation to see an increase in Young's Modulus over the ageing period, between 1 and 14 days (~4 kPa to ~10 kPa; $p \leq 0.05$) (Figure 78c-iii). Similarly, to yield stress, the significant increase in Young's Modulus suggests maturation of the gel structure over time and development of the covalent crosslinking network both in the polycondensation of the silica but also covalent crosslinks facilitated by MPTMS between GelNB and silica. Ageing and hydrogel formulation play a larger role in influencing yield stress compared to the Young's Modulus, whereas the solvent base (1:1 vs 1:2) has a larger impact on the Young's Modulus over time. Yu et al. (325) produced thiol-ene gelatin-based hydrogels, composed of crosslinked GelNB and GelSH. The compressive modulus was measured, taken as the slope of the stress-strain curve in the elastic region, therefore, analogous to Young's Modulus. The 5% (w/v) hydrogel, most comparable to the hydrogels in this present study (5 wt%), had a compressive modulus of ~1 kPa, therefore suggesting that the compressive modulus of the hybrids here was enhanced by the addition of silica within the GelNB network (325).

Toughness (AUC) did not change over the 14 day ageing period for the GelNB-Silica hydrogel (Figure 78a-iv), whereas, changes were observed for the Class II hydrogels (Figure 78b-iv and c-iv). Both Class II hydrogels had the highest toughness (AUC) by 3 days of ageing (~1.9 mJ/m^3 [1:1] and ~1.8 mJ/m^3 [1:2]), which was maintained until 14 days of ageing. There was a significant increase in toughness (AUC) in the Class II hydrogels between 1 and 3 days (~1.2 mJ/m^3 to ~1.9 mJ/m^3, $p \leq 0.05$; [1:1] and ~0.5 mJ/m^3 to ~2.8 mJ/m^3, $p \leq 0.0001$; [1:2]) and 1 and 14 days (~1.2 mJ/m^3 to ~1.9 mJ/m^3, $p \leq 0.05$; [1:1] and ~0.5 mJ/m^3 to ~1.8 mJ/m^3, $p \leq 0.0001$; [1:2]). These results again indicate that the Class II hydrogels could be continuing to form a covalent network across the ageing period; this covalent network includes polycondensation of the silica network but also covalent crosslinks between GelNB and silica from MPTMS as the crosslinker formation. This more extensive 'double' covalent network could result in a change of toughness (AUC) over time. Additionally, the increase in toughness (AUC) by 3 days and 14 days of ageing was more pronounced in the GelNB-MP-Silica (1:2) hydrogel, which can be suggested to be as a consequence of the different DMEM-dH_2O formulation.

Both Class II hydrogels decreased in height between day 1 and day 7 by ~20% in the 1:1 formulation, and ~10% in the 1:2 formulation (both $p \leq 0.05$) (Figure 78b-v and c-v). The height of the Class II hydrogels also decreased between day 1 and day 14 (both $p \leq 0.05$). No significant changes in the height of Class II hydrogel samples were observed during the first three days of ageing. The significant change in the height indicates that continuous development of the gel could lead to formation of a more compact network resulting in shrinkage of the gel during ageing (295). This could reflect increased covalent crosslinking forming over time from a more condensed network. Although shrinkage of the hydrogels could be due to evaporation of H_2O over time, no significant changes of the height of GelNB-

Silica samples were observed which suggests evaporation is not responsible (Figure 78a-v). Future work could involve experiments to determine the extent of condensation within the Class II structures compared to the Class I GelNB-Silica, using ^{29}Si MAS NMR to analyse the connectivity of the silicate network, as used by Mahoney et al. (184).

Overall, ageing time played a more significant role in affecting strength, stiffness, and toughness (AUC) in the Class II hydrogels (GelNB-MP-Silica [1:1] and [1:2]), compared to the Class I hybrid hydrogel (Figure 78). The inclusion of MPTMS, the ratio of DMEM:dH_2O, and ageing time were all found to tailor the mechanical properties of the resulting hydrogels.

4.3.5.2. Constant cyclic compressive testing

Changes in mechanical properties, specifically hysteresis loss here, were investigated between 1 day- and 7 day-aged samples to determine if the hydrogels showed aged-dependent behaviour due to changes in the network structure over time. Hydrogels were subjected to constant cyclic compression to 20% strain, consecutively over 20 cycles. The average unloading modulus was plotted against the cycle number and hysteresis loss was calculated by determining the area under the curve for each loading and unloading phase of each separate cycle. The total hysteresis loss was calculated from the cumulative values for the area under each curve for each consecutive cycle, over the entire cyclic loading test.

When comparing hydrogel formulations there were differences in the hydrogel hysteresis loss. GelNB-Silica had higher hysteresis loss values compared to the Class II formulations. Specifically, at 7 days of ageing the hysteresis loss values range from ~0.35 kPa (1st cycle) to ~0.08 kPa (last cycle) in GelNB-Silica, whereas the values were ~0.08 kPa (1st cycle) to ~0.03 kPa (last cycle) and ~0.03 kPa (1st cycle) to ~0.01 kPa (last cycle) in GelNB-MP-Silica

(1:1) and GelNB-MP-Silica (1:2), respectively (Figure 79). In all hydrogel formulations, the hysteresis loss values were higher for the 7 day-aged hydrogels compared to the 1 day-aged hydrogels. Overall, ageing resulted in hydrogels being less able to dissipate energy due to a higher stiffness, suggesting a more rigid and less deformable network forming over time.

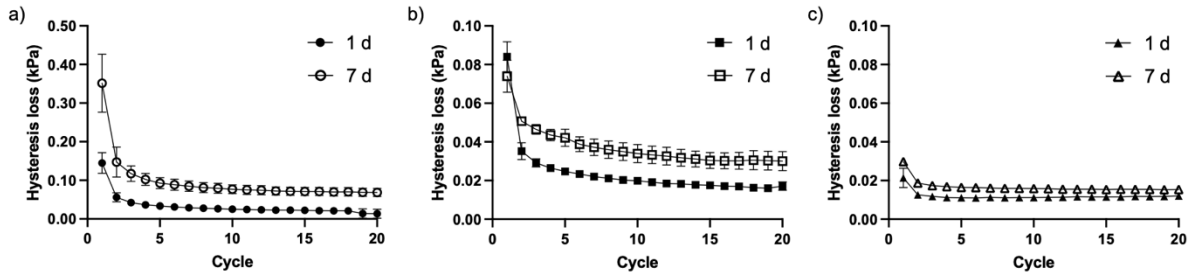


Figure 79. Hysteresis loss from three hydrogel formulations aged for 1 day and 7 days, at constant cyclic compression, 20% strain for 20 cycles, a) GelNB-Silica, b) GelNB-MP-Silica (1:1), c) GelNB-MP-Silica (1:2). Note, the different scale for y axis for a). Error bars represent the SD (n=3).

All hydrogel formulations, for both ageing periods, dissipated higher energy during the first cycle compared to the other cycles, suggesting that the first loading cycle caused some plastic deformation and damage to the hydrogel structure (Figure 79) (326). For all formulations and both ageing times, there was a significant decrease in hysteresis loss from the first cycle to the second cycle. GelNB-MP-Silica (1:2) had a lower hysteresis loss between the first cycle and second cycle (Figure 79c), compared to the other two formulations (Figure 79a and b), and the curve remained plateaued until the final cycle. There was no significant difference in energy dissipation beyond the second cycle to the final cycle in GelNB-MP-Silica (1:2), indicating mechanical stability was achieved quicker than in GelNB-Silica and GelNB-MP-Silica (1:1), as well as exhibiting good reversibility and preservation of its elastic nature (326).

An ordinary ANOVA test and Tukey's multiple comparison were carried out, comparing the hysteresis loss during the first cycle between formulations. After 1 day of ageing, the hysteresis loss was significantly higher in GelNB-Silica vs GelNB-MP-Silica (1:1) [$p \leq 0.01$] and vs GelNB-MP-Silica (1:2) [$p \leq 0.001$] (Figure 80a). Additionally, the hysteresis loss was significantly higher in GelNB-MP-Silica (1:1) compared to GelNB-MP-Silica (1:2) [$p \leq 0.01$] (Figure 80a). After 7 days of ageing, the hysteresis loss on the first cycle was again significantly higher in the GelNB-Silica compared to both GelNB-MP-Silica (1:1) [$p \leq 0.0001$] and GelNB-MP-Silica (1:2) [$p \leq 0.0001$] (Figure 80b).

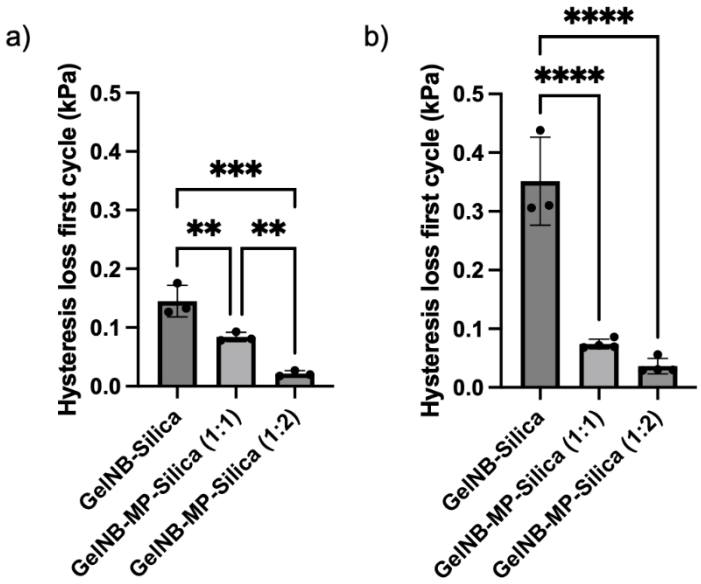


Figure 80. Hysteresis loss from the first cycle of constant cyclic compressive loading for three hydrogel formulations aged for a) 1 day and b) 7 days. The points plot on each bar represent a repeat measure and SD is shown (n=3). Non-significance is not shown, p≤0.01 (**), p≤0.001 (***), and p≤0.0001 (****).

Mechanical functioning of a hydrogel is a key criterion when selecting a material for bone tissue engineering applications. Hysteresis loss reflects the potential of a material, in this case hydrogel, to dissipate energy during loading and unloading cycles, and is viscoelastic in

nature (327–329). Therefore, hysteresis energy dissipation is likely dependent on the viscous phases in bone (i.e. H_2O and collagen) (329). Furthermore, hysteresis loss provides a measure of material toughness and resilience (330,331).

There is a higher amount of energy dissipated during the first loading and unloading cycle in GelNB-Silica at both 1 and 7 days of ageing, compared to the Class II formulations. This indicates that this material has the lowest resistance to permanent plastic deformation, exhibiting less elastic and more plastic behaviour which results in increased energy dissipation. Whereas the lower hysteresis loss in the first cycle of the Class IIs, particularly GelNB-MP-Silica (1:2), demonstrates lower energy dissipation. Less energy dissipation suggests a more elastic nature with the ability to return a larger proportion of energy stored during compression. In the GelNB-MP-Silica (1:2), from the second cycle on, all subsequent cycles followed a similar hysteresis loss value, indicating better reversibility and preservation of its elastic nature compared to the other two hydrogel formulations (326). Covalent crosslinks have previously been reported to impart high elasticity on hydrogels and a better ability to recover to their original state after deformation, indicating potentially a higher degree of MPTMS-facilitated covalent crosslinks in the 1:2 formulation, compared to the 1:1 (332). A hypothesised organic-inorganic structure for the three hydrogel formulations is illustrated in Figure 81.

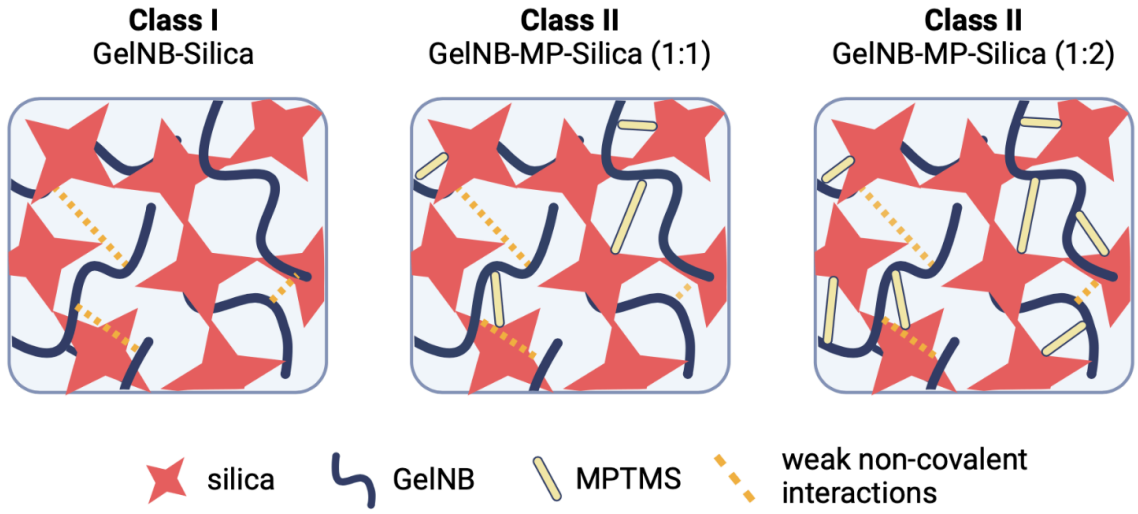


Figure 81. Hypothesised organic-inorganic structure in the GelNB-Silica-based hydrogels, depicting only weak non-covalent interactions in the Class I GelNB-Silica, but both weak non-covalent and MPTMS-facilitated covalent bonding in the Class II hydrogels, with a higher degree of MPTMS-facilitated covalent bonding in the 1:2 formulation. Created on the BioRender website (https://biorender.com) by the author.

The difference in crosslinking mechanisms within the hydrogels could be an explanation for the differences in hysteresis loss. Covalent crosslinks, which are present in the Class II hydrogels, have been reported to provide enhanced structural stability (333). This more stable network could supply a better mechanism by which to dissipate energy, hence, a lower overall energy dissipation.

More obvious hysteresis in the Class I suggests that it may be less suitable for loading bearing applications requiring dynamic mechanical loads, when compared to Class II formulations (327). Class I hybrids only have non-covalent networks within their structure, which include ionic interactions, compared to Class II hybrids which have both non-covalent and covalent. Ionic interactions have previously been reported to rupture when stretched, resulting in a large amount of energy dissipation and a large stress-strain hysteresis (334–336). The hydrogels in the aforementioned studies are in tension, and this present study is compression, and so this comparison should be interpreted with caution. However, Zhao et al.

(337) demonstrated plastic deformation in a biopolymer alginate hydrogel with ionic crosslinks but elastic deformation in the alginate hydrogel with covalent crosslinking, supporting the conclusion drawn here. Slippage of the organic and inorganic phase in the GelNB-Silica hydrogel when under load could also lead to more significant hysteresis of the hydrogel, when compared to Class II formulations, limiting its mechanical stability (338). However, all formulations do stabilise and elastically deform after the first cycle, suggesting that the constant cyclic compressive tests should be repeated at a higher deformation.

Overall, the take home messages are that the Class II hydrogels were better than the Class I hydrogel at dissipating energy, displaying more of an elastic nature. Additionally, ageing from 1 day to 7 days led to an overall increased hysteresis loss in all hydrogel formulations, suggesting crosslinking and network structure changes over time.

4.3.5.3. Incremental cyclic compressive testing

The energy dissipation potential of the hydrogels was studied further by using another cyclic loading-unloading test, however, this test was conducted with successive incremental strain. An incremental cyclic compressive test was used, as unlike a constant cyclic compressive test, it indicates the behaviour of a material under varying compressive loads. The data were used to plot a cyclic envelope by identifying the highest point of stress for each cycle. The elastic region and strain softening of the cyclic envelope were then determined by identifying the yield point, shown as the dotted line, which is the point where strain continued to increase but there was no increase in stress.

All hydrogel formulations demonstrated non-linear elastic-plastic behaviour for every cycle (Figure 82) (339). Typical stress strain curves are presented, which showed an increasing plastic deformation throughout the mechanical test (Figure 82).

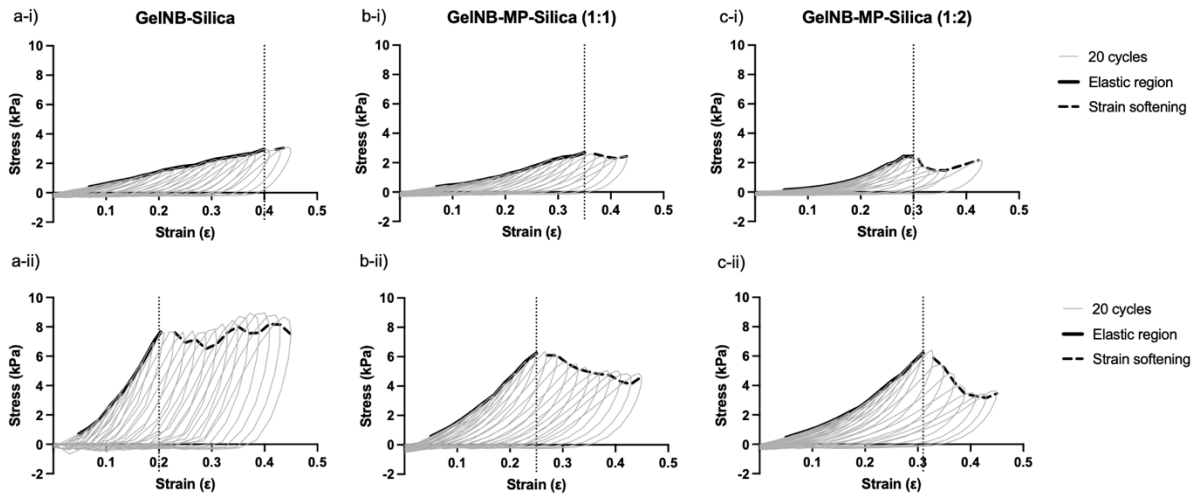


Figure 82. Stress-strain curves for incremental cyclic loading of a) GelNB-Silica, b) GelNB-MP-Silica (1:1), and c) GelNB-MP-Silica (1:2), aged for i) 1 day and ii) 7 days. The cyclic envelopes are shown, with the elastic region and strain softening highlighted. The dotted vertical line represents yield stress (n=3).

For GelNB-Silica aged for 1 day (Figure 82a-i), the length of the elastic region was longer when compared to 7 days of ageing (Figure 82a-ii). A similar trend is observed for GelNB-MP-Silica (1:1) (Figure 82b). An increase in stress and decrease in strain at yield point at 7 days, compared to 1 day, for both GelNB-Silica and GelNB-MP-Silica (1:1) suggests that ageing resulted in the hydrogels becoming stronger, as indicated by higher stress, and less elastic, as indicated by a decrease in strain (Figure 82a and b). Again, this suggests that changes in the hydrogel network and structure occur during ageing. However, this finding for GelNB-Silica contrasts the results from the uniaxial compressive tests that suggested that ageing did not result in increased mechanical properties. A reason for this could be the different instruments used for the two respective tests introducing variations into

experimental results. It is suggested that the uniaxial tests are repeated using the Bose ElectroForce 5500 Test Instrument equipped with a 200 N load cell, as this has a higher sensitivity compared to the uniaxial instrument used.

The strain at which the yield point occurred for GelNB-MP-Silica (1:2) was maintained from 1 to 7 days, therefore, sustaining its elasticity over time. However, the stress at which the yield point occurred increased from ~2.2 kPa to ~6 kPa from 1 day to 7 days, respectively (Figure 82c). This suggests that ageing resulted in a higher resistance to deformation and increased strength. The yield stress values obtained were not comparable to those for bone reported in the literature, where yield stress of bone specimens has been shown to be in the magnitude of MPa (340).

There is a lack of studies in the literature using an incremental cyclic test for similar hydrogel compositions and therefore, it is difficult to draw comparisons with the findings here. However, Dong et al. (340) has reported increased plastic deformation in bone when subjected to progressive loading cycles. Changes in the pre- and post-yield behaviour of human cortical bone were observed when under progressive loading, and the typical stress-strain curve of human cortical bone is similar to those here; with hysteresis curves shifting horizontally as strain increases (Figure 82) (340). Plastic deformation in bone is associated with microdamage, arising through the formation of 'crosshatch' type damages orientated at ~30–40^{o} from the bone's long axis within the tissue (329,341). Compressive cracking in bone is also dependent on mineralisation, size, geometry and microstructure of the Haversian systems – demonstrating the importance of replicating the structure of bone to fully mimic the native tissue (341).

4.3.6. Rheological properties of hybrid hydrogels

The rheological properties of the hydrogels were also determined by performing oscillation rheometry. When conducting an amplitude sweep and frequency sweep, it is standard to first perform the amplitude test in order to determine the non-destructive deformation range, known as the LVE region, to identify a strain within this region for the frequency sweep. However, an amplitude test will lead to irreversible damage and destruction of the hydrogel, therefore, meaning double the number of samples would be needed to conduct both these tests. As the GelNB used in this study was scarce, it was decided to first perform the frequency test by using a frequency value predicted to be well within the LVE region so that hydrogel samples could then be re-used for the amplitude test. However, it is crucial to acknowledge that this would introduce a limitation into the study and so results are interpreted cautiously.

G' and G" are key concepts to understand when interpreting rheological data. G' represents the ability of a material to store energy deformation and describes the elastic/solid-like behaviour of a material, whereas G" provides insight into the ability of a material to dissipate energy and describes the viscous/liquid-like behaviour of a material (342). The balance between these moduli gives an insight into the overall viscoelastic behaviour of a material (343).

4.3.6.1. Frequency sweep (shear strain controlled)

A frequency sweep is used to investigate if a material behaves as a viscoelastic liquid or a solid-like gel and provides information on the behaviour and inner structure of the hydrogels (342,343). In a characteristic hydrogel-like material frequency sweep, G' and G" remain parallel across the frequency range; this was observed in GelNB-MP-Silica (1:1) aged for 7

days, and both ageing conditions for GelNB-MP-Silica (1:2) (Figure 83) (343,344). However, G' and G" are not parallel in either GelNB-Silica aged conditions, as well as GelNB-MP-Silica (1:1) aged for 1 day, suggesting that the response of the hydrogels is frequency-dependent.

In all hydrogel formulations, the G' values were higher than the G" values over the entire frequency sweep range. This confirmed the solid-/gel-like structure of all systems and that the elastic behaviour is always dominant when a load is applied (Figure 83) (345–349).

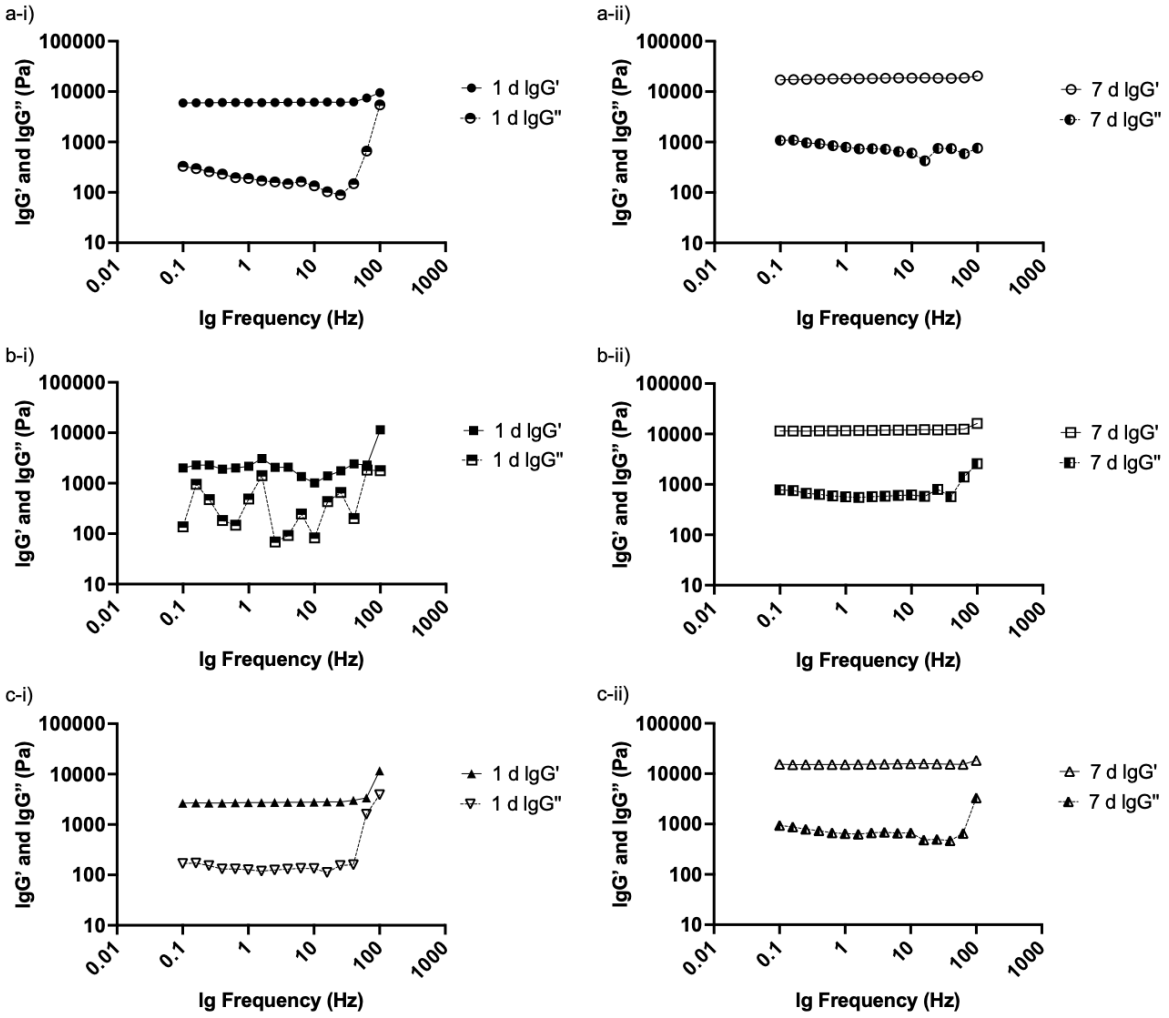


Figure 83. Frequency sweep shear strain controlled curves of a) GelNB-Silica, b) GelNB-MP-Silica (1:1), and c) GelNB-MP-Silica (1:2), aged for i) 1 day and ii) 7 days. G' and G" are shown as a function of frequency. Mean values are shown (n=3 [c-i; n=2]).

The higher G' and G" values at 7 days of ageing compared to at 1 day indicated improved stiffness as the hydrogel has aged (Table 5) (350).

*Table 5. G' and G" at 0.1 and 1 Hz, derived from a frequency sweep of three hydrogel formulations; GelNB-Silica (Class I), GelNB-MP-Silica (1:1) [Class II], and GelNB-MP-Silica (1:2) [Class II]. *Corresponds to the non-linear G" as observed in Figure 83b-i). Mean values are shown, along with SD (n=3 [c-i; n=2]).*

		0.1 Hz		**1 Hz**	
Hydrogel formulation	**Ageing time (day)**	**G' (mean ± SD)**	**G" (mean ± SD)**	**G' (mean ± SD)**	**G" (mean ± SD)**
GelNB-Silica	1	5,957 ± 422	329 ± 32	6,043 ± 411	189 ± 27
	7	17,167 ± 513	1,080 ± 106	18,033 ± 751	791 ± 84
GelNB-MP-Silica (1:1)	1	2,013 ± 299	137 ± 78	2,167 ± 643	489 ± 671*
	7	11,450 ± 420	779 ± 233	11,625 ± 320	568 ± 295
GelNB-MP-Silica (1:2)	1	2,655 ± 1,675	168 ± 71	2,715 ± 1,647	127 ± 36
	7	15,433 ± 7,594	942 ± 460	15,233 ± 6,992	649 ± 288

The non-linear G" seen in GelNB-MP-Silica (1:1) suggests the structure was not completely developed and was unstable (348). However, by 7 days, it can be assumed that the structure was further developed and more stable, due to the linear response, therefore supporting the idea that the hydrogel's structural integrity improved with time.

Jayash et al. (112) formulated a similar hydrogel system using silica synthesised from GLMS, but with chitosan as the biopolymer and investigated the impact of ageing on mechanical properties. Similarly, the G' and G" values in the chitosan-silica-based hybrid hydrogels increased at 7 days compared to when measured immediately after gelling, concluded to be as a result of polycondensation of the silica network (112). The values obtained in this present study were higher than the chitosan-silica systems, as the thiolated-chitosan-silica hydrogel reached a maximum G' value of 790 Pa after 7 days of ageing compared to >11,000 Pa for all three GelNB-Silica-based formulations (112). The differences observed here could be attributed to the higher proportion of silica precursor within the GelNB-Silica-based hydrogels (160 mg/mL of PGMS) compared to the chitosan-silica hydrogels (50 mg/mL of GLMS), leading to increased strength through a higher proportion of polycondensation of the

silica network (112). Additionally, the G' value of a pure GelMA hydrogel immediately after gelling was reported to be 275 ± 1 Pa, again lower than the 1 day values obtained here which were all >1,000 Pa (351). However, it is suggested that the variation in ageing time could contribute to the difference in G' observed, and so for a direct comparison the rheological properties of the GelNB-Silica-based hydrogels in the present study should be investigated immediately after gelling.

4.3.6.2. Amplitude sweep (strain-controlled)

An amplitude sweep strain test, sometimes referred to as an oscillatory stress sweep, is used to examine the viscoelastic behaviour of a material (342,345). It is used to identify the LVE region – the region in which the sample is not destroyed with increasing strain (343). In an amplitude test, there are two modes of controlling deformation: a strain sweep 'strain-controlled' and a stress sweep 'stress-controlled' (343). Using a strain-controlled test will result in results with varied stress, and vice versa (343). A strain-controlled mode was used here as this was the test routinely run using the rheometer. Specific features of an amplitude sweep indicate the properties of a material, for example:

- When G' > G", elastic response dominates over a viscous response and a material has a gel-like solid structure
- When G" > G', a viscous response dominates over an elastic response and material is fluid
- A constant G' with increasing strain is indicative of an elastic gel and,
- A crossover of G' and G" indicates a material has viscoelastic properties and the material begins to behave like a fluid (112,342,345).

The data showed that in all hydrogel formulations at both ageing conditions, G' > G", confirming the gel-like structure (Figure 84) (345–347).

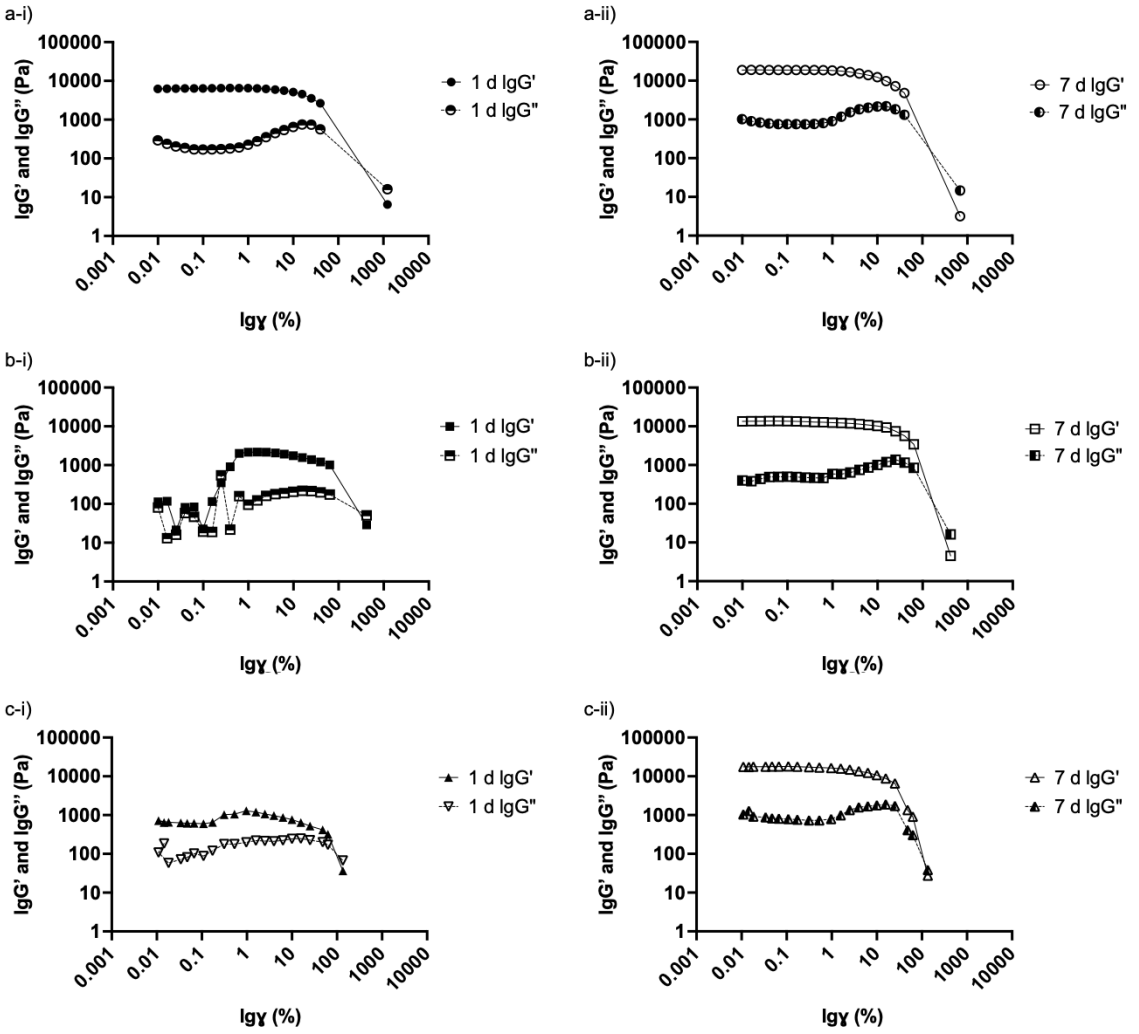


Figure 84. Amplitude sweep strain controlled curves of a) GelNB-Silica, b) GelNB-MP-Silica (1:1), and c) GelNB-MP-Silica (1:2), aged for i) 1 day and ii) 7 days. G'and G" are shown as a function of strain. Mean values are shown (n=3).

At low strains in the Class II formulations aged for 1 day, G' and G" are non-linear, showing inconsistencies before forming the LVE region around 1% strain (Figure 84b-i and c-i). The non-linear regions indicate that the hydrogel network may not be fully developed or there may be incomplete gelation. By 7 days, the crosslinking within the network is more developed, leading to a more stable network with a linear response to low strain (Figure 84b-ii and c-ii). This behaviour is not observed in either GelNB-Silica formulations (1 day vs 7 days), which suggests that by 1 day the hydrogel had gelled and stabilised.

Both the G' and G" LVE regions shift to higher values upon ageing in all three hydrogel formulations, indicating increased stiffness at 7 days (Figure 84). This shift has been previously reported to be a consequence of increased crosslinking and continued polycondensation of the silica network (112,345). The strain at which the G' LVE region became non-linear remained similar for hydrogels aged for 7 days, compared to 1 day.

The crossover points, where G' and G" intersect, indicate that all three hydrogel formulations are viscoelastic. Before the crossover point, the hydrogel has a gel-like structure and acts as a viscoelastic solid material, but when G' and G" crossed over the hydrogels begin to flow and demonstrate a dominant viscous behaviour (342,347). These intersection points remained similar when aged for 1 day compared to 7 days in each hydrogel formulation (Figure 84); this indicates that ageing did not impact the balance between the viscous and elastic properties of the hydrogels. However, the crossover point was at higher strain for GelNB-Silica and GelNB-MP-Silica (1:1) [γ = >100%], compared GelNB-MP-Silica (1:2) [γ = <100%]; a higher deformation was therefore needed to transition GelNB-Silica and GelNB-MP-Silica (1:1) to a viscous response, compared to GelNB-MP-Silica (1:2).

Jayash et al. (112) demonstrated a similar response in chitosan-silica hybrid hydrogels, observing an LVE region at lower strain, followed by an abrupt decrease in the elastic modulus and a crossover point at which the hydrogels became more viscous (112). The G' and G" values obtained in the present study were higher (G': ~10,000 Pa and G": ~1000 Pa) after 7 days of ageing [1% strain]) than those reported by Jayash et al. (112) (G': ~500 Pa and G": ~10 Pa after 7 days of ageing [1% strain]) indicating a stiffer hydrogel. The crossover point was at a lower strain in the GelNB-Silica-based hydrogels after 7 days of ageing (~100% strain) compared to the chitosan-silica hybrid hydrogels (>500% strain); this

suggests that the GelNB-Silica-based systems required a lower level of deformation for the material to behave like a fluid (112). The interpretation of these data in the context of application is key; the application of the chitosan-silica hydrogels was for drug delivery and so high stiffness values are not crucial.

4.3.6.3. Single frequency time sweep – gelation

A single frequency and amplitude time sweep was conducted after 2 minutes of mixing hydrogel starting reagents to determine microstructural evolution and gelation kinetics. Initially during the time sweeps, G" was greater than G', however, the G' and G" reached a crossover point (represented by arrows in Figure 85) just after the test was started. This initial G" > G' indicates that at this point, the hydrogel was in its sol state (352).

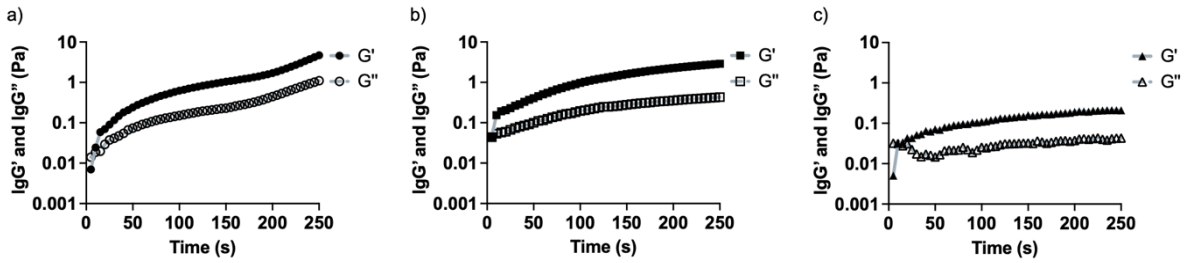


Figure 85. Single frequency time sweep showing gelatin kinetics of a) GelNB-Silica, b) GelNB-MP-Silica (1:1), and c) GelNB-MP-Silica (1:2). The arrows represent the crossover point in each hydrogel formulation (n=3).

The crossover point in a single frequency time sweep can define the gelation time of a hydrogel, suggesting that hydrogel gelation occurred almost immediately in all three formulations (345). A sample of each hydrogel was kept outside of the rheometer and observed using the tilt method, gelation was noted as a self-supporting hydrogel (151). At the time of the crossover point on the rheological data, the hydrogel had not gelled using the tilt method; the gelation time was ~12 minutes for GelNB-Silica and GelNB-MP-Silica (1:1),

and 40 minutes for GelNB-MP-Silica (1:2) using this method (Figure 73). The crossover and sharp increase of G’ and G” have previously been reported by Cai et al. (353) with the use of TEOS in a biopolymer-silica hydrogel formed via sol-gel. However, the crossover point was highlighted as sol particle condensation and a sol-gel transition, processes that would also be occurring in the GelNB-Silica-based sol-gel systems (353). Therefore, the G’ and G” crossover point may not be representative of gelation to the point of a self-supporting hydrogel, but instead more indicative of microstructural evolution and the point at which the network structure begins to form.

In GelNB-Silica and GelNB-MP-Silica (1:1), both G’ and G” showed a sharp increase within ~100 seconds, with a more obvious increase in G' which resulted in the initial crossover point (Figure 85a and b). The faster rate of increase of G’ and G” for GelNB-Silica and GelNB-MP-Silica (1:1) (Figure 85a and b), compared to GelNB-MP-Silica (1:2) (Figure 85c), indicates faster sol-gel reaction and gelation, and stronger gel formation (348,353). Dolinina et al. (311) investigated the relationship between gelation time and hydrogel formation in sol-gel synthesis, demonstrating that faster gelation led to the formation of hydrogels with more condensed and rigid structures, with higher density and lower porosity.

The time sweep measurement of GelNB-MP-Silica (1:2) clearly showed lower G’ values (Figure 85c), plateauing at ~0.1 Pa, whereas, for the other two formulations >1 Pa was achieved by 250 seconds (Figure 85a and b). This observation indicates a lower gel strength in GelNB-MP-Silica (1:2) and formation of a less condensed network and more flexible structure by the equivalent time in the other two formulations (311,348).

The time sweeps were conducted for each formulation in triplicate, however, there was poor reproducibility in the rheological data. This, coupled with the initial crossover point of G' and G", mean that a time sweep is not a reliable method to quantify gelation point in these hydrogel formulations, but it does give an indication of the increase in viscosity, structural development and strength over time. An alternative method, such as DLS, may be more appropriate for gel formation analyses (354,355).

4.3.7. Architectural characterisation

4.3.7.1. CryoSEM

CryoSEM was used to investigate the 3D microarchitecture of hydrolysed and condensed PGMS, gelled GelNB, and all three hydrogel formulations. Notably, the effect of sublimation time on the final image was investigated with GelNB-MP-Silica (1:1) aged for 7 days and a sublimation time of <6 minutes was found to result in inadequate structural information, particularly at 30 seconds and 1 minute (Figure 86). Therefore, a sublimation time of 6 minutes was used for all further samples.

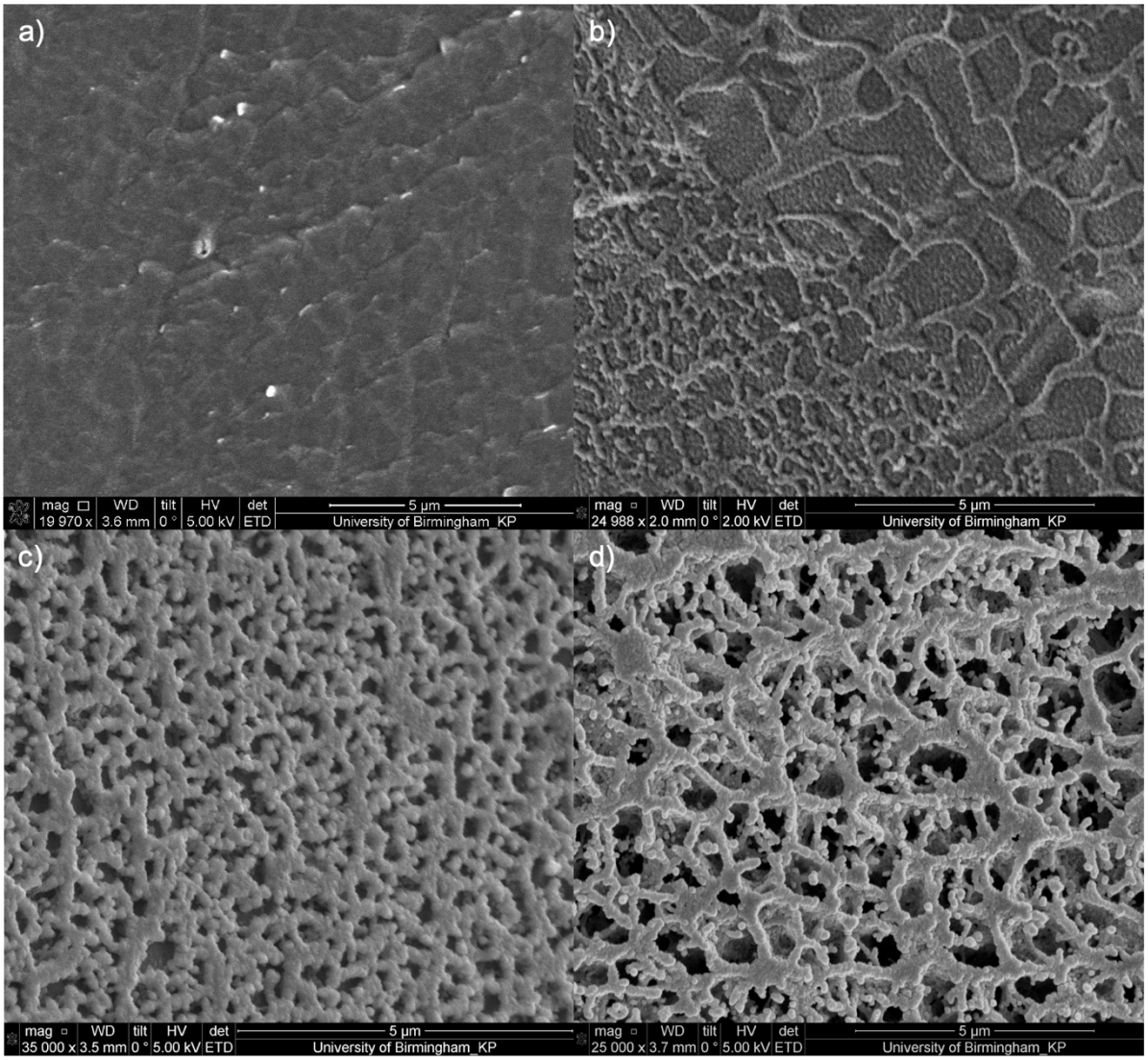


Figure 86. Representative cryo-SEM images of the GelNB-MP-Silica (1:1) hydrogel aged for 7 days, with sublimation time during sample preparation varied; a) 30 seconds, b) 1 minute, c) 2 minutes, and d) 6 minutes. Images were taken at variable magnification (a) 20,000x; b) 25,000x; c) 35,000x; and d) 25,000x. All are shown with a 5 µm scale bar.

Upon examination with cryoSEM, it was observed that hydrolysed and condensed PGMS in its gelled state formed a dense network with pore size <1 µm in diameter (Figure 87a), whereas irradiated, gelled GelNB, crosslinked with DTT produced a flake-like high density polypeptide network with larger pores, up to ~10 µm in size (Figure 87b) (356). The GelNB structure is similar to other gelatin-based materials, such as GelMA, observed using cryoSEM in literature (356–358). It should be noted that DTT was used here as the crosslinker because

preparation of cryoSEM samples necessitated gelation of GelNB, which cannot be achieved with MPTMS alone.

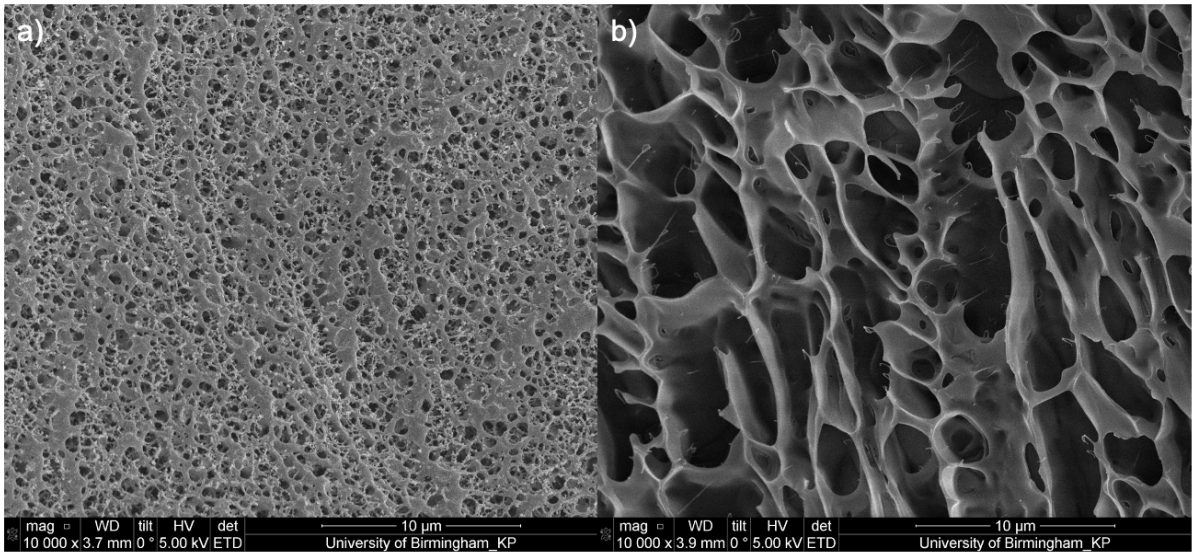


Figure 87. Representative cryo-SEM images of the inorganic and organic component of the GelNB-silica-based hydrogels; a) hydrolysed and condensed silica network from PGMS, and b) irradiated GelNB with DTT as the crosslinker (to ensure gelation for experimental set-up). Images were taken at 10,000x magnification. Both are shown with a 10 µm scale bar.

Hydrogel formulations aged for 1 and 7 days were also examined using cryoSEM (Figure 88). Overall, the inorganic silica phase was the dominant phase in the microarchitecture, as the structures at both 1 day and 7 days more closely resembled that from hydrolysed and condensed PGMS (Figure 87a). This was to be expected due to the higher ratio of inorganic to organic in the hydrogels (40:60 wt% organic to inorganic).

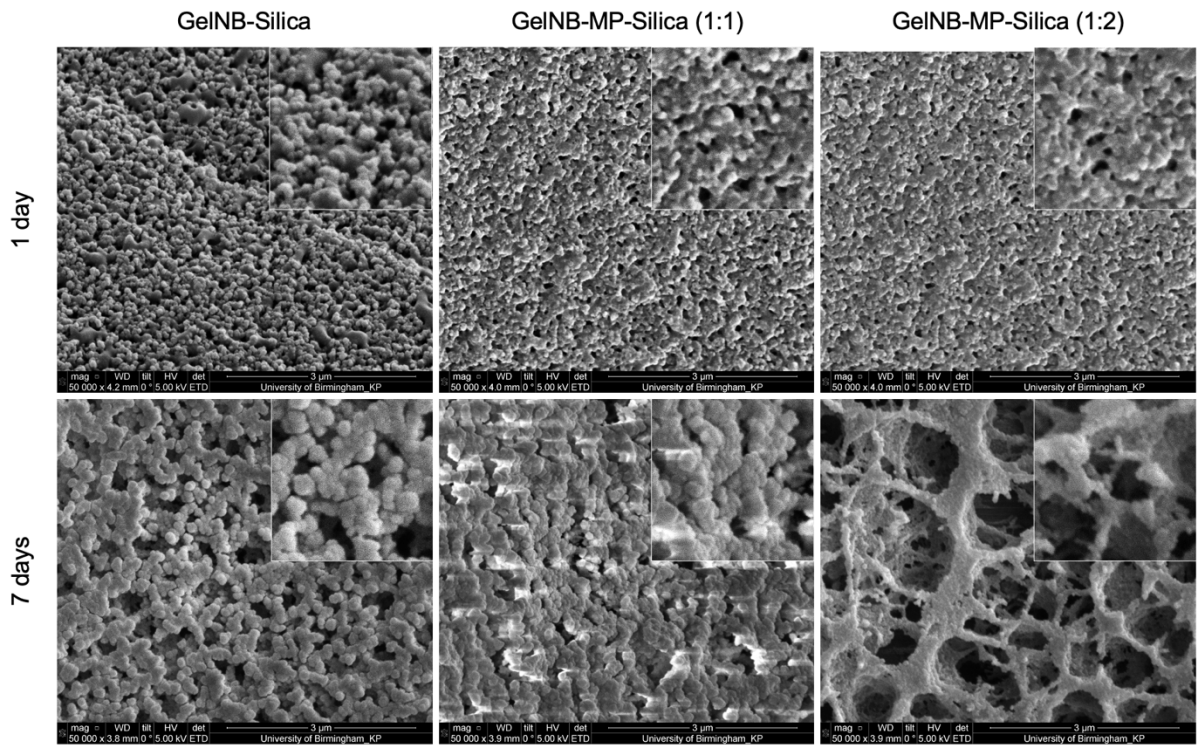


Figure 88. Representative cryo-SEM images of GelNB-Silica, GelNB-MP-Silica (1:1), and GelNB-MP-Silica (1:2), aged for 1 day and 7 days. Images were taken at 50,000x magnification. All images are shown with a 3 μm scale bar. Insets demonstrate a magnified sample of the image.

After 1 day of ageing, all three hydrogel formulations had a dense network with aggregates of spherical submicrometre-sized silica particles, with submicrometre-sized interstices forming the pore structure (Figure 88). This microarchitecture has been observed in other silica-containing organic-inorganic hybrid materials (359). The notable differences between the formulations after 1 day of ageing were the silica particles appeared more discrete in GelNB-Silica compared to the particles in the Class II hydrogels having a merged and less distinct particle appearance (Figure 88).

By 7 days of ageing, the silica particles increased in size in both GelNB-Silica and GelNB-MP-Silica (1:1), and remained discrete in the GelNB-Silica hydrogel and agglomerated in the GelNB-MP-Silica (1:1) hydrogel (Figure 88). However, the microarchitecture of GelNB-MP-

Silica (1:2) changed largely after ageing, exhibiting a more webbed network, composed of agglomerated silica particles with large micrometre-sized voids (Figure 88).

Being able to control microarchitecture features of hydrogels within tissue engineering constructs will allow for better control of cellular adhesion, proliferation, migration and differentiation (1). Various pore sizes have been reported in the literature for BTE, ranging from 20–1,500 μm for scaffolds (360–366). The larger pores and more porous structure in GelNB-MP-Silica (1:2) could have a more positive role on enabling initial cellular migration into the hydrogel, however, the pores are <5 μm and so still far from optimum (20–1,500 μm) for the required pore size for cell migration and bone formation (Figure 88).

4.3.8. Biological characterisation

4.3.8.1. Cell viability

The effect of hydrogel formulation on the viability of Saos-2 cells, commonly used to model human osteoblasts, was investigated. Saos-2 cells were cultured on the surface of a tissue culture plastic control, as well as the three hydrogel formulations, and a LIVE/DEAD assay was used to visualise cell morphology over 7 days (Figure 89), as well as quantify cell viability at 1 and 3 days.

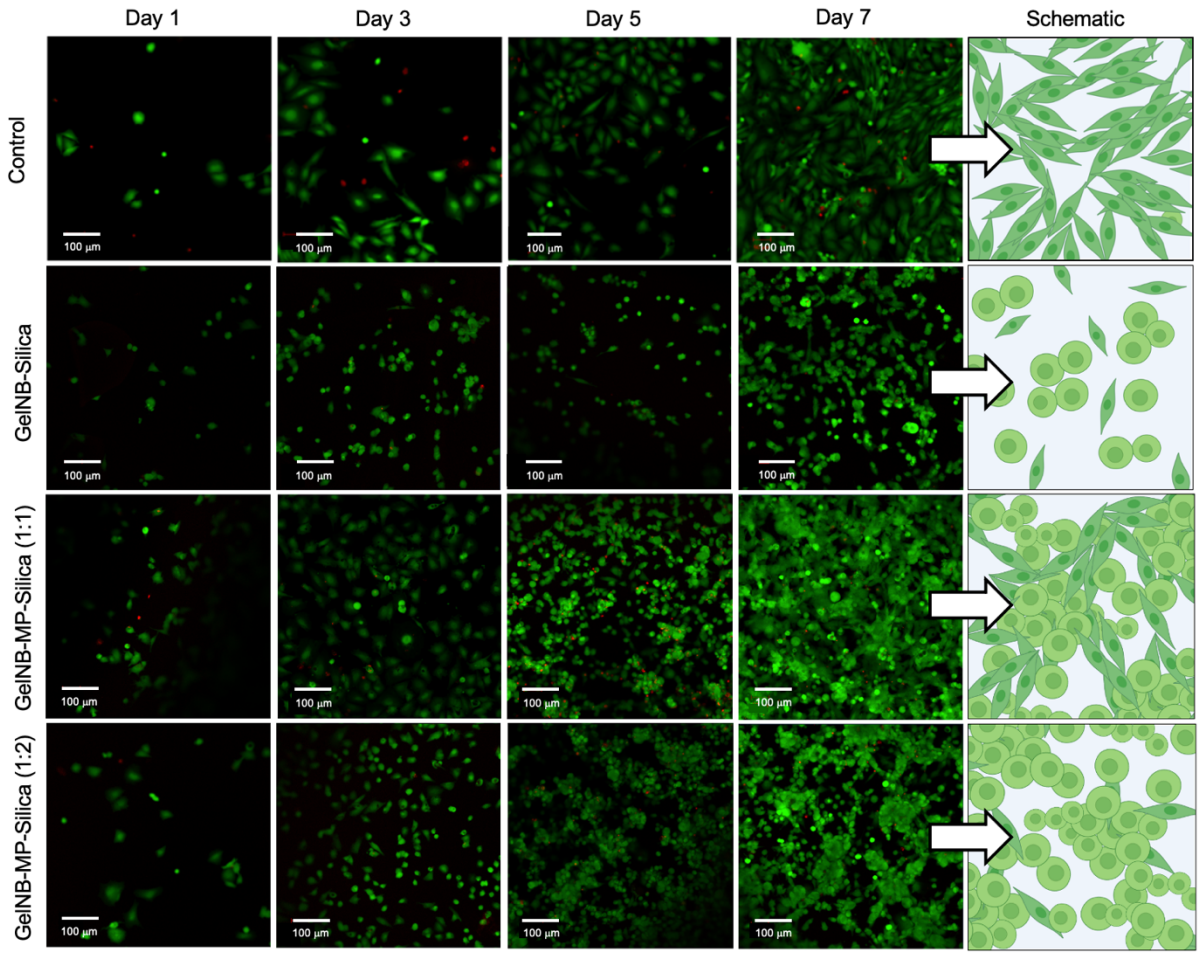


Figure 89. Representative confocal fluorescence microscopy images of 2D-cultured Saos-2 cells for LIVE/DEAD staining on a tissue plastic culture control and three hydrogel formulations; GelNB-Silica, GelNB-MP-Silica (1:1), and GelNB-MP-Silica (1:2) at 1, 3, 5 and 7 days of culture. Images were taken using 494/517 nm (excitation/emission [calcein; live]) and 528/617 nm excitation/emission [ethidium homodimer-1; dead]). An illustration of the live cells at day 7 is presented. Scale bar = 100 µm (biological repeats n=2, technical repeats n=3 due to time constraints). Part of this figure was created on the BioRender website (https://biorender.com) by the author.

The density of cells appeared to increase over the course of the 7 days of culture for all three hydrogel formulations, as well as the control. There were a lower number of Saos-2 cells visible on GelNB-Silica hydrogels, with a rounded morphology dominating for the 7 days of culture. Saos-2 cells began spreading by day 3 on the Class II hydrogels and control, as evidenced by their more elongated morphology. At day 5 this continued for GelNB-MP-Silica (1:1) and by 7 days of culture on GelNB-MP-Silica (1:1), the cells appeared to have formed an interconnected network with cells exhibiting both elongated and round morphology. With

GelNB-MP-Silica (1:2), Saos-2 cells stopped spreading and began to aggregate in the GelNB-MP-Silica at 5 days, continuing to 7 days. The shape of the aggregation of cells was similar to the void formation in the image taken using cryoSEM for 7 day-aged GelNB-MP-Silica (1:2) (Figure 88). Overall, the cells had a more aggregated formation on the Class II hydrogels compared to the control and Class I GelNB-Silica.

The number of live and dead Saos-2 cells was quantified for day 1 and 3 only due to difficulty distinguishing individual cells for counting at day 5 and 7 due to increased cell number, spreading, and aggregation. All three hydrogel formulations had >70% mean cell viability up to day 3 (Figure 90). International Organisation for Standardisation (ISO) guidelines state that a material with cell viability <70% is considered cytotoxic, indicating that all three formulations were not cytotoxic up to 3 days of culture (367).

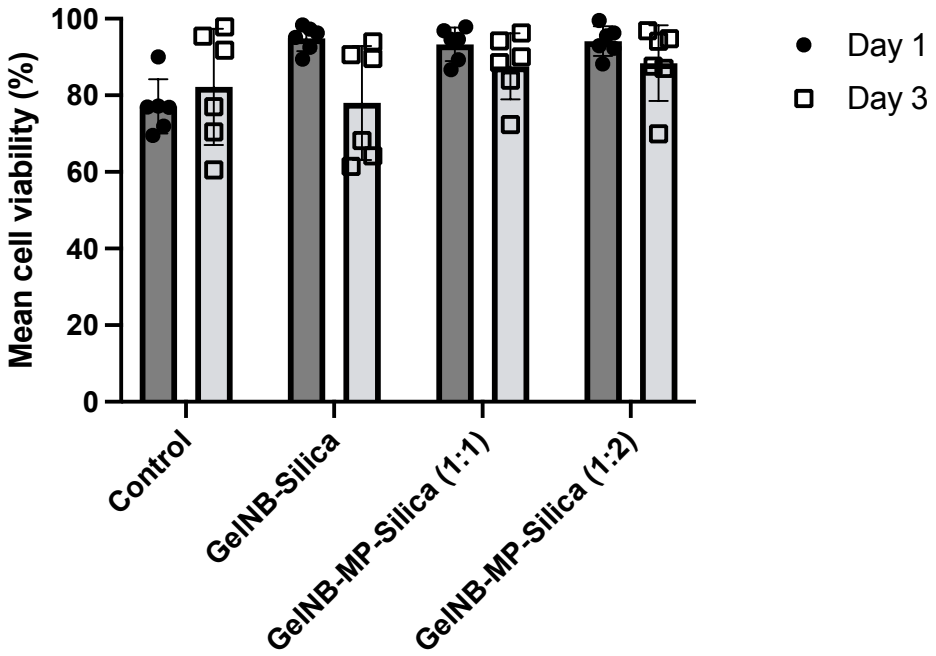


Figure 90. Saos-2 cell viability (%) from LIVE/DEAD at day 1 and day 3 of culture, the control was carried out on tissue culture plastic. Images were taken using confocal fluorescence microscopy and counted with Image J. The points plot on each bar represent the repeat measures and the error bars represent the SD (biological repeats n=2, technical repeats n=3 due to time constraints).

Additionally, there was no significant difference between cell viability of any of the hydrogel formulations for day 1 or day 3 of culture, as well as no difference when compared to the tissue culture plastic control. The mean cell viability on day 1 was higher for all three hydrogel formulations compared to the control, however, the differences were not statistically significant. The mean cell viability did decrease for the hydrogel formulations from day 1 to day 3, although again, the decrease was not statistically significant. These results indicate that the hydrogels were able to provide a non-cytotoxic environment that was similar to the control for up to 3 days of culture.

Metabolic activity of Saos-2 cells over a 14-day period was assessed using a PrestoBlue assay. Metabolic activity, as measured by fluorescence (560/590 nm), increased over the course of the 14 day culture period for the control, whereas the metabolic activity only began to increase at day 14 for the cells cultured on the hydrogels (Figure 91). This was an unexpected finding after having completed a LIVE/DEAD and actin/DAPI stain, which showed cell viability and spreading. A reason for this could be the cell seeding density (2.5 x 10^3) was too low which caused issues with sensitivity; future work should explore this experimental technique but using a higher cell seeding density to be able to test this hypothesis.

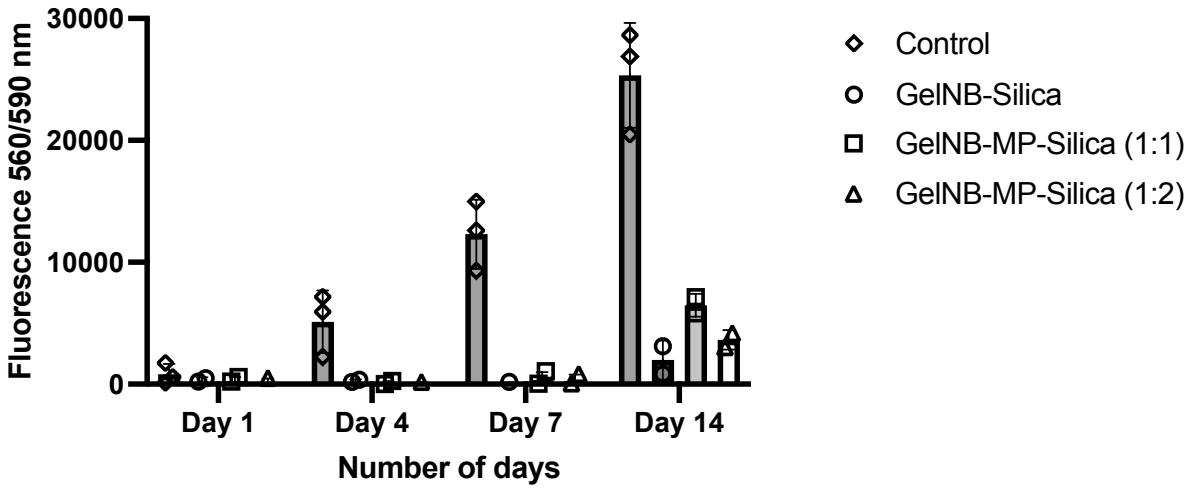


Figure 91. Mean metabolic activity of Saos-2 cells cultured for 14 days on a control (tissue culture plastic), and three hydrogel formulations; GelNB-Silica, GelNB-MP-Silica (1:1) and GelNB-MP-Silica (1:2). The points plot on each bar represent a repeat measure and the error bars represent the SD (biological and technical repeats n=3).

4.3.8.2. Cell spreading and morphology

Actin/DAPI staining was used to qualitatively assess cell morphology and spreading of the Saos-2 cells when cultured on the hybrid hydrogels (Figure 92). Up to 4 days of culture, the Saos-2 cell morphology on the GelNB-Silica were mostly round and had no cell cytoskeleton

organisation. By day 7 and 14, the cells showed cytoskeleton organisation but still less confluence with respect to cell number and spreading, than in Class II hydrogels. The organisation of the cytoskeleton of Saos-2 cells cultured on Class II hydrogels was visible by day 1, particularly in GelNB-MP-Silica (1:2). Cells also demonstrated greater cytoskeleton organisation and confluence by day 14, compared to GelNB-Silica, presenting with a greater density of actin stress fibres by day 14. Hydrogel formulation also impacted cell density with a higher cell density on Class II hydrogels after 14 days, compared to GelNB-Silica, forming a confluent network of cells. The size of Saos-2 cells on the Class II hydrogels at day 14 appeared larger than those growing on the tissue culture plastic, although this was not quantified beyond use of the scale bar. The lower cell density and less visible cytoskeleton fibres qualitatively observed on the cells on GelNB-Silica, compared to a higher cell density with significantly higher level of cell proliferation on the Class II hydrogels is a similar finding to the results from the LIVE/DEAD. These results indicate that incorporation of a covalent crosslinker between GelNB and Silica markedly facilitated cell adhesion and proliferation on the surfaces of GelNB-based hydrogels.

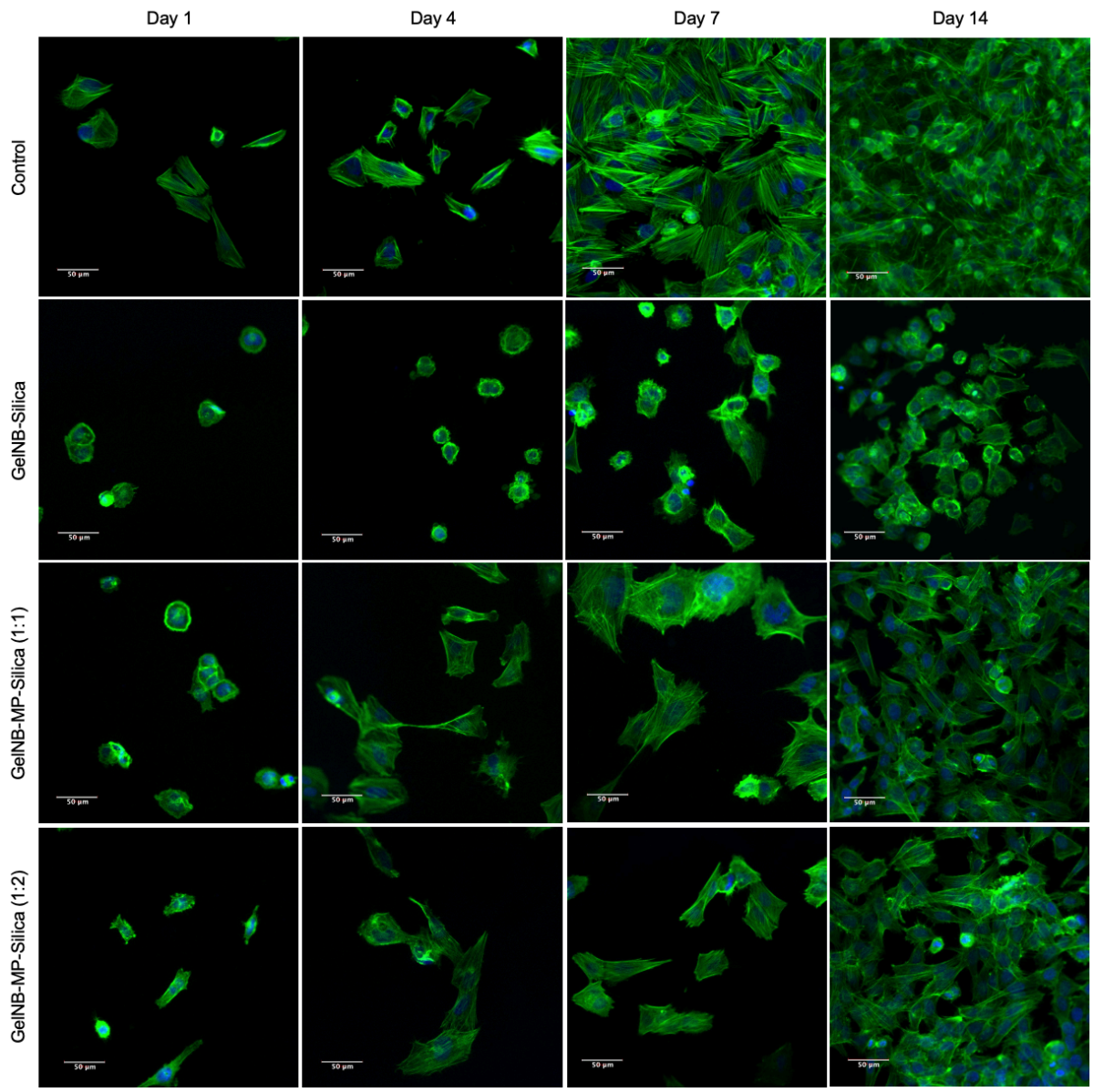


Figure 92. Actin/DAPI images of Saos-2 cells cultured for 1, 4, 7 and 14 days on three hydrogel formulations; GelNB-Silica, GelNB-MP-Silica (1:1) and GelNB-MP-Silica (1:2) and a control (tissue culture plastic). Phalloidin was used to stain the actin cytoskeleton and DAPI to stain the cell nuclei. Fluorescence images taken with confocal fluorescence microscopy of actin and nuclei at 495/518 nm (actin) and 358/461 (DAPI). The images were collected with a magnification of 20x and the scale bar = 50 μm (biological and technical repeats n=3).

The difference in cell morphology, colony formation and cytoskeletal expansion seen between the Class I and Class II hydrogels may be due to the differences observed in the mechanical properties. In Section 4.3.5, a key overall finding was that the compressive mechanical properties of the Class II hydrogels, namely the compressive strength and

stiffness, increased over the course of the ageing period. Changes in the mechanical properties of the GelNB-Silica hydrogel were more inconsistent; uniaxial compressive mechanical properties were generally maintained until 7 days, at which point strength and stiffness began to decrease. Whereas, the mechanical properties of the GelNB-Silica hydrogel increased in the cyclical compressive and rheological tests. Differences in biophysical cues, such as changes in stiffness, have been shown to impact cell spreading, differentiation and migration (58–61). For example, a hydrogel with a varying stiffness gradient (20 kPa to 300 kPa) had the ability to induce different cellular differentiation depending on the stiffness domain the cells were cultured on (57). The viscoelasticity of a hydrogel has been found to promote and regulate the proliferation of cells (68,73). The mechanical remodelling involved in hydrogels with faster stress-relaxing matrices has been shown to result in cell spreading, proliferation, and matrix formation (68,69). This demonstrates how mechanical remodelling in the Class II hydrogels could result in different cellular responses over time, compared to the GelNB-Silica which did not undergo the same mechanical response.

Based on the results from the mechanical and biological studies, it is suggested that the MPTMS-facilitated and silica-based covalent crosslinked network is continuously forming as the Class II hydrogels age. In turn, this could be providing a dynamically changing hydrogel system that results in developing mechanical properties which influence the biophysical cues that cells are exposed to over time.

Alizarin Red S staining was used in an attempt to observe calcium deposition on the hydrogels after Saos-2 cells were cultured for 14 days. Alizarin Red S is a calcium ion-specific stain used to visualise and quantify deposition of calcium and mineralised bone tissue. The aim was to stain the hydrogels and their blanks, which had been cultured under

the same conditions but without cells, and then obtain the absorbance reading of the de-stain. The ‘background’ absorbance from each blank would then be removed from the experimental absorbance to show the absorbance from just the calcium deposition.

The results were unexpected as the blank hydrogels absorbed the Alizarin Red S stain which meant when observed using fluorescent microscopy for qualitative analysis, they appeared stained red (Figure 93b–d). This made it difficult to distinguish true calcium deposits. However, it appears as though mineral content may be visible on GelNB-MP-Silica (1:1), due to the difference in appearance of the texture of the hydrogel compared to its blank, however, the stained background in the hydrogel made it hard to distinguish this difference (Figure 93c). The intention of including blank hydrogels was to ensure the absorbance values were representative of the calcium deposits. As the hydrogels absorbed the stain, when de-staining was conducted, remnants of the stain remained trapped and absorbed within the hydrogel. Therefore, the ‘background’ from the control may not accurately reflect a true baseline and introduces uncertainty into the use of this technique. This meant when calcium deposition was quantified with absorbance values, the results were not reproducible.

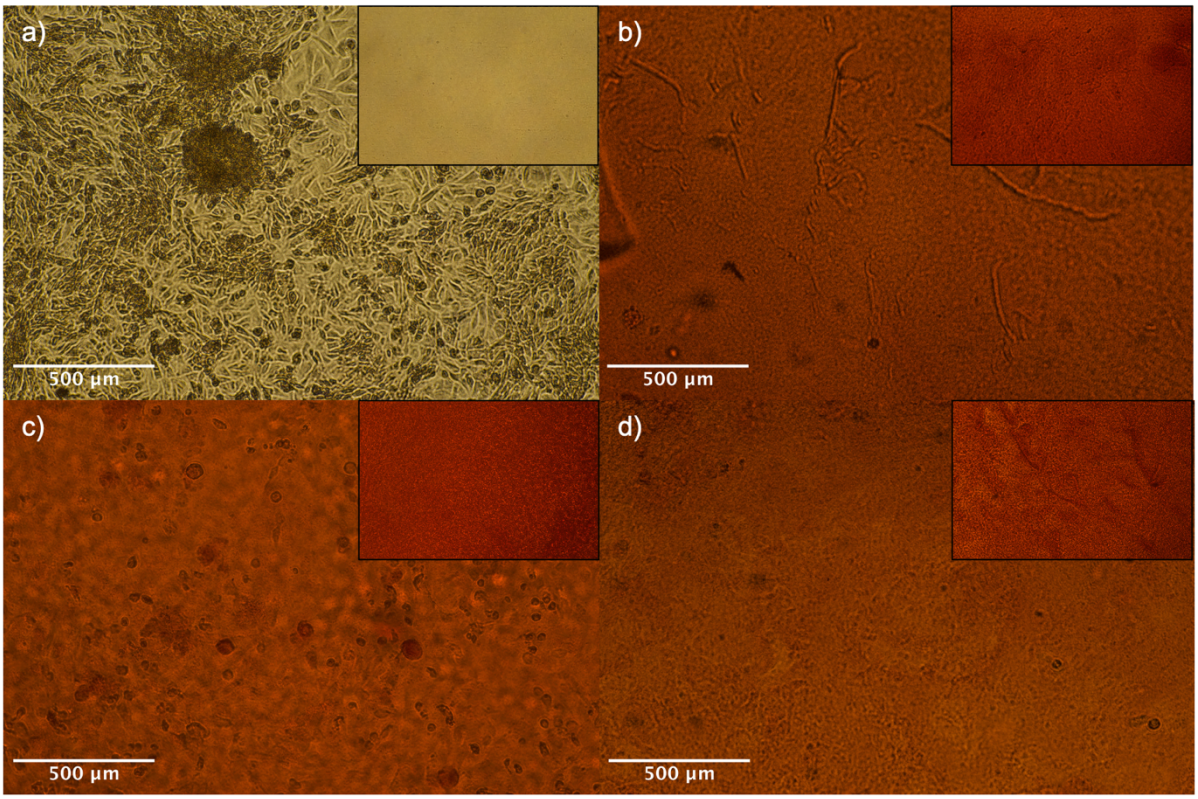


Figure 93. Representative images taken from Alizarin Red S staining of Saos-2 cells cultured for 14 days on a) control (tissue control plastic, b) GelNB-Silica, c) GelNB-MP-Silica (1:1) and d) GelNB-MP-Silica (1:2). Insets represent the blank images taken for each condition, where no cells were cultured. Images were taken at 10x magnification, and the scale bar represents 500 µm (biological and technical repeats n=3).

The dyeing of the hydrogel with Alizarin Red S stain could be attributed to excellent dye adsorption properties of silica due to the high specific surface area and surface charge (368). Capeletti et al. (369) demonstrated the specific binding of the Alizarin Red complex with a silica matrix to result in an encapsulated Alizarin Red species. Silica hydrogels are hydrophilic and when left to swell in a dye solution, dye molecules can transfer from aqueous solution and adsorb to the hydrogel surface through non-covalent interactions such as van der Waals interactions or hydrogen bonding (370,371). Additionally, the complex compositions of the culture medium used in the experiments could contribute to calcium ion-specific dye adsorption in two different ways. The DMEM media used to synthesise the hydrogels contains $CaCl_2$ which introduces calcium into the hydrogel, resulting in calcium-ion binding

of the dye (310). The medium used for culture has also been supplemented with FBS, which includes salts of calcium, and if not fully removed during washing could result in the stain binding (372). These results highlight the limitations of Alizarin Red S staining when using these GelNB-Silica-based hydrogels.

4.3.8.3. Cell migration

Light sheet fluorescence microscopy was employed to image hydrogels and investigate if cells cultured on the surface were able to penetrate within the hydrogel. Images were analysed to quantify cell migration and distribution. Images taken of GelNB-Silica had notably fewer cells inside the hydrogel. Representative light sheet microscopy data are shown in Figure 94.

After 7 days of culture, Saos-2 cells migrated within the hydrogels in all formulations (Figure 94). The maximum depth after 7 days of culture on GelNB-Silica was 1300 μm, however, only a few cells reached between 1,000–1,300 μm in depth, with most cells' location <800 μm (Figure 94a). Cells migrated furthest in GelNB-MP-Silica (1:1), with a maximum penetration depth of ~2,300 μm and then ~1,500 μm in GelNB-MP-Silica (1:2) (Figure 94b and c).

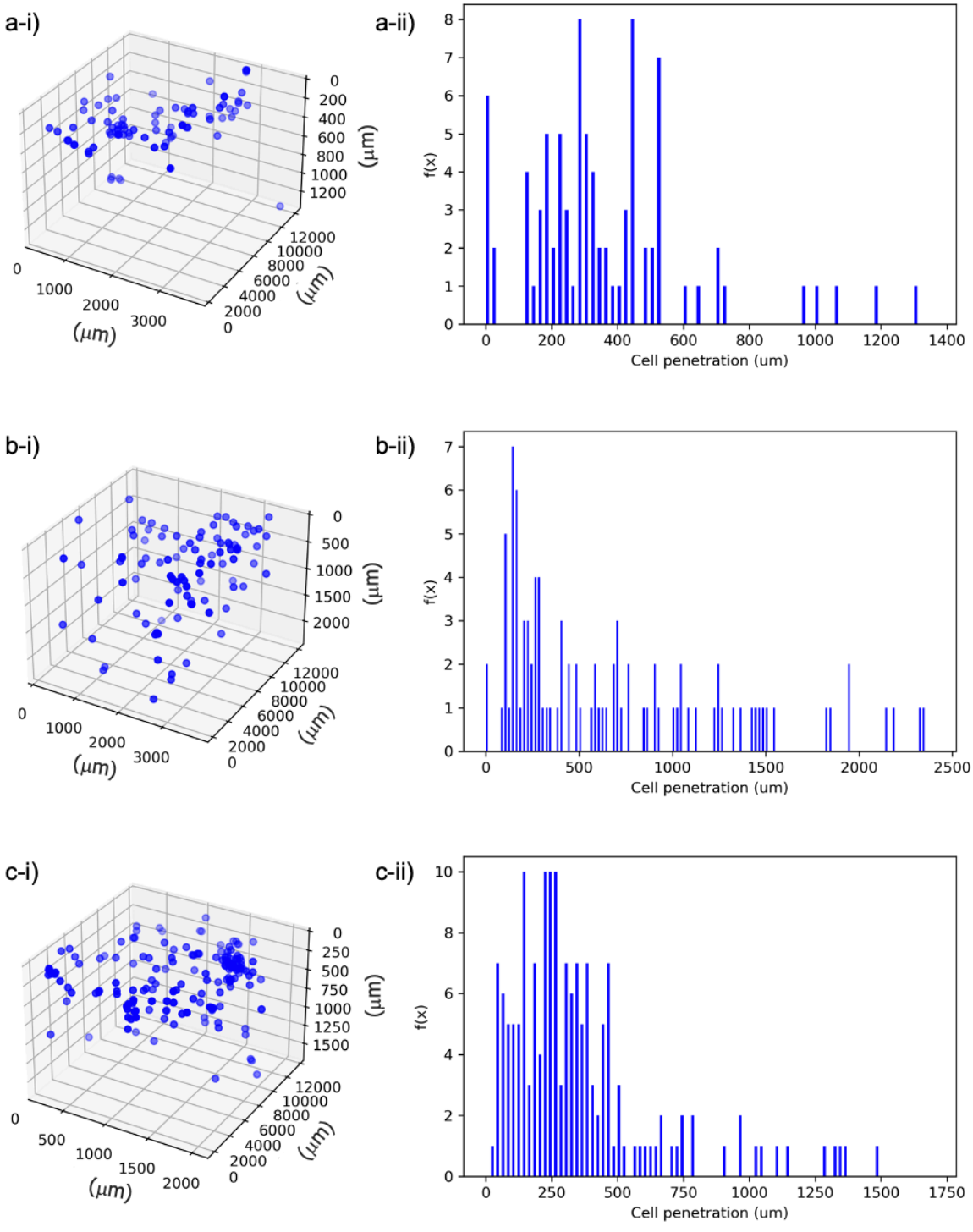


Figure 94. Representative light sheet fluorescence microscopy data for Saos-2 cells cultured on a) GelNB-Silica, b) GelNB-MP-Silica (1:1) and c) GelNB-MP-Silica (1:2) for 7 days, showing i) a 3D scatterplot of cell location within hydrogel samples and ii) the frequency of cells at a specific cell penetration. Note the different axis scale for different samples (biological and technical repeats n=3)..

Although there are a lack of studies reporting cell penetration for hydrogel systems similar to those used in the present study, cell penetration has previously been achieved in PEG-based hydrogels cultured with MSCs (373). The cells cultured on the GelNB-based hydrogels in this present study were able to achieve further depth penetration, compared to the PEG-based hydrogels (500 μm after 10 days of culture) (373).

Additionally, the improved cell penetration in the Class II hydrogels, specifically GelNB-MP-Silica (1:1), indicates that the inclusion of MPTMS-based covalent crosslinks is resulting in properties that are better able to modulate cell invasion when compared to GelNB-Silica (374). It has been suggested numerous times throughout this chapter that the Class II hydrogels experience changes in their mechanical properties over time due to the evolving MPTMS-facilitated and silica-based covalent network, which in turn, could impact the biological properties and direct cell behaviour due to changes in biophysical cues (1).

4.4. Summary

The overall aim of this chapter was to improve the gelatin-based functionalisation reaction by using click chemistry to synthesise an organosilane-functionalised gelatin-based product. The use of a thiol-ene click chemistry reaction to couple GelNB and MPTMS, for use in GelNB-Silica-based hybrid hydrogels was investigated. The optimum conditions for the thiol-ene reaction were determined as a 2:1 thiol- to -ene ratio and 0.03 wt% LAP, under these conditions the reaction reached completion in less than 30 seconds of irradiation.

The presence of MPTMS, forming a Class II hybrid, led to hydrogels with dynamic mechanical properties that developed over time, specifically, an increasing strength and stiffness. This indicates that the presence of covalent crosslinking in hydrogels plays a key role in creating a hydrogel that mechanically evolves with improving structural integrity over time. CryoSEM images showed that the hydrogels possess different microarchitectures and revealed a texture resulting from a merged and less distinct particle appearance in the Class II hydrogels, compared to the Class I hydrogel.

Biological studies revealed notable differences in Saos-2 cellular interactions with the different hydrogel formulations. The incorporation of covalent crosslinks between GelNB and silica seemed to markedly facilitate cell adhesion, migration and organisation. Light sheet images revealed cellular penetration from the hydrogel surface, reaching depths up to 2,300 μm after 7 days of culture. The results demonstrate the influence of hydrogel mechanical properties on the regulation of cellular behaviour.

CHAPTER 5. SUMMARY OF RESULTS AND CONCLUDING REMARKS

5.1. Summary of results

The aim of this thesis was to develop new organic-inorganic hybrid hydrogels for tissue engineered *in vitro* models of bone using sol-gel processing.

The primary objective of the work described in Chapter 2 was to investigate the interaction of gelatin (organic) with polyol-modified silanes (inorganic) when creating hybrid hydrogels. The hydrogels employed GPTPGS as the crosslinker in Class II hydrogels; GPTMS is a coupling agent extensively used in similar hybrid systems but was here modified with PG to replace the methoxy groups in the silyloxy functionality. A variety of Class I and Class II gelatin-silica-based hydrogels were fabricated and characterised with respect to their phase separation, gelation properties and behaviour at different pH values. Phase separation, precipitation and turbidity were common when mixing gelatin with polyol-modified silanes, suggested to be due to unfavourable interactions between the components. These outcomes were particularly prominent when the hydrogel formulations had similar proportions of the organic and inorganic components, i.e. 40:60 or 60:40 (O:I). Here, controlling the reagent concentration proved to be the most appropriate method to regulate phase separation. These results, as well as the limited load-bearing capability of the hydrogels due to phase separation and precipitation, confirmed the need to investigate the material interactions between the organic and inorganic components in gelatin-silica-based hydrogel systems in more detail, starting by focusing on the functionalisation reaction between gelatin and GPTMS.

The primary objective of the work described in Chapter 3 was to study and optimise the reactivity of epoxide electrophiles with gelatin. Significant challenges emerged during this work, including solution gelation which was hypothesised to be as a consequence of premature hydrolysis of the trimethoxylsilyl groups in GPTMS and condensation, pH increase of the reacting solution over the duration of the functionalisation reaction which was also suggested to lead to premature gelation of the reacting solution, and excess GPTMS and reaction by-products remaining within the functionalised product. Therefore, dialysis was utilised as an effective post-processing step to remove small-molecule impurities. To the best of our knowledge, this is the first study to use dialysis to remove excess and undesirable small-molecule by-products in GPTMS functionalisation of gelatin. Results indicated pH played a key role in the efficiency of the functionalisation reaction and it is suggested that pH also impacted the reactivity of the epoxide with amine and carboxylic acid nucleophilic side chains in gelatin, and therefore, could influence position of conjugation on gelatin. It is suggested that in mildly acid pH (~pH 5), the site of conjugation is predominantly on the glutamic acid (carboxylic acid) residues of gelatin. At more basic pH (~pH 8), which occurred when reactions ran for longer durations (>8 hours), reaction through the lysine amino side-chain occurs. A degradation study revealed that when excess GPTMS was removed from the functionalisation product via dialysis and Gel-GP was used to make a hydrogel, there was no difference in degradation rate, as determined by mass loss, between the dialysed hydrogel with the Class I hybrid. This raised questions around the efficiency of the gelatin-GPTMS functionalisation reaction and the extent of GPTMS-facilitated crosslinks in the organic-inorganic network. Insights on the functionalisation reaction mechanisms, including issues around hydrolysis of trimethoxysilyl groups, allowed method optimisation to extend the reaction time. Different solvents were used to perform the reaction and to extend functionalisation time, in an attempt to increase the degree of functionalisation. A series of

characterisation techniques, including titrations, were used in an attempt to further confirm the position of conjugation of GPTMS on gelatin. As far as we are aware, this marks the first use of a titration as a characterisation technique to indicate successful carboxylic acid functionalisation of gelatin with GPTMS. By using DMSO as a solvent, it was possible to extend functionalisation time up to 72 hours and alter the position of conjugation to involve amine conjugation, again, attributed to the higher pH within this reaction (~pH 8). However, the efficiency of the epoxide-based gelatin functionalisation reaction remained an issue and confirmed the need to explore alternative routes for functionalisation of gelatin.

In Chapter 4, the primary objective of this work was to use a thiol-ene click reaction as an alternative method to synthesise organosilane-functionalised gelatin for use in hybrid hydrogels. The thiol-ene reaction conditions were investigated, focusing on irradiation time, thiol- : -ene ratio and photoinitiator concentration; the reaction was complete in less than 30 seconds using a 2:1 (thiol- to -ene) ratio and 0.03 wt% of LAP. Hydrogels with two different dH_2O:media (DMEM) ratios were used. Covalent crosslinking, facilitated by the MPTMS organosilane, in Class II hydrogels resulted in dynamic mechanical properties over time. All compressive and rheological tests demonstrated the compressive strength and stiffness of the Class II hydrogels increased with ageing time. This was also observed in the Class I formulation but less consistently. However, there was a lack of difference in the degradation rate between the hydrogel formulations which was unexpected, and so, further studies investigating degradation rate between formulations are suggested.

Higher Saos-2 cell spreading was observed on the Class II formulations using Actin/DAPI staining and fluorescence microscopy. Additionally, Saos-2 cells migrated from the surface of the hydrogels achieving penetration depths of up to ~2,300 μm in a Class II formulation, as

observed by light sheet fluorescence microscopy. Finally, cryoSEM revealed subtle differences in the microarchitecture of the hydrogels: Class II hydrogels had a merged and less distinct particle appearance compared to the Class I hydrogel, where the silica particles appeared more discrete. We hypothesise that the dynamic mechanical properties of the hydrogels and differences in microarchitecture influence cell attachment, migration, spreading and location.

5.2. Limitations

Although the present work has provided valuable insights into hydrogel formulation, it is important to acknowledge the need for further studies.

5.2.1. Materials used and their limitations

Gelatin and gelatin-based alternatives experience batch-to-batch variation in their composition as they are naturally derived polymers, which affects difficulties in consistency and controllability of material formulation (181,375). The use of alternative, less complex naturally derived biopolymers, such as chitosan or synthetic peptides, could provide products with more consistent physicochemical properties. Similarly, it is important to recognise the reproducibility issues that could arise from the synthesis and use of PGMS in hydrogel formulation. PGMS is hygroscopic and readily undergoes hydrolysis and condensation when exposed to moisture in the air, which meant there could be variations in the chemical structure due to inconsistent H_2O content and variable crosslinking, ultimately impacting the properties of PGMS and the subsequent hydrogels produced. Strategies were put in place to enhance the reproducibility of PGMS, such as dispensing smaller volumes of synthesised material from larger batches to minimise repeated exposure to moisture during handling, as well as storing the PGMS under an argon atmosphere.

5.2.2. Potential adverse cell-material interactions

Although Saos-2 cells are commonly used to model human osteoblast cells, instability has been observed in Saos-2 cells in long-term culture (376). To lower the impact of variability in cell behaviour from passage differences and maintain consistency, cell passage number was <25 across and within cell culture experiments. It is recommended that future cell work should be conducted using MSCs as they better mimic natural conditions and should provide more relevant results (377).

5.3. Concluding remarks

The findings from initial work described in Chapters 2 and 3, led to the development of an alternative functionalisation method, summarised in Chapter 4; this work produced novel MPTMS-functionalised GelNB for gelatin-silica-based hybrid hydrogels. The work presented in this thesis supports the development of cleaner and quicker chemical reactions, such as thiol-ene click chemistry, to modify biopolymers with an organosilane for use in hybrid hydrogels. The formulated Class II hybrid hydrogels demonstrated some beneficial properties for BTE, such as cell interactions, however, the low mechanical strength limits their suitability and attempts should be made to improve this. This thesis presents the complexity of developing hydrogels and the need to understand the chemistry involved in component interactions. An interdisciplinary approach, including chemistry, materials science and cell culture, was taken to gain a comprehensive understanding of the field of tissue engineering. The pathway towards successful *in vitro* modelling for tissue engineering remains complex and is one that requires thorough materials characterisation as the first step. Materials must bio-physicochemically cue cells over a timescale that mimics the complexity of bone to achieve successful bone tissue models; this includes dynamic and suitable mechanical properties, porosity for cellular migration, and relevant biological properties that facilitate

cell-material interactions and mineralised tissue formation. Material design must continue to advance in order to achieve physiologically relevant tissue mimics as an ideal *in vitro* tissue model for beneficial clinical application.

CHAPTER 6. FUTURE WORK

To develop and build on the findings of this research, the following studies have been identified as areas for further work:

CHAPTER 2

- In Chapter 2, analysis of the interactions between gelatin and its derivatives with silica precursors were performed qualitatively, involving visual observations and assessments based on phase separation, precipitation and opacity. Therefore, it is important that methods of characterising the interactions between gelatin and silica are further developed to better quantify the nature of the interactions between the inorganic and organic components in order to answer some of the uncertainties that remain. Future work should use SAXS to quantify microstructure evolution and evaluate the impact of varying the hydrogel formulation on phase separation within each network by determining turbidity and scattering intensity. Such studies would give a better understanding of the interactions between gelatin and silica and allow for development of processes to address and improve the interactions.

CHAPTER 3

- In Chapter 3, a variety of characterisation techniques (^{1}H NMR spectroscopy, titrations and a ninhydrin assay) were used to analyse the product of the GPTMS functionalisation of gelatin under different reaction conditions (i.e. using alternative solvents and reaction durations). Future work should explore the use of dialysis to remove excess reagents, as well as small-molecule by-products, from the alternative functionalisation reactions and then freeze dry the dialysed solutions to analyse the

products using ^{1}H NMR spectroscopy. These investigations would indicate whether or not alternative reactions conditions can improve the extent of functionalisation between gelatin and GPTMS. The products could then be used in hydrogels to repeat the studies to determine if it leads to changes in mechanical or physical properties.

CHAPTER 4

Chemistry

- The GelNB utilised within the GelNB-Silica-based hydrogels was supplied by an external source (Claro™) and had a degree of substitution (DoS) of 65%. Therefore, an important next step in the development of MPTMS-functionalised GelNB via click chemistry is to investigate this reaction using GelNB with a different DoS to determine if varying this has an impact on hydrogel properties.
- There remains scope to vary the GelNB-Silica hydrogel systems beyond just GelNB DoS. It is suggested that more in depth formulation studies are carried out, including varying the O:I ratio, employing alternative thiol-containing organosilane crosslinkers with different properties such as stimuli responsiveness, and using different polyol-modified silanes, to investigate the impact of formulation changes on physical, mechanical and biological properties.
- Batch-to-batch variation is an issue with the use of gelatin and its derivatives. The use of thiol-containing synthetic peptide hydrogels that are biologically relevant would overcome this limitation and hopefully result in improved consistency and reproducibility of these hydrogel systems.

Physical

- A lack of differences between Class I and Class II formulations with respect to degradation rate was a common finding. As previously mentioned in Chapter 4, the degradation studies should be repeated but the collagenase should be refreshed to maintain its activity over time.
- A single frequency sweep was used to investigate the hydrogel gelation kinetics in Chapter 4, however upon analysis it was not an appropriate test to use for these hydrogel formulations. To further probe the hydrogel gelation kinetics, an important future study is to use DLS to investigate the particle size, rate of hydrolysis and condensation and gelation time of the hydrogels.

Mechanical

- The intended use of the hydrogel formulations was for 3D bioprinting, and so more comprehensive rheological measurements should be systematically performed. A shear rate sweep to determine flow behaviour and a three-step flow test to determine recovery of the microstructures when a stress is removed should be performed to test the shear-thinning properties and thixotropic recovery time of the hydrogels, respectively.
- The mechanical tests (uniaxial, constant cyclic and incremental cyclic compressive tests), described in Chapter 4, were conducted in air. The next steps are to repeat these tests but under hydrated or submerged conditions at physiological temperature, to study if the behaviour of the hydrogels alters in a ‘wet’ state. This would provide further understanding of how the hydrogels would behave in environments more representative of *in vivo*. This method could be further developed to test the compressive properties of the hydrogels during enzymatic degradation.

Biological

- The PrestoBlue cell viability assay was conducted using a cell density of 2.5 x 10^3 cells per well in a 96 well plate which gave low absorbance readings at day 1, 4 and 7. It would be interesting to repeat this experiment with a higher cell density to examine if the low absorbance readings at earlier time points were a consequence of a low cell density and cells migrating through the hydrogels or if it was that cell viability took >7 days to increase.
- The mineralisation assay used here, Alizarin Red S staining, was not suitable for use within the GelNB-Silica-based hydrogels due to the stain becoming entrapped within the hydrogel structure. Future work should deploy other methods to quantify mineralisation and calcium deposition, such as quantitative polymerase chain reaction to analyse osteogenic marker genes (e.g. ALP, OCN and Runx2), X-ray diffraction (XRD) to examine mineralised matrix, and SEM for visualisation of mineralised structures.
- In Chapter 4, the cells used for all cell culture experiments were immortalised Saos-2 cells. Future studies should repeat this cell work with MSCs, such as BMSCs, to provide a more relevant and comprehensive understanding of cell interaction and behaviour with the GelNB-Silica-based hydrogels. This work should include 3D cell culture via encapsulation of cells within the hydrogels, as all work here was 2D cell culture.

Application

- The application of the hydrogels developed was for 3D bioprinting; however, it was not possible to investigate this due to time constraints and so a key next step would begin by determining the printing window for all hydrogel formulations, followed by

a resolution test to work out the highest printing resolution that could be obtained. Additionally, it would be interesting to print the hydrogel formulations within a support bath to create more complex 3D structures, to then move onto cell encapsulation within the hydrogel before printing to investigate the potential of the 3D structure for bone tissue engineering and *in vitro* modelling.

LIST OF REFERENCES

1. Lewns FK, Tsigkou O, Cox LR, Wildman RD, Grover LM, Poologasundarampillai G. Hydrogels and Bioprinting in Bone Tissue Engineering: Creating Artificial Stem-Cell Niches for In Vitro Models. Advanced Materials. 2023 Apr 23;35(52):2301670.
2. Reznikov N, Shahar R, Weiner S. Bone hierarchical structure in three dimensions. Acta Biomater. 2014;10(9):3815–26.
3. Reznikov N, Bilton M, Lari L, Stevens MM, Kröger R. Fractal-like hierarchical organization of bone begins at the nanoscale. Science (1979). 2018;360(6388):eaao2189.
4. Manzini BM, Machado LMR, Noritomi PY, da Silva JVL. Advances in Bone tissue engineering: A fundamental review. J Biosci. 2021;46:17.
5. Ott SM. Cortical or Trabecular Bone: What's the Difference? Am J Nephrol. 2018;47(6):373–5.
6. Filipowska J, Tomaszewski KA, Niedźwiedzki Ł, Walocha JA, Niedźwiedzki T. The role of vasculature in bone development, regeneration and proper systemic functioning. Angiogenesis. 2017 Aug 1;20(3):291–302.
7. Salhotra A, Shah HN, Levi B, Longaker MT. Mechanisms of bone development and repair. Nat Rev Mol Cell Biol. 2020;21(11):696–711.
8. Simunovic F, Finkenzeller G. Vascularization strategies in bone tissue engineering. Cells. 2021;10(7).
9. Caplan AI. Are All Adult Stem Cells The Same? Regen Eng Transl Med. 2015;1(1–4):4–10.
10. Lee JH, Kim HW. Emerging properties of hydrogels in tissue engineering. J Tissue Eng. 2018;9:1–4.
11. Geckil H, Xu F, Zhang X, Moon S, Demirci U. Engineering hydrogels as extracellular matrix mimics. Nanomedicine. 2010;5(3):469–84.
12. Ramiah P, du Toit LC, Choonara YE, Kondiah PPD, Pillay V. Hydrogel-Based Bioinks for 3D Bioprinting in Tissue Regeneration. Front Mater. 2020;7:1–13.
13. Nallusamy J, Das RK. Hydrogels and Their Role in Bone Tissue Engineering: An Overview. Asian Journal of Pharmaceutical and Clinical Research. 2021;13:S908-12.
14. Hull SM, Brunel LG, Heilshorn SC. 3D Bioprinting of Cell-Laden Hydrogels for Improved Biological Functionality. Advanced Materials. 2021;34:2103691.

15. Kakarla AB, Kong I, Turek I, Kong C, Irving H. Printable gelatin, alginate and boron nitride nanotubes hydrogel-based ink for 3D bioprinting and tissue engineering applications. Mater Des. 2021;213:110362.
16. Malda J, Visser J, Melchels FP, Jüngst T, Hennink WE, A Dhert WJ, et al. 25th Anniversary Article: Engineering Hydrogels for Biofabrication. Advanced Materials. 2013;25(1):5011–5028.
17. Moroni L, Boland T, Burdick JA, De Maria C, Derby B, Forgacs G, et al. Biofabrication: A Guide to Technology and Terminology. Trends Biotechnol. 2018 Apr 1;36(4):384–402.
18. Murphy S V, Atala A. 3D bioprinting of tissues and organs. Nat Biotechnol. 2014;32(8):773–85.
19. Wang K, Le L, Chun BM, Tiede-lewis LM, Shiflett LA, Campos RS, et al. A Novel Osteogenic Cell Line that Differentiates into GFP- Tagged Osteocytes and forms Mineral with a Bone-like Lacunocanalicular Structure. 2020;34(6):979–95.
20. Iordachescu A, Amin HD, Rankin SM, Williams RL, Yapp C, Bannerman A, et al. An In Vitro Model for the Development of Mature Bone Containing an Osteocyte Network. Adv Biosyst. 2018;2(2):1700156.
21. Iordachescu A, Hughes EAB, Joseph S, Hill EJ, Grover LM, Metcalfe AD. Trabecular bone organoids: a micron-scale ‘humanised’ prototype designed to study the effects of microgravity and degeneration. NPJ Microgravity. 2021;7(17).
22. Akiva A, Melke J, Ansari S, Liv N, van der Meijden R, van Erp M, et al. An Organoid for Woven Bone. Adv Funct Mater. 2021;31(17):2010524.
23. Borciani G, Montalbano G, Baldini N, Cerqueni G, Vitale-Brovarone C, Ciapetti G. Co–culture systems of osteoblasts and osteoclasts: Simulating in vitro bone remodeling in regenerative approaches. Acta Biomater. 2020;108:22–45.
24. Remmers SJA, de Wildt BWM, Vis MAM, Spaander ESR, de Vries RBM, Ito K, et al. Osteoblast-osteoclast co-cultures: A systematic review and map of available literature. PLoS One. 2021;16:1–26.
25. Shiwarski DJ, Hudson AR, Tashman JW, Feinberg AW. Emergence of FRESH 3D printing as a platform for advanced tissue biofabrication. APL Bioeng. 2021;5(1):010904.
26. Cidonio G, Cooke M, Glinka M, Dawson JI, Grover L, Oreffo ROC. Printing bone in a gel: using nanocomposite bioink to print functionalised bone scaffolds. Mater Today Bio. 2019;4:100028.

27. Kang HW, Lee SJ, Ko IK, Kengla C, Yoo JJ, Atala A. A 3D bioprinting system to produce human-scale tissue constructs with structural integrity. Nat Biotechnol. 2016;34(3):312–9.
28. Cui H, Zhu W, Nowicki M, Zhou X, Khademhosseini A, Zhang LG. Hierarchical Fabrication of Engineered Vascularized Bone Biphasic Constructs via Dual 3D Bioprinting: Integrating Regional Bioactive Factors into Architectural Design. Adv Healthc Mater. 2016;5(17):2174–81.
29. Levato R, Jungst T, Scheuring RG, Blunk T, Groll J, Malda J. From Shape to Function: The Next Step in Bioprinting. Advanced Materials. 2020 Mar 1;32(12):1906423.
30. Nelson CM, Bissell MJ. Of Extracellular Matrix, Scaffolds, and Signaling: Tissue Architecture Regulates Development, Homeostasis, and Cancer. Annu Rev Cell Dev Biol. 2006;22:287–309.
31. Calve S, Odelberg SJ, Simon HG. A Transitional Extracellular Matrix Instructs Cell Behavior During Muscle Regeneration. Dev Biol. 2010;344(1):259–71.
32. Hussey GS, Dziki JL, Badylak SF. Extracellular matrix-based materials for regenerative medicine. Nat Rev Mater. 2018;3(7):159–73.
33. Madl CM, Heilshorn SC. Engineering Hydrogel Microenvironments to Recapitulate the Stem Cell Niche. Annu Rev Biomed Eng. 2018;20(1):21–47.
34. Spicer CD. Hydrogel scaffolds for tissue engineering: the importance of polymer choice. Polym Chem. 2020;11(2):184–219.
35. Hernández-González AC, Téllez-Jurado L, Rodríguez-Lorenzo LM. Alginate hydrogels for bone tissue engineering, from injectables to bioprinting: A review. Carbohydr Polym. 2020;229(115514).
36. Xue X, Hu Y, Deng Y, Su J. Recent Advances in Design of Functional Biocompatible Hydrogels for Bone Tissue Engineering. Adv Funct Mater. 2021;31(19):2009432.
37. Kondiah PJ, Choonara YE, Kondiah PPD, Marimuthu T, Kumar P, Du Toit LC, et al. A review of injectable polymeric hydrogel systems for application in bone tissue engineering. Molecules. 2016;21(11):1580.
38. Xue X, Hu Y, Wang S, Chen X, Jiang Y, Su J. Fabrication of physical and chemical crosslinked hydrogels for bone tissue engineering. Bioact Mater. 2022;12:327–39.
39. Lavanya K, Chandran SV, Balagangadharan K, Selvamurugan N. Temperature- and pH-responsive chitosan-based injectable hydrogels for bone tissue engineering. Materials Science and Engineering C. 2020;111:110862.

40. Xu C, Dai G, Hong Y. Recent advances in high-strength and elastic hydrogels for 3D printing in biomedical applications. Acta Biomater. 2019;95:50–9.
41. Albrektsson T, Johansson C. Osteoinduction, osteoconduction and osseointegration. European Spine Journal. 2001;10:S96–101.
42. Li J, Liu Y, Zhang Y, Yao B, Enhejirigala B, Li Z, et al. Biophysical and Biochemical Cues of Biomaterials Guide Mesenchymal Stem Cell Behaviors. Front Cell Dev Biol. 2021;9:1–13.
43. Bakhshandeh B, Ranjbar N, Abbasi A, Amiri E, Abedi A, Mehrabi MR, et al. Recent progress in the manipulation of biochemical and biophysical cues for engineering functional tissues. Bioeng Transl Med. 2022;5(8):e10383.
44. De Witte TM, Fratila-Apachitei LE, Zadpoor AA, Peppas NA. Bone tissue engineering via growth factor delivery: From scaffolds to complex matrices. Regen Biomater. 2018;5(4):197–211.
45. Oliveira ÉR, Nie L, Podstawczyk D, Allahbakhsh A, Ratnayake J, Brasil DL, et al. Advances in growth factor delivery for bone tissue engineering. Int J Mol Sci. 2021;22(2):1–33.
46. Kowalczewski CJ, Saul JM. Biomaterials for the delivery of growth factors and other therapeutic agents in tissue engineering approaches to bone regeneration. Front Pharmacol. 2018;9:513.
47. Freeman FE, Pitacco P, van Dommelen LHA, Nulty J, Browe DC, Shin JY, et al. 3D bioprinting spatiotemporally defined patterns of growth factors to tightly control tissue regeneration. Sci Adv. 2020;6(33):1–15.
48. Yin B, Yang H, Yang M. Integrating Soft Hydrogel with Nanostructures Reinforces Stem Cell Adhesion and Differentiation. Journal of Composites Science. 2022;6(1):19.
49. Cernencu AI, Dinu AI, Stancu IC, Lungu A, Iovu H. Nanoengineered biomimetic hydrogels: A major advancement to fabricate 3D-printed constructs for regenerative medicine. Biotechnol Bioeng. 2022;119(3):762–83.
50. Madl CM, Heilshorn SC. Bioorthogonal Strategies for Engineering Extracellular Matrices. Adv Funct Mater. 2018;28(11):1–21.
51. Li C, Faulkner-Jones A, Dun AR, Jin J, Chen P, Xing Y, et al. Rapid formation of a supramolecular polypeptide-DNA Hydrogel for in situ three-dimensional multilayer bioprinting. Angewandte Chemie - International Edition. 2015;54(13):3957–61.

52. Stoll H, Steinle H, Stang K, Kunnakattu S, Scheideler L, Neumann B, et al. Generation of Large-Scale DNA Hydrogels with Excellent Blood and Cell Compatibility. Macromol Biosci. 2017;17(4):1–13.
53. Ke Y, Castro C, Choi JH. Structural DNA Nanotechnology: Artificial Nanostructures for Biomedical Research. Annu Rev Biomed Eng. 2018;20:375–401.
54. Stewart S, Darwood A, Masouros S, Higgins C, Ramasamy A. Mechanotransduction in osteogenesis. Bone Joint Res. 2020;9(1):1–14.
55. Shellard A, Mayor R. Collective durotaxis along a self-generated stiffness gradient in vivo. Nature. 2021;600(7890):690–4.
56. Plotnikov S V., Pasapera AM, Sabass B, Waterman CM. Force fluctuations within focal adhesions mediate ECM-rigidity sensing to guide directed cell migration. Cell. 2012;151(7):1513–27.
57. Zhang N, Wang Y, Zhang J, Guo J, He J. Controlled domain gels with a biomimetic gradient environment for osteochondral tissue regeneration. Acta Biomater. 2021;135:304–17.
58. Yeung T, Georges PC, Flanagan LA, Marg B, Ortiz M, Funaki M, et al. Effects of substrate stiffness on cell morphology, cytoskeletal structure, and adhesion. Cell Motil Cytoskeleton. 2005;60(1):24–34.
59. Solon J, Levental I, Sengupta K, Georges PC, Janmey PA. Fibroblast adaptation and stiffness matching to soft elastic substrates. Biophys J. 2007;93(12):4453–61.
60. Chen J, Fabry B, Schiffrin EL, Wang N. Twisting integrin receptors increases endothelin-1 gene expression in endothelial cells. Am J Physiol Cell Physiol. 2001;280(6):1475–84.
61. Numaguchi Y, Huang S, Polte TR, Eichler GS, Wang N, Ingber DE. Caldesmon-dependent switching between capillary endothelial cell growth and apoptosis through modulation of cell shape and contractility. Angiogenesis. 2003;6(1):55–64.
62. Huebsch N, Lippens E, Lee K, Mehta M, Koshy ST, Darnell MC, et al. Matrix Elasticity of Void-Forming Hydrogels Controls Transplanted Stem Cell-Mediated Bone Formation. Nat Mater. 2015;14(12):1269–1277.
63. El-Rashidy AA, Moshy S El, Radwan IA, Rady D, Abbass MMS, Dörfer CE, et al. Effect of polymeric matrix stiffness on osteogenic differentiation of mesenchymal stem/progenitor cells: Concise review. Polymers (Basel). 2021;13(17):1–32.

64. Pan W, Petersen E, Cai N, Ma G, Lee JR, Feng Z, et al. Viscoelastic properties of human mesenchymal stem cells. In: Annual International Conference of the IEEE Engineering in Medicine and Biology - Proceedings. IEEE; 2005. p. 4854–7.
65. Chaudhuri O, Cooper-White J, Janmey PA, Mooney DJ, Shenoy VB. Effects of extracellular matrix viscoelasticity on cellular behaviour. Nature. 2020;584(7822):535–46.
66. Galbraith CG, Yamada KM, Galbraith JA. Polymerizing actin fibers position integrins primed to probe for adhesion sites. Science (1979). 2007;315(5814):992–5.
67. Chaudhuri O. Viscoelastic hydrogels for 3D cell culture. Biomater Sci. 2017;5(8):1480–90.
68. Chaudhuri O, Gu L, Klumpers D, Darnell M, Bencherif SA, Weaver JC, et al. Hydrogels with tunable stress relaxation regulate stem cell fate and activity. Nat Mater. 2016;15(3):326–34.
69. Darnell M, Young S, Gu L, Shah N, Lippens E, Weaver J, et al. Substrate Stress-Relaxation Regulates Scaffold Remodeling and Bone Formation in Vivo. Adv Healthc Mater. 2017;6(1):1–17.
70. Drury JL, Mooney DJ. Hydrogels for tissue engineering: Scaffold design variables and applications. Biomaterials. 2003;24(24):4337–51.
71. Discher DE, Janmey P, Wang Y li. Tissue Cells Feel and Respond to the Stiffness of Their Substrate. Materials and Biology. 2005;310:1139–43.
72. Vogel V, Sheetz M. Local force and geometry sensing regulate cell functions. Nat Rev Mol Cell Biol. 2006;7(4):265–75.
73. Bauer A, Gu L, Kwee B, Li WA, Dellacherie M, Celiz AD, et al. Hydrogel substrate stress-relaxation regulates the spreading and proliferation of mouse myoblasts. Acta Biomater [Internet]. 2017;62:82–90. Available from: https://doi.org/10.1016/j.actbio.2017.08.041
74. Vining KH, Stafford A, Mooney DJ. Sequential modes of crosslinking tune viscoelasticity of cell-instructive hydrogels. Biomaterials. 2019;188:187–97.
75. Desai RM, Koshy ST, Hilderbrand SA, Mooney DJ, Joshi NS. Versatile click alginate hydrogels crosslinked via tetrazine-norbornene chemistry. Biomaterials. 2015;50(1):30–7.
76. McKinnon DD, Domaille DW, Cha JN, Anseth KS. Biophysically defined and cytocompatible covalently adaptable networks as viscoelastic 3d cell culture systems. Advanced Materials. 2014;26(6):865–72.

77. Brown TE, Carberry BJ, Worrell BT, Dudaryeva OY, McBride MK, Bowman CN, et al. Photopolymerized dynamic hydrogels with tunable viscoelastic properties through thioester exchange. Biomaterials. 2018;178:496–503.
78. Sommerfeld SD, Elisseeff JH. Time to Relax: Mechanical Stress Release Guides Stem Cell Responses. Cell Stem Cell. 2016;18(2):166–7.
79. Zaman MH, Trapani LM, Sieminski AL, Mackellar D, Gong H, Kamm RD, et al. Migration of tumor cells in 3D matrices is governed by matrix stiffness along with cell-matrix adhesion and proteolysis. Proc Natl Acad Sci U S A. 2006;103(15):15–6.
80. Ehrbar M, Sala A, Lienemann P, Ranga A, Mosiewicz K, Bittermann A, et al. Elucidating the role of matrix stiffness in 3D cell migration and remodeling. Biophys J. 2011;100(2):284–93.
81. Daviran M, Catalano J, Schultz KM. Determining How Human Mesenchymal Stem Cells Change Their Degradation Strategy in Response to Microenvironmental Stiffness. Biomacromolecules. 2020;21(8):3056–68.
82. Lei Y, Gojgini S, Lam J, Segura T. The spreading, migration and proliferation of mouse mesenchymal stem cells cultured inside hyaluronic acid hydrogels. Biomaterials. 2011;32(1):39–47.
83. Friedl P, Wolf K. Plasticity of cell migration: A multiscale tuning model. Journal of Cell Biology. 2010;188(1):11–9.
84. Wolf K, te Lindert M, Krause M, Alexander S, te Riet J, Willis AL, et al. Physical limits of cell migration: Control by ECM space and nuclear deformation and tuning by proteolysis and traction force. Journal of Cell Biology. 2013;201(7):1069–84.
85. Lautscham LA, Kämmerer C, Lange JR, Kolb T, Mark C, Schilling A, et al. Migration in Confined 3D Environments Is Determined by a Combination of Adhesiveness, Nuclear Volume, Contractility, and Cell Stiffness. Biophys J. 2015;109(5):900–13.
86. Peyton SR, Kalcioglu ZI, Cohen JC, Runkle AP, Van Vliet KJ, Lauffenburger DA, et al. Marrow-Derived Stem Cell Motility in 3D Synthetic Scaffold Is Governed by Geometry Along With Adhesivity and Stiffness. Biotechnol Bioeng. 2011;108(5):1181–93.
87. Charras G, Sahai E. Physical influences of the extracellular environment on cell migration. Nat Rev Mol Cell Biol. 2014;15(12):813–24.
88. Abalymov AA, Santos CAB, Van der Meeren L, Van de Walle D, Dewettinck K, Parakhonskiy B V., et al. Nanofibrillar Hydrogels by Temperature Driven Self-

Assembly: New Structures for Cell Growth and Their Biological and Medical Implications. Adv Mater Interfaces. 2021;8(15):2002202.

89. Hadjidakis DJ, Androulakis II. Bone remodeling. Ann N Y Acad Sci. 2006;1092:385–96.
90. Infante A, Rodríguez CI. Osteogenesis and aging: lessons from mesenchymal stem cells. Stem Cell Res Ther. 2018;9(1):244.
91. Loebel C, Mauck RL, Burdick JA. Local nascent protein deposition and remodelling guide mesenchymal stromal cell mechanosensing and fate in three-dimensional hydrogels. Nat Mater. 2019;18(8):883–91.
92. Ferreira SA, Faull PA, Seymour AJ, Yu TTL, Loaiza S, Auner HW, et al. Neighboring cells override 3D hydrogel matrix cues to drive human MSC quiescence. Biomaterials. 2018;176:13–23.
93. Loebel C, Kwon MY, Wang C, Han L, Mauck RL, Burdick JA. Metabolic Labeling to Probe the Spatiotemporal Accumulation of Matrix at the Chondrocyte–Hydrogel Interface. Adv Funct Mater. 2020;30(44):1–10.
94. Leonard AK, Loughran EA, Klymenko Y, Liu Y, Kim O, Asem M, et al. Methods for the visualization and analysis of extracellular matrix protein structure and degradation. Methods Cell Biol. 2018;143:79–95.
95. Mcleod CM, Mauck RL. High fidelity visualization of cell-to-cell variation and temporal dynamics in nascent extracellular matrix formation. Sci Rep. 2016;6:1–12.
96. Ahearne M, Ahearne M. Introduction to cell – hydrogel mechanosensing. 2014;
97. Lutolf MP, Weber FE, Schmoekel HG, Schense JC, Kohler T, Müller R, et al. Repair of bone defects using synthetic mimetics of collagenous extracellular matrices. Nat Biotechnol. 2018;21(5):513–8.
98. Madl CM, Katz LM, Heilshorn SC. Tuning Bulk Hydrogel Degradation by Simultaneous Control of Proteolytic Cleavage Kinetics and Hydrogel Network Architecture. ACS Macro Lett. 2018;7(11):1302–7.
99. Luo Y, Zhang T, Lin X. 3D printed hydrogel scaffolds with macro pores and interconnected microchannel networks for tissue engineering vascularization. Chemical Engineering Journal. 2022;430(P2):132926.
100. Dalby MJ, Gadegaard N, Tare R, Andar A, Riehle MO, Herzyk P, et al. The control of human mesenchymal cell differentiation using nanoscale symmetry and disorder. Nat Mater. 2007;6(12):997–1003.

101. Barnett H, Shevchuk M, Peppas NA, Caldorera-Moore M. Influence of extracellular cues of hydrogel biomaterials on stem cell fate. J Biomater Sci Polym Ed. 2022;33(10):1324–47.
102. Wenz A, Tjoeng I, Schneider I, Kluger PJ, Borchers K. Improved vasculogenesis and bone matrix formation through coculture of endothelial cells and stem cells in tissue-specific methacryloyl gelatin-based hydrogels. Biotechnol Bioeng. 2018;115(10):2643–53.
103. Samani SM, Ahmadi F, Oveisi Z, Amoozgar Z. Chitosan based hydrogels: characteristics and pharmaceutical applications. Res Pharm Sci. 2015;10(1):1–16.
104. Gomez-Florit M, Pardo A, Domingues RMA, Graça AL, Babo PS, Reis RL, et al. Natural-Based Hydrogels for Tissue Engineering Applications. Molecules. 2020 Dec 1;25(24):5858.
105. Hama R, Ulziibayar A, Reinhardt JW, Watanabe T, Kelly J, Shinoka T. Recent Developments in Biopolymer-Based Hydrogels for Tissue Engineering Applications. Biomolecules. 2023 Feb 1;13(2):280.
106. Xu F, Dawson C, Lamb M, Mueller E, Stefanek E, Akbari M, et al. Hydrogels for Tissue Engineering: Addressing Key Design Needs Toward Clinical Translation. Front Bioeng Biotechnol. 2022 May 5;10:849831.
107. Li X, Sun Q, Li Q, Kawazoe N, Chen G. Functional hydrogels with tunable structures and properties for tissue engineering applications. Front Chem. 2018 Oct 1;6:499.
108. Chai Q, Jiao Y, Yu X. Hydrogels for Biomedical Applications: Their Characteristics and the Mechanisms behind Them. Gels. 2017;3(1):6.
109. Liu J, Sun L, Xu W, Wang Q, Yu S, Sun J. Current advances and future perspectives of 3D printing natural-derived biopolymers. Carbohydr Polym. 2019;207:297–316.
110. Jabbari E, Leijten J, Xu Q, Khademhosseini A. The matrix reloaded: The evolution of regenerative hydrogels. Materials Today. 2016;19(4):190–6.
111. Montheil T, Cile Echalier C, Martinez J, Subra G, Mehdi A. Inorganic polymerization: an attractive route to biocompatible hybrid hydrogels. J Mater Chem B. 2018;6:3434–48.
112. Jayash SN, Cooper PR, Shelton RM, Kuehne SA, Poologasundarampillai G. Novel chitosan-silica hybrid hydrogels for cell encapsulation and drug delivery. Int J Mol Sci. 2021;22(22).

113. Mir SH, Nagahara LA, Thundat T, Mokarian-Tabari P, Furukawa H, Khosla A. Review—Organic-Inorganic Hybrid Functional Materials: An Integrated Platform for Applied Technologies. J Electrochem Soc. 2018;165(8):B3137–56.
114. Connell LS, Gabrielli L, Mahony O, Russo L, Cipolla L, Jones JR. Functionalizing natural polymers with alkoxysilane coupling agents: Reacting 3-glycidoxypropyl trimethoxysilane with poly(γ-glutamic acid) and gelatin. Polym Chem. 2017;8(6):1095–103.
115. Martín-Moldes Z, López Barreiro D, Buehler MJ, Kaplan DL. Effect of the silica nanoparticle size on the osteoinduction of biomineralized silk-silica nanocomposites. Acta Biomater. 2021 Jan 15;120:203–12.
116. Hernández-González AC, Téllez-Jurado L, Rodríguez-Lorenzo LM. Preparation of covalently bonded silica-alginate hybrid hydrogels by SCHIFF base and sol-gel reactions. Carbohydr Polym. 2021 Sep 1;267:118186.
117. Nelson M, Li S, Page SJ, Shi X, Lee PD, Stevens MM, et al. 3D printed silica-gelatin hybrid scaffolds of specific channel sizes promote collagen Type II, Sox9 and Aggrecan production from chondrocytes. Materials Science and Engineering C. 2021;123:1–12.
118. Valot L, Maumus M, Brunel L, Martinez J, Amblard M, Noël D, et al. A collagen-mimetic organic-inorganic hydrogel for cartilage engineering. Gels. 2021 Jun 1;7(2):73.
119. Poologasundarampillai G, Yu B, Tsigkou O, Wang D, Romer F, Bhakhri V, et al. Poly(γ-glutamic acid)/silica hybrids with calcium incorporated in the silica network by use of a calcium alkoxide precursor. Chemistry - A European Journal. 2014 Jun 23;20(26):8149–60.
120. Shipovskaya AB, Malinkina ON, Zhuravleva YY, Rogacheva SM. Synthesis of Silicon-Containing Chitosan Hydrogels in a Glycolic Acid Medium. Advances in Materials Science and Engineering. 2016;2016.
121. Hench LL, West JK. The Sol-Gel Process. Chem Rev. 1990;90:33–72.
122. Owens GJ, Singh RK, Foroutan F, Alqaysi M, Han CM, Mahapatra C, et al. Sol-gel based materials for biomedical applications. Prog Mater Sci. 2016 Apr 1;77:1–79.
123. Esposito S. “Traditional” sol-gel chemistry as a powerful tool for the preparation of supported metal and metal oxide catalysts. Materials. 2019;12(4):1–25.
124. Branda F. The Sol-Gel Route to Nanocomposites. In: Advances in Nanocomposites - Synthesis, Characterization and Industrial Applications. 2011. p. 324–40.

125. Young SK. Overview of Sol-Gel Science and Technology. 2002.
126. Jeong B, Kim SW, Bae YH. Thermosensitive sol-gel reversible hydrogels. Adv Drug Deliv Rev. 2012 Dec;64:154–62.
127. Thangprasert A, Tansakul C, Thuaksubun N, Meesane J. Mimicked hybrid hydrogel based on gelatin/PVA for tissue engineering in subchondral bone interface for osteoarthritis surgery. Mater Des. 2019 Dec 5;183(108113).
128. Pepelanova I, Kruppa K, Scheper T, Lavrentieva A. Gelatin-methacryloyl (GelMA) hydrogels with defined degree of functionalization as a versatile toolkit for 3D cell culture and extrusion bioprinting. Bioengineering. 2018 Sep 1;5(55):1–15.
129. Ren L, Tsuru K, Hayakawa S, Osaka A. Novel approach to fabricate porous gelatin-siloxane hybrids for bone tissue engineering. Biomaterials. 2002;23:4765–73.
130. Ren L, Tsuru K, Hayakawa S, Osaka A. Synthesis and characterization of gelatin-siloxane hybrids derived through sol-gel procedure. J Solgel Sci Technol. 2001;21:115–21.
131. Lei B, Shin KH, Noh DY, Jo IH, Koh YH, Choi WY, et al. Nanofibrous gelatin-silica hybrid scaffolds mimicking the native extracellular matrix (ECM) using thermally induced phase separation. J Mater Chem. 2012;22(28):14133–40.
132. Filipowska J, Lewandowska-Łańcucka J, Gilarska A, Niedźwiedzki Ł, Nowakowska M. In vitro osteogenic potential of collagen/chitosan-based hydrogels-silica particles hybrids in human bone marrow-derived mesenchymal stromal cell cultures. Int J Biol Macromol. 2018;113:692–700.
133. Chen S, Chinnathambi S, Shi X, Osaka A, Zhu Y, Hanagata N. Fabrication of novel collagen-silica hybrid membranes with tailored biodegradation and strong cell contact guidance ability. J Mater Chem. 2012;22(41):21885–92.
134. Yu HS, Lee EJ, Seo SJ, Knowles JC, Kim HW. Feasibility of silica-hybridized collagen hydrogels as three-dimensional cell matrices for hard tissue engineering. J Biomater Appl. 2015 Sep 24;30(3):338–50.
135. Lee HY, Kim J, Hwang CH, Kim HE, Jeong SH. Strategy for Preparing Mechanically Strong Hyaluronic Acid–Silica Nanohybrid Hydrogels via In Situ Sol–Gel Process. Macromol Mater Eng. 2018 Sep 1;303:1800213.
136. Handorf AM, Zhou Y, Halanski MA, Li WJ. Tissue stiffness dictates development, homeostasis, and disease progression. Organogenesis. 2015 Jan 1;11(1):1–15.

137. Cha C, Oh J, Kim K, Qiu Y, Joh M, Shin SR, et al. Microfluidics-assisted fabrication of gelatin-silica core-shell microgels for injectable tissue constructs. Biomacromolecules. 2014 Jan 13;15(1):283–90.
138. Kakkar P, Madhan B. Fabrication of keratin-silica hydrogel for biomedical applications. Materials Science and Engineering C. 2016 Sep 1;66:178–84.
139. Gill I, Ballesteros A. Encapsulation of Biologicals within Silicate, Siloxane, and Hybrid Sol-Gel Polymers: An Efficient and Generic Approach. Journal of American Chemical Society. 1998;120(34):8587–98.
140. Brook MA, Chen Y, Guo K, Zhang Z, Brennan JD. Sugar-modified silanes: Precursors for silica monoliths. J Mater Chem. 2004;14(9):1469–79.
141. Brook MA, Chen Y, Guo K, Zhang Z, Jin W, Deisingh A, et al. Proteins entrapped in silica monoliths prepared from glyceroxysilanes. J Solgel Sci Technol. 2004;31:343–8.
142. Hartmann S, Brandhuber D, Hüsing N. Glycol-Modified Silanes: Novel Possibilities for the Synthesis of Hierarchically Organized (Hybrid) Porous Materials. Acc Chem Res. 2007;40(1):885–94.
143. Dave BC, Dunn B, Valentine JS, Zink JI. Sol-gel encapsulation methods for biosensors. Anal Chem. 1994 Nov 15;66(22):1120A-1127A.
144. Avnir D. Organic Chemistry within Ceramic Matrixes: Doped Sol-Gel Materials. Acc Chem Res. 1995 Aug 1;28(8):328–34.
145. Gill I, Ballesteros A. Encapsulation of Biologicals within Silicate, Siloxane, and Hybrid Sol-Gel Polymers: An Efficient and Generic Approach. Journal of American Chemical Society. 1998;120(34):8587–98.
146. Armon R, Dosoretz C, Starosvetsky J, Orshansky F, Saadi I. Sol-gel applications in environmental biotechnology. J Biotechnol. 1996 Nov;51(3):279–85.
147. Patwardhan S V, Hüsing N, Clarson SJ. Macromolecule mediated bioinspired silica synthesis using a diol-modified silane precursor. Silicon Chemistry. 2003;2:279–85.
148. Hüsing N, Brandhuber D, Kaiser P. Glycol-modified organosilanes in the synthesis of inorganic-organic silsesquioxane and silica monoliths. J Solgel Sci Technol. 2006;40(2–3):131–9.
149. Brook MA, Chen Y, Guo K, Zhang Z, Jin W, Deisingh A, et al. Proteins Entrapped in Silica Monoliths Prepared from Glyceroxysilanes. J Solgel Sci Technol. 2004;31:343–8.
150. Shirahama H, Lee BH, Tan LP, Cho NJ. Precise tuning of facile one-pot gelatin methacryloyl (GelMA) synthesis. Sci Rep. 2016 Aug 9;6(31036).

151. Scelsi A, Bochicchio B, Smith A, Workman VL, Castillo Diaz LA, Saiani A, et al. Tuning of hydrogel stiffness using a two-component peptide system for mammalian cell culture. J Biomed Mater Res A. 2019 Mar 1;107(3):535–44.
152. Halstead FD, Hadis MA, Marley N, Brock K, Milward MR, Cooper PR, et al. Violet-Blue Light Arrays at 405 Nanometers Exert Enhanced Antimicrobial Activity for Photodisinfection of Monomicrobial Nosocomial Biofilms. Appl Environ Microbiol. 2019;85(21):e01346-19.
153. Brook MA, Brennan JD, Chen Y. Polyol-Modified Silanes as Precursors for Silica. Vol. 1, European Patent Specification. 2007. p. 1–15.
154. Li X, Chen S, Li J, Wang X, Zhang J, Kawazoe N, et al. 3D culture of chondrocytes in gelatin hydrogels with different stiffness. Polymers (Basel). 2016 Jul 26;8(8):269.
155. Zu G, Meijer M, Mergel O, Zhang H, van Rijn P. 3D-Printable Hierarchical Nanogel-GelMA Composite Hydrogel System. Polymers (Basel). 2021 Aug 1;13(15):2508.
156. Alexa RL, Cucuruz A, Ghițulică CD, Voicu G, Stamat LR, Dinescu S, et al. 3D Printable Composite Biomaterials Based on GelMA and Hydroxyapatite Powders Doped with Cerium Ions for Bone Tissue Regeneration. Int J Mol Sci. 2022 Feb 1;23(3):1841.
157. Falini G, Fermani S, Foresti E, Parma B, Rubini K, Sidoti MC, et al. Films of self-assembled purely helical type I collagen molecules. J Mater Chem. 2004 Jul 21;14(14):2297–302.
158. Ito A, Mase A, Takizawa Y, Shinkai M, Honda H, Hata KI, et al. Transglutaminase-mediated gelatin matrices incorporating cell adhesion factors as a biomaterial for tissue engineering. J Biosci Bioeng. 2003;95(2):196–9.
159. Chen S, Wang Y, Lai J, Tan S, Wang M. Structure and Properties of Gelatin Methacryloyl (GelMA) Synthesized in Different Reaction Systems. Biomacromolecules. 2023 Jun 12;24(6):2928–41.
160. Mikhailov O V. Gelatin as It Is: History and Modernity. Int J Mol Sci. 2023 Feb 1;24(4):3583.
161. Sun M, Sun X, Wang Z, Guo S, Yu G, Yang H. Synthesis and properties of gelatin methacryloyl (GelMA) hydrogels and their recent applications in load-bearing tissue. Polymers (Basel). 2018;10(11):1290.
162. Nichol JW, Koshy ST, Bae H, Hwang CM, Yamanlar S, Khademhosseini A. Cell-laden microengineered gelatin methacrylate hydrogels. Biomaterials. 2010 Jul;31(21):5536–44.

163. Morgan EF, Unnikrisnan GU, Hussein AI. Bone Mechanical Properties in Healthy and Diseased States. Annu Rev Biomed Eng. 2018 Jun 4;20:119–43.
164. Marques AC, Vale M. Macroporosity control by phase separation in sol-gel derived monoliths and microspheres. Materials. 2021 Aug 1;14(15):4247.
165. Yun L, Zhao J, Kang X, Du Y, Yuan X, Hou X. Preparation and properties of monolithic and hydrophobic gelatin–silica composite aerogels for oil absorption. J Solgel Sci Technol. 2017 Jul 1;83(1):197–206.
166. Noh DY, An YH, Jo IH, Koh YH, Kim HE. Synthesis of nanofibrous gelatin/silica bioglass composite microspheres using emulsion coupled with thermally induced phase separation. Materials Science and Engineering C. 2016 May 1;62:678–85.
167. Ishikawa S, Iwanaga Y, Uneyama T, Li X, Hojo H, Fujinaga I, et al. Percolation-induced gel–gel phase separation in a dilute polymer network. Nat Mater. 2023 Dec 1;22(12):1564–70.
168. Li X, Rombouts W, Van Der Gucht J, De Vries R, Dijksman JA. Mechanics of composite hydrogels approaching phase separation. PLoS One. 2019 Jan 1;14(1):e0211059.
169. Qiao R, Deng H, Putz KW, Brinson LC. Effect of particle agglomeration and interphase on the glass transition temperature of polymer nanocomposites. J Polym Sci B Polym Phys. 2011 May 15;49(10):740–8.
170. Coradin T, Bah S, Livage J. Gelatine/silicate interactions: From nanoparticles to composite gels. Colloids Surf B Biointerfaces. 2004;35(1):53–8.
171. Ji Z, Liu H, Yu L, Duan Q, Chen Y, Chen L. pH controlled gelation behavior and morphology of gelatin/hydroxypropylmethylcellulose blend in aqueous solution. Food Hydrocoll. 2020 Jul 1;104:105733.
172. Hafidz M, Yaakob CM, Amin I, Noorfaizan A. Chemical and functional properties of bovine and porcine skin gelatin. Int Food Res J. 2011;18:813–7.
173. Derkach SR, Voron'ko NG, Kuchina YA. Intermolecular Interactions in the Formation of Polysaccharide-Gelatin Complexes: A Spectroscopic Study. Polymers (Basel). 2022 Jul 1;14(14):2777.
174. Bharti B, Meissner J, Klapp SHL, Findenegg GH. Bridging interactions of proteins with silica nanoparticles: The influence of pH, ionic strength and protein concentration. Soft Matter. 2014 Feb 7;10(5):718–28.

175. Twej WAA, Al-Maliki FJ, Chiad BT. Study of R-molar ratio effect on the transformation of tetraethylorthosilicat precursor to gels in sol-gel technique. Baghdad Science Journal. 2009;6(3):590–5.
176. Koyama T, Tanaka H. Volume-shrinking kinetics of transient gels as a consequence of dynamic interplay between phase separation and mechanical relaxation. Phys Rev E. 2018 Dec 26;98(6):062617.
177. Tanaka H. Viscoelastic phase separation in biological cells. Commun Phys. 2022 Dec 1;5(167).
178. Tsurusawa H, Arai S, Tanaka H. A unique route of colloidal phase separation yields stress-free gels. Sci Adv. 2020;6:8107–14.
179. Lu Z, Zhang T, Liu Z, Kong X, Sun Z. Investigation of the tetraethoxysilane-derived sol–gel process by rheological oscillation test and the effect of different synthetic parameters. J Appl Polym Sci. 2023 Jan 10;140(2):e53310.
180. Avallone PR, Raccone E, Costanzo S, Delmonte M, Sarrica A, Pasquino R, et al. Gelation kinetics of aqueous gelatin solutions in isothermal conditions via rheological tools. Food Hydrocoll. 2021;111:106248.
181. Zhu M, Wang Y, Ferracci G, Zheng J, Cho NJ, Bae &, et al. Gelatin methacryloyl and its hydrogels with an exceptional degree of controllability and batch-to-batch consistency. Nature Scientific Reports. 2019;9(6863):1–13.
182. Rebers L, Reichsöllner R, Regett S, Tovar GEM, Borchers K, Baudis S, et al. Differentiation of physical and chemical cross-linking in gelatin methacryloyl hydrogels. Sci Rep. 2021 Dec 1;11(3256).
183. Rebers L, Granse T, Tovar GEM, Southan A, Borchers K. Physical interactions strengthen chemical gelatin methacryloyl gels. Gels. 2019 Mar 1;5(1):4.
184. Mahony O, Tsigkou O, Ionescu C, Minelli C, Ling L, Hanly R, et al. Silica-gelatin hybrids with tailorable degradation and mechanical properties for tissue regeneration. Adv Funct Mater. 2010;20(22):3835–45.
185. Tonda-Turo C, Cipriani E, Gnavi S, Chiono V, Mattu C, Gentile P, et al. Crosslinked gelatin nanofibres: Preparation, characterisation and in vitro studies using glial-like cells. Materials Science and Engineering C. 2013;33(5):2723–35.
186. Vueva Y, Connell LS, Chayanun S, Wang D, McPhail DS, Romer F, et al. Silica/alginate hybrid biomaterials and assessment of their covalent coupling. Appl Mater Today. 2018;11:1–12.

187. Sepulveda P, Jones JR, Hench LL. Bioactive sol-gel foams for tissue repair. J Biomed Mater Res. 2002;59(2):340–8.
188. Zhao X, Lang Q, Yildirimer L, Lin ZY, Cui W, Annabi N, et al. Photocrosslinkable Gelatin Hydrogel for Epidermal Tissue Engineering. Adv Healthc Mater. 2016 Jan 1;5(1):108–18.
189. Kobayashi KU, Oikawa N, Kurita R. Dynamical transition of heat transport in a physical gel near the sol-gel transition. Sci Rep. 2015 Dec 22;5(18667).
190. Mahony O, Yue S, Turdean-Ionescu C, Hanna J V., Smith ME, Lee PD, et al. Silica-gelatin hybrids for tissue regeneration: Inter-relationships between the process variables. J Solgel Sci Technol. 2014;69(2):288–98.
191. Balavigneswaran CK, Venkatesan R, Karuppiah PS, Kumar G, Paliwal P, Krishnamurthy S, et al. Silica Release from Silane Cross-Linked Gelatin Based Hybrid Scaffold Affects Cell Proliferation. ACS Appl Bio Mater. 2020;3(1):197–207.
192. Gabrielli L, Russo L, Poveda A, Jones JR, Nicotra F, Jiménez-Barbero J, et al. Epoxide opening versus silica condensation during sol-gel hybrid biomaterial synthesis. Chemistry - A European Journal. 2013;19(24):7856–64.
193. Greenhalgh RD, Ambler WS, Quinn SJ, Medeiros ES, Anderson M, Gore B, et al. Hybrid sol–gel inorganic/gelatin porous fibres via solution blow spinning. J Mater Sci. 2017;52(15):9066–81.
194. Desimone MF, Hélary C, Mosser G, Giraud-Guille MM, Livage J, Coradin T. Fibroblast encapsulation in hybrid silica-collagen hydrogels. J Mater Chem. 2010;20(4):666–8.
195. Arnett TR. Extracellular pH Regulates Bone Cell Function. The Journal of Nutrition Second International Acid-Base Symposium. 2008;138(2):415–8.
196. Zhang Z, Lai Q, Li Y, Xu C, Tang X, Ci J, et al. Acidic pH environment induces autophagy in osteoblasts. Sci Rep. 2017 Apr 6;7(46161).
197. Pottenger LH, Boverhof DR, Waechter JM. Epoxy Compounds—Olefin Oxides, Aliphatic Glycidyl Ethers and Aromatic Monoglycidyl Ethers. In: Patty's Toxicology. 6th ed. 2012.
198. Gabrielli L, Connell L, Russo L, Jiménez-Barbero J, Nicotra F, Cipolla L, et al. Exploring GPTMS reactivity against simple nucleophiles: Chemistry beyond hybrid materials fabrication. RSC Adv. 2014;4(4):1841–8.

199. Connell LS, Romer F, Suárez M, Valliant EM, Zhang Z, Lee PD, et al. Chemical characterisation and fabrication of chitosan-silica hybrid scaffolds with 3-glycidoxypropyl trimethoxysilane. J Mater Chem B. 2014;2(6):668–80.
200. Liu YL, Su YH, Lai JY. In situ crosslinking of chitosan and formation of chitosan-silica hybrid membranes with using γ-glycidoxypropyltrimethoxysilane as a crosslinking agent. Polymer (Guildf). 2004;45(20):6831–7.
201. Mohamed AL. Silan/biopolymer microgels for functionalization of cotton fabric: Dual responsive pH and temperature and antibacterial properties. J Appl Pharm Sci. 2017;7(7):077–88.
202. Soares SF, Fateixa S, Trindade T, Daniel-da-Silva AL. A versatile synthetic route towards gelatin-silica hybrids and magnetic composite colloidal nanoparticles. Adv Compos Hybrid Mater. 2021;5:884–98.
203. Negahi Shirazi A, Fathi A, Suarez FG, Wang Y, Maitz PK, Dehghani F. A Novel Strategy for Softening Gelatin-Bioactive-Glass Hybrids. ACS Appl Mater Interfaces. 2016;8(3):1676–86.
204. O'Neil MJ. The Merck index : an encyclopedia of chemicals, drugs, and biologicals. 15th ed. Cambridge, UK : Royal Society of Chemistry, 2013.; 2013. 826 p.
205. Deruiter J. Carboxylic Acid Structure and Chemistry : Part 2. 2005;1–10.
206. Nelson M, Tallia F, Page SJ, Hanna J V., Fujita Y, Obata A, et al. Electrospun cotton–wool-like silica/gelatin hybrids with covalent coupling. J Solgel Sci Technol. 2021;97(1):11–26.
207. Casagrande CA, Jochem LF, Repette WL. Analysis of the 3-glycidoxypropyltrimethoxysilane (GPTMS) hydrolysis by infrared spectroscopy. Revista Materia. 2020;25(3):1–11.
208. Trujillo S, Pérez-Román E, Kyritsis A, Gõmez Ribelles JL, Pandis C. Organic-inorganic bonding in chitosan-silica hybrid networks: Physical properties. J Polym Sci B Polym Phys. 2015;53(19):1391–400.
209. Cui JY, Li CY. Hepatic Toxicology. In: Comprehensive Toxicology (Third Edition). 2018.
210. Galeano-Duque Y, Poveda-Jaramillo JC, Mesa M. Considerations about 3-glycidoxypropyltrimethoxysilane reactivity in function of the complexity of aqueous and plasma gel media. J Mol Struct. 2023 Jul 15;1284(135334).
211. Mahony O, Jones JR. Porous bioactive nanostructured scaffolds for bone regeneration: A sol-gel solution. Nanomedicine. 2008;3(2):233–45.

212. Elving PJ, Markowitz JM, Rosenthal I. Preparation of buffer systems of constant ionic strength. Anal Chem. 1956;28(7):1179–80.
213. AAT Bioquest Inc. Phosphate Buffer (pH 5.8 to 7.4) Preparation and Recipe. 2023.
214. Nelson M. 3D Silica-Gelatin Hybrid Scaffolds for Tissue Regeneration. Imperial College London; 2016.
215. Tindall GW. Mobile-Phase Buffers, Part I — The Interpretation of pH in Partially Aqueous Mobile Phases. LC Troubleshooting. 2002;20(11):10–2.
216. Rodin V V., Izmailova VN. NMR method in the study of the interfacial adsorption layer of gelatin. Colloids Surf A Physicochem Eng Asp. 1996 Jan 22;106(2–3):95–102.
217. Lapomarda A, Cerqueni G, Geven MA, Chiesa I, De Acutis A, De Blasi M, et al. Physicochemical Characterization of Pectin-Gelatin Biomaterial Formulations for 3D Bioprinting. Macromol Biosci. 2021 Sep 1;21(2100168).
218. Rosenberg IM. Protein analysis and purification: benchtop techniques. Vol. 141, Springer Science & Business Media. 2013.
219. Hongmei J, Zhen Z, Zhiming L, Xinling W. Effects of temperature and solvent on the hydrolysis of alkoxysilane under alkaline conditions. Ind Eng Chem Res. 2006 Dec 6;45(25):8617–22.
220. de Buyl F, Kretschmer A. Understanding hydrolysis and condensation kinetics of γ-glycidoxypropyltrimethoxysilane. Journal of Adhesion. 2008 Feb;84(2):125–42.
221. Karmakar P, Ray S, Mandal A, Mondal S, Mallick S, Bera BK, et al. Mechanistic and kinetic investigations on the interaction of model platinum(II) complex with ligands of biological significance in reference to the antitumor activity. Synthesis and Reactivity in Inorganic, Metal-Organic and Nano-Metal Chemistry. 2013 Nov 26;43(10):1563–70.
222. Lide DR. Handbook of Chemistry and Physics. 72nd Edition. CRC Press; 1991.
223. Mahmoodani F, Ardekani VS, See SF, Yusop SM, Babji AS. Optimization and physical properties of gelatin extracted from pangasius catfish (Pangasius sutchi) bone. J Food Sci Technol. 2014 Nov 1;51(11):3104–13.
224. Nguyen D, Chen C, Pettitt BM, Iwahara J. NMR Methods for Characterizing the Basic Side Chains of Proteins: Electrostatic Interactions, Hydrogen Bonds, and Conformational Dynamics. Methods Enzymol. 2019 Jan 1;615:285–332.
225. Xue Y, Wang L, Shao Y, Yan J, Chen X, Lei B. Facile and green fabrication of biomimetic gelatin-siloxane hybrid hydrogel with highly elastic properties for biomedical applications. Chemical Engineering Journal. 2014 Sep 1;251:158–64.

226. Ng HW, Zhang Y, Naffa R, Prabakar S. Monitoring the Degradation of Collagen Hydrogels by Collagenase Clostridium histolyticum. Gels. 2020;6(4):46.
227. Corona-Escalera AF, Tinajero-Díaz E, García-Reyes RA, Luna-Bárcenas G, Seyfoddin A, Padilla-de la Rosa JD, et al. Enzymatic Crosslinked Hydrogels of Gelatin and Poly (Vinyl Alcohol) Loaded with Probiotic Bacteria as Oral Delivery System. Pharmaceutics. 2022 Dec 1;14(12):2759.
228. Caliari SR, Burdick JA. A practical guide to hydrogels for cell culture. Nat Methods. 2016 May 1;13(5):405–14.
229. Vesković A, Nakarada Đ, Popović Bijelić A. A novel methodology for hydrogel water content determination by EPR: The basis for real-time monitoring of controlled drug release and hydrogel swelling and degradation. Polym Test. 2021 Jun 1;98(107187).
230. Turner J, Nandakumar A, Anilbhai N, Boccaccini AR, Jones JR, Jell G. The effect of Si species released from bioactive glasses on cell behaviour: A quantitative review. Vol. 170, Acta Biomaterialia. Acta Materialia Inc; 2023. p. 39–52.
231. Shie MY, Ding SJ, Chang HC. The role of silicon in osteoblast-like cell proliferation and apoptosis. Acta Biomater. 2011;7(6):2604–14.
232. Wang X, Tolba E, Der HCS, Neufurth M, Feng Q, Diehl-Seifert BR, et al. Effect of bioglass on growth and biomineralization of saos-2 cells in hydrogel after 3d cell bioprinting. PLoS One. 2014 Nov 10;9(11).
233. Uribe P, Johansson A, Jugdaohsingh R, Powell JJ, Magnusson C, Davila M, et al. Soluble silica stimulates osteogenic differentiation and gap junction communication in human dental follicle cells. Sci Rep. 2020 Dec 1;10(1).
234. Götz W, Tobiasch E, Witzleben S, Schulze M. Effects of silicon compounds on biomineralization, osteogenesis, and hard tissue formation. Vol. 11, Pharmaceutics. MDPI AG; 2019.
235. Obata A, Ogasawara T, Kasuga T. Combinatorial effects of inorganic ions on adhesion and proliferation of osteoblast-like cells. J Biomed Mater Res A [Internet]. 2019 May 1;107(5):1042–51. Available from: https://doi.org/10.1002/jbm.a.36623
236. Jugdaohsingh R. Silicon and bone health. J Nutr Health Aging. 2007;11(2):99–110.
237. Carlisle E. Silicon: an essential element for the chick. Science (1979). 1972;178(4061):619–21.
238. Gough JE, Jones JR, Hench LL. Nodule formation and mineralisation of human primary osteoblasts cultured on a porous bioactive glass scaffold. Biomaterials. 2004;25(11):2039–46.

239. Ravarian R, Craft M, Dehghani F. Enhancing the biological activity of chitosan and controlling the degradation by nanoscale interaction with bioglass. J Biomed Mater Res A. 2015;103(9):2898–908.
240. Reyes-Peces M V., Pérez-Moreno A, De-Los-santos DM, Mesa-Díaz MDM, Pinaglia-Tobaruela G, Vilches-Pérez JI, et al. Chitosan-gptms-silica hybrid mesoporous aerogels for bone tissue engineering. Polymers (Basel). 2020;12(11):1–24.
241. Feinle A, Elsaesser MS, Hüsing N. Sol-gel synthesis of monolithic materials with hierarchical porosity. Chem Soc Rev. 2016;45(12):3377–99.
242. Tjong SC. Nanocrystalline Materials : Their Synthesis-Structure-Property Relationships and Applications. In: Nanocrystalline Materials. 2nd ed. 2014.
243. Heravi MM, Ghavidel M, Mohammadkhani L. Beyond a solvent: Triple roles of dimethylformamide in organic chemistry. RSC Adv. 2018;8(49):27832–62.
244. Nouri-Felekori M, Khakbiz M, Nezafati N, Mohammadi J, Eslaminejad MB. Comparative analysis and properties evaluation of gelatin microspheres crosslinked with glutaraldehyde and 3-glycidoxypropyltrimethoxysilane as drug delivery systems for the antibiotic vancomycin. Int J Pharm. 2019;557:208–20.
245. Zatorski JM, Montalbine AN, Ortiz-Cárdenas JE, Pompano RR. Quantification of fractional and absolute functionalization of gelatin hydrogels by optimized ninhydrin assay and 1 H NMR. Anal Bioanal Chem. 2020;412(24):6211–20.
246. Kasman LM, Barua S, Lu P, Rege K, Voelkel-Johnson C. Polymer-enhanced adenoviral transduction of CAR-negative bladder cancer cells. Mol Pharm. 2009 Oct 5;6(5):1612–9.
247. Pietrucci F, Saitta AM. Formamide reaction network in gas phase and solution via a unified theoretical approach: Toward a reconciliation of different prebiotic scenarios. Proc Natl Acad Sci U S A. 2015 Dec 8;112(49):15030–5.
248. Bordwell FG. Equilibrium acidities in dimethyl sulfoxide solution. Acc Chem Res. 1988 Dec 1;21(12):456–63.
249. Kenchington AW, Ward AG. The titration curve of gelatin. Biochem J. 1954;58(2):202–7.
250. Cannan RK. The Acid-Base Titration of Proteins. Chem Rev. 1942;30(395):395–412.
251. Kuijpers AJ, Engbers GHM, Krijgsveld J, Zaat SAJ, Dankert J, Feijen J. Cross-linking and characterisation of gelatin matrices for biomedical applications. J Biomater Sci Polym Ed. 2000;11(3):225–43.

252. van Hoorick J, Dobos A, Markovic M, Gheysens T, van Damme L, Gruber P, et al. Thiol-norbornene gelatin hydrogels: Influence of thiolated crosslinker on network properties and high definition 3D printing. Biofabrication. 2020;13(015017).
253. Van Hoorick J, Tytgat L, Dobos A, Ottevaere H, Van Erps J, Thienpont H, et al. (Photo-)crosslinkable gelatin derivatives for biofabrication applications. Acta Biomater. 2019 Oct 1;97:46–73.
254. Burchak V, Koch F, Siebler L, Haase S, Horner VK, Kempter X, et al. Evaluation of a Novel Thiol – Norbornene-Functionalized Gelatin Hydrogel for Bioprinting of Mesenchymal Stem Cells. 2022;23(14):7939.
255. Yao Y, Molotnikov A, Parkington HC, Meagher L, Forsythe JS. Extrusion 3D bioprinting of functional self-supporting neural constructs using a photoclickable gelatin bioink. Biofabrication. 2022;14(3).
256. Mũnoz Z, Shih H, Lin CC. Gelatin hydrogels formed by orthogonal thiol-norbornene photochemistry for cell encapsulation. Biomater Sci. 2014;2(8):1063–72.
257. Zhao C, Wu Z, Chu H, Wang T, Qiu S, Zhou J, et al. Thiol-Rich Multifunctional Macromolecular Crosslinker for Gelatin-Norbornene-Based Bioprinting. Biomacromolecules. 2021;22(6):2729–39.
258. Killops KL, Campos LM, Hawker CJ. Robust, efficient, and orthogonal synthesis of dendrimers via thiol-ene “click” chemistry. J Am Chem Soc. 2008;130(15):5062–4.
259. Magenau AJD, Chan JW, Hoyle CE, Storey RF. Facile polyisobutylene functionalization via thiol-ene click chemistry. Polym Chem. 2010;1(6):831–3.
260. Nolan MD, Schüttel M, Scanlan EM, Nielsen AL. Nanomole-scale photochemical thiol-ene chemistry for high-throughput late-stage diversification of peptide macrocycles. Peptide Science. 2023 Jan 1;116:e24310.
261. Iha RK, Wooley KL, Nyström AM, Burked DJ, Kade MJ, Hawker CJ. Applications of orthogonal “Click” Chemistries in the synthesis of functional soft materials. Chem Rev. 2009;109(11):5620–86.
262. Russo L, Sgambato A, Visone R, Occhetta P, Moretti M, Rasponi M, et al. Gelatin hydrogels via thiol-ene chemistry. Monatsh Chem. 2016;147(3):587–92.
263. Li X, Xiong Y. Application of “Click” Chemistry in Biomedical Hydrogels. ACS Omega. 2022 Oct 25;7(42):36918–28.
264. Northrop BH, Coffey RN. Thiol-ene click chemistry: Computational and kinetic analysis of the influence of alkene functionality. J Am Chem Soc. 2012;134(33):13804–17.

265. Fairbanks BD, Love DM, Bowman CN. Efficient Polymer-Polymer Conjugation via Thiol-ene Click Reaction. Macromol Chem Phys. 2017 Sep 1;218(1700073).
266. Kelemen V, Bege M, Eszenyi D, Debreczeni N, Bényei A, Stürzer T, et al. Stereoselective Thioconjugation by Photoinduced Thiol-ene Coupling Reactions of Hexo- and Pentopyranosyl d- and l-Glycals at Low-Temperature—Reactivity and Stereoselectivity Study. Chemistry - A European Journal. 2019 Nov 18;25(64):14555–71.
267. Wiley KL, Ovadia EM, Calo CJ, Huber RE, Kloxin AM. Rate-based approach for controlling the mechanical properties of “thiol-ene” hydrogels formed with visible light. Polym Chem. 2019 Aug 28;10(32):4428–40.
268. Fairbanks BD, Schwartz MP, Bowman CN, Anseth KS. Photoinitiated polymerization of PEG-diacrylate with lithium phenyl-2,4,6-trimethylbenzoylphosphinate: polymerization rate and cytocompatibility. Biomaterials. 2009 Dec;30(35):6702–7.
269. Williams CG, Malik AN, Kim TK, Manson PN, Elisseeff JH. Variable cytocompatibility of six cell lines with photoinitiators used for polymerizing hydrogels and cell encapsulation. Biomaterials. 2005 Apr;26(11):1211–8.
270. Bryant SJ, Nuttelman CR, Anseth KS. Cytocompatibility of UV and visible light photoinitiating systems on cultured NIH/3T3 fibroblasts in vitro. J Biomater Sci Polym Ed. 2000 Jan 1;11(5):439–57.
271. Tigner TJ, Rajput S, Gaharwar AK, Alge DL. Comparison of Photo Cross Linkable Gelatin Derivatives and Initiators for Three-Dimensional Extrusion Bioprinting. Biomacromolecules. 2020 Feb 10;21(2):454–63.
272. Hoyle CE, Bowman CN. Thiol-ene click chemistry. Angewandte Chemie - International Edition. 2010;49(9):1540–73.
273. Hoyle CE, Lee TY, Roper T. Thiol-enes: Chemistry of the past with promise for the future. J Polym Sci A Polym Chem. 2004;42(21):5301–38.
274. Cramer NB, Reddy SK, O’Brien AK, Bowman CN. Thiol - Ene Photopolymerization Mechanism and Rate Limiting Step Changes for Various Vinyl Functional Group Chemistries. Macromolecules. 2003 Oct 21;36(21):7964–9.
275. Long KF, Bongiardina NJ, Mayordomo P, Olin MJ, Ortega AD, Bowman CN. Effects of 1°, 2°, and 3° Thiols on Thiol-Ene Reactions: Polymerization Kinetics and Mechanical Behavior. Macromolecules. 2020 Jul 28;53(14):5805–15.

276. Lin CC, Raza A, Shih H. PEG hydrogels formed by thiol-ene photo-click chemistry and their effect on the formation and recovery of insulin-secreting cell spheroids. Biomaterials. 2011 Dec;32(36):9685–95.
277. Anderson SB, Lin CC, Kuntzler D V., Anseth KS. The performance of human mesenchymal stem cells encapsulated in cell-degradable polymer-peptide hydrogels. Biomaterials. 2011 May;32(14):3564–74.
278. Liang J, Zhang X, Chen Z, Li S, Yan C. Thiol-ene click reaction initiated rapid gelation of PEGDA/silk fibroin hydrogels. Polymers (Basel). 2019;11(12):2102.
279. Ooi HW, Mota C, Tessa Ten Cate A, Calore A, Moroni L, Baker MB. Thiol-Ene Alginate Hydrogels as Versatile Bioinks for Bioprinting. Biomacromolecules. 2018;19(8):3390–400.
280. Holmes R, Yang X Bin, Dunne A, Florea L, Wood D, Tronci G. Thiol-ene photo-click collagen-PEG hydrogels: Impact of water-soluble photoinitiators on cell viability, gelation kinetics and rheological properties. Polymers (Basel). 2017;9(6):226.
281. Michel SES, Rogers SE, Briscoe WH, Galan MC. Tunable Thiol-Ene Photo-Cross-Linked Chitosan-Based Hydrogels for Biomedical Applications. ACS Appl Bio Mater. 2020 Nov 16;3(11):8075–83.
282. Andreazza R, Morales A, Pieniz S, Labidi J. Gelatin-Based Hydrogels: Potential Biomaterials for Remediation. Polymers (Basel). 2023;15(4):1–12.
283. Perera MM, Ayres N. Gelatin based dynamic hydrogels: Via thiol-norbornene reactions. Polym Chem. 2017;8(44):6741–9.
284. Van Hoorick J, Gruber P, Markovic M, Rollot M, Graulus GJ, Vagenende M, et al. Highly Reactive Thiol-Norbornene Photo-Click Hydrogels: Toward Improved Processability. Macromol Rapid Commun. 2018;39(14):1–7.
285. Dobos A, Van Hoorick J, Steiger W, Gruber P, Markovic M, Andriotis OG, et al. Thiol–Gelatin–Norbornene Bioink for Laser-Based High-Definition Bioprinting. Adv Healthc Mater. 2020;9(15):1–9.
286. Göckler T, Haase S, Kempter X, Pfister R, Maciel BR, Grimm A, et al. Tuning Superfast Curing Thiol-Norbornene-Functionalized Gelatin Hydrogels for 3D Bioprinting. Adv Healthc Mater. 2021;10(14):1–13.
287. Soliman BG, Major GS, Atienza-Roca P, Murphy CA, Longoni A, Alcala-Orozco CR, et al. Development and Characterization of Gelatin-Norbornene Bioink to Understand the Interplay between Physical Architecture and Micro-Capillary Formation in Biofabricated Vascularized Constructs. Adv Healthc Mater. 2022;11(2):1–16.

288. Francis LF. Starting Materials. In: Materials Processing. Elsevier; 2016. p. 21–103.
289. Shahrokhinia A, Biswas P, Reuther JF. Orthogonal synthesis and modification of polymer materials. Journal of Polymer Science. 2021 Aug 15;59(16):1748–86.
290. McCall JD, Anseth KS. Thiol-ene photopolymerizations provide a facile method to encapsulate proteins and maintain their bioactivity. Biomacromolecules. 2012;13(8):2410–7.
291. Roberts JJ, Bryant SJ. Comparison of photopolymerizable thiol-ene PEG and acrylate-based PEG hydrogels for cartilage development. Biomaterials. 2013 Dec;34(38):9969–79.
292. Wang G, Yuan N, Li N, Wei Q, Qian Y, Zhang J, et al. Vascular Endothelial Growth Factor Mimetic Peptide and Parathyroid Hormone (1-34) Delivered via a Blue-Light-Curable Hydrogel Synergistically Accelerate Bone Regeneration. ACS Appl Mater Interfaces. 2022 Aug 10;14(31):35319–32.
293. Arkenberg MR, Koehler K, Lin CC. Heparinized Gelatin-Based Hydrogels for Differentiation of Induced Pluripotent Stem Cells. Biomacromolecules. 2022 Oct 10;23(10):4141–52.
294. Rizwan M, Chan SW, Comeau PA, Willett TL, Yim EKF. Effect of sterilization treatment on mechanical properties, biodegradation, bioactivity and printability of GelMA hydrogels. Biomedical Materials (Bristol). 2020 Nov 1;15(065017).
295. Krupa I, Nedelčev T, Račko D, Lacík I. Mechanical properties of silica hydrogels prepared and aged at physiological conditions: Testing in the compression mode. J Solgel Sci Technol. 2010 Jan;53(1):107–14.
296. Allum J, Moetazedian A, Gleadall A, Silberschmidt V V. Interlayer bonding has bulk-material strength in extrusion additive manufacturing: New understanding of anisotropy. Addit Manuf. 2020 Aug 1;34(101297).
297. Burmester A, Luthringer B, Willumeit R, Feyerabend F. Comparison of the reaction of bone-derived cells to enhanced MgCl2-salt concentrations. Biomatter. 2014;4:e967616.
298. Contessi Negrini N, Angelova Volponi A, Sharpe PT, Celiz AD. Tunable Cross-Linking and Adhesion of Gelatin Hydrogels via Bioorthogonal Click Chemistry. ACS Biomater Sci Eng. 2021 Sep 13;7(9):4330–46.
299. Gleede T, Rieger E, Homann-Müller T, Wurm FR. 4-Styrenesulfonyl-(2-methyl)aziridine: The First Bivalent Aziridine-Monomer for Anionic and Radical Polymerization. Macromol Chem Phys. 2018;219(1):1700145.

300. Sy Piecco KWE, Aboelenen AM, Pyle JR, Vicente JR, Gautam D, Chen J. Kinetic Model under Light-Limited Condition for Photoinitiated Thiol-Ene Coupling Reactions. ACS Omega. 2018 Oct 29;3(10):14327–32.
301. Claudino M, Jonsson M, Johansson M. Utilizing thiol-ene coupling kinetics in the design of renewable thermoset resins based on d-limonene and polyfunctional thiols. RSC Adv. 2014;4(20):10317–29.
302. Nguyen HD. Thiol-Norbornene Hydrogels With Tunable Mechanical Properties for Engineered Extracellular Matrices. Vol. May. Purdue University; 2019.
303. Cao Y, Cheng P, Sang S, Xiang C, An Y, Wei X, et al. 3D printed PCL/GelMA biphasic scaffold boosts cartilage regeneration using co-culture of mesenchymal stem cells and chondrocytes: In vivo study. Mater Des. 2021 Nov 15;210(110065).
304. Xu H, Casillas J, Krishnamoorthy S, Xu C. Effects of Irgacure 2959 and lithium phenyl-2,4,6-trimethylbenzoylphosphinate on cell viability, physical properties, and microstructure in 3D bioprinting of vascular-like constructs. Biomedical Materials (Bristol). 2020;15(055021).
305. Dimitriadi M, Zinelis S, Zafiropoulou M, Silikas N, Eliades G. Self-etch silane primer: Reactivity and bonding with a lithium disilicate ceramic. Materials. 2020 Feb 1;13(3):641.
306. Lee SH, Kwon D, Yoon TH. An optimized dispersion of manufactured nanomaterials forin vitro cytotoxicity assays. Toxicol Environ Health Sci. 2010;2(3):207–13.
307. Qiao C, Wang X, Zhang J, Yao J. Influence of salts in the Hofmeister series on the physical gelation behavior of gelatin in aqueous solutions. Food Hydrocoll. 2021;110:106150.
308. Das S, Basu T, Majumdar S. Molecular interactions of acids and salts with polyampholytes. J Chem Phys. 2024 Feb 1;160(5):054901.
309. Bansal N. Influence Of Several Metal Ions on the Gelation Activation Energy Of Silicon Tetraethoxide. In: 90th Annual Meeting of the American Ceramic Society. 1988.
310. Dulbecco R, Freeman G. Plaque production by the polyoma virus. Virology. 1959;8(3):396–7.
311. Dolinina ES, Kraev AS, Parfenyuk E V. Effect of sol–gel synthesis conditions on the physical properties of silica hydrogels. Mendeleev Communications. 2020 Nov 1;30(6):812–4.

312. Nicolaidou V, Wong MM, Redpath AN, Ersek A, Baban DF, Williams LM, et al. Monocytes induce STAT3 activation in human mesenchymal stem cells to promote osteoblast formation. PLoS One. 2012 Jul 3;7(7):e39871.
313. Cinar AG, Munir I, Yesiloz G. Investigating Physical Properties of Hybrid Hyaluronic Acid and Collagen Compositions of GelMA Microgels toward Tissue Engineering and Organ-on-Chip Applications. ACS Appl Polym Mater. 2023 Oct 13;5(10):8121–32.
314. Koshy ST, Ferrante TC, Lewin SA, Mooney DJ. Injectable, porous, and cell-responsive gelatin cryogels. Biomaterials. 2014 Mar;35(8):2477–87.
315. Turner PA, Thiele JS, Stegemann JP. Growth factor sequestration and enzyme-mediated release from genipin-crosslinked gelatin microspheres. J Biomater Sci Polym Ed. 2017 Nov 2;28(16):1826–46.
316. Wang Y, Ma M, Wang J, Zhang W, Lu W, Gao Y, et al. Development of a photo-crosslinking, biodegradable GelMA/PEGDA hydrogel for guided bone regeneration materials. Materials. 2018;11(8):6–8.
317. Zhai X, Ruan C, Ma Y, Cheng D, Wu M, Liu W, et al. 3D-Bioprinted Osteoblast-Laden Nanocomposite Hydrogel Constructs with Induced Microenvironments Promote Cell Viability, Differentiation, and Osteogenesis both In Vitro and In Vivo. Advanced Science. 2018 Mar 1;5(3).
318. Schröder HC, Wang XH, Wiens M, Diehl-Seifert B, Kropf K, Schloßmacher U, et al. Silicate modulates the cross-talk between osteoblasts (SaOS-2) and osteoclasts (RAW 264.7 cells): Inhibition of osteoclast growth and differentiation. J Cell Biochem. 2012;113(10):3197–206.
319. Suvarnapathaki S, Nguyen MA, Wu X, Nukavarapu SP, Camci-Unal G. Synthesis and characterization of photocrosslinkable hydrogels from bovine skin gelatin. RSC Adv. 2019;9(23):13016–25.
320. Prasadh S, Wong RCW. Unraveling the mechanical strength of biomaterials used as a bone scaffold in oral and maxillofacial defects. Oral Sci Int. 2018 Jul 1;15(2):48–55.
321. Xing W, Tang Y. On mechanical properties of nanocomposite hydrogels: Searching for superior properties. Nano Materials Science. 2022 Jun 1;4(2):83–96.
322. Tosh SM, Marangoni AG, Hallett FR, Britt IJ. Aging dynamics in gelatin gel microstructure. Food Hydrocoll. 2003;17(4):503–13.
323. Danks AE, Hall SR, Schnepp Z. The evolution of “sol-gel” chemistry as a technique for materials synthesis. 2016;3:91–112.

324. Cai MH, Chen XY, Fu LQ, Du WL, Yang X, Mou XZ, et al. Design and Development of Hybrid Hydrogels for Biomedical Applications: Recent Trends in Anticancer Drug Delivery and Tissue Engineering. Front Bioeng Biotechnol. 2021 Feb 17;9(630943):1–18.
325. Yu C, Miller KL, Schimelman J, Wang P, Zhu W, Ma X, et al. A sequential 3D bioprinting and orthogonal bioconjugation approach for precision tissue engineering. Biomaterials. 2020 Nov 1;258(120294):1–12.
326. Dey K, Agnelli S, Borsani E, Sartore L. Degradation-dependent stress relaxing semi-interpenetrating networks of hydroxyethyl cellulose in gelatin-peg hydrogel with good mechanical stability and reversibility. Gels. 2021 Dec 1;7(4):277.
327. Lei H, Dong L, Li Y, Zhang J, Chen H, Wu J, et al. Stretchable hydrogels with low hysteresis and anti-fatigue fracture based on polyprotein cross-linkers. Nat Commun. 2020 Dec 1;11(4032):1–10.
328. Yang H, Sinha SK, Feng Y, McCallen DB, Jeremić B. Energy dissipation analysis of elastic–plastic materials. Comput Methods Appl Mech Eng. 2018;331:309–26.
329. Nyman JS, Leng H, Neil Dong X, Wang X. Differences in the mechanical behavior of cortical bone between compression and tension when subjected to progressive loading. J Mech Behav Biomed Mater. 2009 Dec;2(6):613–9.
330. Brinker CJeffrey, Scherer GW. Sol-gel science : the physics and chemistry of sol-gel processing. Academic Press; 1990. 908 p.
331. Boonstra AH, Bernards TNM. The dependence of the gelation time on the hydrolysis time in a two-step SiO2 sol-gel process. J Non Cryst Solids. 1988;105(3):207–13.
332. Li J, Liu H, Wang C, Huang G. A facile method to fabricate hybrid hydrogels with mechanical toughness using a novel multifunctional cross-linker. RSC Adv. 2017;7(56):35311–9.
333. Xu J, Liu X, Ren X, Gao G. The role of chemical and physical crosslinking in different deformation stages of hybrid hydrogels. Eur Polym J. 2018 Mar 1;100:86–95.
334. Lu H, Wang X, Shi X, Yu K, Fu YQ. A phenomenological model for dynamic response of double-network hydrogel composite undergoing transient transition. Compos B Eng. 2018 Oct 15;151:148–53.
335. Matsuda T, Nakajima T, Fukuda Y, Hong W, Sakai T, Kurokawa T, et al. Yielding Criteria of Double Network Hydrogels. Macromolecules. 2016 Mar 9;49(5):1865–72.
336. Gong JP, Katsuyama Y, Kurokawa T, Osada Y. Double-network hydrogels with extremely high mechanical strength. Advanced Materials. 2003 Jul 17;15(14):1155–8.

337. Zhao X, Huebsch N, Mooney DJ, Suo Z. Stress-relaxation behavior in gels with ionic and covalent crosslinks. J Appl Phys. 2010;107(6):063509.
338. Xiong J, Wang X, Li L, Li Q, Zheng S, Liu Z, et al. Low-Hysteresis and High-Toughness Hydrogels Regulated by Porous Cationic Polymers: the Effect of Counteranions. Angewandte Chemie - International Edition. 2024;63:e2023163.
339. Bose S, Li S, Mele E, Silberschmidt V V. Dry vs. wet: Properties and performance of collagen films. Part II. Cyclic and time-dependent behaviours. J Mech Behav Biomed Mater. 2020 Dec 1;112:104040.
340. Dong XN, Luo Q, Wang X. Progressive post-yield behavior of human cortical bone in shear. Bone. 2013 Mar;53(1):1–5.
341. Ebacher V, Tang C, McKay H, Oxland TR, Guy P, Wang R. Strain redistribution and cracking behavior of human bone during bending. Bone. 2007 May;40(5):1265–75.
342. Cooke ME, Rosenzweig DH. The rheology of direct and suspended extrusion bioprinting. APL Bioeng. 2021;5(011502):1–20.
343. Ramli H, Zainal NFA, Hess M, Chan CH. Basic principle and good practices of rheology for polymers for teachers and beginners. Chemistry Teacher International. 2022 Dec 1;4(4):307–26.
344. Herrada-Manchón H, Fernández MA, Aguilar E. Essential Guide to Hydrogel Rheology in Extrusion 3D Printing: How to Measure It and Why It Matters? Gels. 2023 Jul 1;9(7):517.
345. Stojkov G, Niyazov Z, Picchioni F, Bose RK. Relationship between structure and rheology of hydrogels for various applications. Gels. 2021 Dec 1;7(4):255.
346. Podevyn A, Van Vlierberghe S, Dubruel P, Hoogenboom R. Design and Synthesis of Hybrid Thermo-Responsive Hydrogels Based on Poly(2-oxazoline) and Gelatin Derivatives. Gels. 2022 Feb 1;8(2).
347. Jastram A, Claus J, Janmey PA, Kragl U. Rheological properties of hydrogels based on ionic liquids. Polym Test. 2021 Jan 1;93(106943):1–8.
348. Kokol V, Pottathara YB, Mihelčič M, Perše LS. Rheological properties of gelatine hydrogels affected by flow- and horizontally-induced cooling rates during 3D cryo-printing. Colloids Surf A Physicochem Eng Asp. 2021 May 5;616(126356):1–10.
349. Cuomo F, Cofelice M, Lopez F. Rheological characterization of hydrogels from alginate-based nanodispersion. Polymers (Basel). 2019 Feb 3;11(2):259.
350. Garcia-Orue I, Santos-Vizcaino E, Sanchez P, Gutierrez FB, Aguirre JJ, Hernandez RM, et al. Bioactive and degradable hydrogel based on human platelet-rich plasma

fibrin matrix combined with oxidized alginate in a diabetic mice wound healing model. Biomaterials Advances. 2022 Apr 1;135(112695):1–12.

351. Choi BY, Chalisserry EP, Kim MH, Kang HW, Choi IW, Nam SY. The influence of astaxanthin on the proliferation of adipose-derived mesenchymal stem cells in gelatin-methacryloyl (GelMA) hydrogels. Materials. 2019 Aug 1;12(15):2416.
352. Deng S, Li X, Yang W, He K, Ye X. Injectable in situ cross-linking hyaluronic acid/carboxymethyl cellulose based hydrogels for drug release. J Biomater Sci Polym Ed. 2018 Sep 2;29(13):1643–55.
353. Cai Z, Wu J, Wu M, Li R, Wang P, Zhang H. Rheological characterization of novel carboxymethylated curdlan-silica hybrid hydrogels with tunable mechanical properties. Carbohydr Polym. 2020 Feb 15;230(115578):1–9.
354. Matsunaga T, Shibayama M. Gel point determination of gelatin hydrogels by dynamic light scattering and rheological measurements. Phys Rev E Stat Nonlin Soft Matter Phys. 2007 Sep 27;76(3).
355. Shibayama M, Shibayama AM, Norisuye T. Accounts Gel Formation Analyses by Dynamic Light Scattering. Bull Chem Soc Jpn. 2002;75:641–59.
356. Chansoria P, Asif S, Polkoff K, Chung J, Piedrahita JA, Shirwaiker RA. Characterizing the Effects of Synergistic Thermal and Photo-Cross-Linking during Biofabrication on the Structural and Functional Properties of Gelatin Methacryloyl (GelMA) Hydrogels. ACS Biomater Sci Eng. 2021 Nov 8;7(11):5175–88.
357. Boyd-Moss M, Firipis K, O'Connell CD, Rifai A, Quigley A, Boer G, et al. Shining a light on the hidden structure of gelatin methacryloyl bioinks using small-angle X-ray scattering (SAXS). Mater Chem Front. 2021 Nov 21;5(22):8025–36.
358. Freeman S, Ramos R, Alexis Chando P, Zhou L, Reeser K, Jin S, et al. A bioink blend for rotary 3D bioprinting tissue engineered small-diameter vascular constructs. Acta Biomater. 2019 Sep 1;95:152–64.
359. Tuncaboylu DC, Okay O. Hierarchically macroporous cryogels of polyisobutylene and silica nanoparticles. Langmuir. 2010 May 18;26(10):7574–81.
360. Annabi N, Nichol JW, Zhong X, Ji C, Koshy S, Khademhosseini A, et al. Controlling the Porosity and Microarchitecture of Hydrogels for Tissue Engineering. TISSUE ENGINEERING: Part B. 2010;16(4):371–83.
361. Whang K, Healy KE, Elenz DR, Nam EK, Tsai DC, Thomas CH, et al. Engineering Bone Regeneration with Bioabsorbable Scaffolds with Novel Microarchitecture. Tissue Eng. 1999 Feb 1;5(1):35–51.

362. Klawitter JJ, Bagwell JG, Weinstein AM, Sauer BW, Pruitt JR. An evaluation of bone growth into porous high density polyethylene. J Biomed Mater Res. 1976 Mar 1;10(2):311–23.
363. Chen MC, Chiu HC, Kuo PJ, Chiang CY, Fu MM, Fu E. Bone formation with functionalized 3D printed poly-ε-caprolactone scaffold with plasma-rich-fibrin implanted in critical-sized calvaria defect of rat. J Dent Sci. 2021 Oct 1;16(4):1214–21.
364. Nehrer S, Breinan+ HA, Ramappa A, Young G, Shortkroff S, Louie+ LK, et al. Matrix collagen type and pore size influence behaviour of seeded canine chondrocytes. Biomaterials. 1997;16:769–76.
365. Lee SJ, Lee IW, Lee YM, Lee HB, Khang G. Macroporous biodegradable natural/synthetic hybrid scaffolds as small intestine submucosa impregnated poly(D,L-lactide-co-glycolide) for tissue-engineered bone. J Biomater Sci Polym Ed. 2004;15(8):1003–17.
366. Williams JM, Adewunmi A, Schek RM, Flanagan CL, Krebsbach PH, Feinberg SE, et al. Bone tissue engineering using polycaprolactone scaffolds fabricated via selective laser sintering. Biomaterials. 2005 Aug;26(23):4817–27.
367. ISO 10993-5. Biological evaluation of medical devices. Part 5: Tests for in vitro cytotoxicity. 2009.
368. Lahiri SK, Liu L. Fabrication of a Nanoporous Silica Hydrogel by Cross-Linking of SiO2-H3BO3-Hexadecyltrimethoxysilane for Excellent Adsorption of Azo Dyes from Wastewater. Langmuir. 2021 Jul 27;37(29):8753–64.
369. Capeletti LB, Dos Santos JHZ, Moncada E, Da Rocha ZN, Pepe IM. Encapsulated alizarin red species: The role of the sol–gel route on the interaction with silica matrix. Powder Technol. 2013;237:117–24.
370. Gong R, Ye J, Dai W, Yan X, Hu J, Hu X, et al. Adsorptive removal of methyl orange and methylene blue from aqueous solution with finger-citron-residue-based activated carbon. Ind Eng Chem Res. 2013 Oct 2;52(39):14297–303.
371. Gao H, Jiang J, Huang Y, Wang H, Sun J, Jin Z, et al. Synthesis of hydrogels for adsorption of anionic and cationic dyes in water: ionic liquid as a crosslinking agent. SN Appl Sci. 2022 Apr 1;4(118).
372. Pedraza CE, Chien YC, McKee MD. Calcium oxalate crystals in fetal bovine serum: Implications for cell culture, phagocytosis and biomineralization studies in vitro. J Cell Biochem. 2008 Apr 1;103(5):1379–93.

373. Zhang N, Milleret V, Thompson-Steckel G, Huang NP, Vörös J, Simona BR, et al. Soft Hydrogels Featuring In-Depth Surface Density Gradients for the Simple Establishment of 3D Tissue Models for Screening Applications. SLAS Discovery. 2017 Jun 1;22(5):635–44.
374. Fisher SA, Anandakumaran PN, Owen SC, Shoichet MS. Tuning the Microenvironment: Click-Crosslinked Hyaluronic Acid-Based Hydrogels Provide a Platform for Studying Breast Cancer Cell Invasion. Adv Funct Mater. 2015 Dec 9;25(46):7163–72.
375. Grijalva Garces D, Appoldt LJ, Egner J, Leister N, Hubbuch J. The Effect of Gelatin Source on the Synthesis of Gelatin-Methacryloyl and the Production of Hydrogel Microparticles. Gels. 2023 Dec 1;9(12):927.
376. Hausser HJ, Brenner RE. Phenotypic instability of Saos-2 cells in long-term culture. Biochem Biophys Res Commun. 2005 Jul 22;333(1):216–22.
377. Dvorakova J, Wiesnerova L, Chocholata P, Kulda V, Landsmann L, Cedikova M, et al. Human cells with osteogenic potential in bone tissue research. Biomed Eng Online. 2023 Dec 1;22:33.
378. Fairbanks BD, Schwartza MP, Bowmana CN, Anseth KS. Photoinitiated polymerization of PEG-diacrylate with lithium phenyl-2,4,6-trimethylbenzoylphosphinate: polymerization rate and cytocompatibility. Biomaterials. 2009;30(35):6702–7.
379. Benton JA, Deforest CA, Vivekanandan V, Anseth KS. Photocrosslinking of gelatin macromers to synthesize porous hydrogels that promote valvular interstitial cell function. Tissue Eng Part A. 2009;15(11):3221–30.

APPENDICES

Appendix A

A.2.3.5. Degradation behaviour of gelatin-based-silica hybrid hydrogels

A.2.3.5.1. Change in mass

When considering the overall degradation rate per hour (%) for the 28-day period, it was 0.09% (GelMA-Silica), 0.07% (Gel-GPTPGS-Silica), and 0.06% (GelMA-GPTPGS-Silica), with no significant difference between any of the formulations (Appendix Figure A.1)

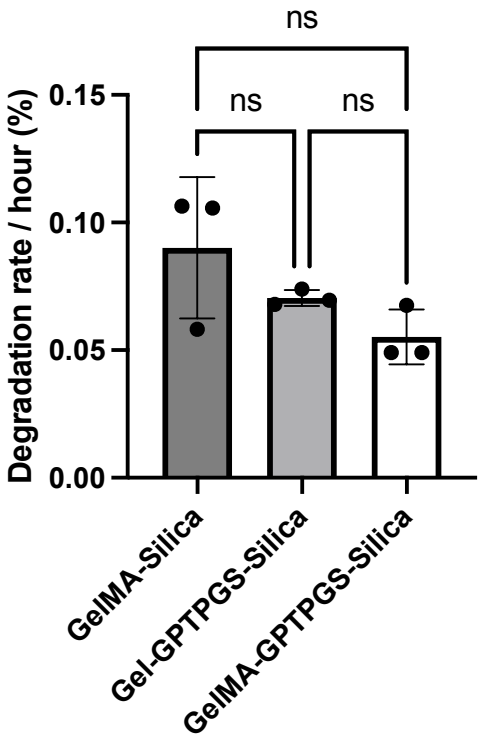


Figure A.1. Overall degradation rate / hour (%) for GelMA-Silica, Gel-GPTPGS-Silica, and GelMA-GPTPGS-Silica hybrid hydrogel formulations. Degradation rate was calculated by dividing the overall mass lost (%) by the duration of the assay (hours). Individual plots are repeat measures and error bars represent the SD (n=3).

All three formulations followed the same trend of a high degree of mass lost within the initial degradation period (up to 24 hours), with 78.1% (GelMA-Silica), 76.5% (Gel-GPTPGS-Silica), and 81.3% (GelMA-GPTPGS-Silica) mass remaining at 24 hours (Appendix Figure A.2a). This is a degradation rate of 0.91% (GelMA-Silica), 0.98% (Gel-GPTPGS-Silica), and 0.78% (GelMA-GPTPGS-Silica) per hour within this 24-hour period.

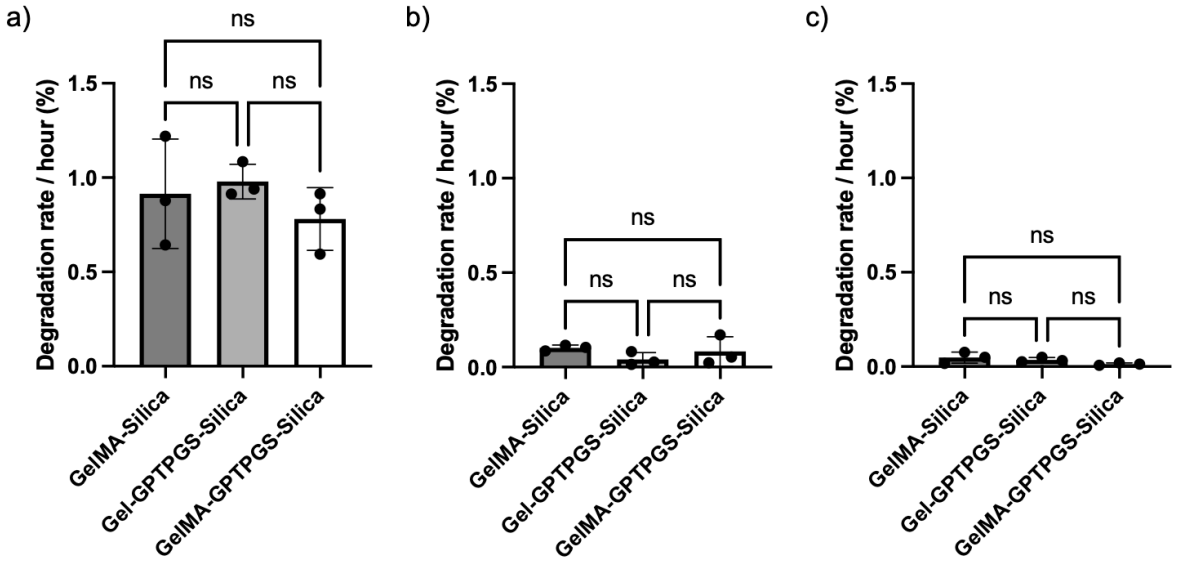


Figure A.2. Degradation rate / hour (%) for the distinct regions of the assay GelMA-Silica, Gel-GPTPGS-Silica, and GelMA-GPTPGS-Silica hybrid hydrogel formulations; a) initial degradation rate, b) intermediate degradation rate and c) plateau degradation rate. Degradation rate was calculated by dividing the overall mass lost (%) by the duration of either the initial, intermediate, or plateaued region. Individual plots are repeat measures and error bars represent the SD (n=3).

This was followed by intermediate, slower degradation between 24 hours to 5 days, with a degradation rate of 0.10% (GelMA-Silica), 0.04% (Gel-GPTPGS-Silica), and 0.08% (GelMA-GPTPGS-Silica) per hour from 24 hours to 7 days (Appendix Figure A.2b). By 7 days, there was 63.4% (GelMA-Silica), 70.6% (Gel-GPTPGS-Silica), and 69.4% (GelMA-GPTPGS-Silica) mass remaining. Finally, in the plateau region, the degradation rate slowed to 0.05% (GelMA-Silica), and 0.01% (GelMA-GPTPGS-Silica) per hour but continued at the same rate of 0.04% for Gel-GPTPGS-Silica), from 7 to 28 days (Appendix Figure A.2c).

Appendix B

Table B.1. Gelatin-based GPTMS reactions in literature, with focus on reaction variables; length, temperature, source of gelatin, concentration of gelatin, GPTMS:gelatin, and solvent.

	Reaction variables						
	Reaction length (h)	**Temperature (°C)**	**Source of gelatin**	**Gelatin bloom**	**Concentration of gelatin (wt%)**	**GPTMS: gelatin**	**Solvent**
Nelson et al. 2021 (117)	3 or 14	/	Bovine, Type A	/	5	CF0, CF250, CF500, CF750, CF1000	$HCl_{(aq)}$ (10 mM)
Balavigneswaran et al. 2020 (191)	Overnight	70	Poly(D,L-lactide)-b-gelatin	/	10	"equal molar ratio"	$HCl_{(aq)}$ (10 mM)
Greenhalgh et al. 2018 (193)	13	40	Porcine, Type A	300	10	"addition of GPTMS to 92 ul g^{-1} of gelatin"	PBS
Connell et al. 2017 (114)	48	40	/	/	5	"molar ratio of gelatin monomer units to GPTMS of 10"	D_2O
Negahi Shirazi et al. 2016 (203)	12	40	Type A	/	10	92 uL [GPTMS] per gram of GelMA	PBS
Mahony et al. 2014 (190)	14	40	Porcine, Type A	100, 175 and 300	5	CF750	$HCl_{(aq)}$

Tonda-Turo et al. 2013 (185)	1	50	Porcine, Type A	/	/	92 uL [GPTMS] per gram of gelatin	dH_2O
Mahony et al. 2010 (184)	14	/	Bovine, Type A	/	5	CF0, CF100, CF250, CF500, CF1000, CF1500, CF2000	$HCl_{(aq)}$ (10 mM)

Table B.2. Gelatin-based GPTMS reactions in literature, with focus on verification technique to determine successful functionalisation.

	Verification technique				
	FTIR	**NMR**	**TGA**	**DSC**	**Ninhydrin**
Nelson et al. 2021 (117)		✓	✓		✓
Balavigneswaran et al. 2020 (191)	✓		✓	✓	
Greenhalgh et al. 2018 (193)					
Connell et al. 2017 (114)		✓			
Negahi Shirazi et al. 2016 (203)	✓				✓
Mahony et al. 2014 (190)					
Tonda-Turo et al. 2013 (185)	✓				
Mahony et al. 2010 (184)	✓	✓			

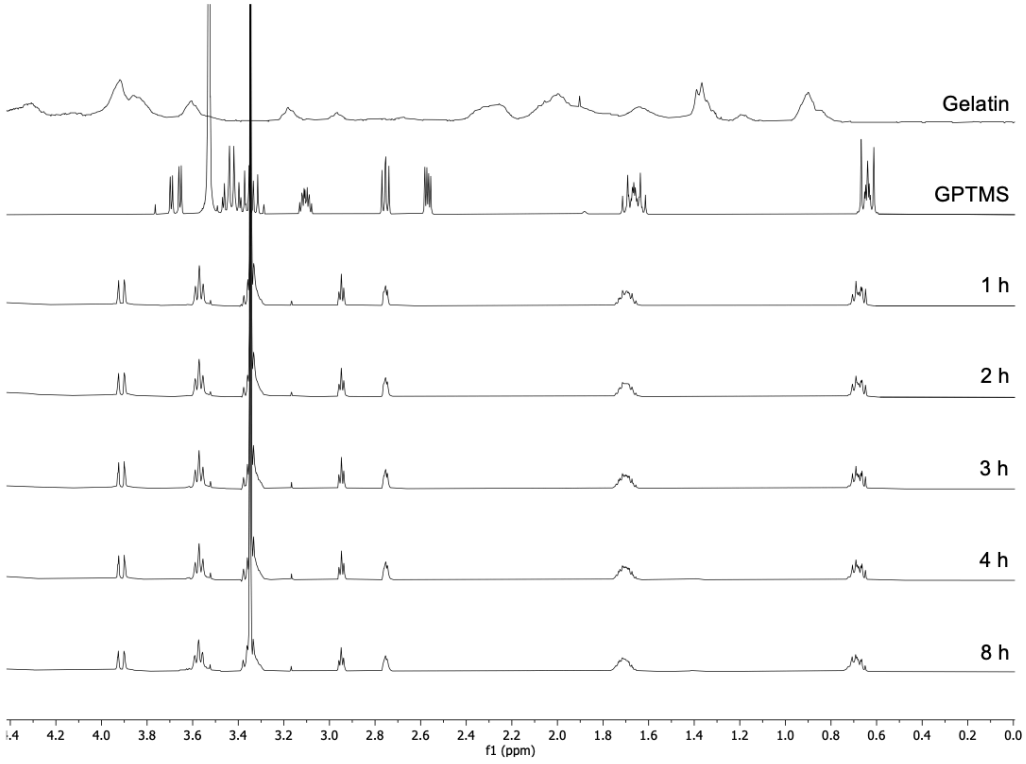


Figure B.1. ^{1}H NMR spectra of starting reagents gelatin (D_2O, 400 Hz) and GPTMS ($CHCl_3$, 400 Hz), and the progressing reaction at 1, 2, 3, 4 and 8 hours in $HCl_{(aq)}$, manually altering the pH to pH 4.9 (± 0.02) every 1 hour (D_2O, 400 Hz) [h = hours].

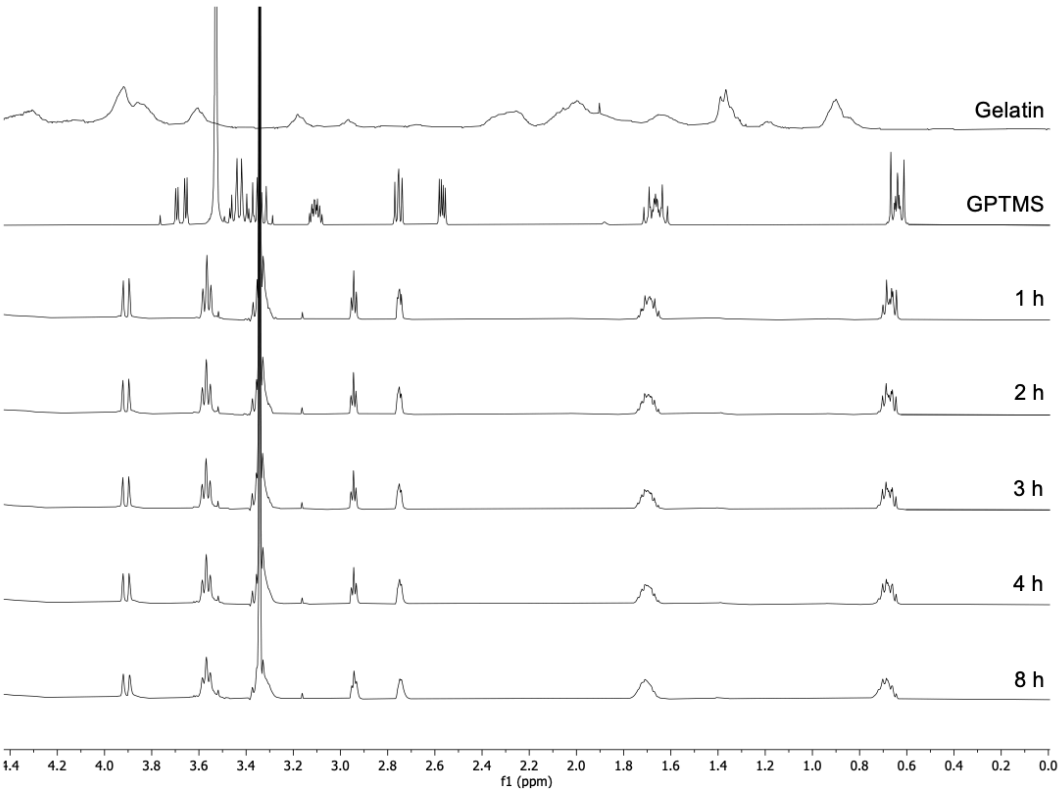


Figure B.2. ^{1}H NMR spectra of starting reagents gelatin (D_2O, 400 Hz) and GPTMS ($CDCl_3$, 400 Hz), and the progressing reaction at 1, 2, 3, 4 and 8 hours in PB (D_2O, 400 Hz) [PB = phosphate buffer; h = hours].

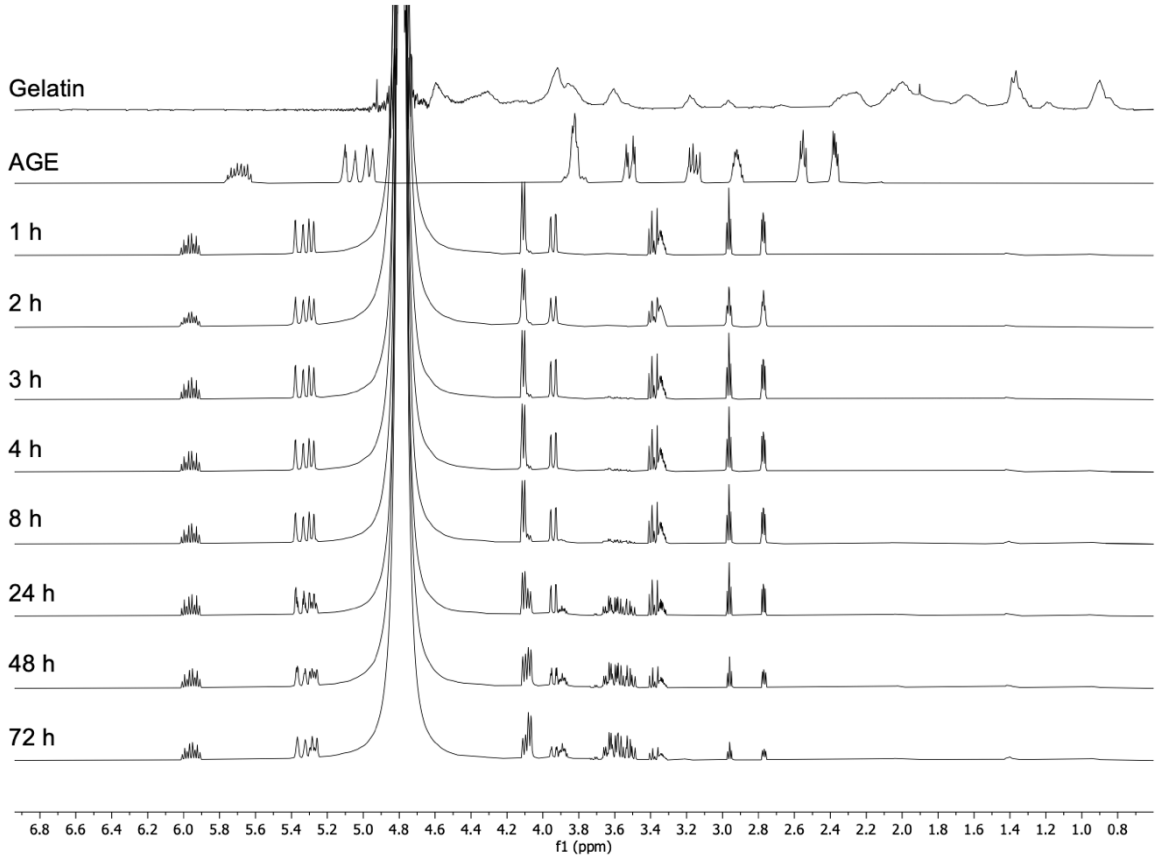


Figure B.3. ^{1}H NMR spectra of starting reagents gelatin (D_2O, 400 Hz) and AGE ($CDCl_3$, 400 Hz), and the progressing reaction at 1, 2, 3, 4, 8, 24, 48, and 72 hours in $HCl_{(aq)}$ (D_2O, 400 Hz), manually altering the pH to pH 4.9 (± 0.02) every 1 hour within the first 8 hours, and then every 24 hours onwards (h = hours).

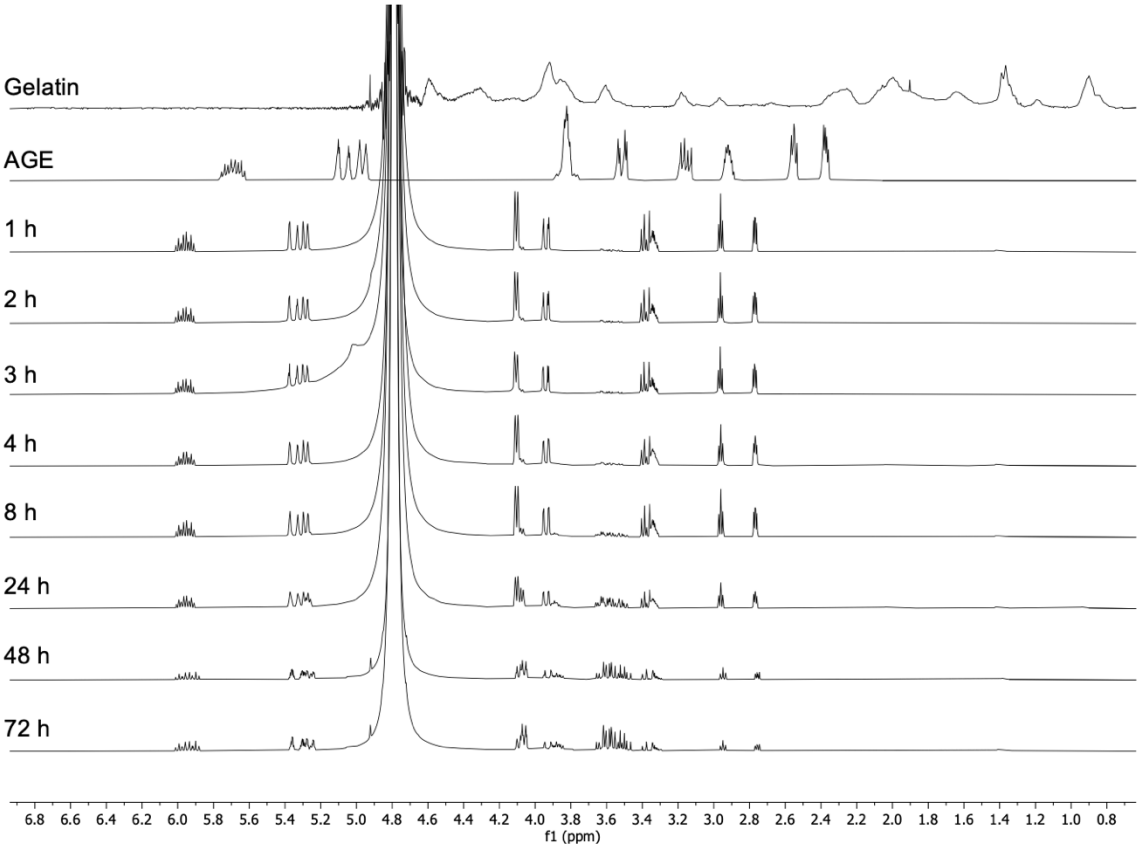


Figure B.4. ^{1}H NMR spectra of starting reagents gelatin (D_2O, 400 Hz) and AGE ($CDCl_3$, 400 Hz), and the progressing reaction at 1, 2, 3, 4, 8, 24, 48, and 72 hours in PB (D_2O, 400 Hz) [PB = phosphate buffer; h = hours].

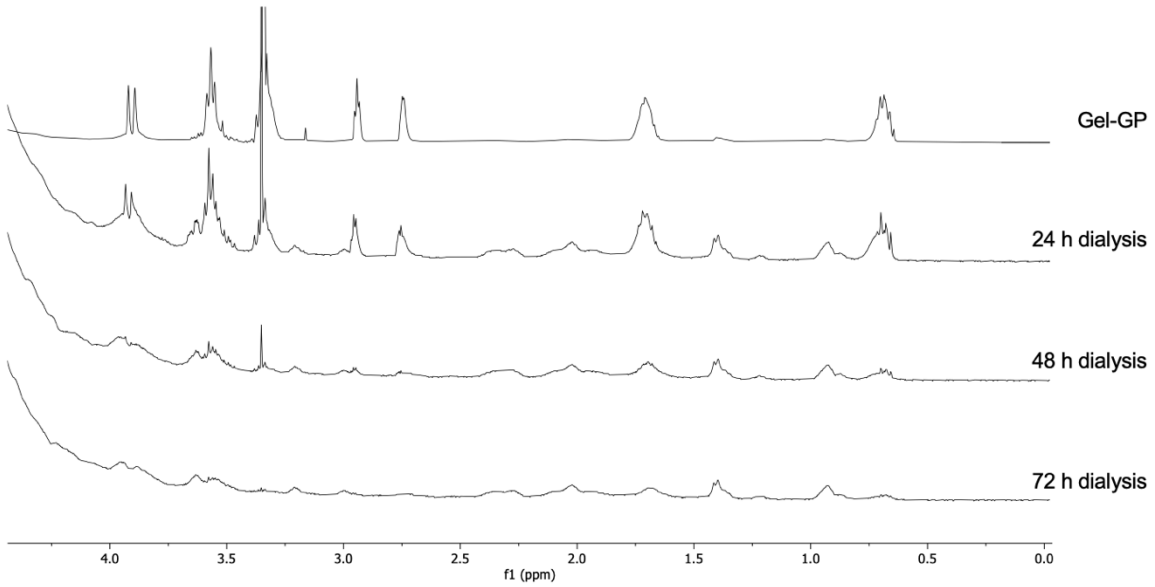


Figure B.5. ^{1}H NMR of the Gel-GP product from PB reaction conditions and further dialysis reaction for 72 hours (D_2O, 400 Hz) [h = hours].

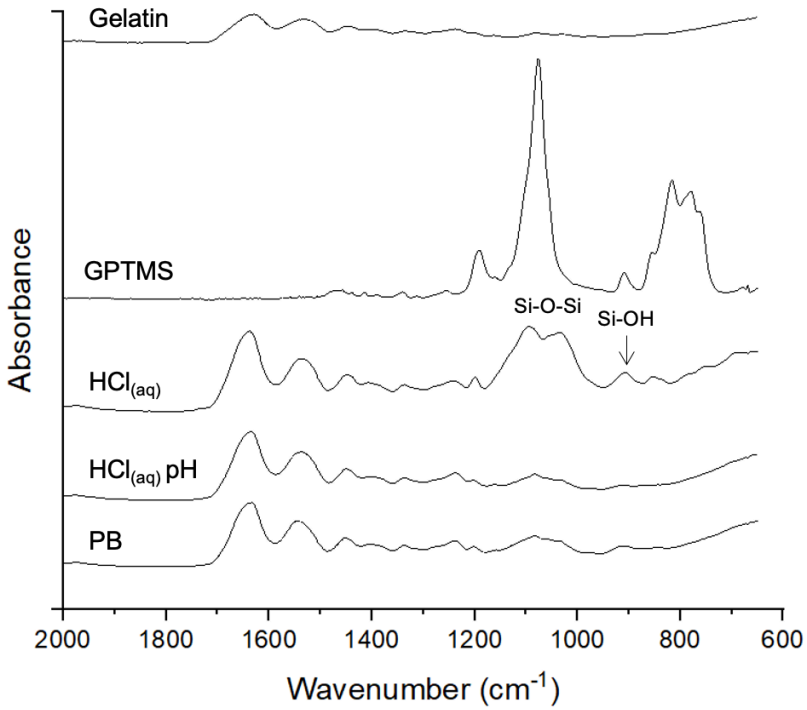


Figure B.6. FTIR spectra of gelatin and GPTMS, as well as their products when reacted in the three following conditions: $HCl_{(aq)}$, $HCl_{(aq)}$ pH, and PB. Resonances corresponding to Si–O–Si and Si–OH are noted (PB = phosphate buffer).

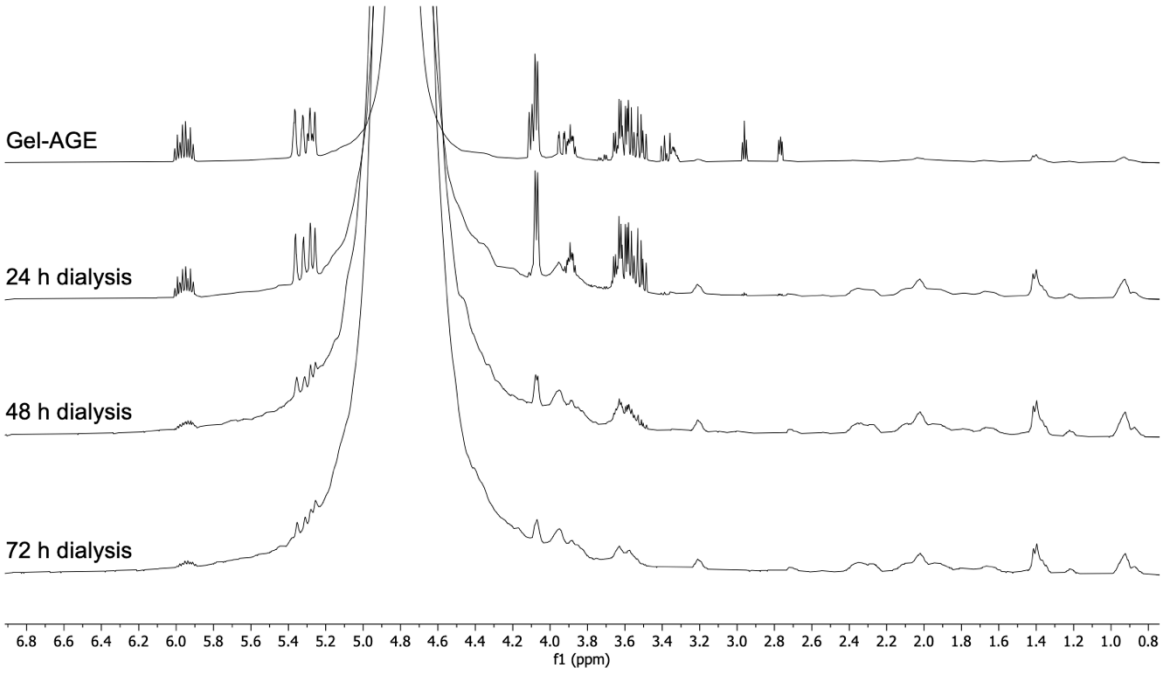


Figure B.7. ^1H NMR of the Gel-AGE product from $HCl_{(aq)}$ pH reaction conditions and further dialysis reaction for 72 hours (D_2O, 400 Hz) [h = hours].

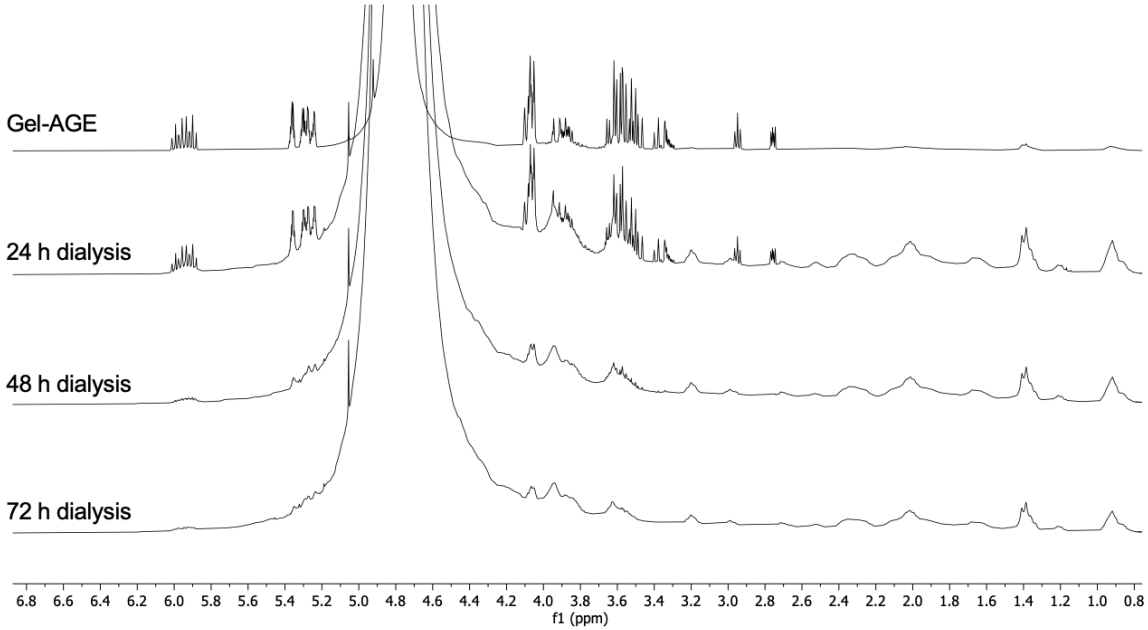


Figure B.8. ^{1}H NMR of the Gel-AGE product from PB reaction conditions and further dialysis reaction for 72 hours (D_2O, 400 Hz) [PB = phosphate buffer; h = hours].

Appendix C

C.4.2. Methods

C.4.2.2. GelNB-MPTMS functionalisation reaction controls

C.4.2.2.1. Effect of removing LAP or MPTMS

The method in Section 4.2.2 was followed, but MPTMS or LAP was removed from the reaction.

C.4.2.2.2. Effect of using oxidised MPTMS

MPTMS was mixed with H_2O and left sealed for 24 hours to oxidise. The oxidised disulfide was then used as usual in the GelNB functionalisation reaction, with aliquots taken at 10, and 30 seconds, as well as 1, 2, and 4 minutes for ^{1}H NMR spectroscopic analysis.

C.4.3. Results

C.4.3.1.4. GelNB-MPTMS functionalisation reaction controls

Control reactions were run to investigate the possibility of other reactions occurring in parallel with the thiol-norbornene reaction. The control reactions included: (1) LAP-free conditions, (2) MPTMS-free, and (3) using oxidised-MPTMS, i.e. the disulfide, instead of MPTMS. There was no reaction between GelNB and MPTMS in the absence of LAP as shown by maintenance of the alkene resonance at δ_H = 6.15 ppm (Appendix Figure C.1). Therefore, the use of LAP is critical for the thiol-ene reaction to take place. LAP was selected as the photoinitiator in this study due to its solubility in water, as well as its lower associated cytotoxicity due visible light initiation and the lower concentrations needed when compared to I2959, another commonly used photoinitiator that uses UV light and is not water soluble (378,379).

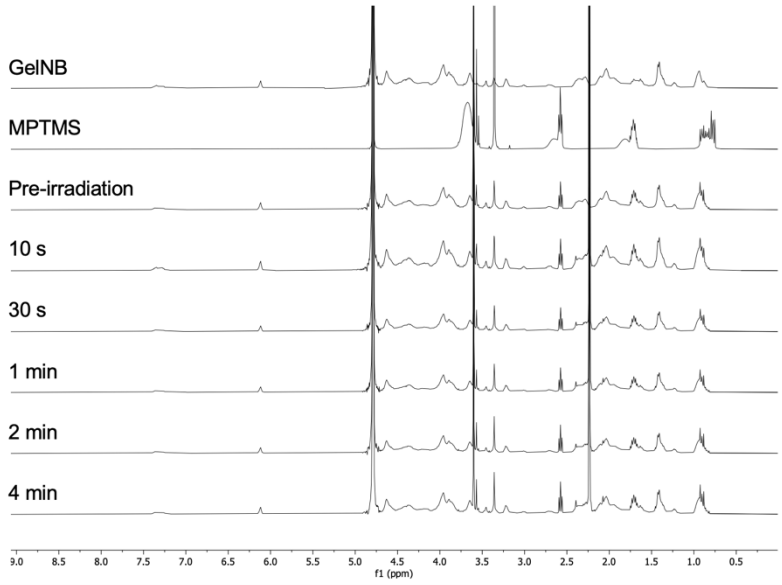


Figure C.1. ^{1}H NMR spectra of GelNB reacted with MPTMS (1:2), without the presence of LAP as a photoinitiator, for 4 minutes, 405 nm irradiation. Spectra shown for starting reagents GelNB and MPTMS, as well as samples taken pre-irradiation, and 10 and 30 seconds, and 1, 2 and 4 minutes of irradiation (D_2O, 400 MHz) [min = minutes; s = seconds].

When GelNB was reacted with LAP, without the presence of MPTMS, the resonance at δ_H = 6.15 ppm decreased over time within the 4-minute reaction (Appendix Figure C.2a). Therefore, it is hypothesised that GelNB and LAP react without the presence of MPTMS. This is likely due to reaction of the alkene with itself to form long chain GelNB polymers. However, the rate of reaction is slower, demonstrated through the slower consumption of the norbornene alkene double bond responsible for the resonance at δ_H = 6.15 ppm and the resonance still being present after 4 minutes (Appendix Figure C.2b). This information, alongside the thiol-norbornene reaction data, indicates that GelNB favours the thiol-ene reaction over polymerisation – shown by the faster consumption of the alkene in the thiol-norbornene reaction.

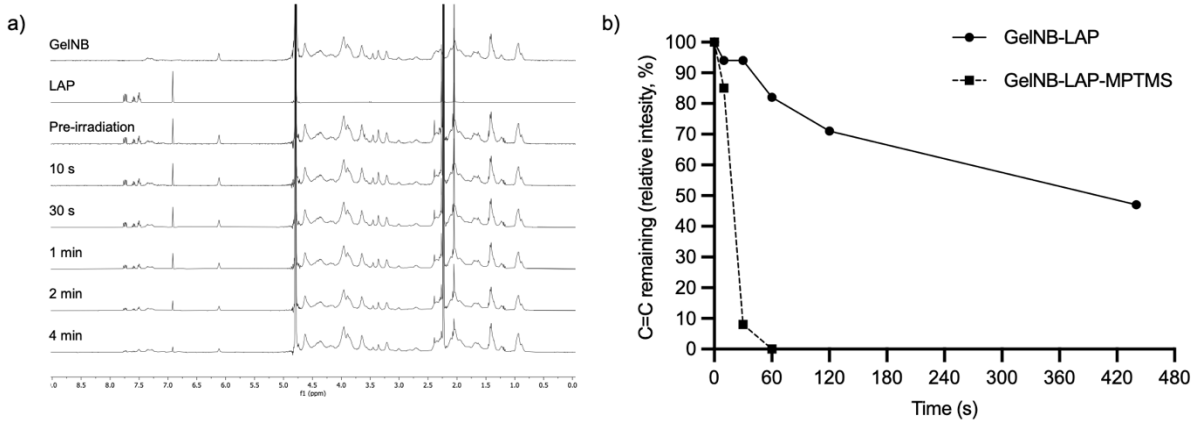


Figure C.2. a) ^{1}H NMR spectra of GelNB reacted with LAP (0.3 wt%) for 4 minutes, 405 nm irradiation. Spectra shown for starting reagents GelNB and LAP, as well as samples taken pre-irradiation, and 10 and 30 seconds, and 1, 2 and 4 minutes of irradiation (D_2O, 400 MHz) and b) Relative intensity of δ_H = 6.15 ppm signal (C=C) converted to % in GelNB and LAP reaction with, and without, MPTMS (min = minutes; s = seconds).

Thiols are easily oxidised to disulfides. Hence, the importance of investigating the role oxidised MPTMS could play in the thiol-norbornene reaction. When GelNB was reacted with the disulfide (oxidised-MPTMS), thiol-norbornene characteristic spectral changes were observed – complete loss of the resonance at δ_H = 6.15 ppm and appearance of a new resonance at δ_H = 2.70 ppm (Appendix Figure C.3). Full conversion of the alkene had occurred by 30 seconds. It can be suggested that a disulphide is also a substrate for this GelNB-MPTMS reaction leading to successful functionalisation.

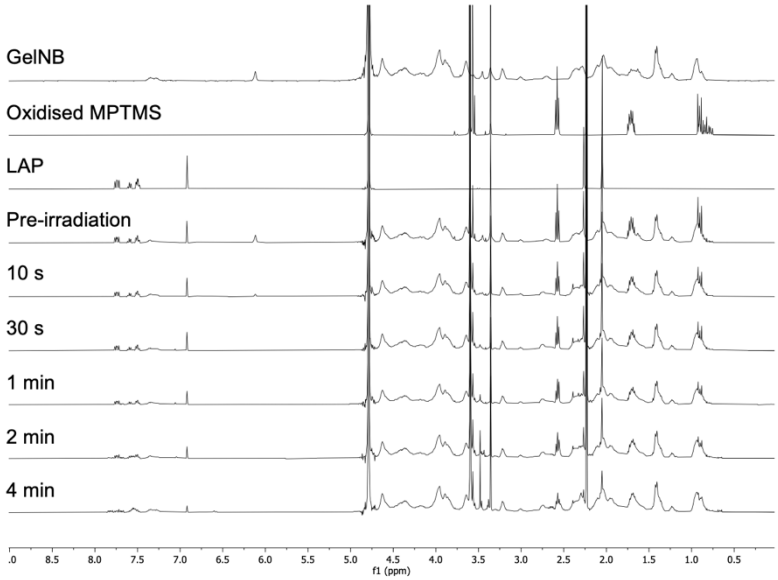


Figure C.3. ^{1}H NMR spectra of GelNB reacted with oxidised MPTMS (1:2) in the presence of LAP (0.3 wt%) for 4 minutes, 405 nm irradiation. Spectra shown for starting reagents GelNB, oxidised MPTMS and LAP, as well as samples taken pre-irradiation, and 10 and 30 seconds, and 1, 2 and 4 minutes of irradiation (D_2O, 400 MHz) [min = minutes; s = seconds].

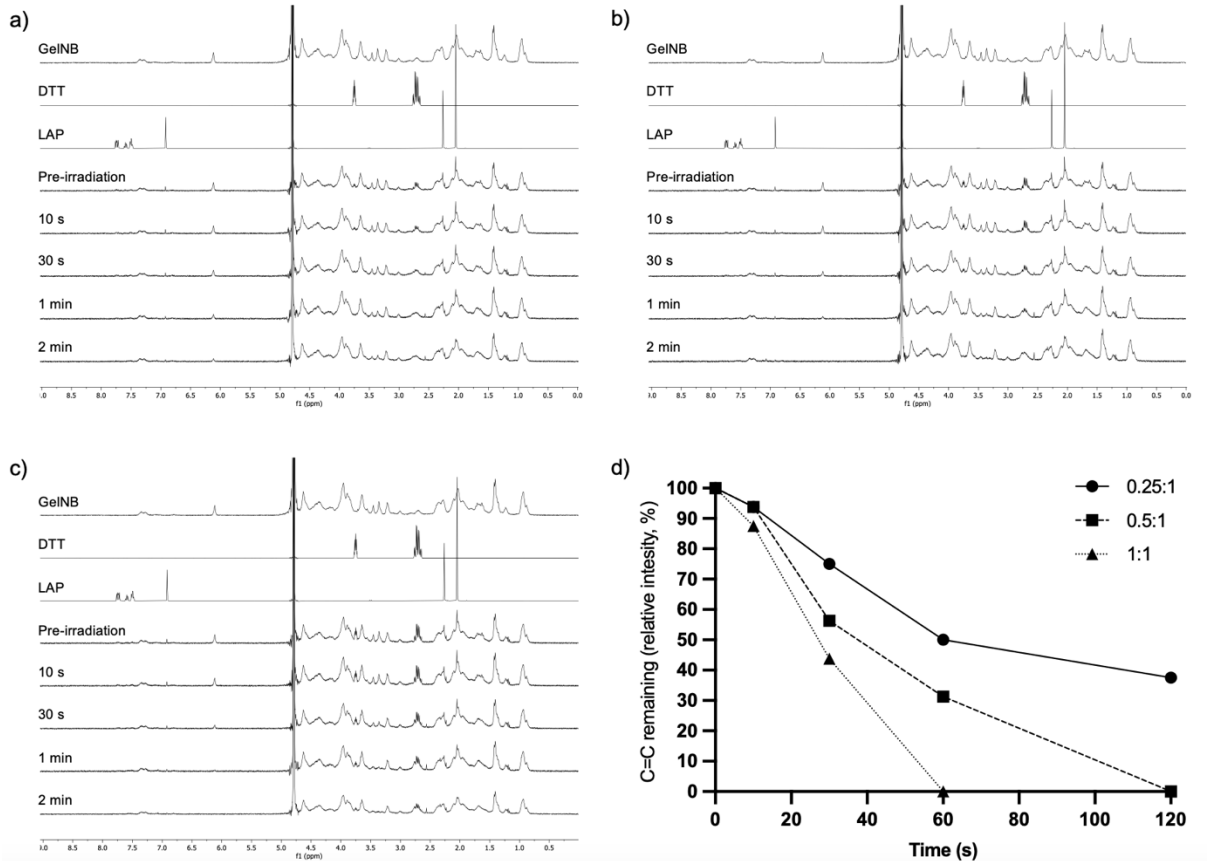


Figure C.4. ^{1}H *NMR spectra of GelNB reacted with varying ratios of DTT:GelNB, a) 0.25:1.00, b) 0.5:1.0, and c) 1:1, in the presence of LAP (0.3 wt%) for 2 minutes, 405 nm irradiation. Spectra shown for starting reagents GelNB, DTT and LAP, as well as samples taken pre-irradiation, and 10 and 30 seconds, and 1 and 2 minutes of irradiation (D_2O, 400 MHz), and b) Relative intensity of* δ_H *= 6.15 ppm signal (C=C) converted to % in GelNB and DTT reaction with, varying ratios of DTT:GelNB (min = minutes; s = seconds).*

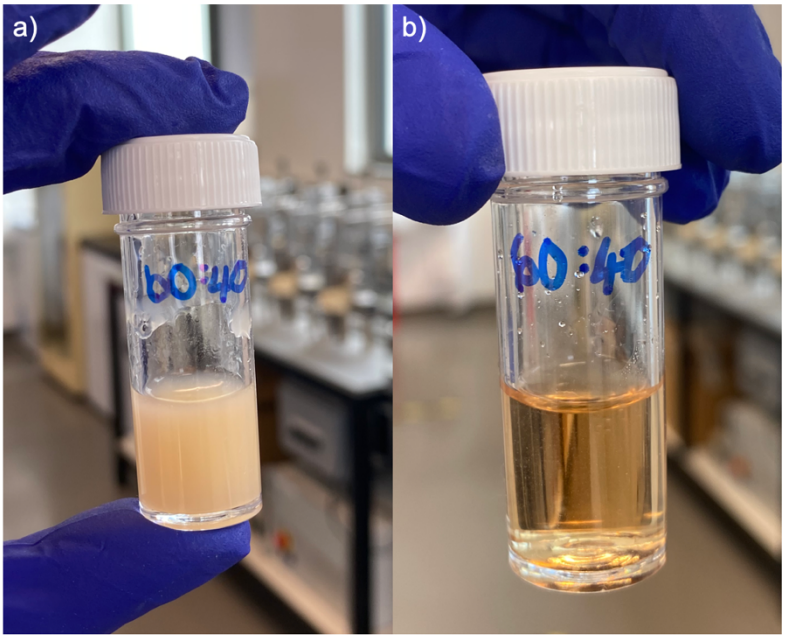


Figure C.5. Preliminary experiments showing GelNB-MP-Silica hydrogels of a 60:40 (organic:inorganic) formulation, mixed with DMEM:dH_2O at a ratio of a) 1:0 and b) 1:1.